COYOTE SERIES DATA REPORT
LLNL/NWC 1981 LNG SPILL TESTS
DISPERSION, VAPOR BURN, AND
RAPID-PHASE-TRANSITION

H.C. Goldwire, Jr.
H.C. Rodean
R.T. Cederwall
E.J. Kansa
R.P. Koopman
J.W. McClure
T.G. McRae
L.K. Morris
L. Kamppinen
R.D. Kiefer
P.A. Urtiew
of LLNL
C.D. Lind of NWC

October 1983

Lawrence Livermore Laboratory

DISCLAIMER

Page Range	Domestic Price	Page Range	Domestic Price
001-025	$ 7.00	326-350	$ 26.50
026-050	8.50	351-375	28.00
051-075	10.00	376-400	29.50
076-100	11.50	401-426	31.00
101-125	13.00	427-450	32.50
126-150	14.50	451-475	34.00
151-175	16.00	476-500	35.50
176-200	17.50	501-525	37.00
201-225	19.00	526-550	38.50
226-250	20.50	551-575	40.00
251-275	22.00	576-600	41.50
276-300	23.50	601-up[1]	
301-325	25.00		

Add 1.50 for each additional 25 page increment, or portion thereof from 601 pages up.

BEST AVAILABLE COPY

FOR ORIGINAL REPORT

CALL

REPORTS LIBRARY

X37097

Acknowledgements

The data reported here represent the work of many people from several organizations. We would like to acknowledge the hard work and dedication of the following individuals and organizations:

LLNL/Livermore

John Baker

Greg Bianchini

Rex Blocker

Marilyn Borton

Jeff Davis

Cleo Fry

David Hipple

Bill Hogan

Gale Holladay

Gary Johnson

Dave Morgan

William O'Neal

Joe Shinn

Diane Soto

Myles Spann, Jr.

EG&G Special Measurements Department, LVO
EG&G Remote Measurements Department, LVO

150r/23r

CONTENTS

Tables

150r/23r

ABSTRACT

The Coyote series of liquefied natural gas (LNG) spill experiments was performed at the Naval Weapons Center (NWC), China Lake, California, during the summer and fall of 1981. These tests were a joint effort of the Lawrence Livermore National Laboratory (LLNL) and the NWC and were sponsored by the U.S. Department of Energy (DOE) and the Gas Research Institute. There were ten Coyote experiments, five primarily for the study of vapor dispersion and burning vapor clouds, and five for investigating the occurrence of rapid-phase-transition (RPT) explosions. Each of the last four of the five RPT tests consisted of a series of three spills. Seven experiments were with LNG, two were with liquid methane (LCH_4), and one was with liquid nitrogen (LN_2). Three arrays of instrumentation were deployed. An array of RPT diagnostic instruments was concentrated at the spill pond and was operated during all of the tests, vapor burn as well as RPT. The wind-field array was operated during the last nine experiments to define the wind direction and speed in the area upwind and downwind of the spill pond. The gas-dispersion array was deployed mostly downwind of the spill pond to measure gas concentration, humidity, temperature, ground heat flux, infrared (IR) radiation, and flame-front passage during three of the vapor dispersion and burn experiments (Coyotes 3, 5, and 6). High-speed color motion pictures were taken during every test, and IR imagery (side and overhead) was obtained during some vapor-burn experiments. Data was obtained by radiometers during Coyotes 3, 6, and 7. This report presents a comprehensive selection of the data obtained. It does not include any data analysis except that required to determine the test conditions and the reliability of the data. Data analysis is to be reported in other publications.

150r/23r

1. INTRODUCTION

Since 1978, LLNL and NWC have been conducting field experiments with LNG at China Lake, California, under the joint sponsorship of the DOE and the Gas Research Institute. The purpose of the Burro series, conducted in the summer of 1980, was to determine the transport and dispersion of vapor from spills of LNG on water. The Coyote series was conducted in the summer and fall of 1981 to investigate further RPT explosions observed during two Burro experiments and to determine the characteristics of fires resulting from ignition of vapor clouds from LNG spills.

This report is similar in content and purpose to the Burro Data Report [1]. Its purpose is to make the Coyote data available in a format that will be of the most use to the largest number of people. The Coyote data set is voluminous, consisting of several million words of digital data stored in a LLNL data base. Not all data are included in this report; judgement has been exercised in selecting the data presented. In addition, it is not feasible to include the motion pictures and complete IR imagery sequences. If the users of this report need data that are not given here, or data in a different format, they are advised to contact the authors of this report. This report contains only essential analysis needed to define the test conditions and evaluate data quality. Analysis of data presented here will be published elsewhere.

2. TEST SUMMARIES

The Coyote series consisted of ten experiments, five emphasizing the study of vapor-cloud fires and five for investigating RPT explosions. A brief summary of the Coyote series is presented in Table 1.

The first vapor-burn experiment, Coyote 2, was with a small spill (8 m^3) of LNG and was conducted to assess instrument capability and survivability in vapor fires. Coyotes 3, 5, and 6 involved larger spills of LNG ranging from 14.6 to 28 m^3, and Coyote 7 was a spill of 26 m^3 of liquid methane. The wind velocity ranged from 4.6 to 9.7 m/s and the atmospheric stability from unstable to neutral. Table 2 presents the instrumentation for each of the five vapor-burn tests. The instrument arrays (see Sections 3 and 4) were fully operational during the Coyote 3, 5, and 6 vapor-burn tests. The vapor

TABLE 1.
Coyote Series Test Summary

Coyote Test	Date	Test Type	Material Spilled	Spill Rate (m^3/min)	Spill Volume (m^3)	RPTs
1	7/30	RPT	LNG	6	14	small early large late
2	8/20	vapor burn	LNG	16	8	small early
3	9/2	vapor burn	LNG	13.5	14.6	none
4	9/25	RPT	LNG	6.8 12.1 18.5	3.8 6.0 5.2	small early none large early
5	10/7	vapor burn	LNG	17.1	28	large late
6	10/27	vapor* burn	LNG	16.6	22.8	none
7	11/12	vapor* burn	LCH_4	14.0	26	none
8	11/13	RPT	LCH_4	7.5 14.2 19.4	3.7 5.4 9.7	none none none
9	11/16	RPT	LN_2	7.2 9.9 13.3	3.6 3.3 8.2	none none none
10	11/24	RPT	LNG	13.8 19.3 18.8	4.6 4.5 5.0	none none large early

*Jet ignitor used, but it functioned successfully on only Coyote 7. Coyote 6 was ignited with a back-up flare.

TABLE 2.
Extent of coverage of the Coyote vapor-burn experiments by various
types of instrumentation to measure the wind field, vapor dispersion,
and vapor-burn phenomena.

| | Arrays | | Color | IR Imagery | | External |
Coyote	Wind Field	Gas and Turbulence	Motion Pictures	Side	Overhead	Radiometers
2	X		X			
3	X	X	X	X		X
5	X	X	X	X		
6	X	X	X	X	X	X
7	X		X	X	X	X

clouds were centered fully within the arrays for only Coyotes 5 and 6. Color
motion pictures were taken during all the Coyote experiments, and IR imagery
was obtained during Coyotes 3 and 5-7 (see Section 4). In summary, some data
are available for every vapor-burn experiment; a fairly complete set of data
is available for Coyote 3, but the most complete sets are for Coyotes 5 and 6.

The first RPT test, Coyote 1, was with a spill of 14 m^3 at a rate of
6 m^3/min as a result of a spill valve malfunction. The remaining RPT tests
(Coyotes 4 and 8-10) consisted of a series of three spills (A, B, and C)
ranging from 3.3 to 9.7 m^3 at nominal rates of 5, 10, and 20 m^3/min.
Coyotes 1, 4, and 10 were conducted with LNG, Coyote 8 with liquid methane,
and Coyote 9 with liquid nitrogen. The RPT instrumentation was located on or
around the spill pond and was operated during all the Coyote experiments.
RPTs occurred during three of the five RPT tests (Coyotes 1, 4, and 10) and
two of the five vapor-burn tests (Coyotes 2 and 5).

A complete set of spill, ignition, and meteorological parameters is given
in Table 3 for Coyotes 3-10 when the meteorological array and sensors were
operational. The array centerline was fixed at 227° for the duration of the
series. Using wind-field data from the twenty 2-m-high anemometer stations,

TABLE 3. DETAILED TEST SUMMARY FOR COYOTES 3 - 10.

Test name	Coyote 3	Coyote 4a	Coyote 4b	Coyote 4c
Test type	Vapor Burn	RPT	RPT	RPT
Material	LNG	LNG	LNG	LNG
Composition	Methane 79.4%	Methane 78.8%	Methane 78.8%	Methane 78.8%
	Ethane 16.4%	Ethane 17.3%	Ethane 17.3%	Ethane 17.3%
	Propane 4.2%	Propane 3.9%	Propane 3.9%	Propane 3.9%
Date	3 Sep 1981	25 Sep 1981	25 Sep 1981	25 Sep 1981
Valve begins to open	15:38:24 PDT	17:30:22 PDT	17:52:33 PDT	18:16:01 PDT
Valve open (zero time)	15:38:26 PDT	17:30:24 PDT	17:52:35 PDT	18:16:03 PDT
Valve begins to close	15:39:28 PDT	17:30:52 PDT	17:52:56 PDT	18:16:14 PDT
Valve closed	15:39:30 PDT	17:30:54 PDT	17:52:58 PDT	18.16:16 PDT
Spill rate	13.5 m^3/min	6.8 m^3/min	12.1 m^3/min	18.5 m^3/min
Spill volume	14.6 m^3	3.8 m^3	6 m^3	5.2 m^3
Spill duration	65 s	34 s	30 s	17 s
Dump pipe height	1.5 m	1.5 m	1.5 m	1.5 m
Ignition time				
After valve opens	99.7 s			
After valve closes	37.3 s			
Ignition location				
X coordinate	61 m			
Y coordinate	20 m			
Array centerline	227°	227°	227°	227°
Average wind direction (theta)	205°	181°	190°	197°
Standard deviation	11°	5°	5°	3°
Average 10-s sigma theta	6.0°	5.5°	5.5°	4.7°
Average wind speed	6.0 m/s	6.2 m/s	6.0 m/s	7.4 m/s
Standard deviation	0.9 m/s	0.6 m/s	0.7 m/s	0.7 m/s
Upwind vertical profile				
At 1 m	6.12 m/s	3.44 m/s	5.32 m/s	7.91 m/s
At 3 m	6.77 m/s	4.96 m/s	6.28 m/s	8.96 m/s
At 8 m	7.33 m/s	7.06 m/s	6.92 m/s	9.50 m/s
U star	0.280 m/s	0.280 m/s	0.269 m/s	0.328 m/s
Percent cloud cover	15%	30%	30%	30%
Temperature at 2 m	37.91°C	30.72°C	29.90°C	28.29°C
Temperature at 0.5 m	39.55°C	31.30°C	30.31°C	28.58°C
Temperature at 1 m	38.30°C	30.75°C	29.87°C	28.21°C
Temperature at 4 m	37.23°C	30.29°C	29.53°C	27.97°C
T star	-1.02°C	-0.43°C	-0.32°C	-0.24°C
Barometric pressure	936 millibars	942 millibars	942 millibars	942 millibars
Upwind humidity (TI)	11.3%	12.5%	12.4%	14.7%
Turbulent Prandtl no.	0.64	0.81	0.85	0.92
Sensible heat flux	-313.5 watt/m^2	-81.3 watt/m^2	-52.8 watt/m^2	-40.2 watt/m^2
Momentum diffusivity (2 m)	0.352 m^2/s	0.276 m^2/s	0.255 m^2/s	0.286 m^2/s
Richardson no (2 m)	-0.317	-0.083	-0.06	-0.025
Monin-Obukhov length	-6.32 m	-24.2 m	-33.3 m	-79.4 m

TABLE 3. (Continued)

Test name	Coyote 5	Coyote 6	Coyote 7	Coyote 8a
Test type	Vapor burn	Vapor burn	Vapor burn	RPT
Material	LNG	LNG	LNG	LNG
Composition	Methane 74.9%	Methane 81.8%	Methane 99.5%	Methane 99.7%
	Ethane 20.5%	Ethane 14.6%	Ethane 0.5%	Ethane 0.3%
	Propane 4.6%	Propane 3.6%		
Date	7 Oct 1981	27 Oct 1981	12 Nov 1981	13 Nov 1981
Valve begins to open	12:08:48 PDT	16:43:21 PST	15:24:38 PST	14:59:04 PST
Valve open (zero time)	12:08:50 PDT	16:43:23 PST	15:24:41 PST	14:59:06 PST
Valve begins to close	12:10:37 PDT	16:44:39 PST	15:26:38 PST	14:59:35 PST
Valve closed	12:10:39 PDT	16:44:40 PST	15:26:40 PST	14:59:37 PST
Spill rate	17.1 m^3/min	16.6 m^3/min	14.0 m^3/min	7.5 m^3/min
Spill volume	28.0 m^3	22.8 m^3	26.0 m^3	3.7 m^3
Spill duration	98 s	82 s	111 s	30 s
Dump pipe height	1.5 m	1.5 m	1.5 m	1.5 m
Ignition time				
After valve opens	132.7 s	108.0 s	146.1 s	
After valve closes	+25.4 s	+32.5 s	+29.0 s	
Ignition location				
X coordinate	79 m	79 m	85 m	
Y coordinate	0 m	0 m	20 m	
Array centerline	227°	227°	227°	227°
Average wind direction (theta)	229°	220°	210°	206°
Standard deviation	7°	5°	5°	5°
Average 10-s sigma theta	5.1°	5.1°	4.8°	5.0°
Average wind speed	9.7 m/s	4.6 m/s	6.0 m/s	8.4 m/s
Standard deviation	1.3 m/s	0.6 m/s	0.7 m/s	1.1 m/s
Upwind vertical profile				
At 1 m	10.22 m/s	4.99 m/s	6.07 m/s	8.07 m/s
At 3 m	10.47 m/s	5.04 m/s	6.72 m/s	9.03 m/s
At 8 m	11.91 m/s	5.93 m/s	7.38 m/s	9.88 m/s
U star	0.437 m/s	0.197 m/s	0.260 m/s	0.372 m/s
Percent cloud cover	44%	60%	75%	85%
Temperature at 2 m	27.90°C	24.37°C	25.54°C	23.15°C
Temperature at 0.5 m	29.27°C	24.13°C	25.41°C	23.50°C
Temperature at 1 m	28.34°C	24.11°C	25.34°C	23.10°C
Temperature at 4 m	27.14°C	24.31°C	25.39°C	22.88°C
T star	−0.95°C	0.11°C	0.02°C	−0.25°C
Barometric pressure	939 millibars	942 millibars	944 millibars	945 millibars
Upwind humidity (TI)	22.1%	22.8%	19.2%	20.6%
Turbulent Prandtl no.	0.82	1.14	1.03	0.93
Sensible heat flux	−283.5 watt/m^2	9.42 watt/m^2	4.61 watt/m^2	−47.1 watt/m^2
Momentum diffusivity (2 m)	0.426 m^2/s	0.139 m^2/s	0.202 m^2/s	0.319 m^2/s
Richardson no (2 m)	−0.076	0.027	0.006	−0.02
Monin-Obukhov length	−26.5 m	73.6 m	345.2 m	−98.6 m

TABLE 3. (Continued)

Test name	Coyote 8b	Coyote 8c	Coyote 9a	Coyote 9b
Test type	RPT	RPT	RPT	RPT
Material	LNG	LNG	LN_2	LN_2
Composition	Methane 99.7%	Methane 99.7%		
	Ethane 0.3%	Ethane 0.3%		
Date	13 Nov 1981	13 Nov 1981	16 Nov 1981	16 Nov 81
Valve begins to open	15:25:15 PST	15:54:16 PST	15:00:35 PST	15:19:16 PST
Valve open (zero time)	15:25:17 PST	15:54:18 PST	15:00:37 PST	15:19:18 PST
Valve begins to close	15:25:37 PST	15:54:55 PST	15:01:07 PST	15:19:36 PST
Valve closed	15:25:39 PST	15:54:57 PST	15:01:09 PST	15:19:38 PST
Spill rate	14.2 m^3/min	19.4 m^3/min	7.2 m^3/min	9.9 m^3/min
Spill volume	5.4 m^3	9.7 m^3	3.6 m^3	3.3 m^3
Spill duration	23 s	30 s	30 s	20 s
Dump pipe height	1.5 m	1.5 m	1.5 m	1.5 m
Ignition time				
After valve opens				
After valve closes				
Ignition location				
X coordinate				
Y coordinate				
Array centerline	227°	227°	227°	227°
Average wind direction (theta)	209°	214°	158°	193°
Standard deviation	4°	6°	16°	6°
Average 10-s sigma theta	5.0°	5.5°	7.5°	5.3°
Average wind speed	9.0 m/s	8.5 m/s	2.6 m/s	4.2 m/s
Standard deviation	1.1 m/s	1.1 m/s	0.6 m/s	0.5 m/s
Upwind vertical profile				
At 1 m	9.72 m/s	9.64 m/s	2.15 m/s	4.22 m/s
At 3 m	10.71 m/s	10.19 m/s	2.66 m/s	4.57 m/s
At 8 m	11.80 m/s	11.22 m/s	3.36 m/s	4.93 m/s
U star	0.396 m/s	0.370 m/s	0.120 m/s	0.189 m/s
Percent cloud cover	85%	85%	1%	1%
Temperature at 2 m	22.77°C	22.10°C	26.52°C	26.89°C
Temperature at 0.5 m	22.89°C	22.05°C	26.69°C	27.16°C
Temperature at 1 m	22.65°C	21.93°C	26.37°C	26.75°C
Temperature at 4 m	22.57°C	21.95°C	26.27°C	26.64°C
T star	-0.12°C	-0.02°C	-0.16°C	-0.20°C
Barometric pressure	945 millibars	945 millibars	xxx millibars	xxx millibars
Upwind humidity (TI)	20.2%	21.1%	21.0%	18.7%
Turbulent Prandtl no.	0.97	1.0	0.69	0.81
Sensible heat flux	-20.0 watt/m^2	-0.07 watt/m^2	-16.8 watt/m^2	-24.2 watt/m^2
Momentum diffusivity (2 m)	0.325 m^2/s	0.296 m^2/s	0.139 m^2/s	0.186 m^2/s
Richardson no (2 m)	-0.007	-0.0	-0.216	-0.079
Monin-Obukhov length	-278.9 m	-66466.0 m	-9.26 m	-25.2 m

102r/23r

TABLE 3. (Continued)

Test name	Coyote 9c	Coyote 10a	Coyote 10b	Coyote 10c
Test type	RPT	RPT	RPT	RPT
Material	LN$_2$	LNG	LNG	LNG
Composition		Methane 70.2%	Methane 70.2%	Methane 70.2%
		Ethane 17.2%	Ethane 17.2%	Ethane 17.2%
		Propane 12.6%	Propane 12.6%	Propane 12.6%
Date	16 Nov 1981	24 Nov 1981	24 Nov 1981	24 Nov 1981
Valve begins to open	15:38:46 PST	11:32:11 PST	12:01:47 PST	14:08:25 PST
Valve open (zero time)	15:38:48 PST	11:32:13 PST	12:01:49 PST	14:08:27 PST
Valve begins to close	15:39:45 PST	11:32:31 PST	12:02:00 PST	14:08:45 PST
Valve closed	15:39:47 PST	11:32:33 PST	12:02:02 PST	14:08:47 PST
Spill rate	13.3 m^3/min	13.8 m^3/min	19.3 m^3/min	18.8 m^3/min
Spill volume	8.2 m^3	4.6 m^3	4.5 m^3	5.0 m^3
Spill duration	37 s	20 s	14 s	16 s
Dump pipe height	1.5 m	1.5 m	1.5 m	1.5 m
Ignition time				
After valve opens				
After valve closes				
Ignition location				
X coordinate				
Y coordinate				
Array centerline	227°	227°	227°	227°
Average wind direction (theta)	187°	223°	229°	248°
Standard deviation	5°	6°	5°	7°
Average 10-s sigma theta	5.4°	4.9°	5.3°	5.3°
Average wind speed	4.2 m/s	7.6 m/s	8.6 m/s	7.2 m/s
Standard deviation	0.5 m/s	1.1 m/s	1.1 m/s	0.9 m/s
Upwind vertical profile				
At 1 m	3.72 m/s	xxx m/s	xxx m/s	xxx m/s
At 3 m	4.46 m/s	xxx m/s	xxx m/s	xxx m/s
At 8 m	4.86 m/s	xxx m/s	xxx m/s	xxx m/s
U star	0.185 m/s	0.339 m/s	0.381 m/s	0.322 m/s
Percent cloud cover	1%	50%	50%	30%
Temperature at 2 m	26.49°C	21.28°C	21.36°C	22.00°C
Temperature at 0.5 m	26.51°C	21.80°C	21.76°C	22.51°C
Temperature at 1 m	26.28°C	21.31°C	21.38°C	22.07°C
Temperature at 4 m	26.34°C	20.95°C	21.07°C	21.62°C
T star	-0.04°C	-0.36°C	-0.29°C	-0.38°C
Barometric pressure	xxx millibars	942 millibars	942 millibars	942 millibars
Upwind humidity (TI)	18.8%			
Turbulent Prandtl no.	0.97	0.88	0.93	0.86
Sensible heat flux	-1.87 watt/m^2	-71.1 watt/m^2	-57.9 watt/m^2	-74.4 watt/m^2
Momentum diffusivity (2 m)	0.151 m^2/s	0.307 m^2/s	0.330 m^2/s	0.298 m^2/s
Richardson no (2 m)	-0.007	-0.041	-0.023	-0.049
Monin-Obukhov length	-303.7 m	-49.4 m	-86.3 m	-40.5 m

the mean and standard deviations for 10-s averages of wind direction and wind speed were calculated over a 3-min period that began at the start of the spill; averages of the 10-s standard deviation of the wind direction (σ_θ) were also calculated for the same 3-min period. The descriptive atmospheric-stability category is based on the Richardson number (R). The numerical values for atmospheric-stability indices and other meteorological parameters were determined as described below.

The temperature and temperature-difference values were measured on the upwind turbulence tower T01. Temperature (T) was measured at a height of 0.5 m, and temperature difference was measured between the 0.5-m sensor and the sensors at 1, 2, and 4 m. T star (T_*) was calculated by linear regression, using the formula

$$T_* = \frac{\partial T}{\partial (\ln z)}, \tag{1}$$

where z is the height above ground level. The T_* values did not vary significantly during the course of any experiment.

The diabatically adjusted friction velocity, U star (U_*), was derived from turbulence-tower and wind-field data, using the relationships

$$U(z) = \frac{U_*}{k} \left(\ln \frac{z}{z_0} - \psi \right), \tag{2}$$

$$U_* = \frac{k}{\phi} \frac{\partial U}{\partial (\ln z)}, \tag{3}$$

where $k = 0.4$ (von Karman's constant), U = wind speed (space-averaged), z_0 is the roughness length, and ψ and ϕ are functions of the Richardson number. For neutral-stability tests, the scaling parameters ϕ and ψ approach asymptotic values ($\psi \rightarrow 0$ and $\phi \rightarrow 1$ as $R \rightarrow 0$). One can then iteratively solve the wind-profile equation for the roughness length. At China Lake, the roughness length was approximately constant at a value of $z_0 = 2.05 \times 10^{-4}$m.

The Richardson number R, is defined by the relation

$$R = \frac{\frac{g}{T} \left(\frac{\partial T}{\partial z} + \frac{g}{C_p} \right)}{\left(\frac{\partial U}{\partial z} \right)^2}, \tag{4}$$

where g = 9.8 m/s^2 and C_p = 1005 W s kg^{-1} °C^{-1}. If R is assumed to be equal to z/L, where L is the Monin-Obukhov length, the reciprocal of the turbulent Prandtl number, α, and the parameters ϕ and ψ can be expressed as

$$\alpha = \frac{1}{\phi},$$

$$\phi = (1 - 16R)^{-\frac{1}{4}} \qquad \text{for } R \leq 0, \qquad (5)$$

$$\psi = 1.1(-R)^{\frac{1}{2}},$$

and

$$\alpha = \frac{1}{\phi},$$

$$\phi = 1 + 5R, \qquad \text{for } R > 0, \qquad (6)$$

$$\psi = -5R,$$

according to the theory of Dyer and Businger [2,3], as modified from Lettau [4] with our approximations.

The sensible heat flux, H, defined to be negative upward, is calculated from

$$H = \rho C_p k\alpha^2 U_* \left(T_* + \frac{gz}{C_p}\right), \qquad (7)$$

where ρ = 1.13 x 10^{-3} g/cm^3 (± 1% for 30 to 40°C).

The diabatically adjusted momentum diffusivity, K, and the Monin-Obukhov length are calculated from the formulas

$$K = \frac{U_* kz}{\phi}, \qquad (8)$$

and

$$L = \frac{\dfrac{U_*^3}{k}}{\dfrac{g}{T}\left(\dfrac{H}{\rho C_p}\right)}. \qquad (9)$$

3. FACILITY, EQUIPMENT, AND DATA

3.1 NWC Spill Facility

Since 1973, Dr. C.D. Lind of the NWC has been investigating the fire and explosion hazards of liquefied fuels. As part of this program, a facility was constructed in 1980 capable of spilling up to 40 m^3 of liquefied fuels on a water test basin to study the combustion or dispersion of the vapor produced [5]. This facility has been used for test spills of LNG, liquefied petroleum gas, gasoline, liquefied nitrogen, and liquefied ammonia.

Figure 1 is a site plan showing the layout of the facility. The 40-m^3 spill tank is a vacuum-jacketed tank 10.7-m-long by 3.5-m in diameter, with a total volume of 52 m^3; its design operating pressure is 2.4 bars. The liquid fuel is forced out of the tank through a 20-cm-diameter vertical stainless steel diptube when the tank is pressurized with gaseous nitrogen. A 25-cm-diameter insulated stainless steel spill line runs from the 40-m^3 tank to a junction north of the 5.7-m^3 tank. A 25-cm-diameter line continues from this point to the center of the water test basin, while a 15-cm-diameter insulated stainless steel spill line extends from this point to the edge of the 15 m^3 dry pond.

A splash plate was installed below the spill pipe outlet to limit the penetration of the LNG into the water, and to protect the facility from damage by RPTs. The plate was generally set at shallow depths during the vapor-burn and dispersion tests, but was placed at greater depths during the RPT tests.

The water test basin has an average diameter of 58 m, with an average water level about 1.5 m below the surrounding ground level. The average depth of the water is approximately 1 m. The slopes of all but the south bank have also been reduced to provide less turbulent wind flow over the water test basin.

Large heat-shield structures are used to provide thermal protection for both spill tanks, while a smaller heat shield protects the cooldown and spill valves. The heat shield protecting the 40-m^3 tank also provides protection for the nitrogen supply trailer.

The tank is loaded from an over-the-road trailer at a loading point 15 m from the tank through a 10-cm-diameter insulated stainless steel loading line. During loading, the tank is vented by means of a 20-cm-diameter vent
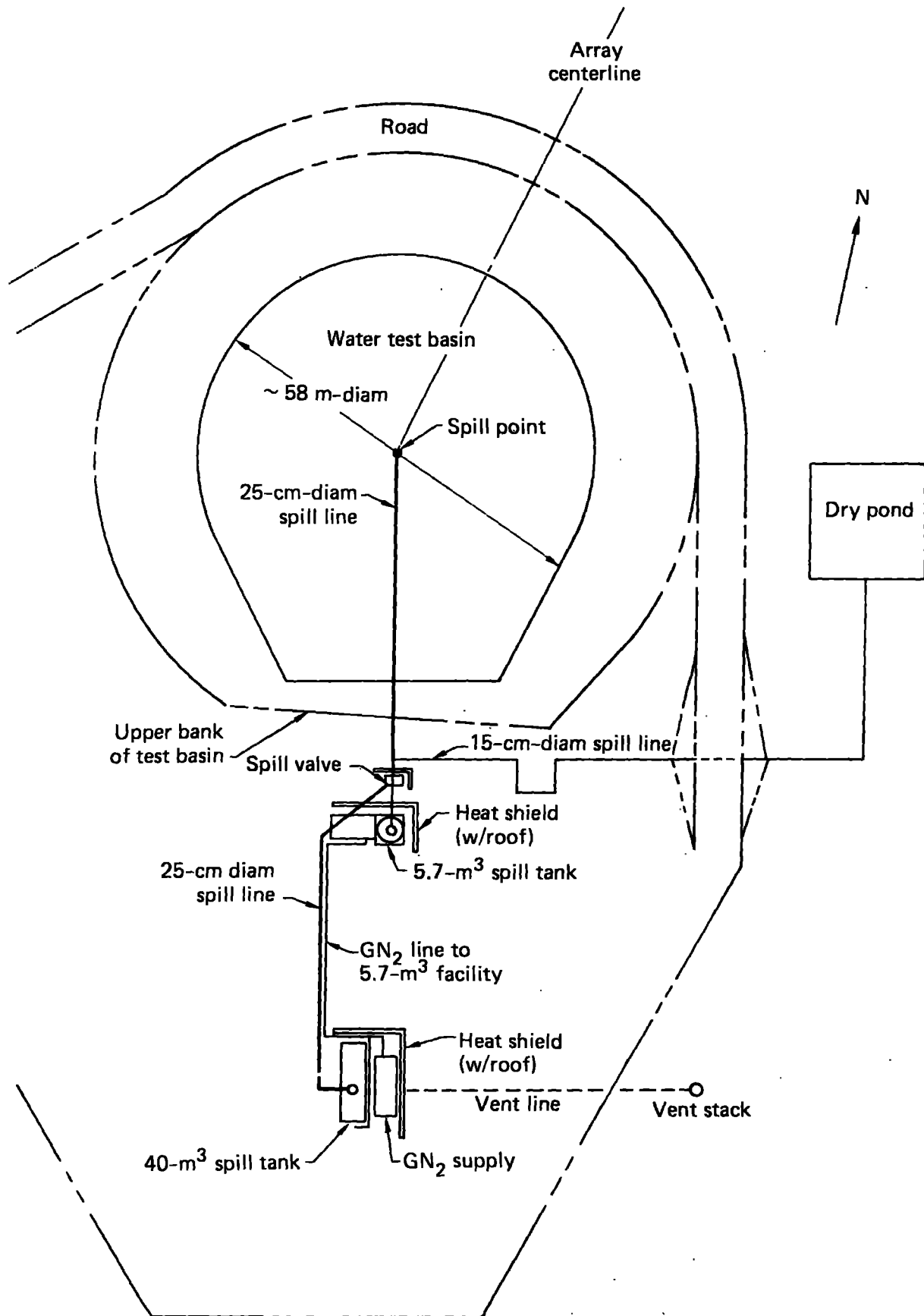
Fig. 1. Site plan of Naval Weapons Center (NWC) spill facility at China Lake.

line and an 18-m-high vent stack. After the tank is loaded, a sample is taken for later analysis.

Pressurization of the tank prior to a spill is achieved through three stages of pressure reduction from approximately 138 bars at the gaseous nitrogen trailer down to the operating pressure of the tank, 2.4 bars. This pressurization is remotely controlled and monitored from the control van.

The control van, located 250 m northwest of the tank, also contains controls for the remote operation of the vent system and the cooldown and spill valves. In addition, remote monitoring of the tank liquid level, tank and spill-line temperatures, tank internal pressure, nitrogen supply pressure, and liquid flow rate is done at the control van.

Prior to a spill, all personnel are cleared from the spill site and the spill is controlled remotely. The remote vent valve is closed, the three stages of pressure regulation are set, and the spill tank is pressurized. The cooldown valve is opened, permitting a small flow of LNG to cool the spill line. The spill valve is then opened and the test conducted. A "heel" of approximately 1.2 m^3 is usually left at the bottom of the tank after the test.

3.2 Instrumentation Arrays

The arrays of wind-field and gas-plus-turbulence stations are modifications of those used in the Burro series [1]. They are similar to the Burro arrays in that they are deployed upwind and downwind of the spill point along a bearing of 47° from true north, which coincides with the prevailing south-westerly wind direction during the summer months. (A nominal bearing of 45° from true north is indicated in Fig. 2.) Modifications were made because of (a) the Burro experience, (b) the environments associated with RPT explosions and vapor-cloud fires, and (c) the addition of RPT diagnostics and flame-related sensors.

The Burro experience showed that gas sensors beyond 400 m from the spill point were of limited value because of very low gas concentrations, and gas sensors as close as 57 m were adversely affected by water and mud thrown up by RPT explosions. Therefore, all but six of the 31 gas and turbulence stations were relocated to sites between 140 and 400 m, and five of the 20 wind-field array stations were repositioned accordingly. The locations of the stations
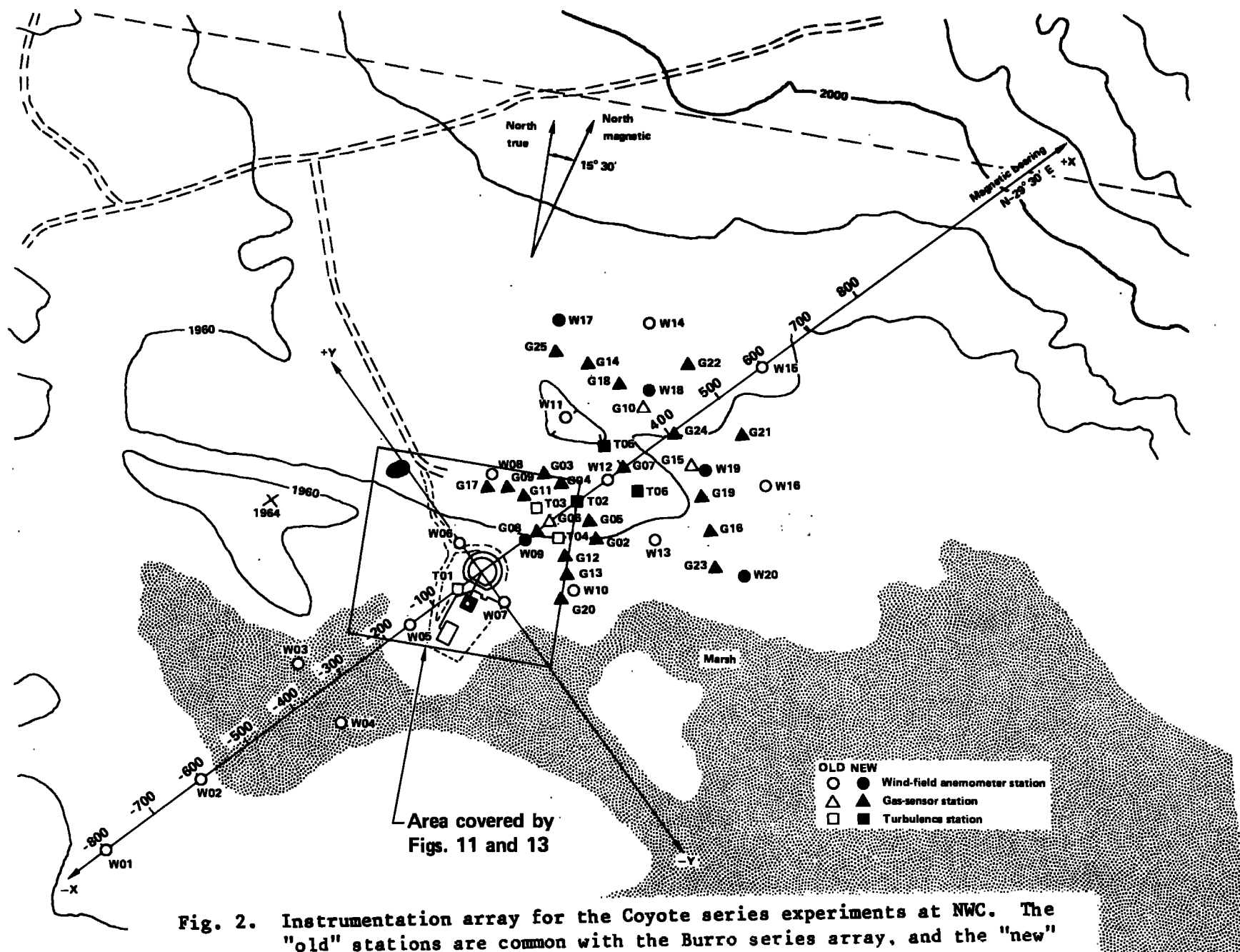
150r/23r

Fig. 2. Instrumentation array for the Coyote series experiments at NWC. The "old" stations are common with the Burro series array, and the "new" stations are different from the Burro series array in either location or designation.

in these arrays are given in Table 4 and shown in Fig. 2. There were a total of 25 gas stations during the Burro series, but only 24 during the Coyote experiments because the data channels for station G01 were used for RPT diagnostic data at the spill pond and temperature-profile data at station T01.

The wind-field array instrumentation consisted of two-axis, cup-and-vane anemometers mounted at an elevation of $z = 2$ m, as shown in Fig. 3. The type, number, and locations of sensors on the gas and turbulence stations for Coyotes 3-6 are given in Table 5. The Burro experience was also used to determine which type of gas sensor to install at which elevation on a tower (e.g., ISTs were fielded at $z = 8$ m on the close-in stations). Gas station G06 is shown in Fig. 4; it had all types of sensors except bivane anemometers which were installed on turbulence stations. In the Burro series, all six turbulence stations had bivane anemometers for measuring turbulent wind-velocity fluctuations. The construction of these anemometers is such that they are subject to damage by fire, so these anemometers were installed on only stations T01 (62 m upwind) and T06 (300 m downwind) for the Coyote series. The different instruments are described in Sections 4.1-4.3, together with other means of obtaining data about the vapor cloud dispersion and burning (photography, IR imagery, and external radiometer).

The RPT diagnostic array is illustrated in Fig. 5 and the instruments are described in Section 4.4.

The data were acquired at different rates from the sensors on the different kinds of stations. The wind-field station data consisted of 10-s averages for speed, direction, and (new on the Coyote series) standard deviation of direction. The sensors on the gas stations were sampled at intervals of 1 s and those on the turbulence stations at intervals of 0.3 s. The RPT diagnostic instrumentation was sampled at intervals of 1 s.

TABLE 4. Tower array coordinates relative to the spill point and the array centerline (Fig. 2). Station designations or locations different from those in the Burro Data Report [1] are indicated by an asterisk.

Tower	x (meters)	y (meters)	Elevation (meters)
W01	-800	0	595.33
W02	-600	0	590.54
W03	-350	60	591.24
W04	-350	-60	591.24
W05	-150	0	590.17
T01	-62	0	592.89
W06	0	60	593.12
W07	0	-60	591.91
W09*	90	0	597.17
W08	104	120	597.77
W10	104	-120	591.77
G08*	110	0	597.06
G17*	91.5	106	598.09
G09*	112	84	597.89
G11*	127	58	597.77
T03	137	30	597.64
G06	140	0	597.12
T04	137	-30	595.58
G12*	127	-58	593.53
G13*	112	-84	591.53
G20*	91.5	-106	591.21
G03*	186.5	72	596.87
G04*	196.6	36.9	596.80
T02*	200	0	596.71
G05*	196.6	-36.9	594.55
G02*	186.5	-72	593.65
W11	275	130	595.02
W12	275	0	594.83
W13	275	-130	593.30
T05*	296	48.3	594.76
G07*	300	0	594.98
T06*	296	-48.3	595.20
W17*	355	275	597.76
W20*	355	-275	593.40
G25*	330	226	597.08
G14*	360	174	596.59
G18*	382	118	596.27
G10	395.5	59.8	595.58
G24*	400	0	594.01
G15	395.5	-59.8	593.91
G19*	382	-118	593.98
G16*	360	-174	594.63
G23*	330	-226	593.42
W18*	410	85	595.95
W19*	410	-85	595.75
W14	480	170	596.39
W16	480	-170	592.65
G22*	495	71.2	596.56
G21*	495	-71.2	593.88
W15	600	0	595.11
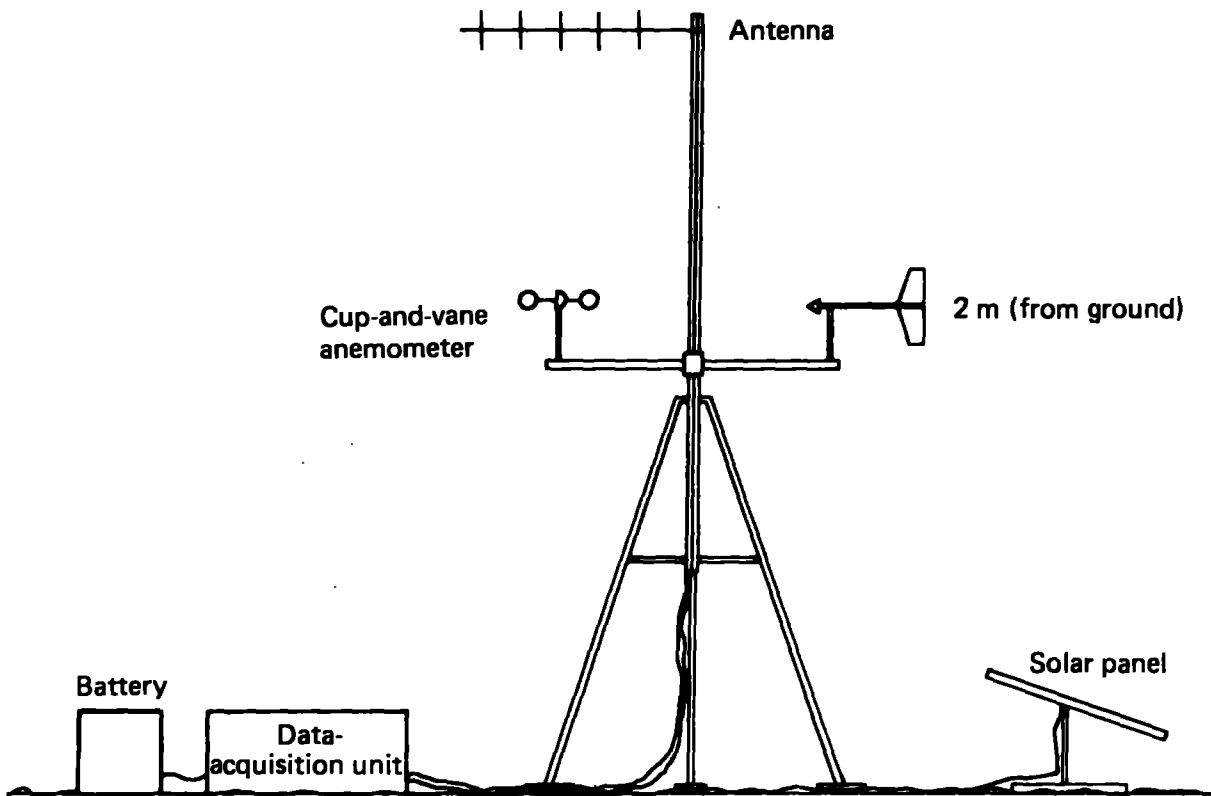
Fig. 3. Typical wind-field anemometer station.

TABLE 5.
Type, number, and locations of sensors in the array of gas and
turbulence stations for the vapor-burn experiments (Coyotes 3, 5, and 6).

Arc (m)	Station	Gas Con	Temp	HtFlx	Hum	Flm Vel	Cal	BiVn
-62	T01	0	3,4	0	1	0	0	3
110	G08	3	5	1	1	3	1	0
140	G17	3	3	0	0	0	0	0
	G09	3	4	0	0	0	0	0
	G11	4	4	0	0	0	0	0
	T03	3	4	0	0	3	1	0
	G06	3	7	1	1	3	1	0
	T04	3	4	0	0	3	1	0
	G12	3	4	0	0	0	0	0
	G13	3	4	0	0	0	0	0
	G20	3	4	0	0	0	0	0
200	G03	3	4	0	0	0	0	0
	G04	3	6	1	1	3	0	0
	T02	3	5	0	0	3	0	0
	G05	3	6	1	1	3	0	0
	G02	3	4	0	0	0	0	0
300	T07	3	4	0	0	3	0	0
	G07	4	4	1	1	0	0	0
	T06	3	4	0	0	3	0	3
400	G25	3	3	0	0	0	0	0
	G14	3	4	0	0	0	0	0
	G18	3	3	0	0	0	0	0
	G10	3	4	1	1	0	0	0
	G24	3	3	0	0	0	0	0
	G15	3	4	1	1	0	0	0
	G19	3	3	0	0	0	0	0
	G16	3	3	0	0	0	0	0
	G23	3	4	0	0	0	0	0
500	G22	3	4	0	0	0	0	0
	G21	3	4	0	0	0	0	0

Table 5. (continued)

<u>Notes</u>

Gas Con   Gas concentration sensors. If 3, at z = 1, 3, and 8 m. If 4, the
fourth is added at z = 1 m to make a pair of IR sensors at that
elevation: one from the Jet Propulsion Laboratory (JPL) and one
from LLNL. In addition to JPL and LLNL IR sensors, International
Sensor Technology (IST) and Mine Safety Appliance (MSA) sensors were
used. See Section 3.2 for more information.

Temp   Temperature sensors. At T01, three thermocouples at z = 1, 3, and
8 m plus four resistive temperature devices on the G01 data channels:
one for absolute T and three for ΔT at z = 0.5, 1, 2, and 4 m.
Thermocouples at all other stations:

if 3, z = 1, 3, and 8 m;
if 4, z = 1, 3, 5, and 8 m except z = 0, 1, 3, and 8 m for G10,
    G15, G21, and G22; and z = 0.5, 1, 3, and 8 m for T02-T06;
if 5, z = 0, 1, 3, 5, and 8 m except z = 0.25, 0.5, 1, 3, and
    8 m for T02;
if 6, z = 0, 0.25, 0.5, 1, 3, and 8 m; and
if 7, z = 0, 0.25, 0.5, 1, 3, 5, and 8 m.

For z = 0, read z = -0 (in ground).

HtFlx   Heat-flux sensor in ground (z = -0 m).

Hum   Humidity sensor at z = 2 m.

Flm Vel   Flame-velocity sensors at z = 1.5, 3.5, and 8.5 m.

Cal   Calorimeter at z = 1 m.

BiVn   Bivane anemometers at z = 1.36, 3, and 8 m.
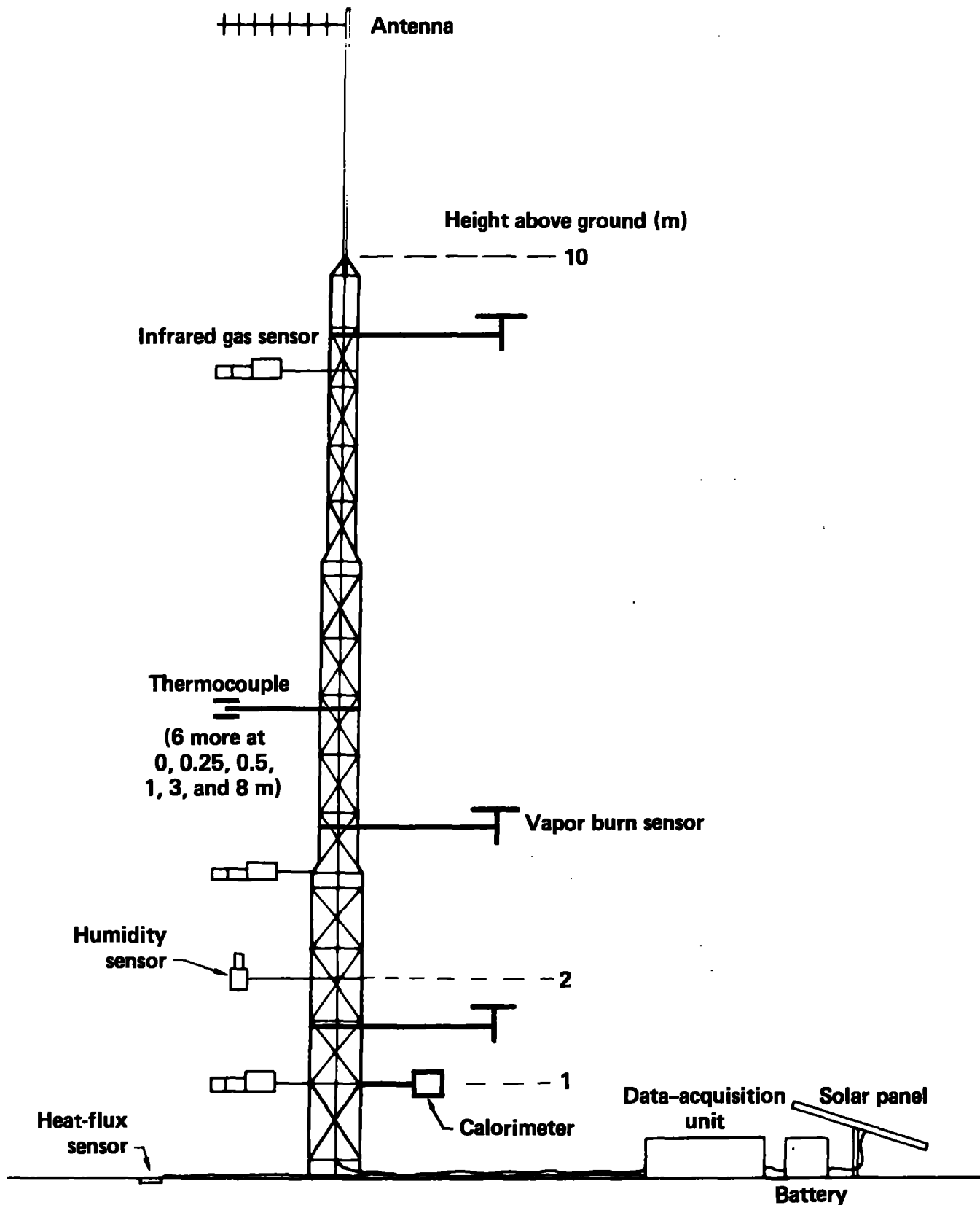
Fig. 4. Station G06. This station had all types of instrumentation except
bivane anemometers (see Table 5).
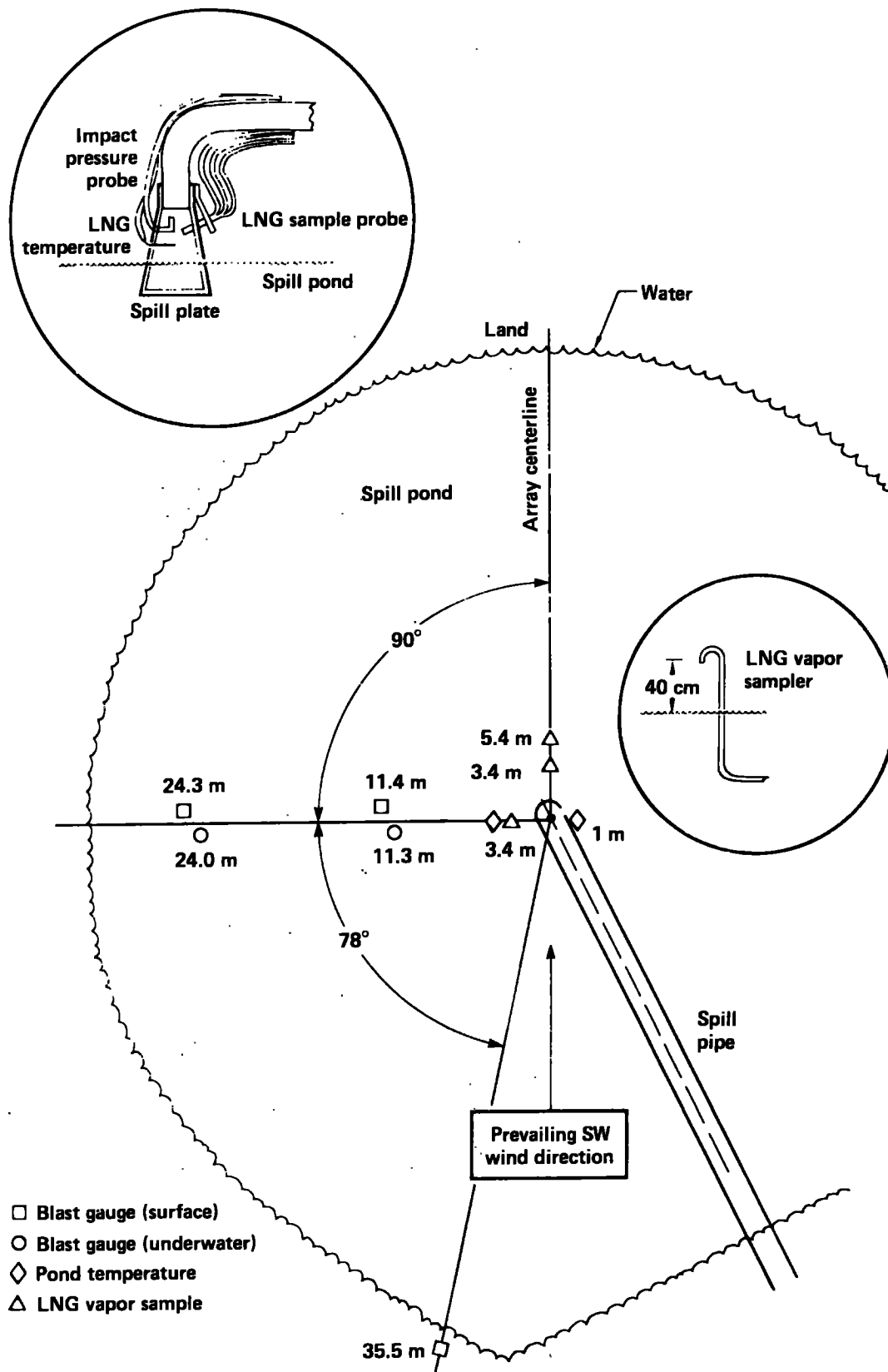
Fig. 5. Array of RPT diagnostic instrumentation.

3.3 Data Acquisition System

Our data acquisition system is flexible and powerful. It utilizes UHF radio telemetry for command and data transmission and is designed to acquire data from sensors distributed over an area with a diameter of up to 10 miles [6]. The remote data acquisition units and sensors are battery powered, portable, sealed, and ruggidized. Batteries are recharged by solar cells. Twenty of the portable data acquisition units acquire wind-field data from two-axis anemometers. The remaining 31 data acquisition units are used to acquire data from a wide variety of sensors. This network of 51 units acquired data from up to 700 channels with data rates and channel assignments programmable remotely from the data acquisition trailer. Each of the data acquisition units consists of a Pacific Cyber/Metrix Model PPS-1201 microprocessor, up to 8 K words of RAM, instrumentation amplifiers, relays to turn on sensors, radio transmitter and receiver, solar cells, and battery. Data acquired from the various sensors are packed into one of two 2 K-byte buffers in a double buffering scheme. The buffers are filled in 10 s to 4 min, depending on the data acquisition rate, number of channels, data resolution, and type of data. Each of the three subsystems (gas, turbulence, and wind-field) functions independently and communicates with its own minicomputer in the data-recording trailer. These minicomputers sequentially poll the remote stations in their network requesting that they transmit their full data buffers back to the data-recording trailer at 4800 or 19.2 K-baud. These trailer systems each consist of a DEC LSI-11/23 minicomputer, a 10-MB disk unit, and a graphics display video terminal, with shared magnetic tape and floppy disk units. Wind-field data are presented in real time enabling the determination of when test conditions are optimal. Gas and turbulence station raw data are recorded on disk for subsequent processing.

The ROM-based data acquisition and operating system for the remote microprocessor was written at LLNL. LSI-11 acquisition, control, and processing programs run under RT-11 and were written at LLNL and EG&G. The real-time data acquisition programs handle interrupt-driven two-way communications, user commands, data acquisition, double buffering, and error checking. Data bases on the LSI-11 can be edited and downline loaded to remotely vary the data acquisition parameters. Raw and calibrated data can also be plotted in the field.

3.4 Data Recording and Storage

After each test, raw data are converted on the LSI-11 using sensor cali-
bration tables to fully calibrated data sets. These are written to an ASCII
magnetic tape and transferred to the LLNL Computation Center for archival
preservation. In order to be able to manipulate this large amount of data,
i.e. select data from the data base and perform an operation on it, we employ
an LLNL-developed, data base management system called FRAMIS [7]. This is a
relational system which was developed mainly for the scientific community, so
that it handles numerical input conveniently. The tables produced by FRAMIS
are stored on an off-line mass storage system, and are readily available for
analysis.

Data manipulation, IR sensor data processing, and plotting were done on a
CDC 7600 computer, using the high-quality computational and graphics output
devices available at LLNL. Gas concentration contour generation was done with
programs [8] written specifically for this purpose using GRAFLIB [9]. Acquisi-
tion of calibration data from the various types of sensors were done on LSI-11
minicomputers. Processing the large number of individual calibration data sets
was handled on a dedicated machine. Calibration files produced were used in
the conversion of raw to calibrated sensor data.

4.   INSTRUMENTATION

4.1 Meteorological Sensors

4.1.1   Wind-field anemometers
The wind-field measurements were made by commercially available two-axis
cup-and-vane anemometers (Met-One) located at 20 stations, 2 m above the
ground, both upwind and downwind of the spill point. They have a starting
threshold of 0.2 m/s and a response-distance constant of 1.5 m. One-second
speed and direction data taken by these instruments were vector-averaged for
10 s before being transmitted to the data-recording trailer. The standard
deviation of the individual directions about the 10-s scalar mean direction
was also transmitted. The wind-field anemometers were calibrated with respect
to three other 'standard' sensors selected from the same production group.

The standards were then sent to the National Bureau of Standards for calibration in a wind tunnel, and the results of this calibration were used for final calibration of the field instruments. The uncertainty in speed for these instruments is the largest of ± 1% or 0.07 m/s. Pointing accuracy was measured after setup and found to be ± 2°.

4.1.2. Turbulence anemometers

These instruments are standard, commercially available Gill bivane anemometers (R.M. Young Co.). Their construction is such that they are vulnerable to damage by fire, so they were installed on only two of the six turbulence stations (TO1 and TO6). Three of these anemometers were mounted on each of the two towers at heights of 1.36, 3, and 8 m so that the vertical wind profile, as well as the various parameters related to atmospheric turbulence, could be determined. These anemometers have a starting threshold of 0.1-0.2 m/s and a response-distance constant of 1.0 m. Factory-supplied calibration curves were used, and data were taken every 0.3 s. Absolute pointing accuracy was estimated to be better than ± 5° horizontally. Vertical error generally was larger, but data were corrected by subtracting the apparent prezero vertical mean angle. Speed and horizontal direction were generally in good agreement with the two-axis anemometers.

4.1.3. Humidity sensors

Eight humidity sensors were mounted at stations throughout the array, including one at upwind turbulence station TO1. These sensors were developed at LLNL specifically for use in cold fog. The sensitive element is the commercially available Humicap (Vaisala). The Humicap cannot tolerate contact with liquid water so it is protected by a porous sintered frit that is heated to 40°C to evaporate the water droplets. Calibration data indicate a linear response over the 10-60% relative humidity range at 40°C and a nonlinear response below 10%. The average sensor calibration accuracy is ± 0.5% relative humidity. Side-by-side comparisons of the instruments show agreement to better than ± 2%, while long-term drift is estimated to be less than ± 3% relative humidity. The overall accuracy of the data is estimated to be about ± 4% relative humidity.

4.1.4. Ground heat-flux sensors

The ground heat-flux sensors were standard, commercially available heat-flux plates (Hy-Cal Engineering). They consisted of two layers of thermopiles separated by material of known thermal conductivity, forming a thin rectangular wafer that was buried just below the soil surface. These devices, along with the humidity sensors, were installed at seven downwind gas stations close to the array centerline. Factory calibration curves were employed. Sensor-to-sensor variation was less than ± 2% at full scale.

4.1.5. Thermocouples

Standard Chromel-Alumel (type K) thermocouples were collocated with each gas sensor to provide temperature measurements of the gas cloud. As noted in Table 2, additional thermocouples were installed at other elevations and in the ground at some stations. The 10 mil thermocouples had a response time of about 0.5 s in a 5 m/s wind, corresponding roughly with the IR gas sensors on the gas stations, which averaged data for 1 s. The thermocouple amplifier offsets ($\sim$ 1-2°C) did not allow temperature-difference data to be used to determine the vertical temperature gradient in the ambient atmosphere (0.02-0.2°C/m in the lower 15 m). However, relative temperature variations due to the presence of the cloud (10-30°C) during the course of an experiment were quite accurately determined. Individual data sets were adjusted to a single pretest ambient temperature measured at station T01.

4.1.6. Resistive temperature devices

The sensing element for the resistive temperature device (RTD) is an 1000-ohm platinum resistor mounted in an aspirated solar shield. Four RTDs were mounted on the upwind turbulence station T01 at elevations of 0.5, 1, 2, and 4 m, with the 0.5-m reading defined as the absolute (reference) air temperature. After signal conditioning, differencing amplifiers perform subtractions to give these temperature differentials which define the atmospheric temperature gradient. The accuracy after calibration is estimated to be ± 0.1°C.

4.2. Gas-Concentration Sensors

In the Coyote series, a total of 89 gas-concentration sensors were deployed on 24 gas and five of the six turbulence stations as shown in Table 5.

150r/23r
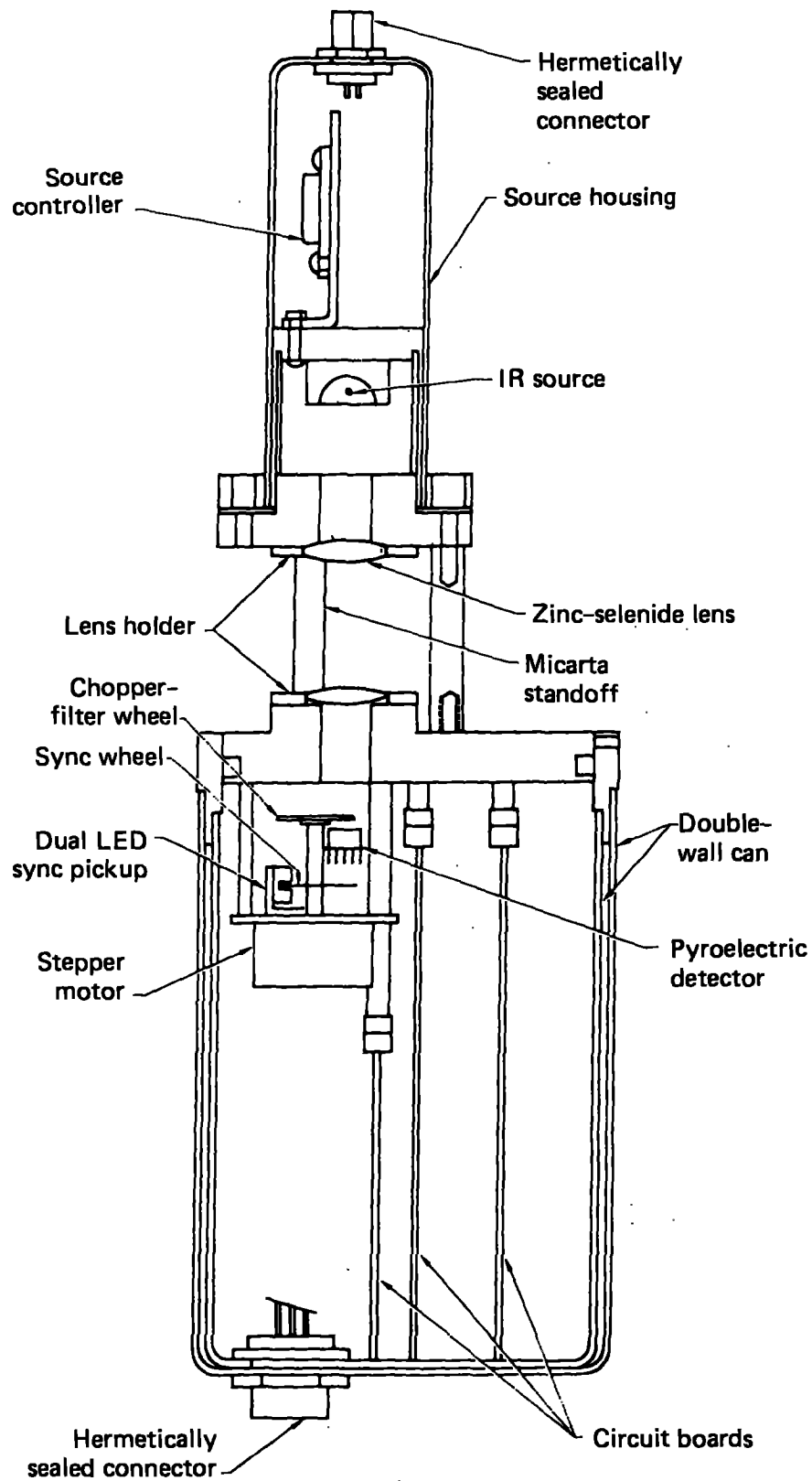
Fig. 6. Cross section of the LLNL IR sensor.

Of these, 41 were IR sensors, 32 LLNL and nine JPL. Of the remaining, 36 were IST solid-state sensors and 12 were MSA catalytic sensors.

Only IR sensors were installed on the turbulence stations. On the gas stations, the IR sensors were installed at z = 1 and 3 m with almost all concentrated in the central part of the array from the 140-m arc to the 300-m arc. At two stations, LLNL and JPL sensors were collocated at z = 1 m. The MSA sensors were used in only the 400-m arc, and the IST sensors everywhere else. In particular, IST stations were used close-in at the 8-m height.

4.2.1   LLNL IR sensors.

A sensor evaluation program (Avocet Series), undertaken in 1978 [10,11] at China Lake, determined that suitable gas sensors for use in the field experiments did not exist. In response to this finding, a fast, portable, differential-IR-absorption sensor that would work in the dense fog associated with LNG spills and detect separately methane and ethane-plus-propane was developed at LLNL [12] for use in the Burro series.

The LLNL-developed IR gas sensor has successfully met our expectations. The gas calibration of the sensor was done in the laboratory before going to China Lake in the summer of 1981, and several checks in the field have shown that the calibrations are quite stable, and did not change appreciably over the six-month period of the Coyote series operations in the extremes of the desert environment.

A schematic drawing of the sensor is shown in Fig. 6. Infrared radiation from the source passes through an optical path open to the atmosphere. If hydrocarbons are present, then absorption occurs, and the amounts of absorption specific to methane, ethane-plus-propane, and cold-induced, water vapor fog are detected at the pyroelectric detector. Absorption specific to these species is defined by four narrow bandpass filters between 3.0 and 3.9 μm. The optical paths exposed to the atmosphere were either 5 or 15 cm in length, so the instrument readings were for average concentrations in volumes of 19.4 and 58.1 cm^3, respectively. The optical paths were enclosed by cylindrical screened volumes of 219 and 540 cm^3, respectively. The screen was made of stainless steel wire with a diameter of 0.330 mm and square spacing of 0.847 mm. These screens were designed to damp out turbulent fluctuations on a time scale shorter than the sampling time to prevent aliasing [13]. The 5-cm optical paths were used at the stations closer to the spill point, and the 15-cm paths at greater distances.

150r/23r

In the absence of fog, two channels serve primarily to determine the methane and ethane gas concentrations. Two other channels are used as reference channels to compensate for shifts in system throughput due to dust on the lenses or to temperature-induced baseline shifts. Relatively little cross-gas sensitivity is experienced within the two main channels. The instruments were calibrated using methane concentrations of 0-50% and ethane concentrations of 0-30%. Expressed as a percentage of the gas sensor reading, the averaged single-gas calibration uncertainties were ± 5.5% and ± 2.5% of the reading for methane and ethane, respectively. If the reference channels were not used for compensation, methane uncertainties did not change markedly, but ethane uncertainties increased to ± 6.0% of the sensor reading.

Two methane/ethane gas mixtures with 30/17% and 12/28% were analyzed with the instruments as part of the calibration procedure. Inaccuracies in the ethane results were only slightly larger than those obtained for the ethane-only calibration runs. However, for the mixtures studied, the methane results were found to be too high by about 10% of the reading. These biases are thought to be due to the form of the calibration algorithm employed but, in view of the limited number of mixtures studied, no corrections were attempted. The methane error should be smaller for the Coyote test circumstances where ethane concentrations were generally much smaller than the test mixtures. By design, the sensor responds to propane essentially as it does to ethane, but with an increased sensitivity of about 40%. Thus 1% propane appears as 1.4% ethane in the ethane-plus-propane channel.

The Coyote series tests generally did not produce large amounts of fog as far out as 140 m. With few exceptions, data was reduced using the two pair of ratioed channels to solve simultaneously for methane and ethane, including the effects of cross-gas sensitivities. In cases when the amount of gas was quite small, a single pair of channels was used to solve for methane, assuming no ethane was present. After processing, the data was smoothed, using running 11-s averaging, to approximate the time constants of the other gas sensors.

In the presence of fog, the two bands on either side of the methane and ethane-plus-propane bands are used to correct for the spectral scattering due to fog particles. Reference levels are determined from data acquired before and after the spill. The algorithm developed to make this correction is based on Mie scattering calculations and experimental data. The calculations showed that, for a given particle size distribution, the extinction coefficient in

150r/23r

the four absorption bands varies linearly with the total particle number density. However, the ratios of the extinction coefficients in the four absorption bands are functions of the particle size distribution. Consequently, a 40-m^3 liquid nitrogen spill (Burro 1) was used to empirically determine the wavelength dependence of the fog attenuation during actual field environmental conditions. In the desert environment, this dependence was found to change very little with time or position in the fog, apparently indicating little change in particle size distribution.

When this empirically determined relationship is used together with the fog-free calibration results, the methane and ethane-plus-propane gas concentrations can be determined even in the dense fog. The solution is sensitive to noise fluctuations however, and requires using smoothed raw data (time constant of ∿ 10 s) as input to the reduction algorithm. The overall accuracy of the gas concentrations determined in this manner can be estimated by self-consistency examination of the data from Burro 1 which had fog but no hydrocarbon gas. First, for tests with hydrocarbons but with little or no fog present, the results agree fairly well with the fog-free determinations. Second, for the great majority of the data from Burro 1, the results properly show quite variable fog concentrations but essentially no apparent hydrocarbon. For example, for the period of time that fog was present, the averaged indicated methane and ethane-plus-propane concentrations, for three of the four sensors in the dense fog, indicate 0.1 and 0.9%, respectively; however, spikes with peak apparent values as high as 4 and 18%, respectively, were seen. Since the gas concentrations appeared to vary continuously with time, this suggests that the character of the fog did deviate substantially on occasions from the averaged character. That these deviations occurred in times of both dense and tenuous fog also supports this supposition. Finally, the specific filter characteristics (i.e., temperature sensitivity), together with the form of the fog calibration algorithm, cause the largest apparent errors to appear in the ethane results. This is fortunate in the respect that LNG is primarily methane, but it makes accurate determination of ethane-specific effects, such as differential boiloff, difficult. For the Coyote series, only a few data sets required processing with the fog algorithm.

The LLNL IR sensor responded to flame in two ways. First, as the flame front approached the sensor from the optics side, flame emission was seen, primarily in the fog channel. This broad band, relatively slow signal (2-5 s)

IR SOURCE
100% MIRROR

AC HYSTERESIS SYNCHRO   MOTOR

"O" RING SEALED BOX

CHOPPER

LIGHT SWITCH

LENS

ELECTRONICS

100% MIRROR

50% MIRROR 2 REQD

HEAT TRANSFER

DETECTOR + FILTER
4 REQD

WINDOW

50% MIRROR

LENS 2 REQ'D

THERMO ELECTRIC COOLER
HEAT TRANSFER TO BOX WALL

FOUR BAND
DIFFERENTIAL RADIOMETER
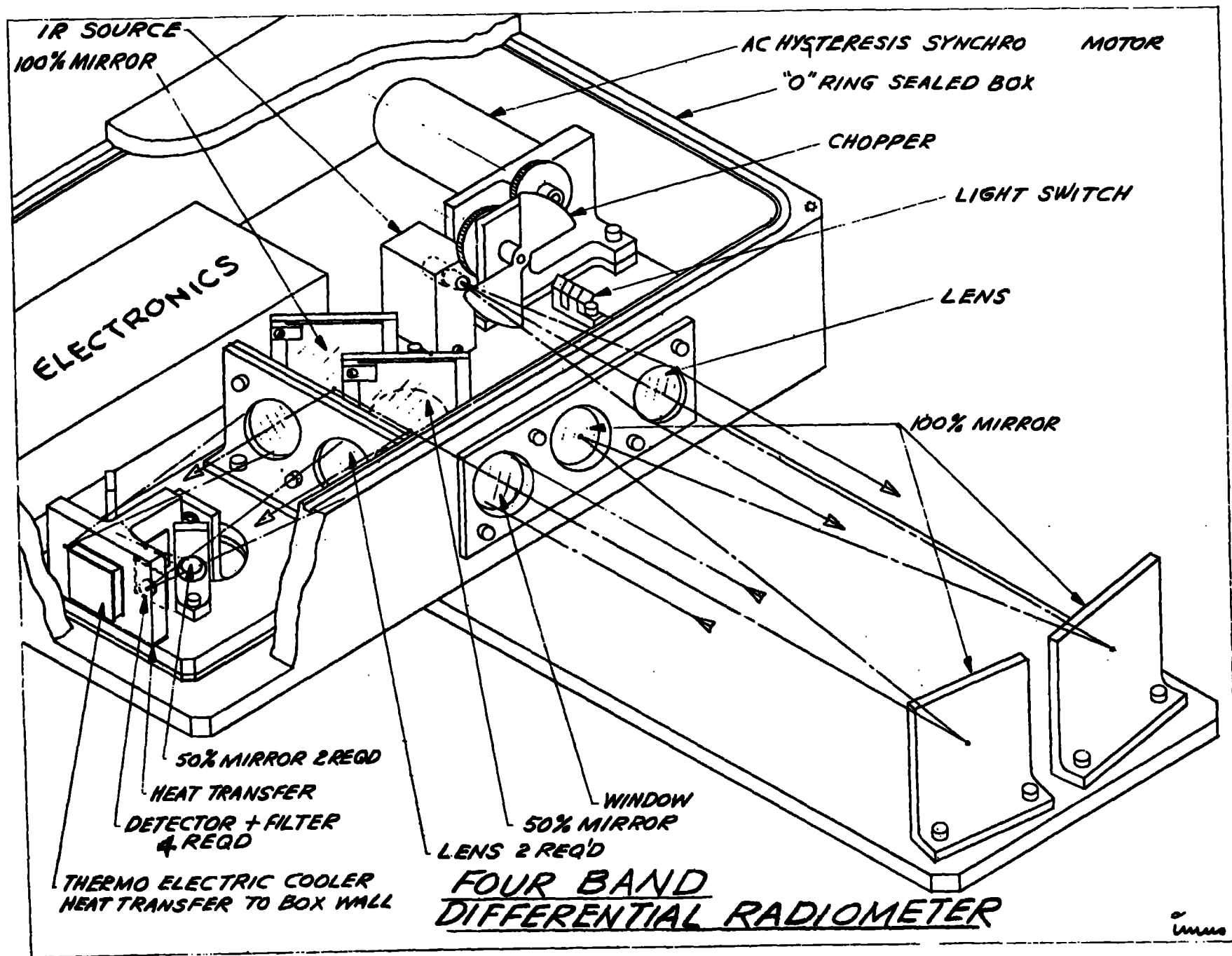
Fig. 7. Pictorial sketch of the JPL IR sensor.

had a characteristic shape in all four channels. The processing algorithm was not insensitive to this, and would somewhat overpredict the amount of gas present. We attempted to correct the data sets for this effect. Second, if the combustion passed over the sensor, flame products were seen immediately, producing deep absorption in all channels which was interpreted as very large amounts of gas. After the flame passed, very little gas was detected, indicating almost complete combustion or expulsion of the gas in the region. This correction was more difficult to accomplish and data sets are somewhat uncertain for the period of flame passage. Postprocessing smoothing of the data to a 10-s response also distorts the shape of a flame-enveloped curve and can incorrectly show the presence of gas for up to 5 s after passage of the flame.

4.2.2. JPL IR sensors

The JPL IR sensors are four-band radiometers similar to the LLNL sensors, except they are designed to work in fog-free regions and to detect separately methane, ethane, and propane. The sensor was developed by JPL [14] for use in the China Lake tests, with one prototype unit being tested on the last two Burro tests. Eight of the JPL units were fielded for the Coyote tests. Most of the units were installed on turbulence stations in the 300-m arc because the sensor could not be operated in regions containing fog; however, at the risk of exposure to fog, three of them were employed close-in at the 140-m arc in order to provide a detailed breakdown of the hydrocarbon species.

JPL selected the spectral region of the 2.0 to 2.5 μm bands of methane, ethane, and propane because of the availability of inexpensive components and high-performance room-temperature detectors. The four bands centered at 2.02, 2.36, 2.46, and 2.51 μm were chosen to enable detection of any of the three species down to 0.4% with an accuracy of 0.2% or 10% of concentration level, whichever is greater. JPL calibrated the instruments and developed a data-reduction algorithm. Figure 7 shows a schematic of the detector, which used four crossings of a 15 cm region to provide an effective path length of 60 cm. An incandescent lamp operating at approximately 1850 K, provides a source beam which was chopped by a motor-driven blade. After exiting the unit and passing through the LNG vapor cloud, the beam reenters the housing, is split by a partially silvered mirror to produce four beams which are focused on the interference filters and PbS detector. The detector assembly was cooled with a thermoelectric cooler in order to stabilize the detector response and the filter pass bands. The sampling rate was up to 10 measurements per second. 150r/23r
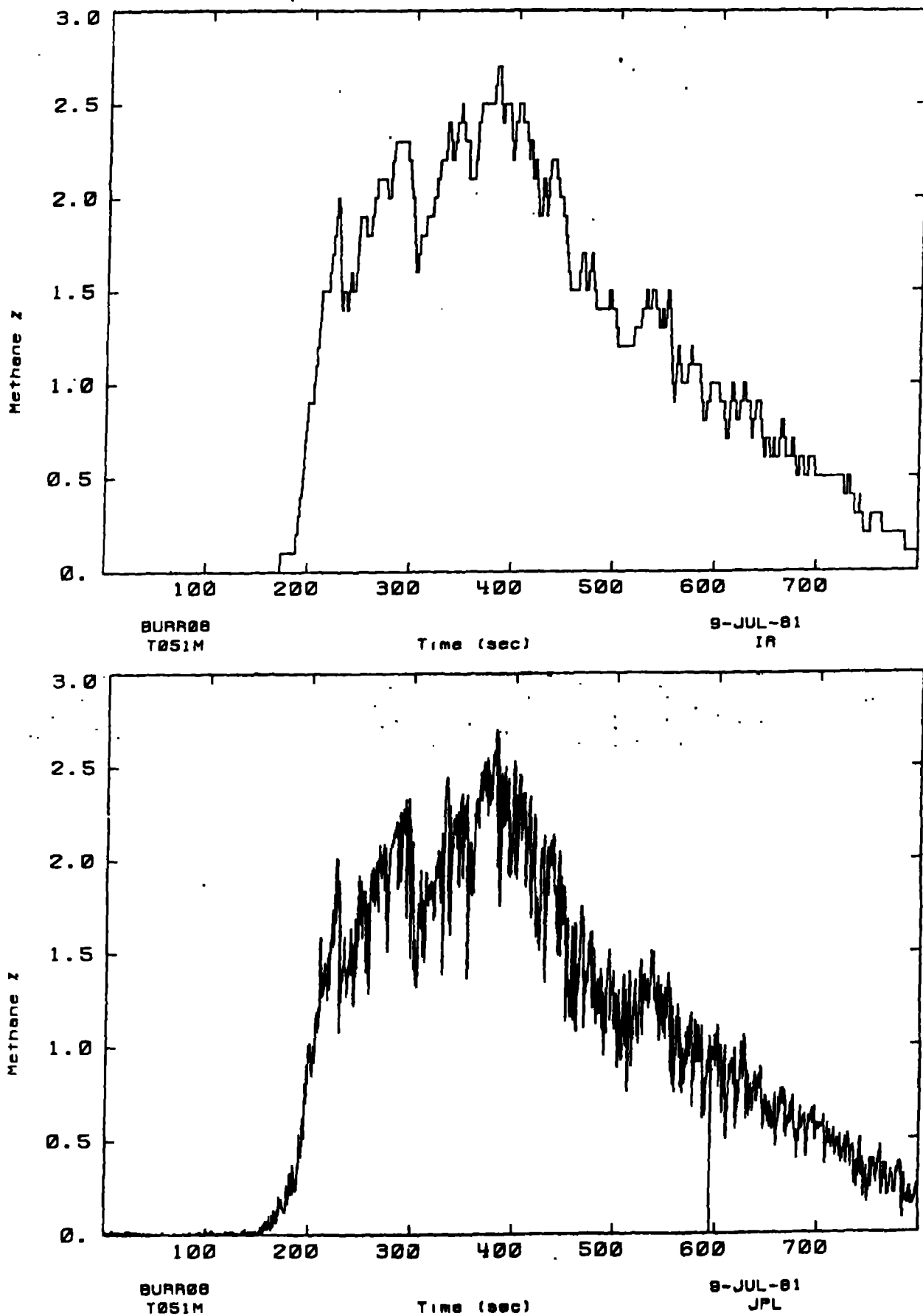
Fig. 8. Side-by-side comparison of the LLNL (above) and JPL (below) IR sensors (Burro 8, station T05, z = 1 m).

Analysis of the Burro series data collected by the prototype JPL unit showed that the JPL algorithm did not converge for much of the data. We successfully modified the algorithm to solve only for methane and ethane. The problem was traced to large degrees of cross-gas sensitivity in the filter responses. The high signal-to-noise ratio demonstrated by the sensor was sufficient to solve reliably for methane and ethane, but not for propane in addition.

In practice, the sensor demonstrated extremely stable baselines in the four channels, provided they were operated within appropriate voltage levels. Power requirements were relatively large, however, and on many of the data sets oscillations of approximately 6-s periods appeared because of operation at too low a voltage. This required averaging (filtering) out the oscillations, prior to calculating the gas concentrations. The technique was successful and methane/ethane gas measurements down to about 0.2% were obtained. The estimated overall accuracy of the methane and ethane measurements was ± 8% and ± 3%, respectively. The JPL sensors were not exposed to fog on any of the Coyote tests. A comparison of the methane, measured by two side-by-side LLNL and JPL sensors, is shown in Fig. 8. The JPL sensor is capable of faster time response than the LLNL sensor, but the agreement is excellent. Since the two types of units operate in different spectral regions, at different sampling rates, and were calibrated by different organizations, this agreement indicates both IR sensor types performed very well.

4.2.3 IST solid-state sensors

The IST sensors had not been evaluated in the field during the Avocet series of tests in 1978, but had been extensively tested in the laboratory during 1979. The IST sensor was selected as a result of this laboratory testing, because it was capable of measuring gas concentrations as high as 20%, and because it has been successfully temperature-compensated. Unfortunately, some problems with it still remained to be discovered in the field. The sensor proved to be sensitive to humidity in the presence of methane, a sensitivity which varied with the methane concentration. Using humidity sensor data (the humidity sensor was not sensitive to hydrocarbon gases) from the field and a laboratory calibration of the ISTs for both methane and humidity, we were able to correct the field data for this effect. The humidity effect was greater than 50% for several of the sensors which were exposed to gas during the test series, but, on the average, was about 10% of the reading for gas concentrations of less than 2%, typical for most of the tests.

150r/23r

The IST sensors also showed variable sensitivity to the higher hydrocarbons, ethane and propane. In the worst cases, some sensors were many times as sensitive to ethane and propane as they were to methane. Six sensors showed sensitivity ratios of 10 or more, and the average of the remaining sensors was about six. Knowing the response of each sensor and using the ethane/methane ratios measured as a function of time by the IR sensor stations, an attempt was made to correct the IST sensor data for this effect.

Some of the IST sensors exhibited calibration changes and gain changes during the course of the experiments. The sensors were all recalibrated in the laboratory after being brought back from China Lake, and these calibrations were generally used with the data. The result of all of the corrections to the IST sensor data is a fairly high residual uncertainty in its accuracy. Our current best estimate is that for concentrations below 5% the uncertainty is less than 20% of the indicated value, and above 5% it is approximately 50% of the value with uncertainties varying greatly from sensor to sensor. Comparison between side-by-side IST and LLNL IR sensors at the same location on both Burros 8 and 9 showed agreement to within about 10% of reading.

Sensor-rise time was the order of 6-10 s. The fall time generally was longer, but data were correctable for this effect. The ISTs were also sensitive to flame products and small corrections were made as appropriate.

4.2.4. MSA catalytic sensors

MSA sensors are well-understood, standard commercial units that operate on the catalytic principle and work well as long as they are not exposed to flames, high winds, or gas concentrations approaching the stoichiometric mixture (10% for methane). The sensor response is very linear, and the uncertainty is about 10% of reading. Sensors were individually calibrated. Posttest calibrations were used to correct for changes in sensor sensitivity. The MSA sensor generally worked well for the outer regions (in the absence of flames) and were not sensitive to moisture. They were, however, somewhat sensitive to wind. Response times were about 10 s.

4.3 Flame-Related Sensors

Some of the above-described instrumentation served to provide time-of-arrival for flames at various locations in the array of gas and turbulence

stations for Coyotes 3, 5, and 6: ground heat-flux sensors (Section 4.1.4), thermocouples (Section 4.1.5), and the IR gas-concentration sensors (Sections 4.2.1 and 4.2.2). Two other types of flame-sensing instruments were also deployed in this array for Coyotes 3, 5, and 6 as indicated in Table 5: calorimeters and flame-velocity sensors. Flame-related data were also obtained from outside the array as shown in Table 1 by means of cameras (Coyotes 2, 3, 5, 6, 7), IR imagery (Coyotes 3, 5, 6, 7), and radiometers (Coyotes 3, 6, 7). In addition, overhead IR imagery was obtained from a helicopter during Coyotes 6 and 7. The most valuable sources of information for flame propagation and fire structure were photography and IR imagery.

4.3.1. Calorimeters

Four "disc type" total heat-flux calorimeters were deployed at stations G06, G08, T03 and T04. These sensors were located 1-m above ground with the 1-cm-diameter sensory element pointing away from the pond. Each calorimeter had nominal range of 0-30 watt/cm^2, a rise time of 0.25 s, and a surface emissivity of 0.89 over the spectral range from 0.2 to 30 μm. Each sensor was provided with a calibration curve by the manufacturer, Hy-Cal Engineering, Santa Fe Springs, California; however, they all indicated a linear response to within 2%. Each calorimeter was mounted in a 10-cm-diameter by 10-cm-long aluminum heat sink as illustrated in Fig. 9. This allowed the sensors to operate without water cooling at near full-scale heat loads for periods up to 30 s. The manufacturer stated accuracy was ± 3% of full scale, or ± 0.9 watt/cm^2 for these particular sensors.

4.3.2. Flame-velocity sensors

LLNL developed a sensor that was intended for measuring local flame velocities. Its operation is based on the principle that ionization in the flame front will break down the electric potential across a small gap between two electrodes. Each flame-velocity sensor consists of four electrode pairs at the four vertices of an equilateral tetrahedron. A unit is shown in Fig. 10 together with a closeup view of an electrode pair.

The output of the sensor is the flame-front arrival time at each of four electrode pairs. A local flame velocity can be calculated from the four arrival times, the sensor geometry, and the dimensions of the sensor if the flame front is assumed to be planar as it passes over the sensor arms. Relative

150r/23r
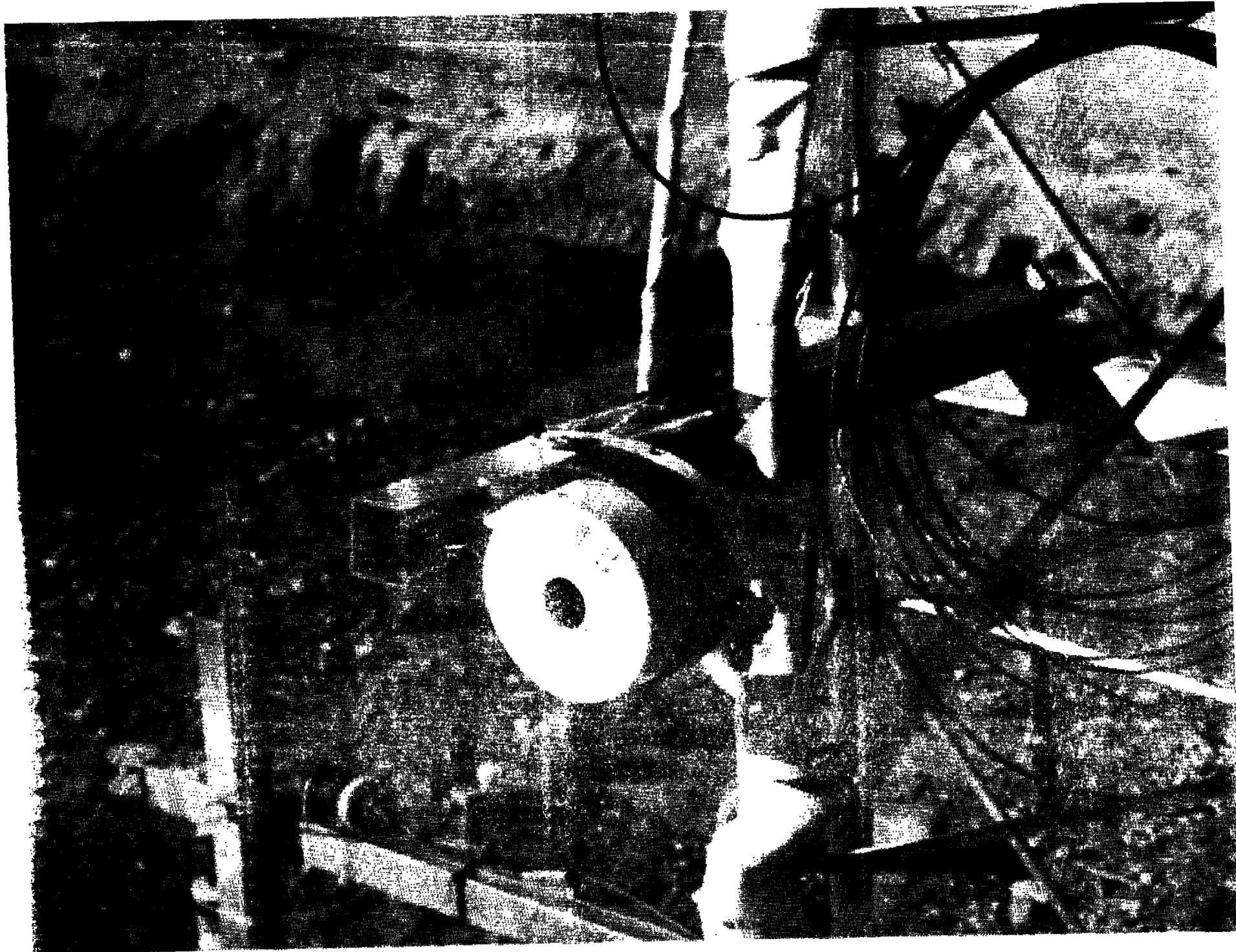
Fig. 9. A photograph of a calorimeter-heat sink installation.
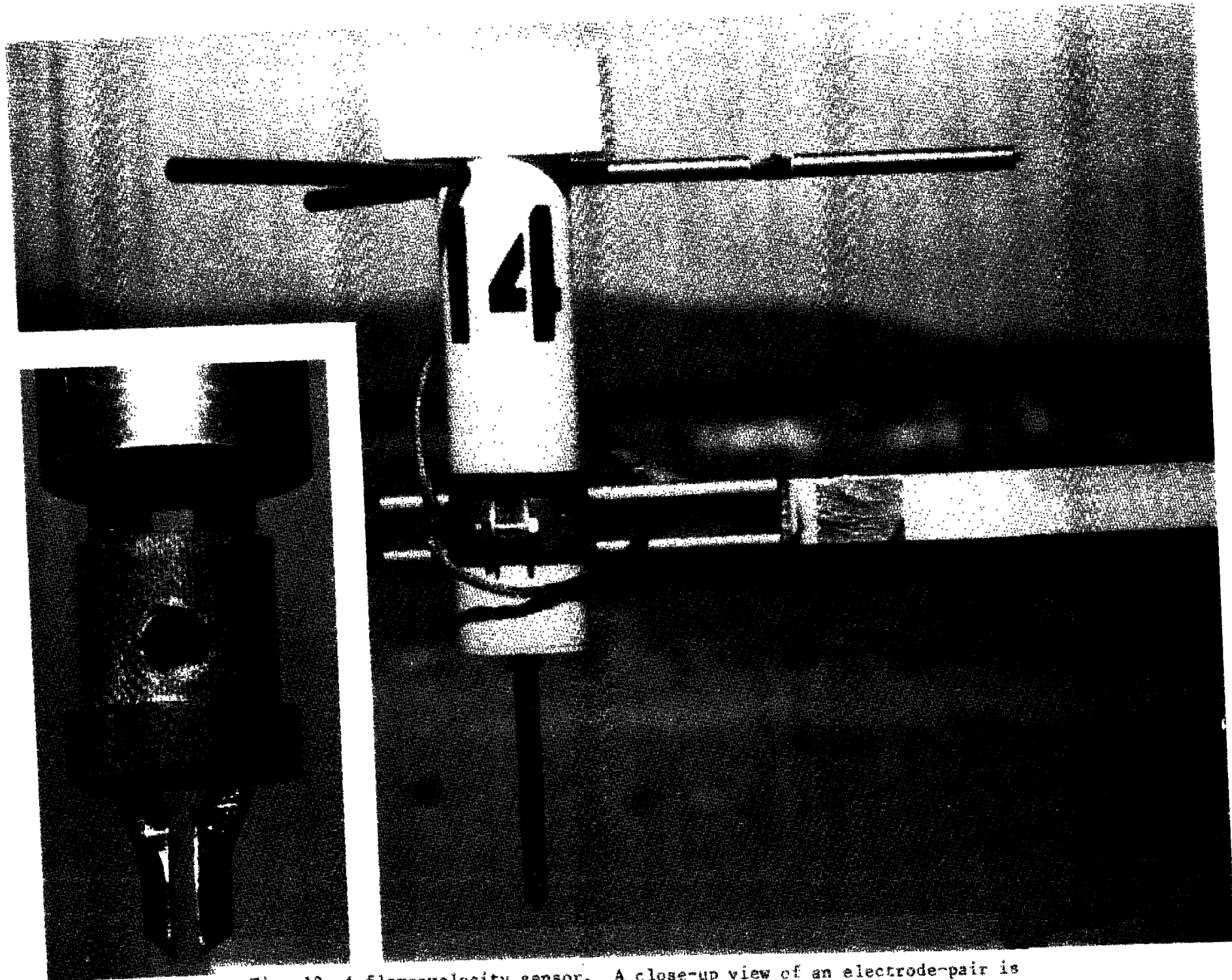
Fig. 10. A flame-velocity sensor. A close-up view of an electrode-pair is

timing accuracy for all electrode pairs on a tower was 10 μs. Absolute timing for Coyotes 6 and 7 was better than 60 ms. A length of 0.5 m was selected for the edges of the tetrahedron based on the timing precision and its relation to accurate determination of velocity. Twenty-seven of these units were installed at elevations z = 1.5, 3.5, and 8.5 m on stations T02-T06, G04-G06, and G08.

The sensors worked and many events were recorded. Local flame velocities were calculated for a few stations and elevations for Coyotes 5-7. However, the magnitudes and directions of the velocity vectors appeared to be random and they could not be related to larger scale flame velocities calculated from flame arrival times at different stations (see the next paragraph), photography (see Section 4.3.3), and IR imagery (see Section 4.3.4). It was concluded that the flame front was not sufficiently planar over the sensor region and the 0.5-m dimension is not appropriate for obtaining flame velocities in burning clouds of this size.

However, the time-of-arrival of the burning gases as determined by the flame-velocity sensors were comparable to the arrival times from adjacent sensors of the other types (e.g., thermocouples) and of high precision. Station-to-station flame velocities calculated from these sensor data are in qualitative agreement with velocities derived from photography and IR imagery. Therefore, average flame arrival times are provided for the flame-velocity sensors.

4.3.3. Photography

Five remotely controlled 16-mm motion-picture cameras loaded with color film were operated during the Coyote series. Two overhead cameras provided information about the structure of the fires in the horizontal plane. They were suspended at an elevation of approximately 30 m between two 60 m towers. One camera was aimed at the spill pond and the other toward the igniter locations; their fields of view are illustrated in Fig. 11. A third camera was mounted on top of the NWC bunker and provided information about the vertical structure of the fires; its field of view is approximately that of the side IR imager shown in Fig. 11. A fourth camera, also on top of the bunker, had a field-of-view that slightly overlapped that of the third camera and included the spill pond. The fifth camera was located upwind of the spill pond; it provided views of the spill interaction with the pond.

Field of view of side IR imager

Array
centerline

Spill
pond

Fields of view of overhead
motion picture cameras
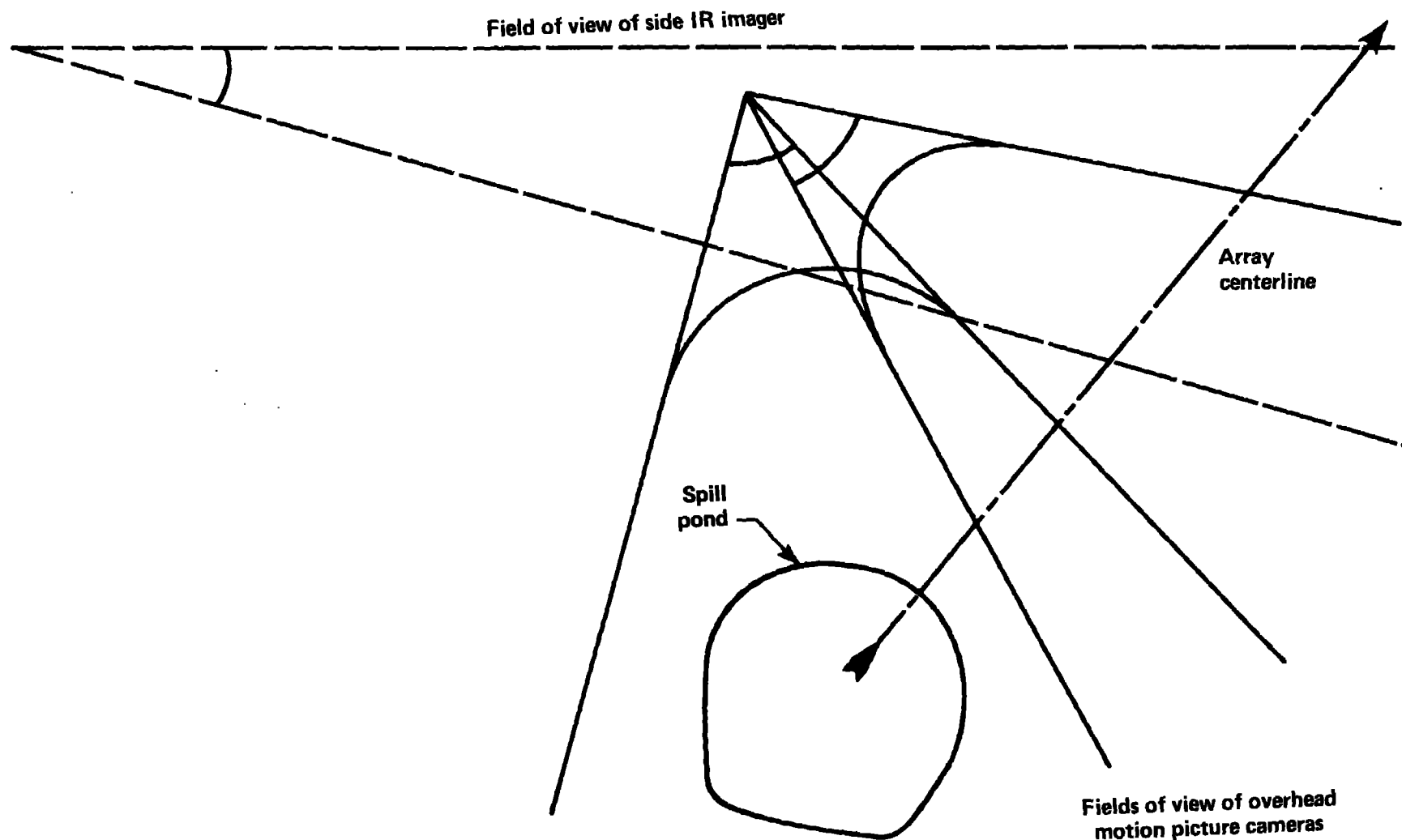
Fig. 11. Fields of view of the motion-picture cameras and the side IR imager.
The field of view of one of the cameras mounted on the control bunker
is centered on that of the side IR imager which is shown. The field
of view of the other bunker-mounted camera slightly overlapped that of
the other camera and included a view of the spill pond.

4.3.4. IR imagery

Side-on IR images of the Coyotes 3, 5, 6, and 7 burns were obtained using a Xedar Model 408-8 IR Imager camera system. This system uses a pyroelectric vidicon detector optimized for the 8-14 μm spectral region. The camera was used in a starring mode (chopped at 15 Hz), and its location and field-of-view are shown in Fig. 11. The IR images were recorded on video tape in standard TV format.

The NWC also fielded a side-on IR imaging system consisting of two AGA Model 661 Thermovision cameras. This system was located approximately due north of the spill pond at a range of 500 m. Images with 1.9 to 5.5 μm and the 8-12 μm spectral bands were recorded on video tape for Coyote 6. No attempt has been made to spatially calibrate this system, hence the results are of limited value at present.

Overhead IR images of the Coyote 6 and 7 burns were obtained using a heli-copter and IR imaging system provided by EG&G Airborne Measurements Group, Las Vegas, Nevada. The system used was an Inframetrics Model 525 dual band thermal imager. This instrument recorded data in two wavelength regions simultaneously: 3.3-3.5 μm and 8.5-12.5 μm. In addition to the fire images, a strong methane IR-absorption band between 7 and 8.5 μm also allows the preignition cloud to be imaged in the long-wavelength channel, using the ground as a thermal radiation source. This system was considerably more sensitive than the Xedar, and had a much higher image resolution. This data was also recorded on video tape in standard TV format. Imagers were computer-enhanced by EG&G and processed to provide thermal contours [15].

4.3.5. External radiometers

Nine radiometers were deployed by the NWC for the purpose of measuring both the radiative heat flux at several distances from the vapor cloud fires and the emissive power of the fire. Radiant flux measurements were made with four Model R-8015 Hy-Therm wide-angle radiometers manufactured by Hy-Cal Engineering of Santa Fe Springs, California. These are basically slug-type calorimeters with optical windows covering the 1.6-cm-diameter sensing element. Their response times are about 0.5 s and the total view angle is about 150°. One of these wide-angle radiometers had an IRTRAN 4 window while the other three had sapphire windows. All four wide-angle radiometers were calibrated by the manufacturer for source radiance values up to 3 watt/cm^2 without
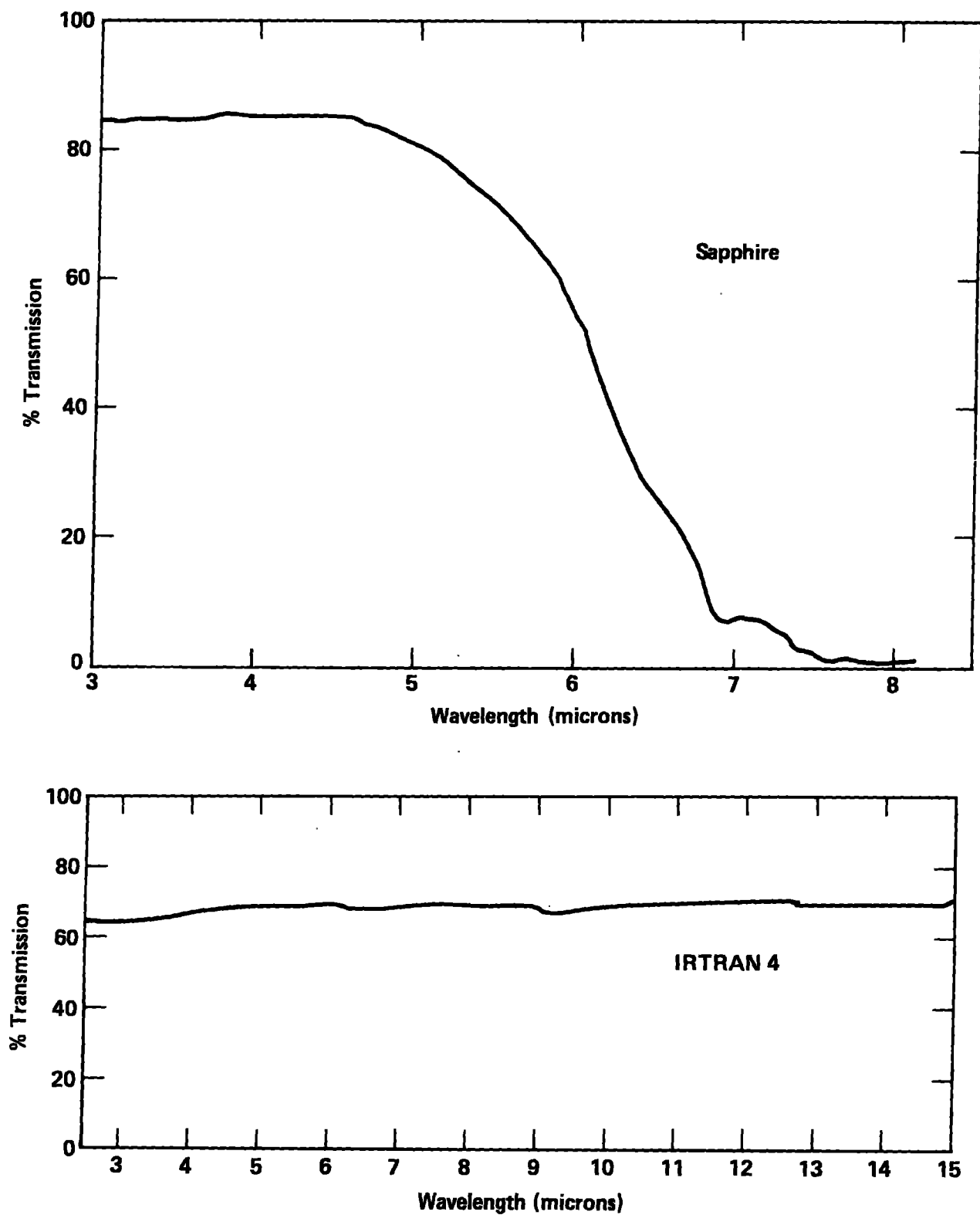
Fig. 12. Transmission characteristics of the windows of the external radiometers.

windows. The transmission of the IRTRAN 4 window and a typical sapphire window are shown in Fig. 12. The data presented for these wide-angle radiometers (see Section 8) will have to be corrected for these window transmissions as well as for the flame-view factor.

Flame emissive power measurements were made by using five Model 8101 Hy-Therm H narrow-view angle radiometers, which were also manufactured by Hy-Cal Engineering. All of these radiometers had 7° view angles, response times of 0.5 s, and IRTRAN 4 windows. The narrow-angle radiometers were calibrated by the manufacturer (with windows) for source radiance values up to 30 watt/cm^2.

Although both the narrow- and wide-angle radiometers were designed to be water cooled, no cooling was supplied for any of the tests.

Nine radiometers were positioned to the side of the instrument array at x ≃ +65 m: Two wide-angle sensors (R01-R02) and five narrow-angle sensors (R03-R07) at y ≃ 57 m, and two wide-angle sensors (R08-R09) at y = 100 m. All radiometers were mounted on tripods 1.7 m above the ground and were aimed horizontally towards the array centerline. The narrow-angle radiometers were aimed at centerline locations ranging from x = 50 m to x = 150 m. All wide-angle radiometers were aimed at x = 75 m on the array centerline. These locations and fields-of-view are shown in Fig. 13.

4.4 RPT Diagnostics

A number of measurements were made at or near the spill pipe exit for the purpose of better understanding the RPT explosion phenomena. The locations of each of these diagnostics are shown in Fig. 5. Data were obtained during every test in the Coyote series, not only the dedicated RPT tests, because RPTs could occur during any test.

4.4.1 LNG composition at the spill pipe outlet

The LNG composition is an important parameter in the study of RPT explosions, hence an attempt was made to measure the methane, ethane, and propane concentrations of the LNG as it was being spilled. A gas-analysis system for this purpose included a "heated" sample probe located at the spill pipe outlet and a three-channel, nondispersive IR gas analyzer built for LLNL by Anarad, Inc., of Santa Barbara, California.

A cross-sectional view of the water-heated LNG sample probe is shown in Fig. 14. The water was supplied to the probe at approximately 7 liters/min by

150r/23r

**Fields of view of
wide-angle radiometers**

R-8, 9

R-1, 2

**Array
centerline**

R-7

R-6

R-5

R-4

R-3

**Fields of view of
narrow-angle radiometers**

**Spill
pond**
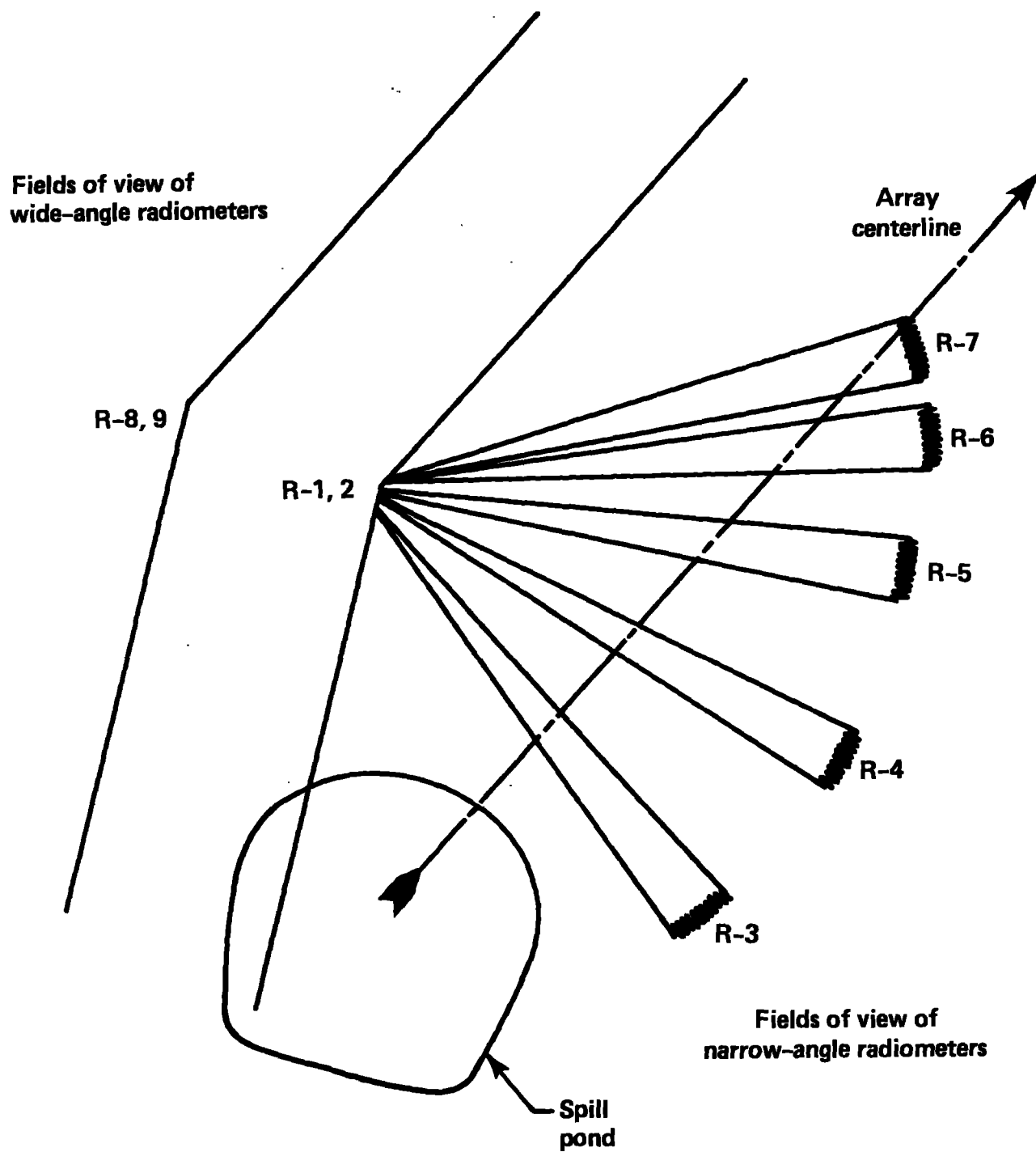
Fig. 13. Fields of view of the external radiometers.

Gas
sample

Stainless
steel

Water
out

Water
in

Annular
space

Copper
tubing

Orifice
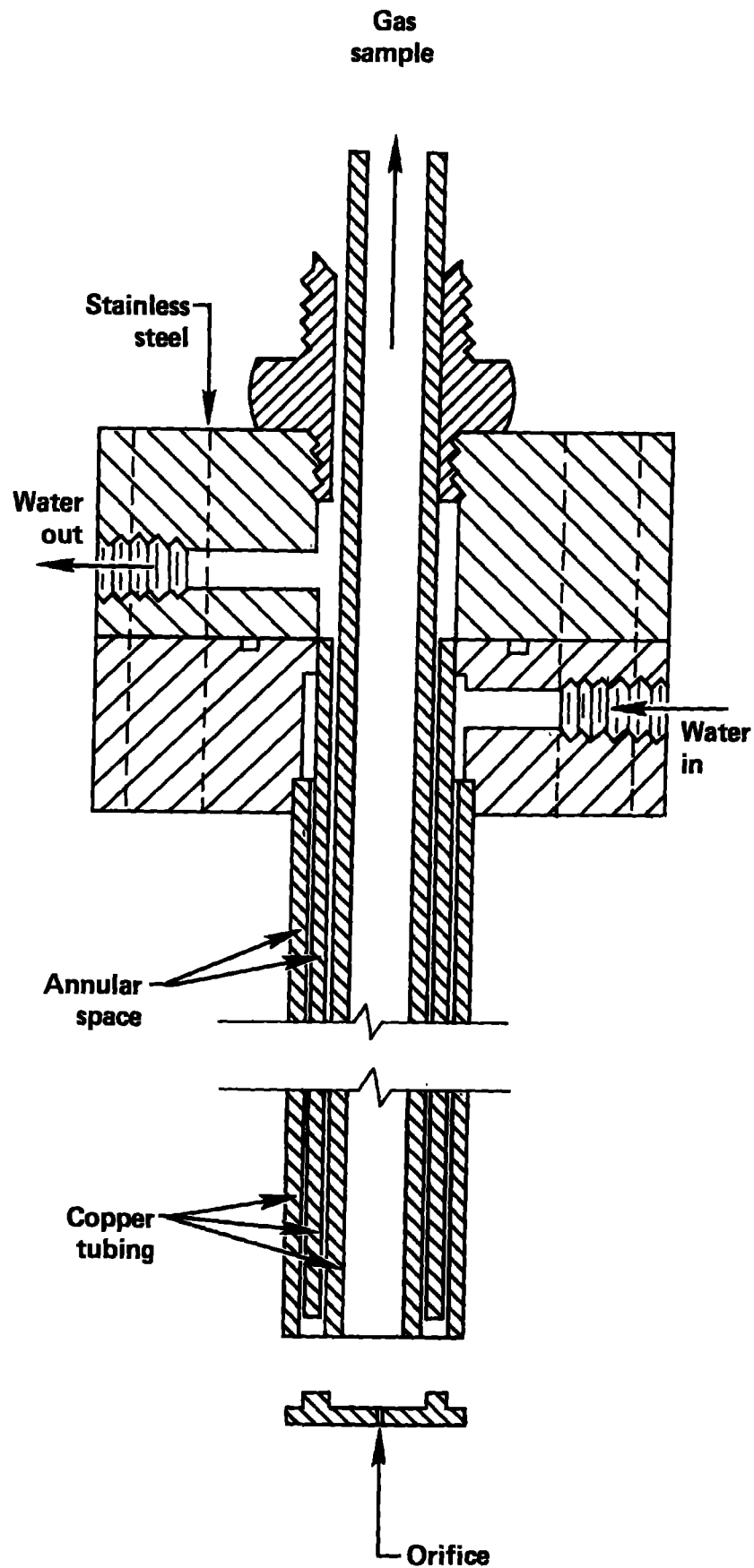
Fig. 14. Cross section of the heated sample probe.

a 1/2-hp pump. This was a closed-loop system in which the water was stored in a 30-gallon container which was heated by the sun. The probe was mounted at the end of the spill pipe so as to protrude into the LNG as it spilled out. A small amount of the cryogen was drawn through the 0.4 mm orifice, where it was flash vaporized in the warm, large area inner channel of the probe. This vapor was representative of the LNG composition as a function of time and was pumped through 50 m of rubber hose to the Anarad gas sensor system where it was analyzed in real time for methane, ethane, and propane content, and the results transmitted to the data-recording trailer.

The heated probe was first operational for the Coyote 4 RPT spill series. It suffered some damage because of its proximity to the explosions. The large RPT explosions of Coyote 5 sheared the probe from its mounting and stripped several brackets holding the gas sample and water supply hoses to the spill pipe, allowing the probe to fall into the pond upwind of the spill point. This allowed water to be drawn into the Anarad gas analyzer. The system was repaired before the next spill test (Coyote 6), however the Anarad did not perform adequately for the remainder of the test series. Because of the large uncertainty of these results, the data are not presented here.

4.4.2   LNG pressure and temperature at the spill pipe outlet

Measurements of the LNG impact pressure and exit temperature were made for each spill. The measurement point was approximately 30 cm directly below the center of the spill pipe outlet. The pressure was recorded with a Validyne Model P24 differential pressure transducer. The 0-50 psid transducer was calibrated at the LLNL force and pressure calibration facility just prior to installation at China Lake, and was found to be accurate to within ± 0.25 psid and linear to within ± 1%. The pressure recorded was the difference between the local ambient pressure and the total, or stagnation pressure, of the fluid. The stagnation pressure of the LNG was sensed by the transducer through a 10-m-length of 0.635-cm-diameter stainless steel tube whose open end was pointed directly upward into the fluid flow. The total system response time was less than 0.5 s. The system was checked for accuracy several times during the test series using a water column as a pressure standard.

The LNG exit temperature was measured with a sheathed, 10-mil-diameter Chromel-Alumel (type K) thermocouple, which had a time constant of about 2 s. This system was also checked periodically in situ using ice baths and liquefied nitrogen. Estimated accuracy was ± 1°C, even at -160°C.

150r/23r
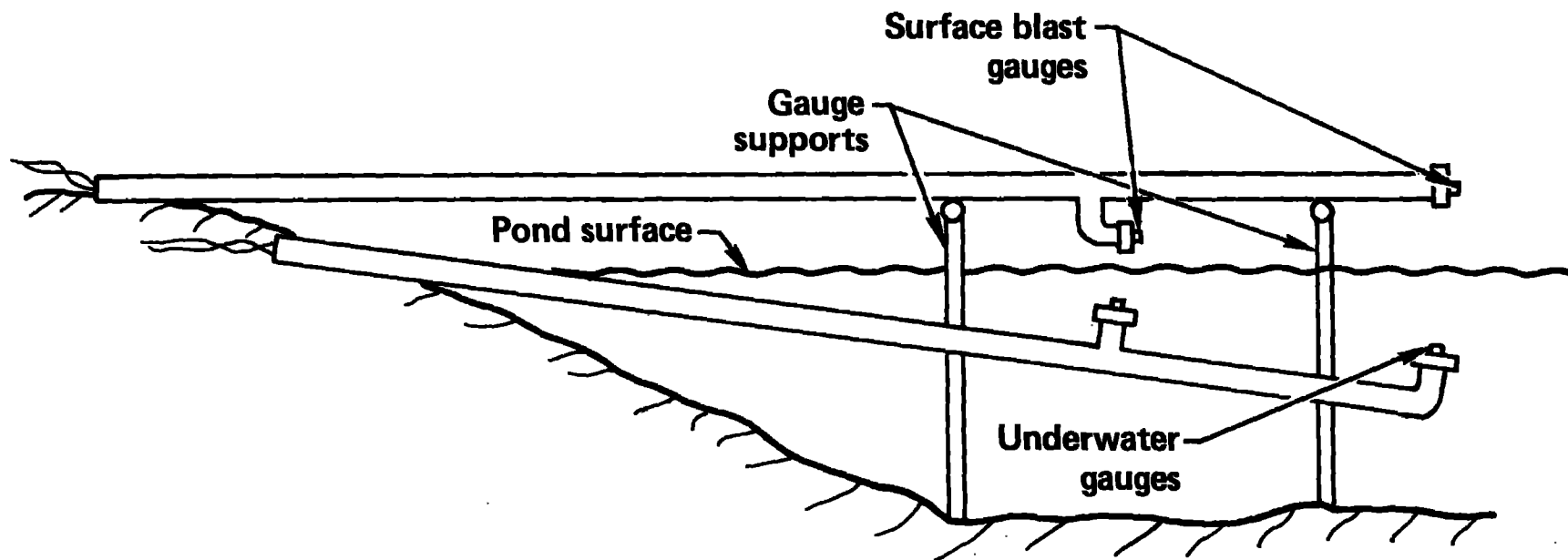
Fig. 15. Arrangement of the above-surface and subsurface RPT blast gauges.

4.4.3   LNG vapor concentration above the spill pond

Measurements of the methane and ethane-plus-propane concentrations directly above the LNG on the pond were made at the three locations shown in Fig. 5. Each sample was extracted approximately 40 cm above the water surface and pumped through 50 m of rubber tubing to an enclosed LLNL IR gas sensor (Section 4.2.1) located upwind. The delay time of the gas sample system was approximately 19 s. The source time histories shown in Appendix 2 are from the following locations shown in Fig. 5: x = 5.4 m, y = 0 m for Coyotes 3 and 5, and x = 0 m, y = 3.4 m for Coyote 6.

4.4.4   Pond temperature

The pond water temperature was measured at two locations (see Fig. 5) at a depth of about 20 cm. The sensors were platinum RTDs (resistive temperature devices) manufactured by Hy-Cal Engineering of Santa Fe Springs, California. The RTDs had a specified accuracy of ± 0.25°C at 0°C, and were linear to within ± 0.07°C over the range of 10-50°C. The time response of these sensors was faster than 0.5 s.

Some problems were encountered during the test series due to the highly alkaline pond water penetrating the RTD cabling. As a result, for some spills only one pond temperature sensor was operational.

4.4.5   Blast-wave overpressures

Measurements of the RPT blast overpressures at five different locations (Fig. 5), both above and below the water surface, were provided by the NWC. The blast-gauge configuration for the crosswind measurements is shown in Fig. 15. The air-blast overpressures are due to reflected shock waves. No data were obtained from the underwater blast gauges during any of the tests due to an electrical grounding problem. The fifth air-blast gauge was mounted in a large metal block and was also a reflected overpressure measurement (i.e., facing the explosion).

All of the pressure gauges were acceleration compensated, quartz-crystal devices manufactured by PCB Piezotronics of Buffalo, New York. These gauges all have rise times of about 1 μs, measurement resolution of less than 0.04 psia, were linear to within 2% of full scale, and were capable of measuring pressures up to 1000 psia. The highly transient signals were recorded on a FR600 Ampex FM tape recorder with a 50 kHz upper band edge.

The gauges were not temperature compensated, consequently there is some uncertainty about the overpressure data obtained when the gauge was immersed in the cold gas cloud. This phenomenon did not affect the early type RPT overpressure measurements, or those obtained during the short, three-sequence spills (Coyotes 4, 8-10). Recording system voltage calibrations were conducted periodically throughout the test series, but no absolute pressure calibrations of the gauges were performed. The manufacturer's calibrations were used for the data processing.

5. METEOROLOGICAL DATA

5.1 Wind Field

The wind field during all but the first of the Coyote experiments was measured by an array of 20 anemometers (see Section 4.1.1) mounted at a height of 2 m above the ground. The array covered an area from 800 m upwind of the spill point to 600 m downwind, as shown in Fig. 2. Wind speed and direction were measured approximately every second and averaged within the remote stations for a 10-s period. Mean values of speed and direction, and RMS values (σ_θ) about the mean wind direction for the 10-s period were calculated and transmitted to the data-recording trailer.

A sample plot of the wind data is shown in Fig. 16. The arrows indicate the direction toward which the wind is blowing, and the arrow length is proportional to wind speed, as given by the scale in the upper left corner of the plot. The wind-sensor locations labeled W01-W20 are at the base of each arrow; the label for W01 at 800 m upwind is omitted because of the presence of the vertical axis. The horizontal axis is aligned with the array centerline (SW to NE). Similar plots were available in real time and used to determine when to conduct a test.

The wind field is a primary factor in estimating the dispersion of the gas cloud. In order to provide a preliminary estimate of cloud transport and dispersion, trajectory plots were constructed from the wind-field data interpolated and extrapolated to a 100-m grid shown in Fig. 17. These data were then used to track computer-generated marker particles released every 10 s during the spill. The centerline of cloud travel is indicated in the sample plot (see

COYOTE 3   TIME =   51 SEC.
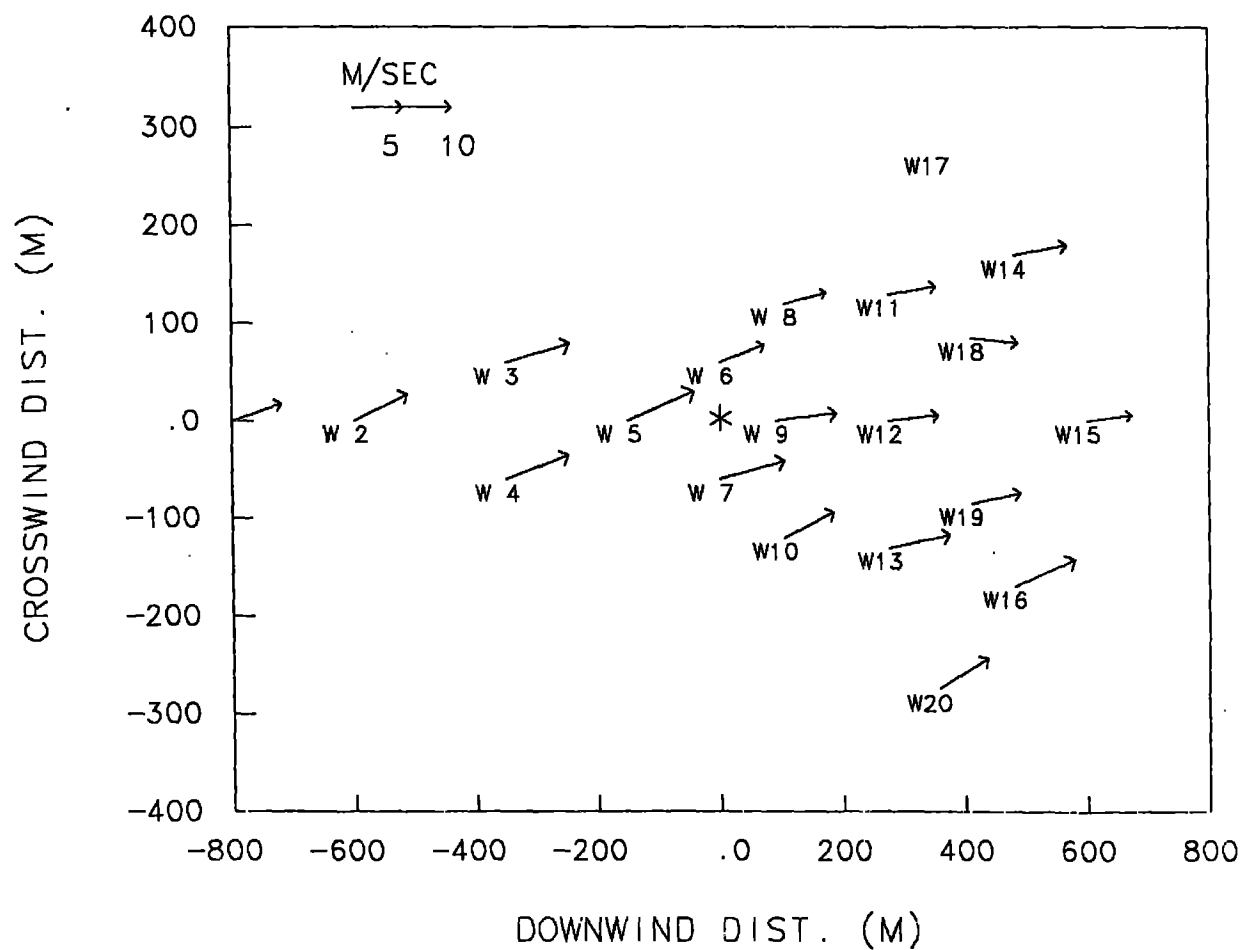
Fig. 16. A sample of the wind-field data. The asterisk (*) marks the location of the spill pond.

COYOTE 3   TIME =   51 SEC.
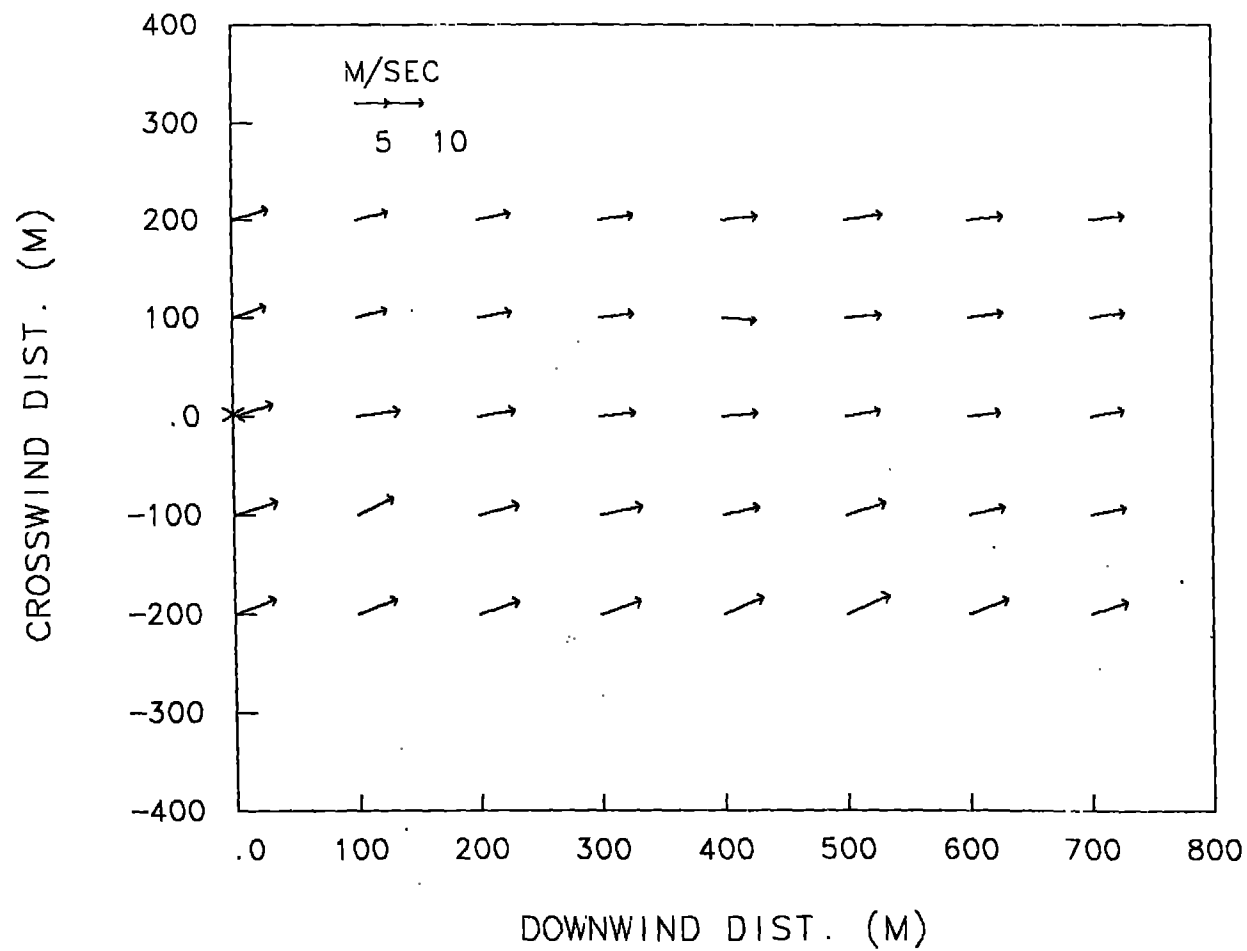
Fig. 17. Sample of the wind field constructed from Fig. 16.
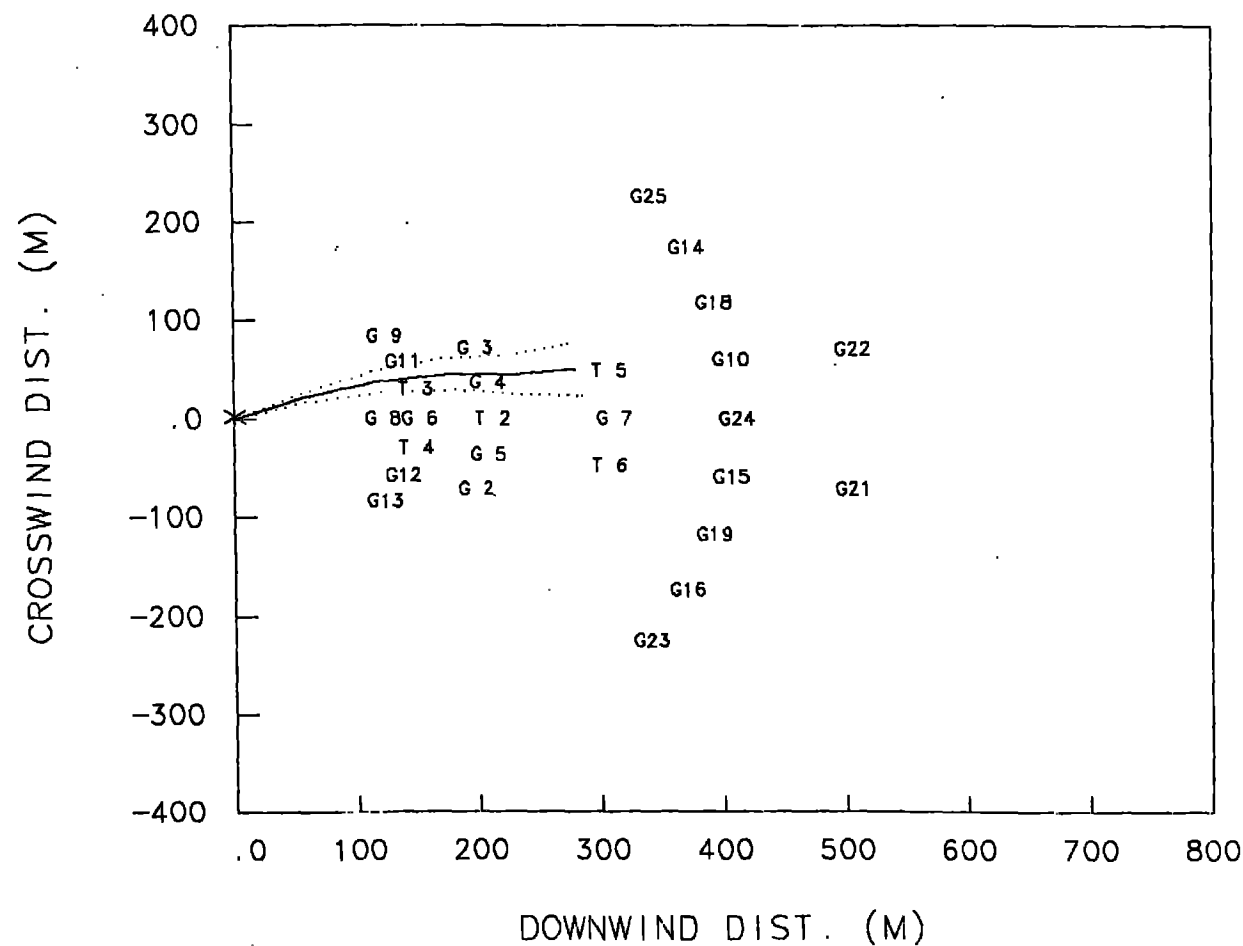
Fig. 18. Sample of the constructed synthetic particle trajectory constructed from the wind-field data. The solid line is the mean trajectory, and the dotted lines are the one-sigma variations about the mean trajectory.

Fig. 18) by a solid line. Using interpolated σ_θ data, trajectories were also constructed for marker particles tracked along wind directions of $\theta \pm \sigma_\theta$. These trajectories, indicated by dotted lines, display the lateral cloud dispersion associated with wind fluctuations of $\pm 1 \sigma$. Pairs of wind-field and trajectory plots, like Figs. 16 and 18, respectively, are presented in Appendix 1 for 10-s periods during Coyotes 3, 5, and 6.

On Coyote 6, the local wind field was clearly influenced by cloud combustion. Ignition occurred at 104.2 s and 79 m downwind of the spill point indicated by the asterisk. Sensor W09 is located 11 m downwind of the igniter and 90 m downwind of the spill point. As can be seen in Fig. 19, at 114 s the wind speed is noticeably accelerated and has shifted direction. This anomaly lasted for about 30 s.

5.2 Humidity

Absolute humidity values, in grams of water per cubic meter, have been plotted for Coyotes 3, 5, and 6 at several downwind locations. As an indication of LNG vapor cloud presence, gas concentration values, in volume percent, have also been plotted. Table 6 shows, for each test, which stations recorded humidity data in the presence of detectible amounts of gas. Humidity values were measured at a height of 2 m; gas concentration values were logarithmically interpolated to 2 m using measured values at heights of 1 and 3 m.

Absolute humidity values were calculated from measured values of relative humidity and ambient temperature, using the Magnus formula (Eq. (10)) for saturation vapor pressure and then obtaining absolute humidity by the equation of state (Eq. (11)):

$$e_s = 6.108 \exp \left[17.42 \frac{T}{(T + 239.7)} \right], \tag{10}$$

and

$$\rho_v = \frac{(\frac{r}{100}) \, e_s}{R_v \, (T + 273.16)}, \tag{11}$$

where T is ambient temperature in °C, e_s is saturation vapor pressure in millibars, r is relative humidity in percent, R_v is the appropriate gas constant $(4.615 \times 10^{-3}$ mb m^3 g^{-1} deg$^{-1})$, and ρ_v is the absolute humidity in g/m^3.

150r/23r

COYOTE 6   TIME =   114 SEC.
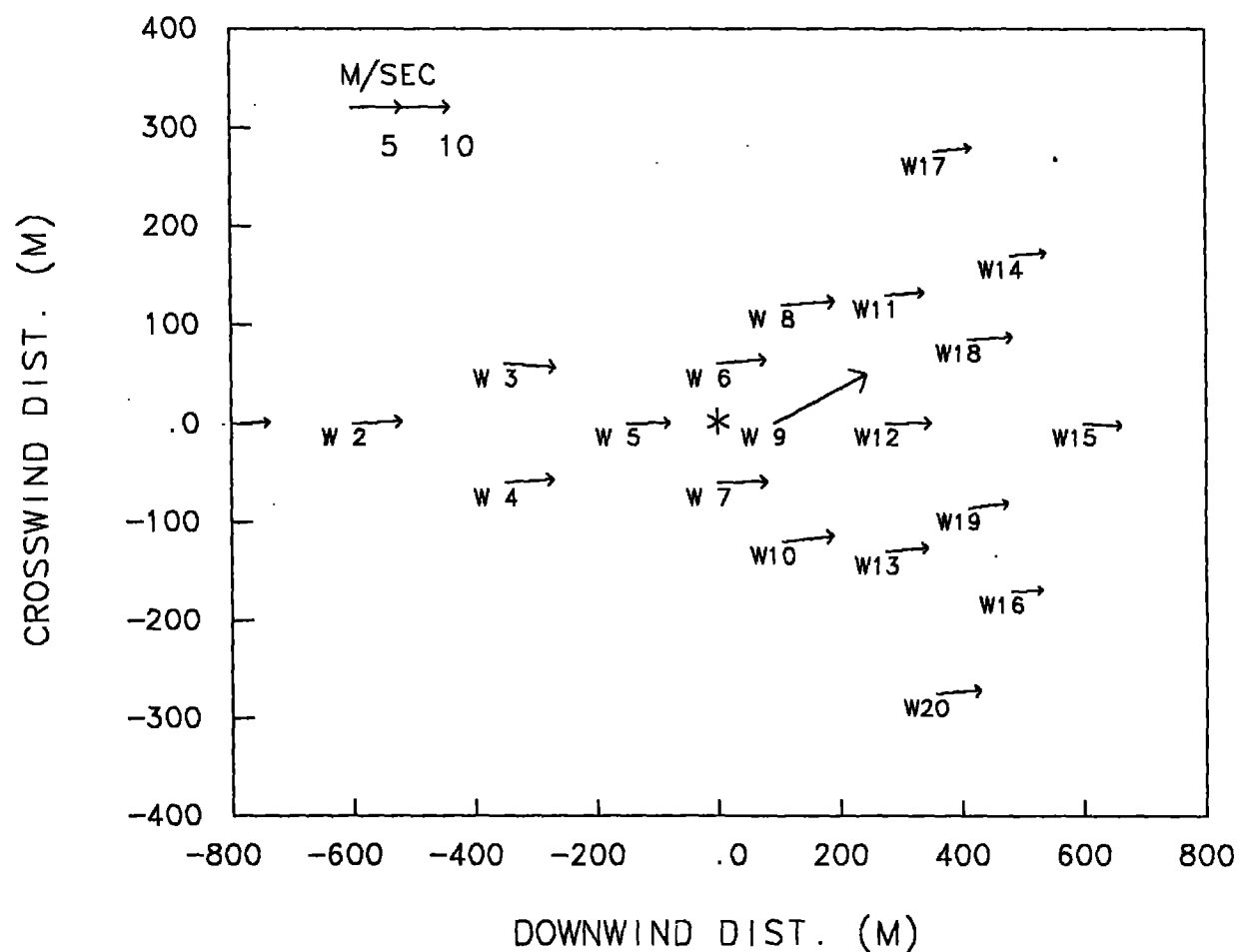
Fig. 19. The wind field at 114 s during the Coyote 6 burn. The asterisk (*) marks the location of the spill pond. The ignition was at 104 s, 79 m downwind of the spill pond and 11 meters upwind of station W09.

During the Coyote series, ambient temperature ranged from 38°C down to 22°C, with associated relative humidities of 6.5 to 18%; this results in a range of absolute humidity of about 3 to 3.5 g/m^3. In such dry conditions, the accuracy of the humidity measurements is reduced. Sensor response is nonlinear, requiring up to fourth-degree polynomials to fit the calibration data. Despite the additional effort to reduce uncertainty in the humidity measurements in dry conditions, the prespill data, shown in Figs. 20-22, suggest that variability in absolute humidity as measured at the various locations is about 1.3 g/m^3. The individual sensors had an average variability of 0.06 g/m^3 during prespill periods.

Figures 20-22 show a consistent enhancement of absolute humidity during vapor cloud passage, with the relative increase proportional to the gas concentration. The same tendency was observed during the Burro series. Casual mechanisms for this phenomena have not been determined. The effects of the vapor burn on absolute humidity were noticeable at station G05 after 150 s. It is not known how much of this perturbation is due to combustion products and how much to the temperature transient and its subsequent effect on the relative humidity measurement.

TABLE 6.
Summary of Humidity Plots (Figs. 20-22)

Station Number and Location	Experiments		
	Coyote 3	Coyote 5	Coyote 6
G04 (200 m, right)[a]	X	X	X
G05 (200 m, left)[a]		X	
G06 (140 m, center)	X		X
G07 (300 m, center)		X	X
G08 (110 m, center)	X	X	X
G10 (400 m, right)	X	X	X
G15 (400 m, left)		X	

Note   a. Left and right refer to array centerline looking upwind toward the spill pond.

COYOTE 3 G4   200M
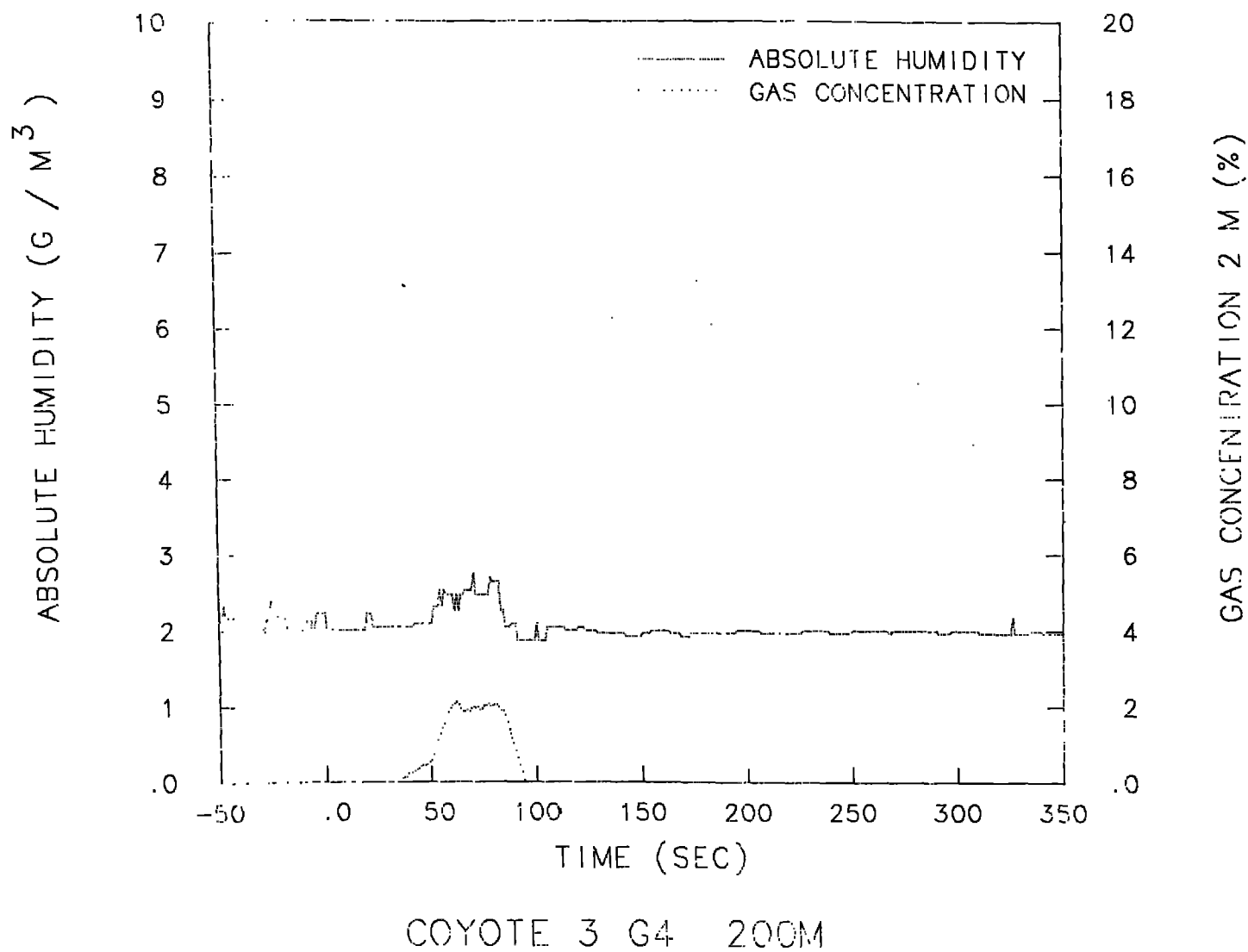
Fig. 20a. Plots of humidity (measured) and gas concentration (estimated) at an elevation of 2 m at Station G04 during Coyote 3.
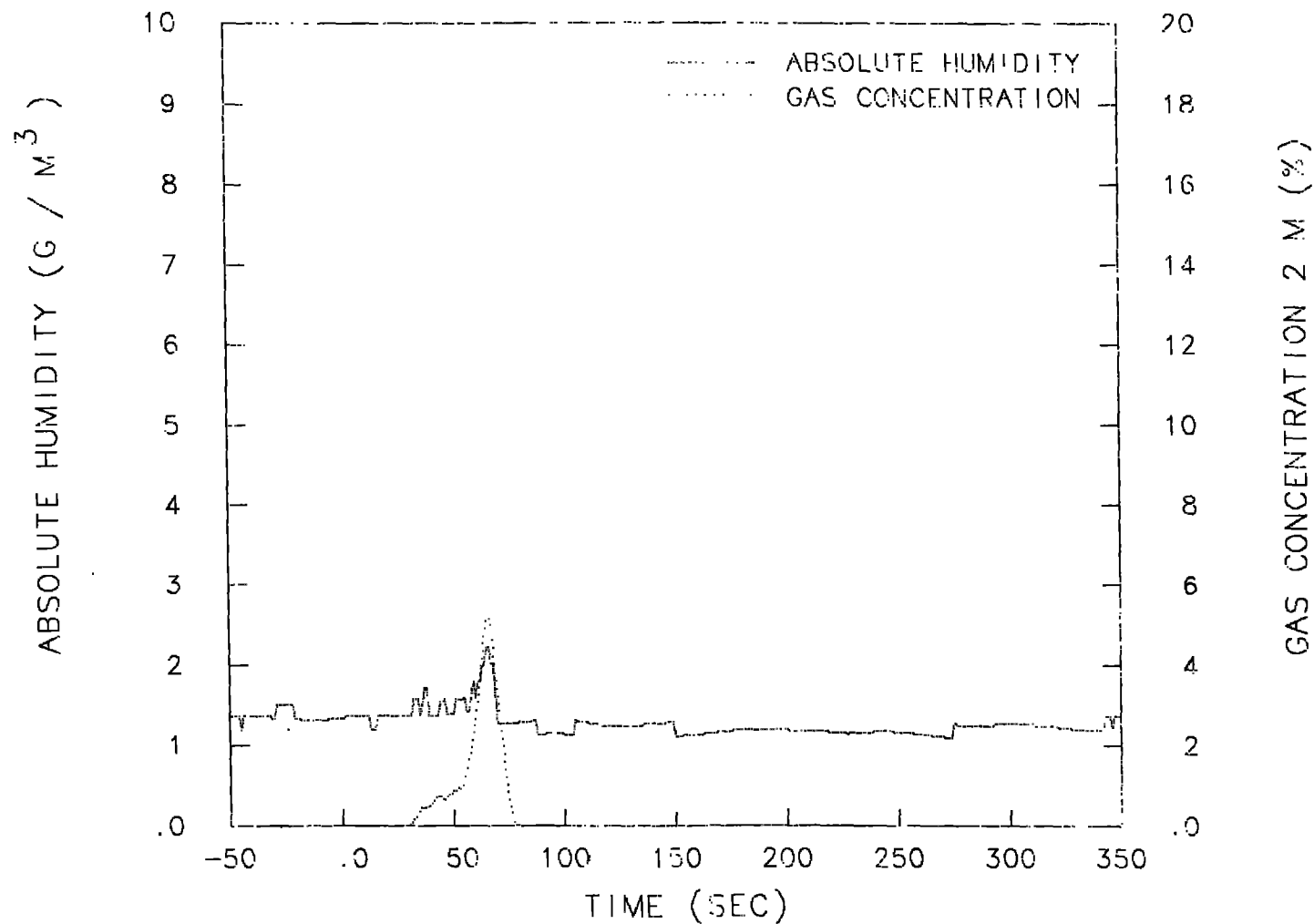
Fig. 20b. Plots of humidity (measured) and gas concentration (estimated) at an elevation of 2 m at Station GO6 during Coyote 3.
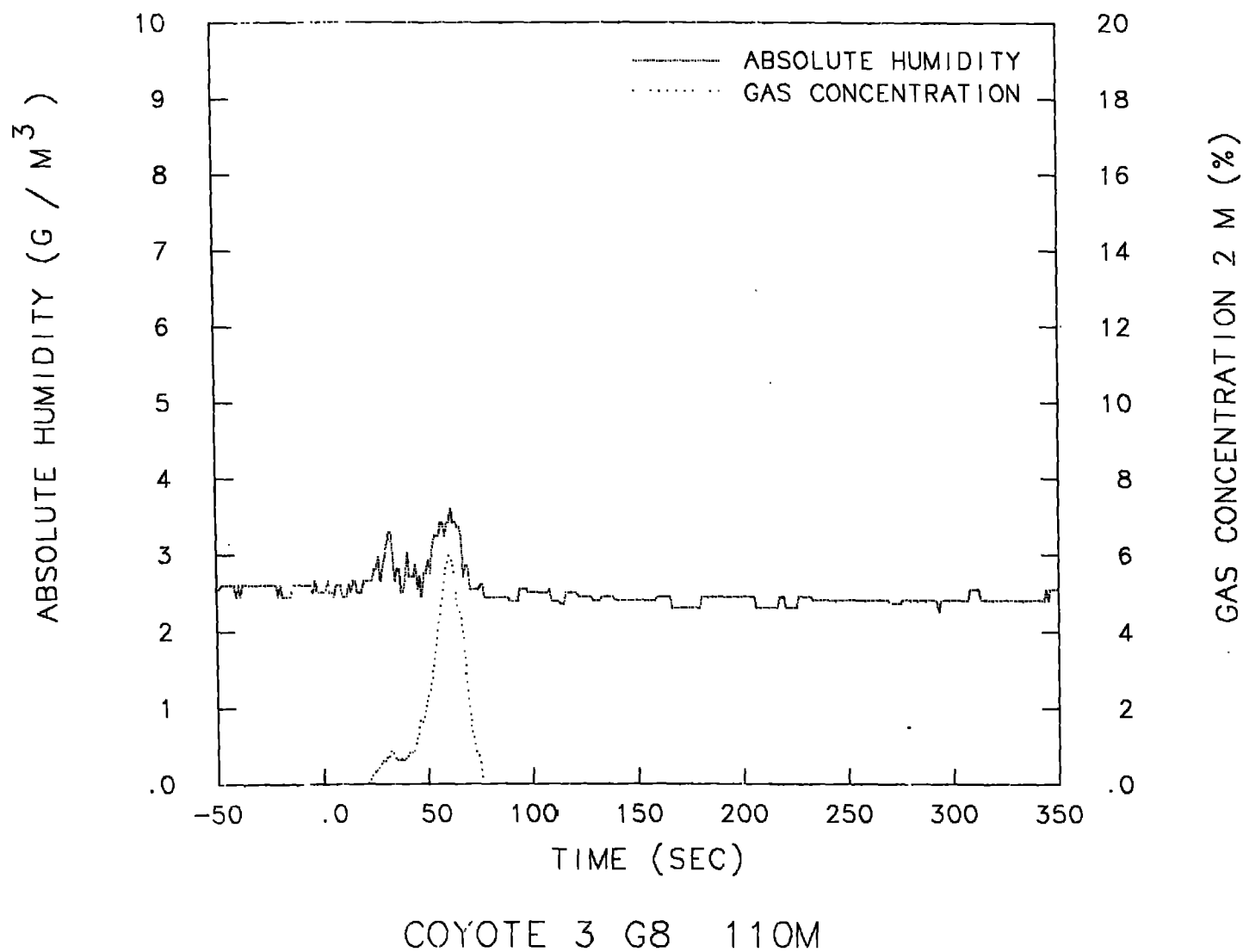
Fig. 20c. Plots of humidity (measured) and gas concentration (estimated) at an elevation of 2 m at Station G08 during Coyote 3.
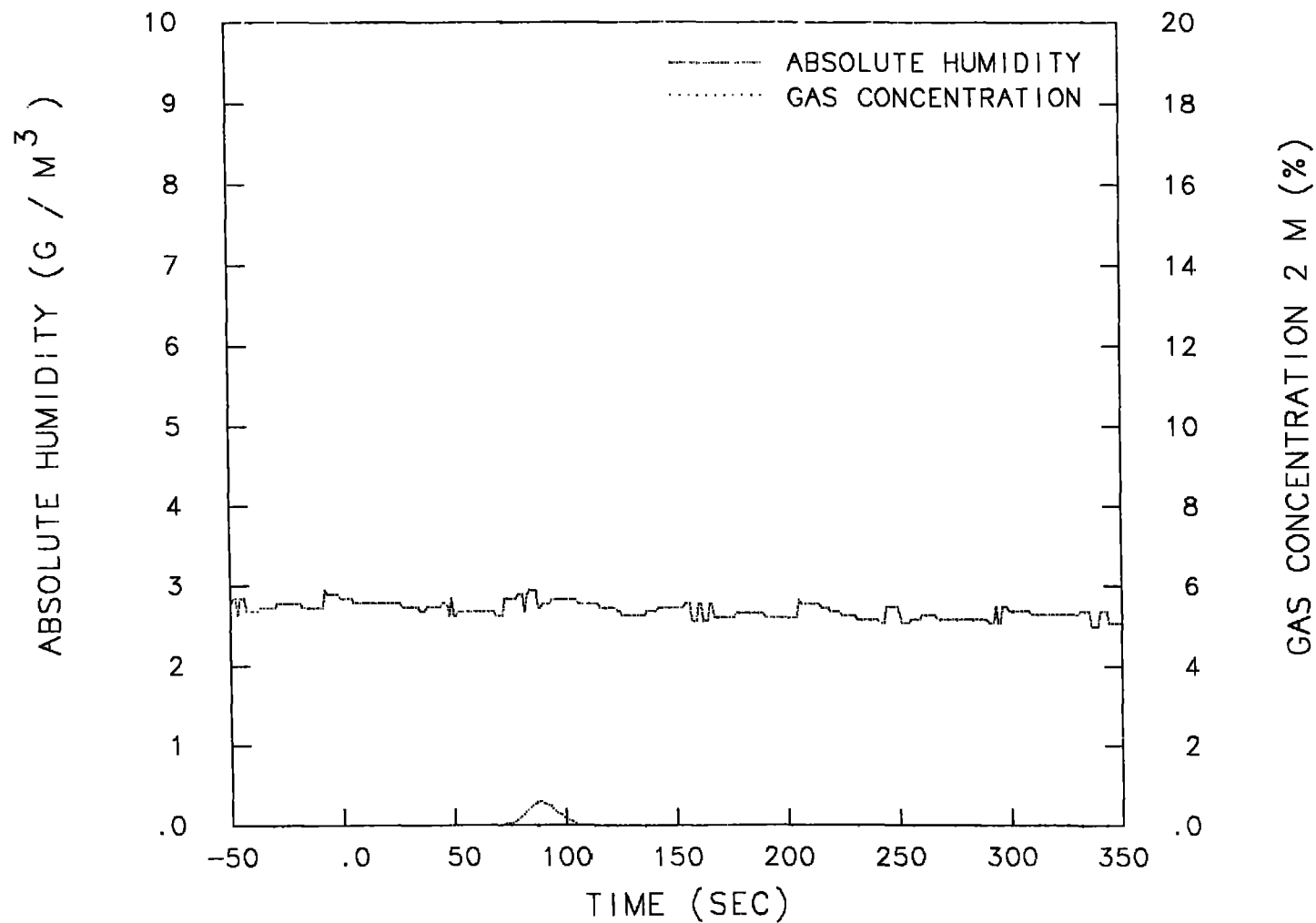
Fig. 20d. Plots of humidity (measured) and gas concentration (estimated) at an elevation of 2 m at Station G10 during Coyote 3.

ABSOLUTE HUMIDITY

GAS CONCENTRATION

ABSOLUTE HUMIDITY (G / M^3)

GAS CONCENTRATION 2 M (%)

TIME (SEC)
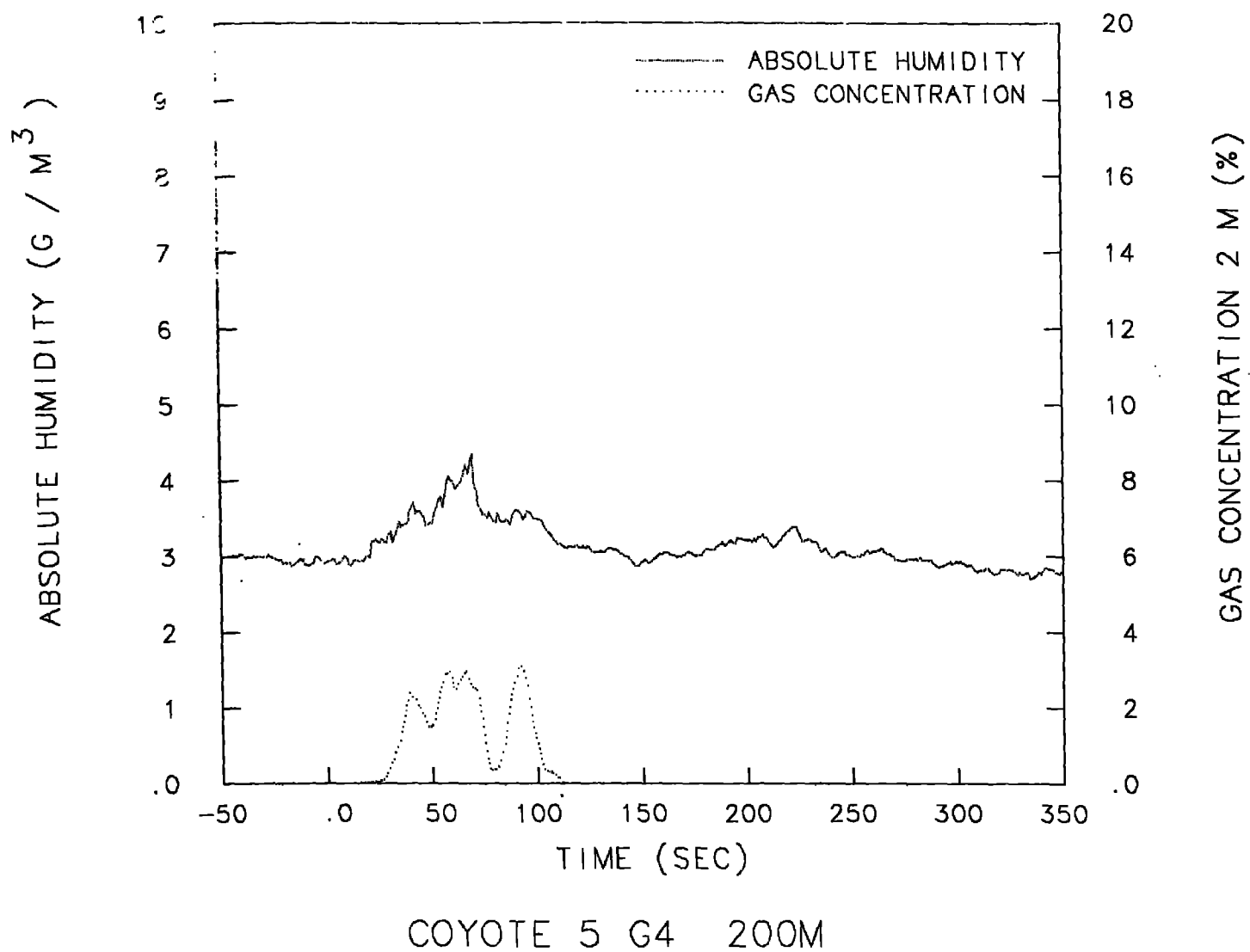
COYOTE 5 G4 200M

Fig. 21a. Plots of humidity (measured) and gas concentration (estimated) at an elevation of 2 m at Station G04 during Coyote 5.
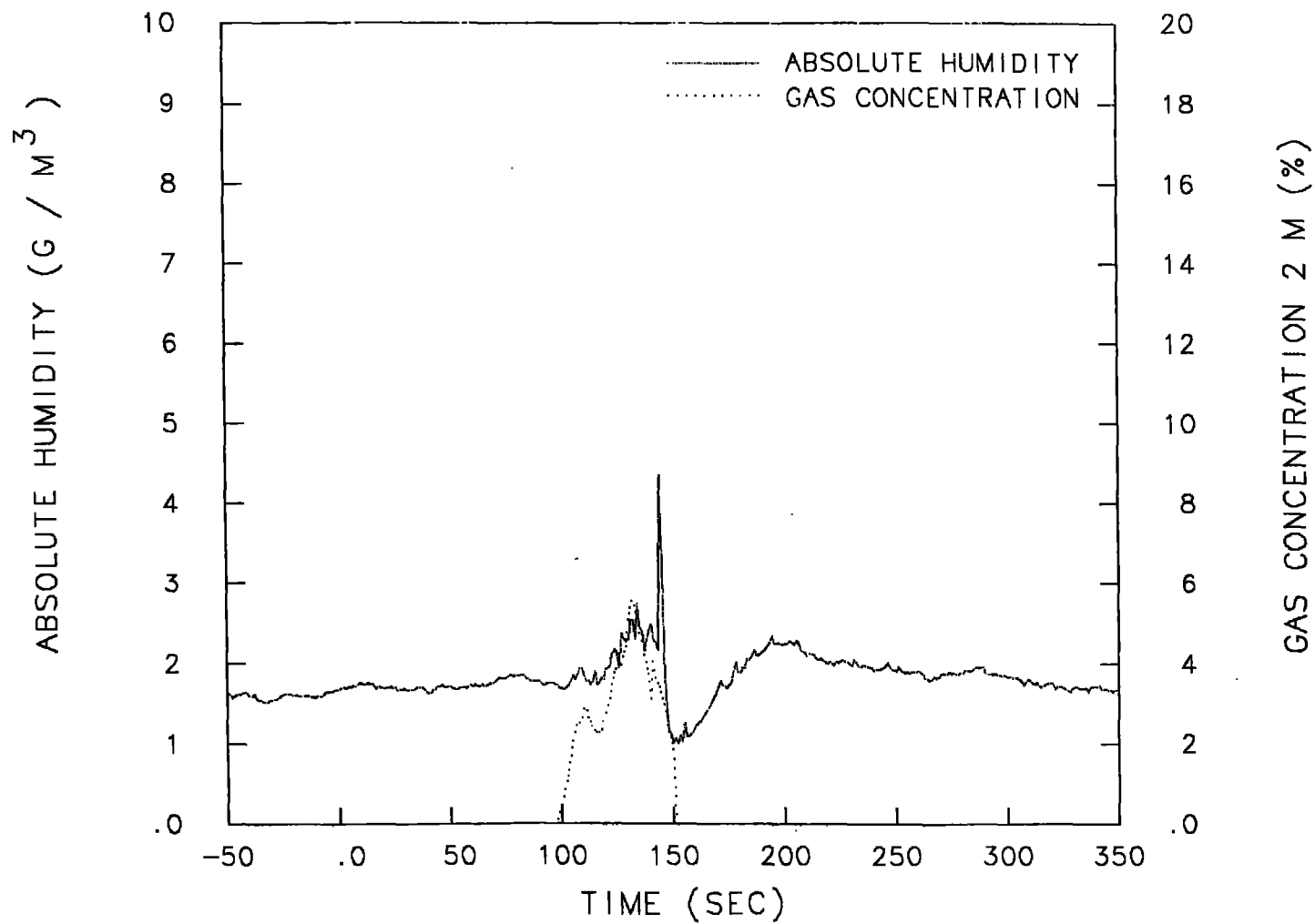
Fig. 21b. Plots of humidity (measured) and gas concentration (estimated) at an
elevation of 2 m at Station G05 during Coyote 5.

COYOTE 5 G7 300M
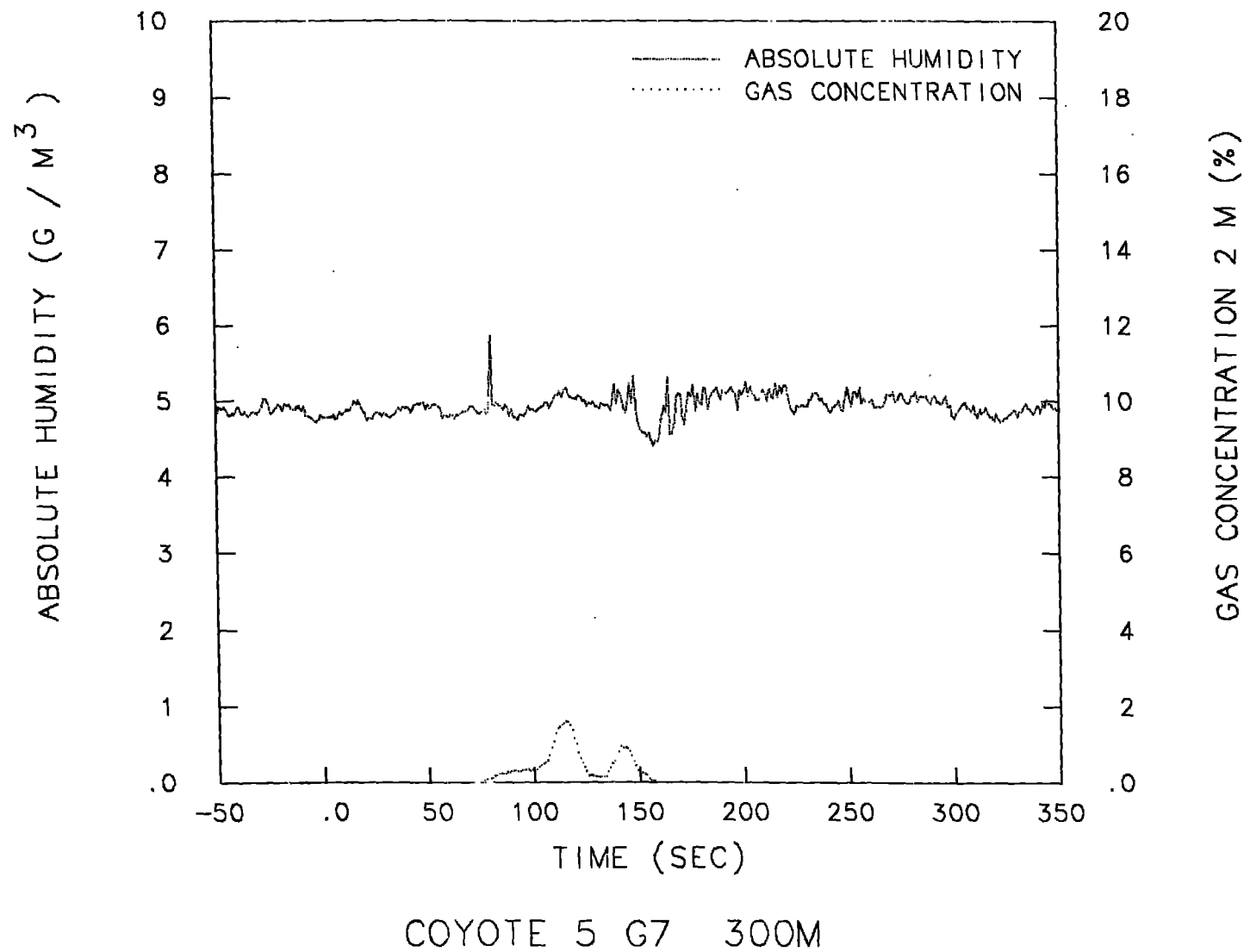
Fig. 21c. Plots of humidity (measured) and gas concentration (estimated) at an elevation of 2 m at Station G07 during Coyote 5.

COYOTE 5 G8   110M
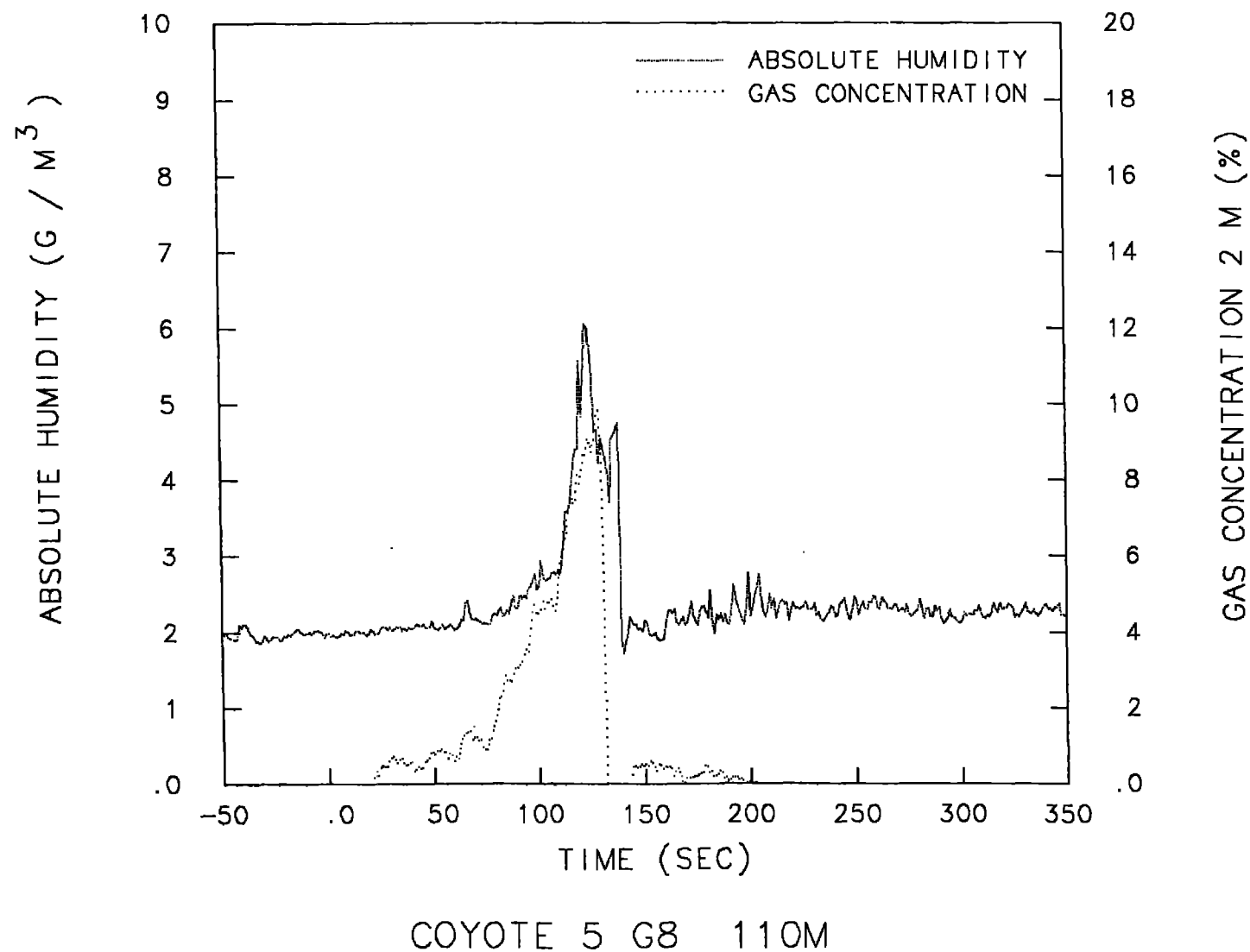
Fig. 21d. Plots of humidity (measured) and gas concentration (estimated) at an elevation of 2 m at Station GO8 during Coyote 5.
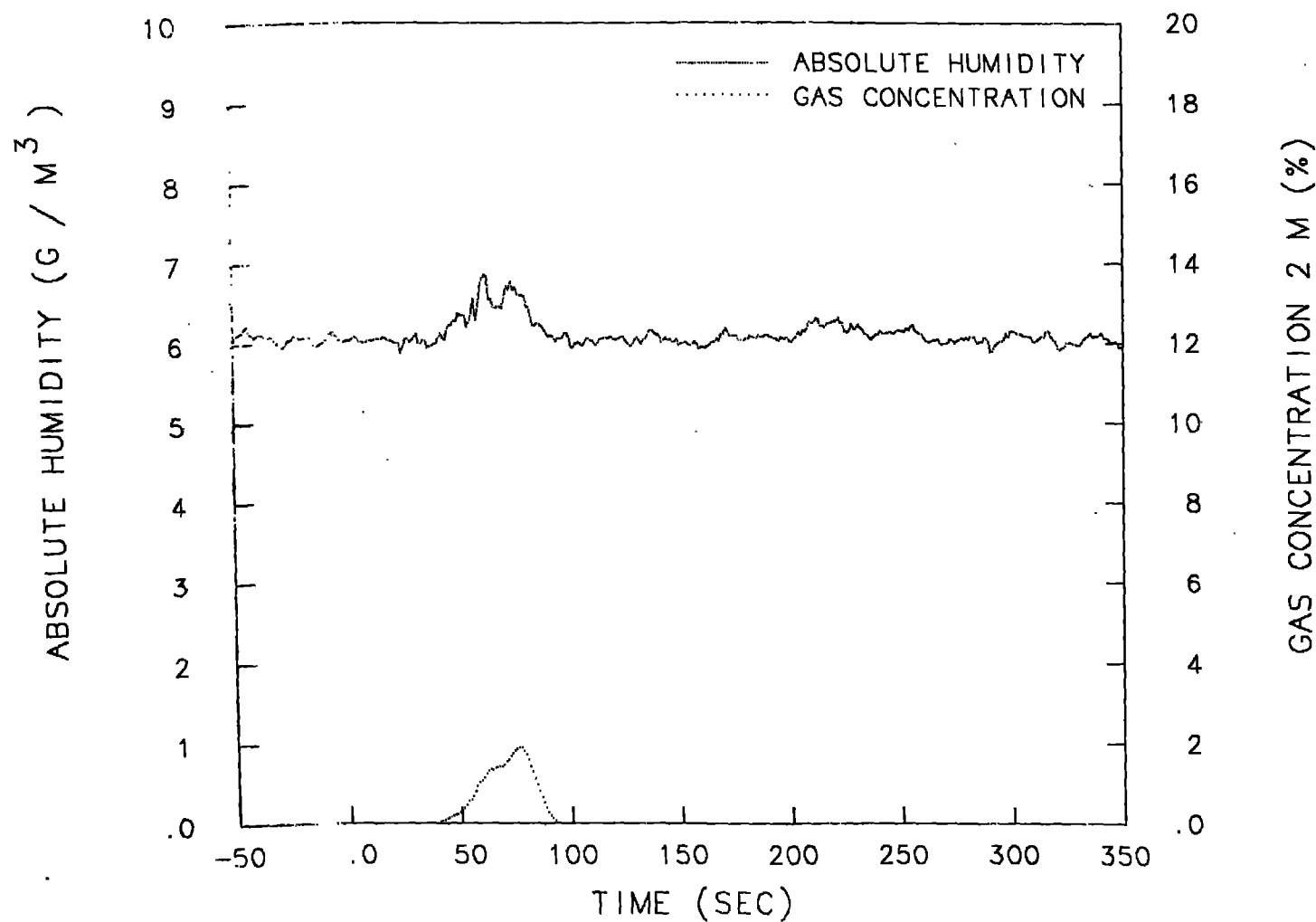
COYOTE 5 G10 400M

Fig. 21e. Plots of humidity (measured) and gas concentration (estimated) at an elevation of 2 m at Station G10 during Coyote 5.
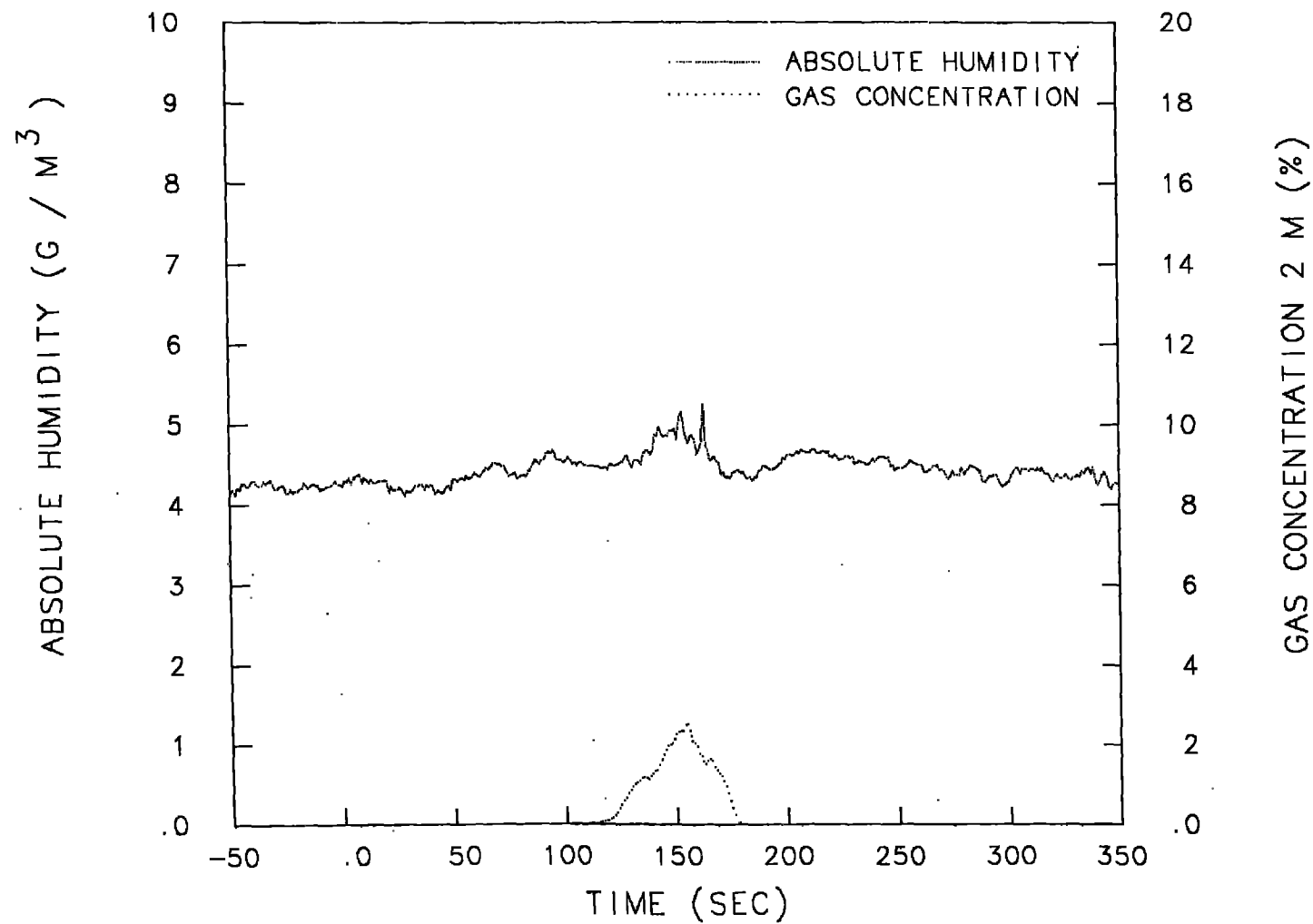
COYOTE 5 G15 400M

Fig. 21f. Plots of humidity (measured) and gas concentration (estimated) at an elevation of 2 m at Station G15 during Coyote 5.
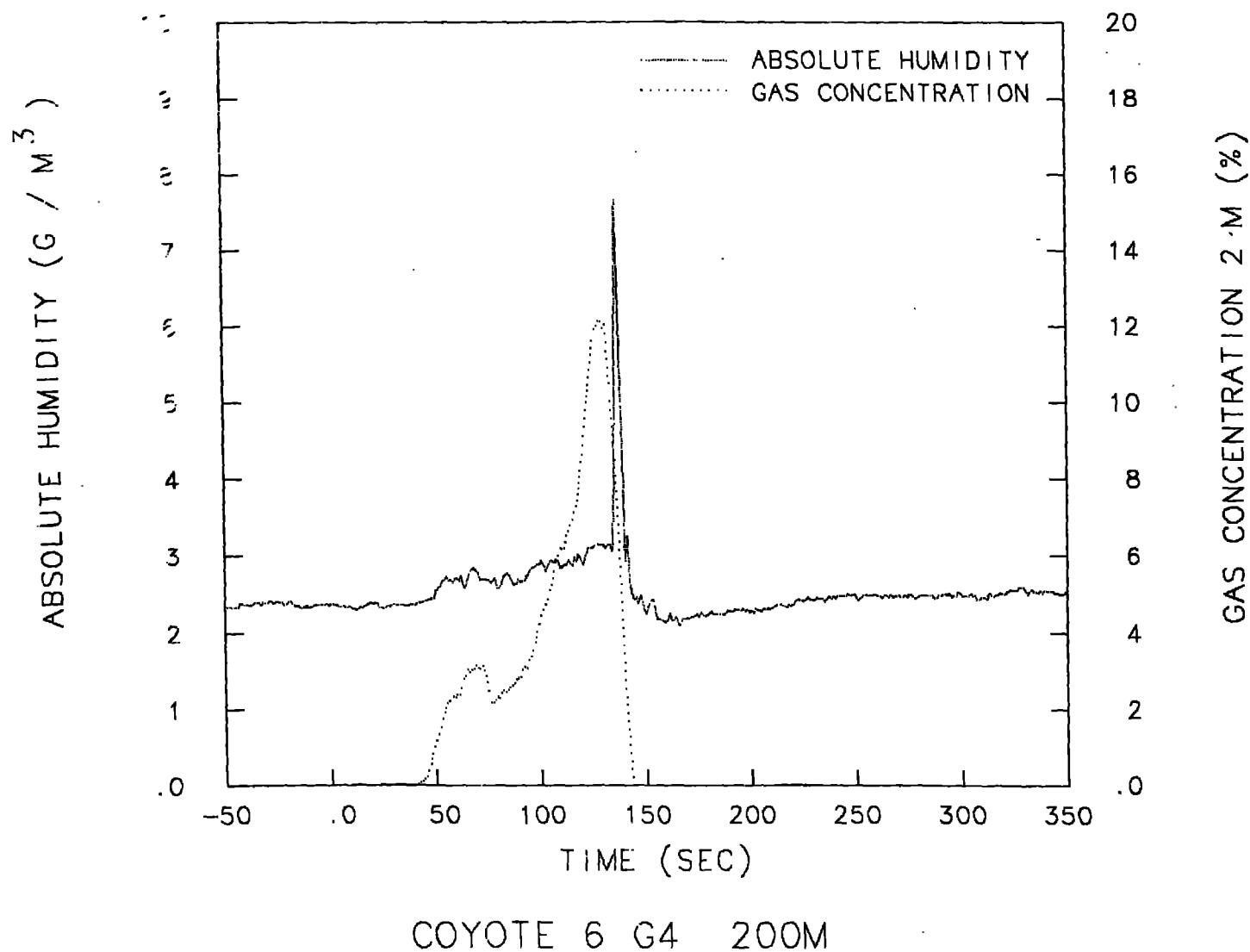
Fig. 22a. Plots of humidity (measured) and gas concentration (estimated) at an elevation of 2 m at Station G04 during Coyote 6.
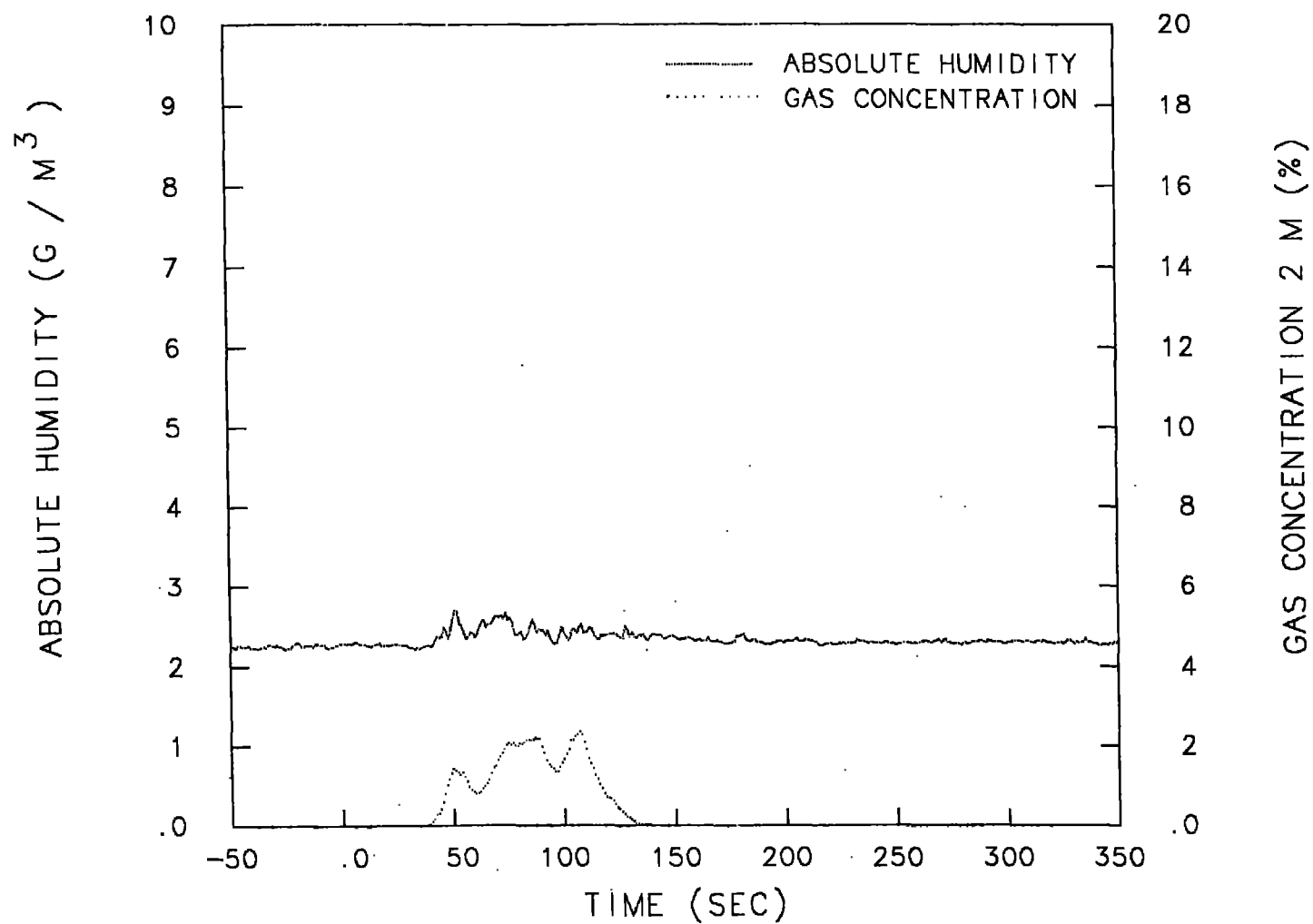
COYOTE 6 G6   140M

Fig. 22b. Plots of humidity (measured) and gas concentration (estimated) at an elevation of 2 m at Station G06 during Coyote 6.
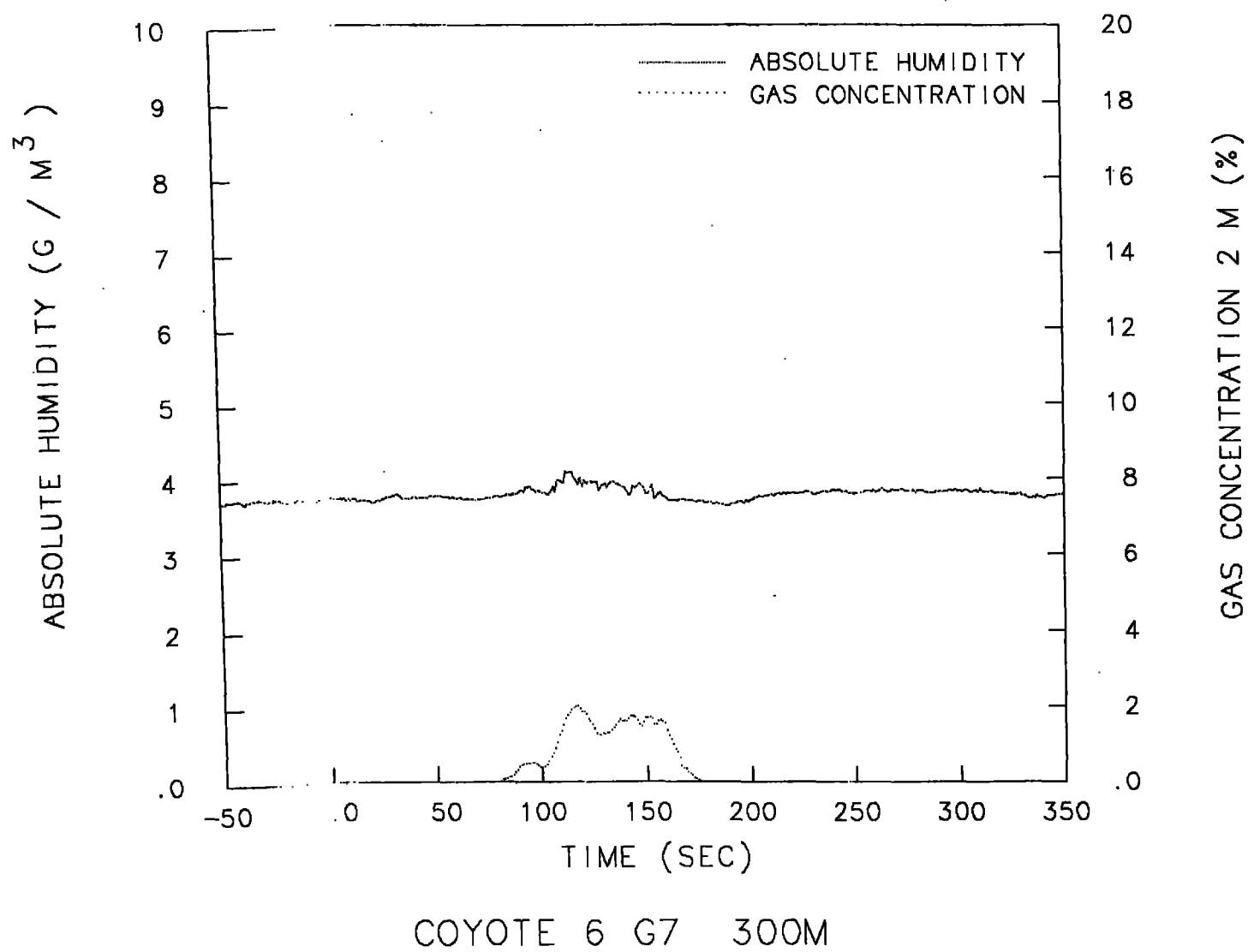
Fig. 22c. Plots of humidity (measured) and gas concentration (estimated) at an elevation of 2 m at Station GO7 during Coyote 6.
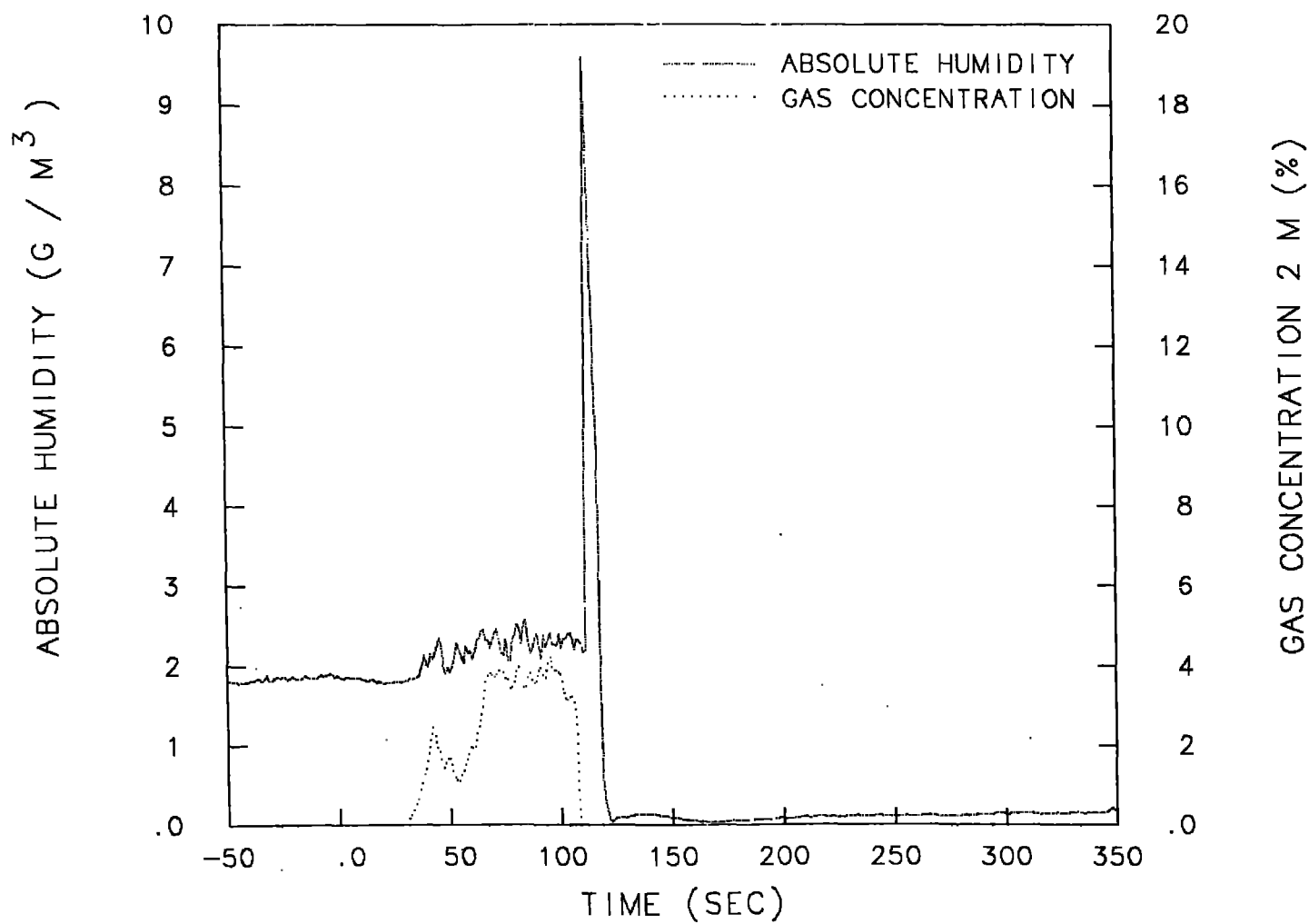
Fig. 22d. Plots of humidity (measured) and gas concentration (estimated) at an elevation of 2 m at Station G08 during Coyote 6.
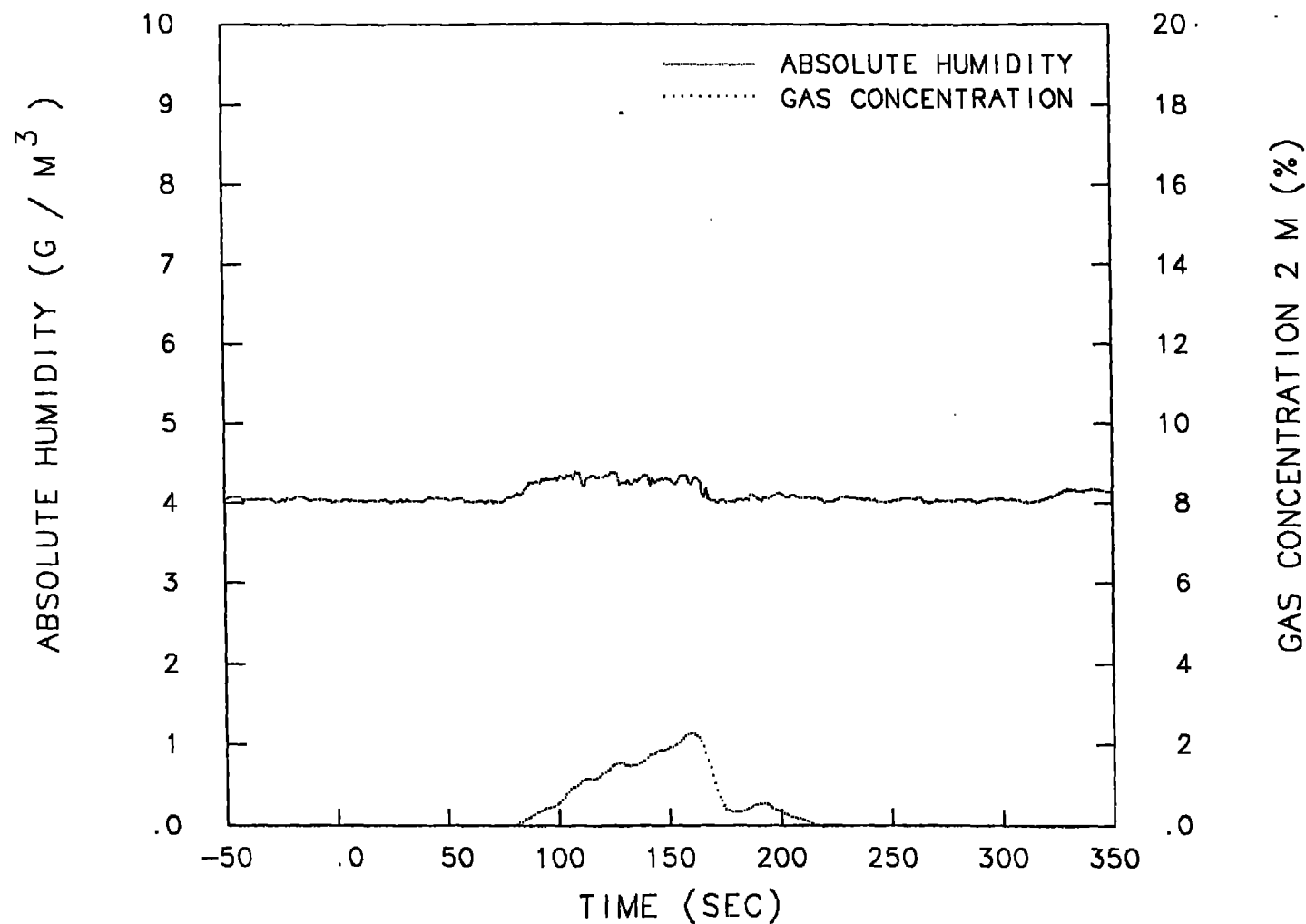
COYOTE 6 G10 400M

Fig. 22e. Plots of humidity (measured) and gas concentration (estimated) at an elevation of 2 m at Station G10 during Coyote 6.

5.3   Ground Heat-Flux Data

Heat-flux data were collected at seven downwind locations to help determine the contribution of ground heat flux to the energy balance of the LNG vapor cloud. Table 7 summarizes where the vapor cloud was present, as indicated by the measured air temperature at the 1-m height. Both heat flux and temperature at a depth of about 0.5 cm are plotted for a 400-s period (50 s before spill to 350 s after spill); see Figs. 23-25. The following sign convention was adopted for the heat sensors: a negative heat flow indicates heat flowing into the ground from above and a positive heat flow indicates heat flowing upward from the ground.

Two separate responses of the ground heat flux to the LNG vapor cloud are evident in the Coyote data. First, there is a tendency after the spill and before ignition for heat to be transferred from the ground to the cooler over-laying vapor cloud. Depending upon the initial prespill conditions (a strong function of the time of day), (1) the heat flux can change from a larger to a smaller negative value (a decrease of heat flow into the ground); (2) it can change from a negative to a positive value (a change from heat flow into the ground to out of the ground); or (3) it can change from a smaller to a larger positive value (an increase of heat flow out of the ground). Secondly, after ignition and during the passage of the hot burning gases, there is a noticeable flux of heat into the ground. This is especially evident on Coyote 5 (G05, G06, and G08), and Coyote 6 (G04 and G08). On Coyote 6, the heat-flux sensor scale was increased; measured peak excursions on G04 and G08 during vapor burn were -2000 and -1000 watts/m^2, respectively.

TABLE 7.
Summary of Ground Heat-Flux Plots (Figs. 23-25)

Station Number and Location		Experiments		
		Coyote 3	Coyote 5	Coyote 6
G04	(200 m, right)[a]	X	X	X[b]
G05	(200 m, left)[a]		X[b]	X
G06	(140 m, center)		X[b]	X
G07	(300 m, center)		X	X
G08	(110 m, center)	X	X[b]	X[b]
G10	(400 m, right)			X
G15	(400 m, left)		X	

Notes   a.   Left and right refer to array centerline looking upwind toward the spill pond.

b.   Heat-flux and temperature sensors went off-scale during vapor burn. See text for Coyote 6 values.
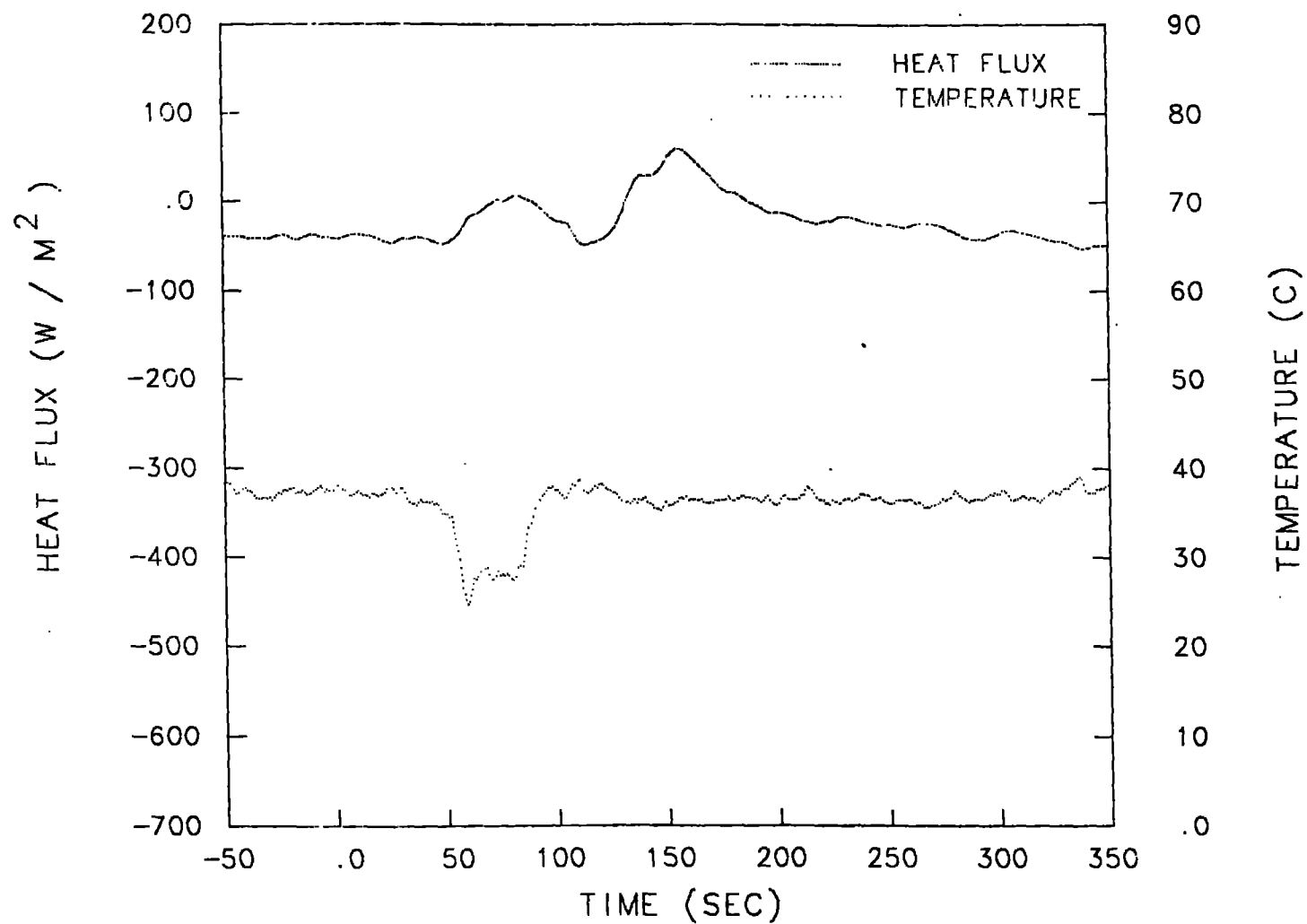
COYOTE 3 G4   200M 1L

Fig. 23a. Plots of heat flux at the ground surface at Station G04 during
Coyote 3.
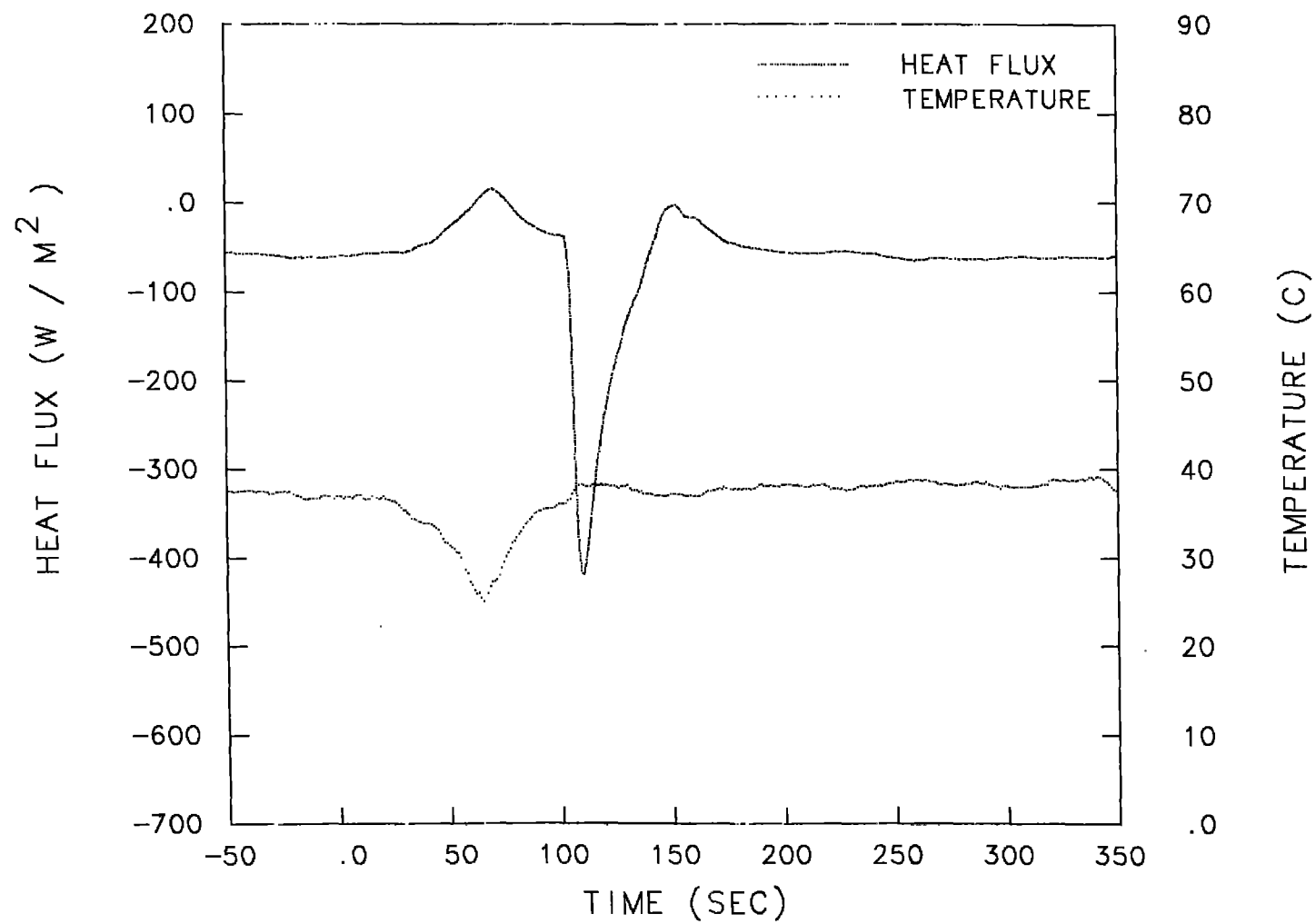
COYOTE 3 G8 110M CL

Fig. 23b. Plots of heat flux at the ground surface at Station G08 during Coyote 3.
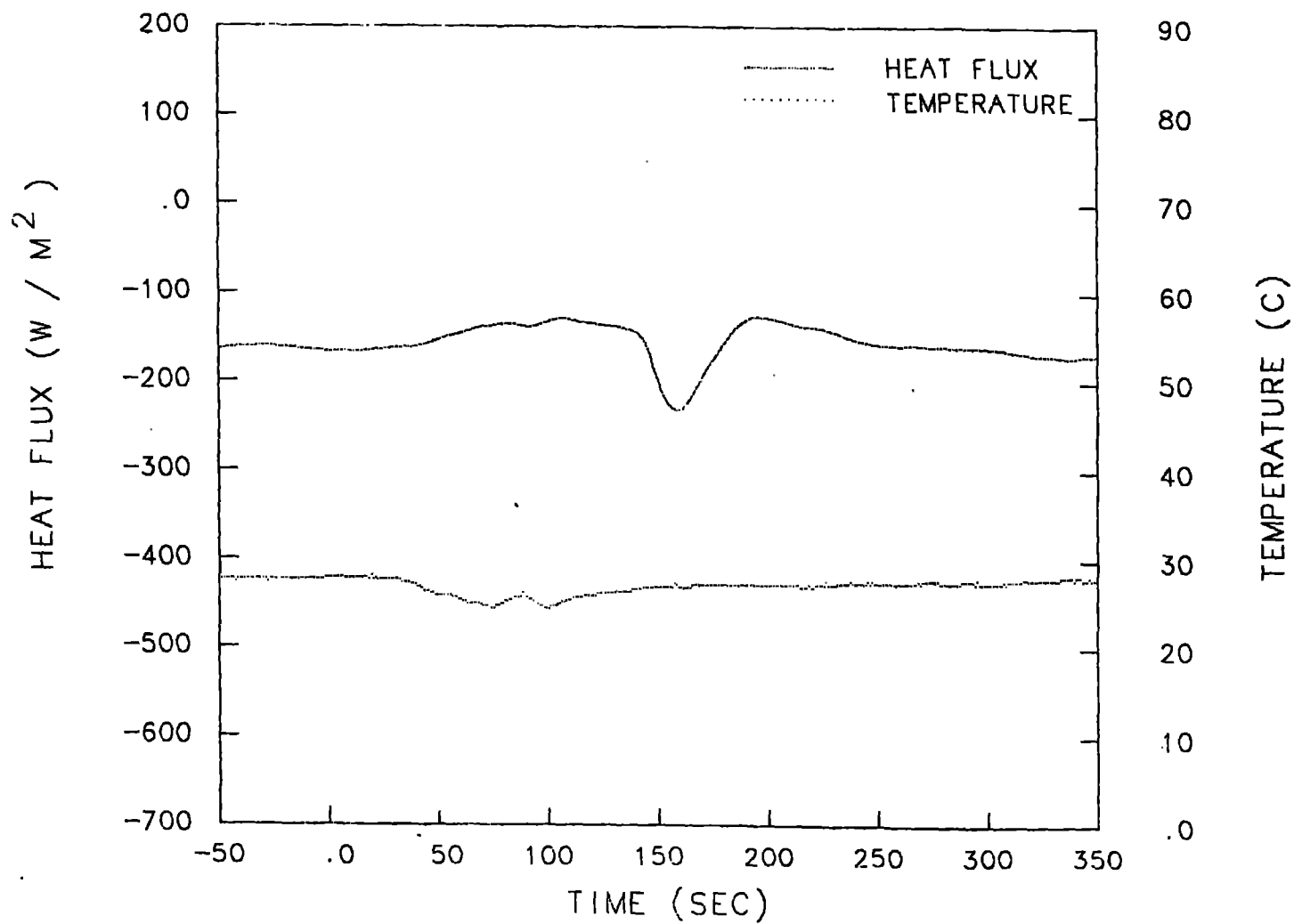
COYOTE 5 G4   200M 1L

Fig. 24a. Plots of heat flux at the ground surface at Station G04 during Coyote 5.
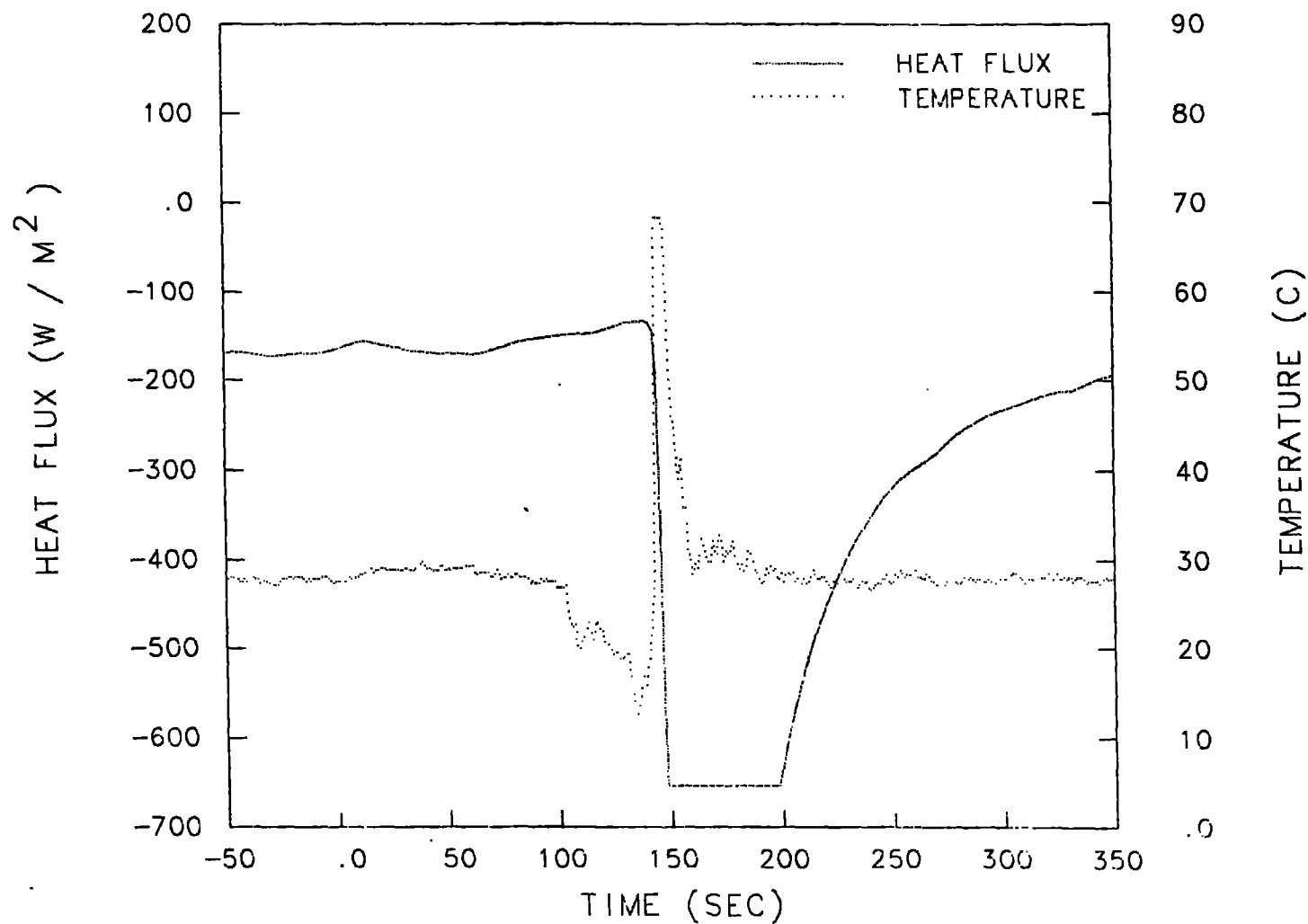
Fig. 24b. Plots of heat flux at the ground surface at Station GO5 during Coyote 5.
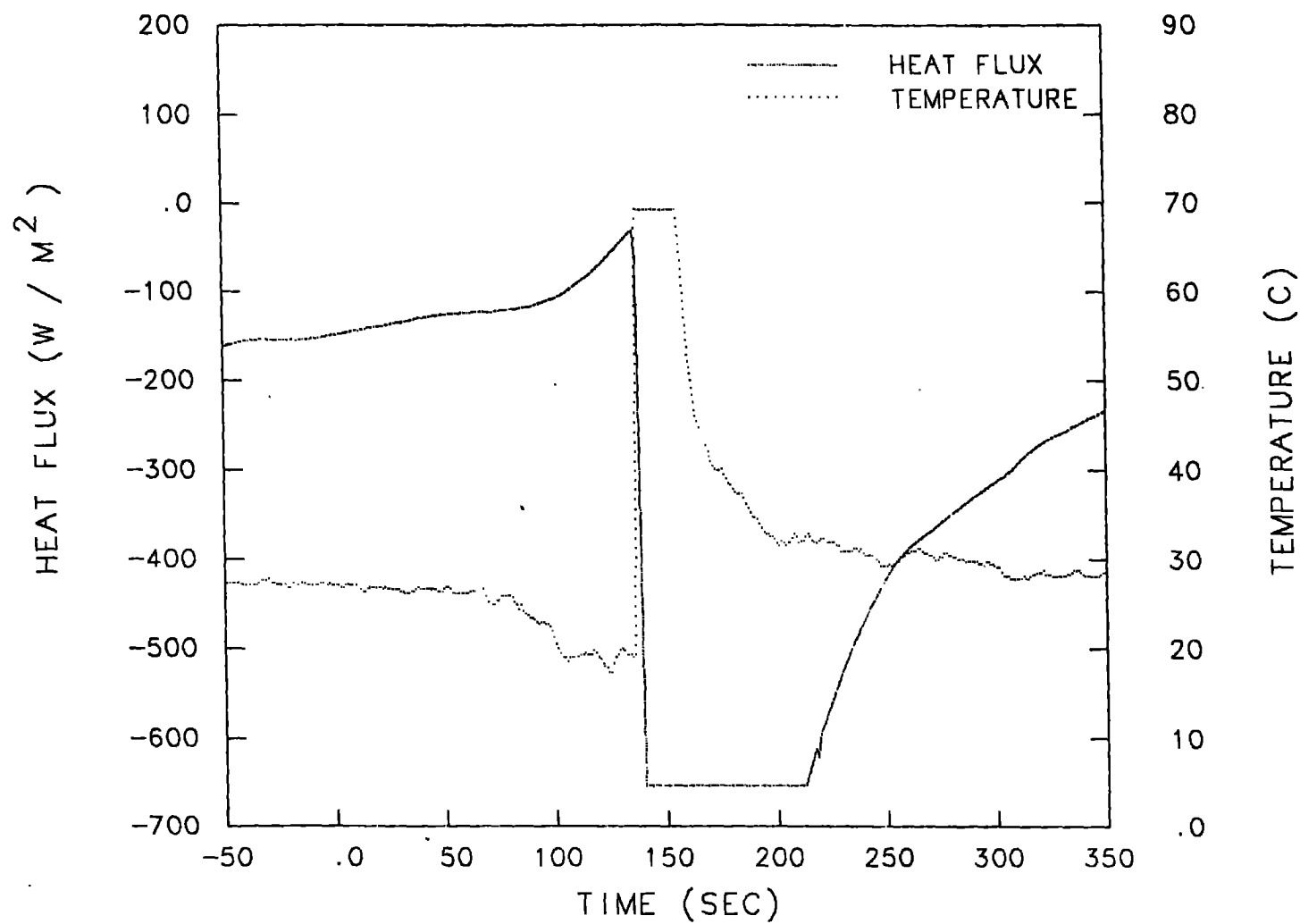
COYOTE 5 G6   140M CL

Fig. 24c. Plots of heat flux at the ground surface at Station G06 during Coyote 5.
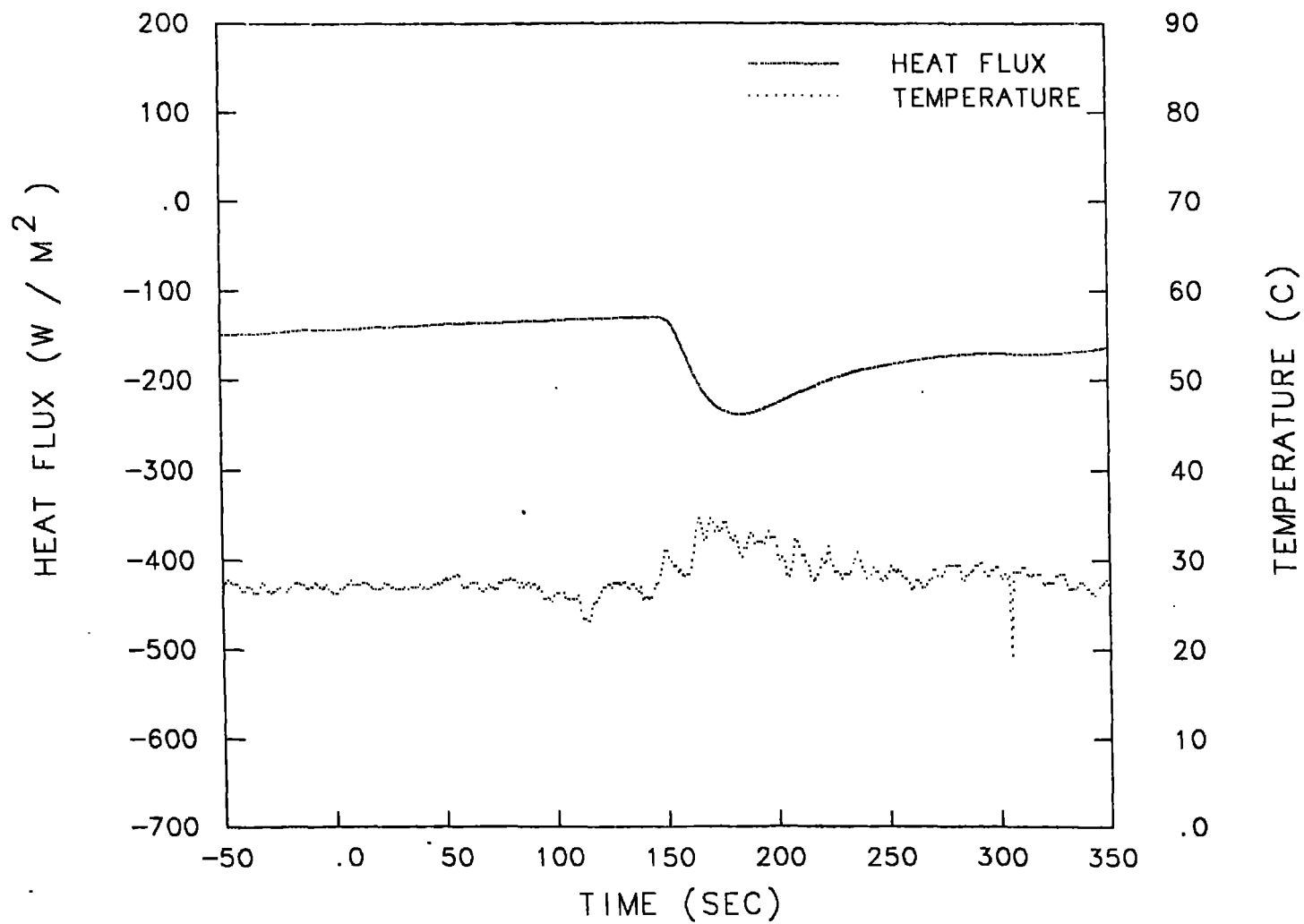
Fig. 24d. Plots of heat flux at the ground surface at Station G07 during
Coyote 5.
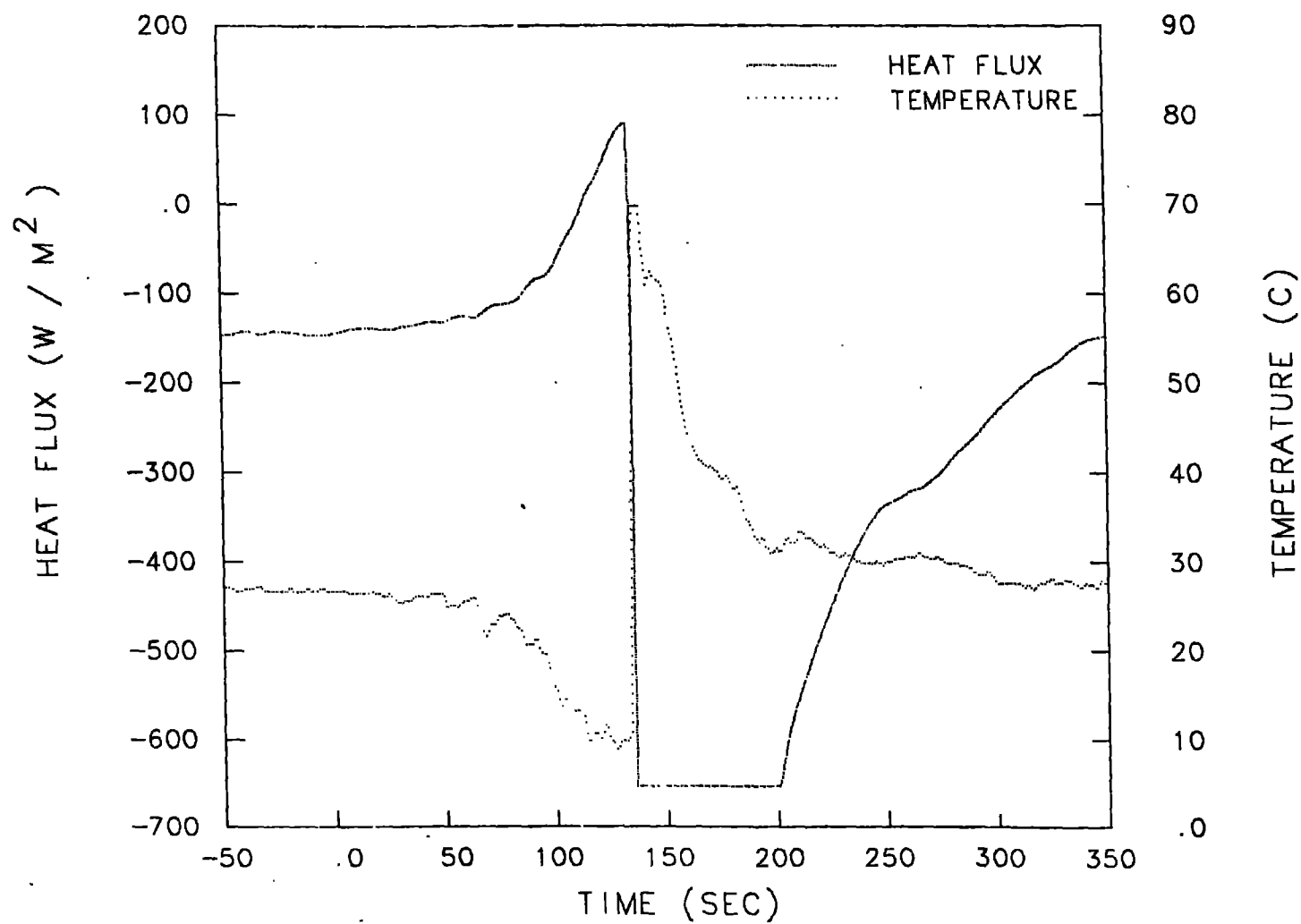
COYOTE 5 G8 110M CL

Fig. 24e. Plots of heat flux at the ground surface at Station G08 during Coyote .
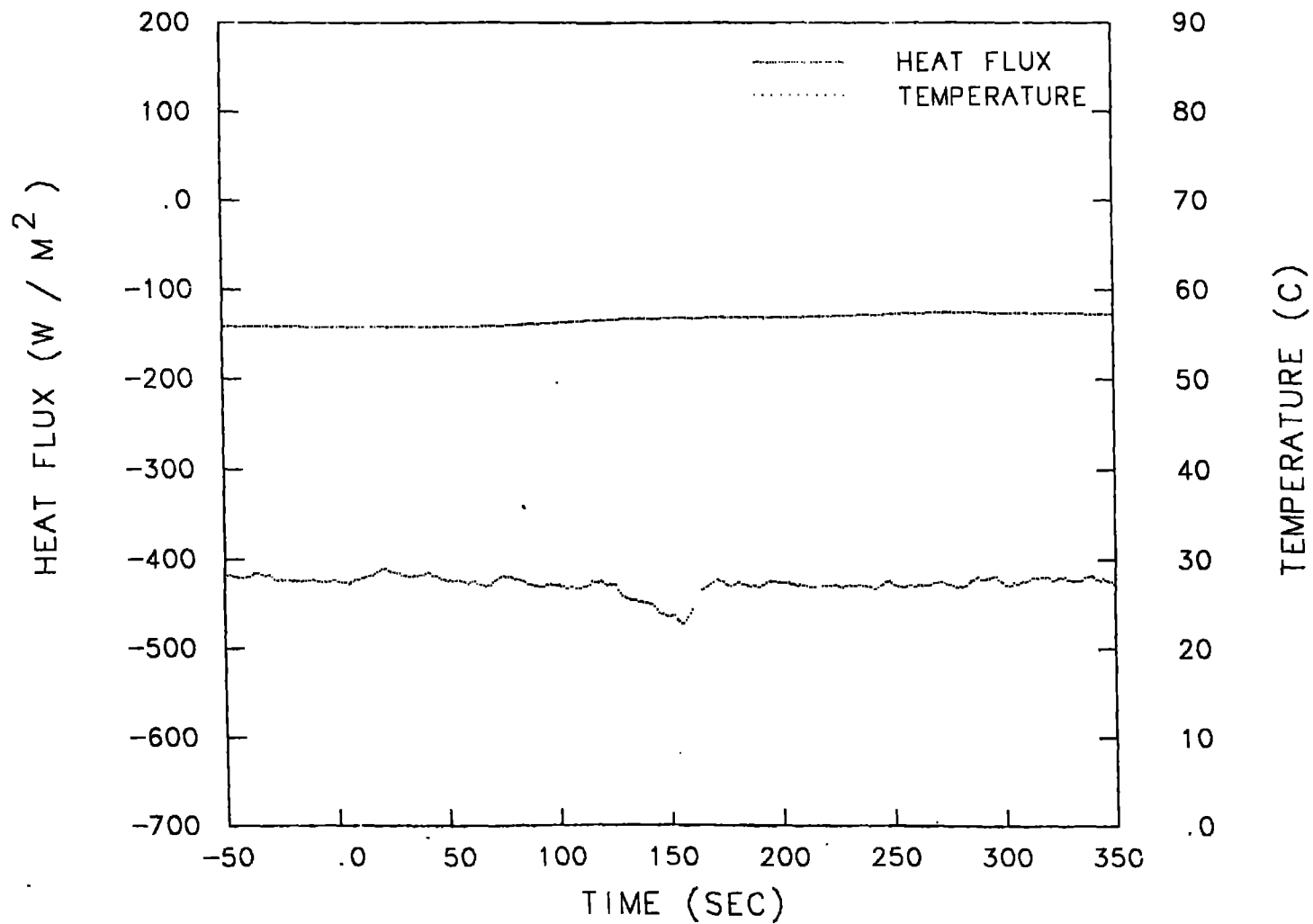
COYOTE 5 G15 400M 1R

Fig. 24f. Plots of heat flux at the ground surface at Station G15 during Coyote .
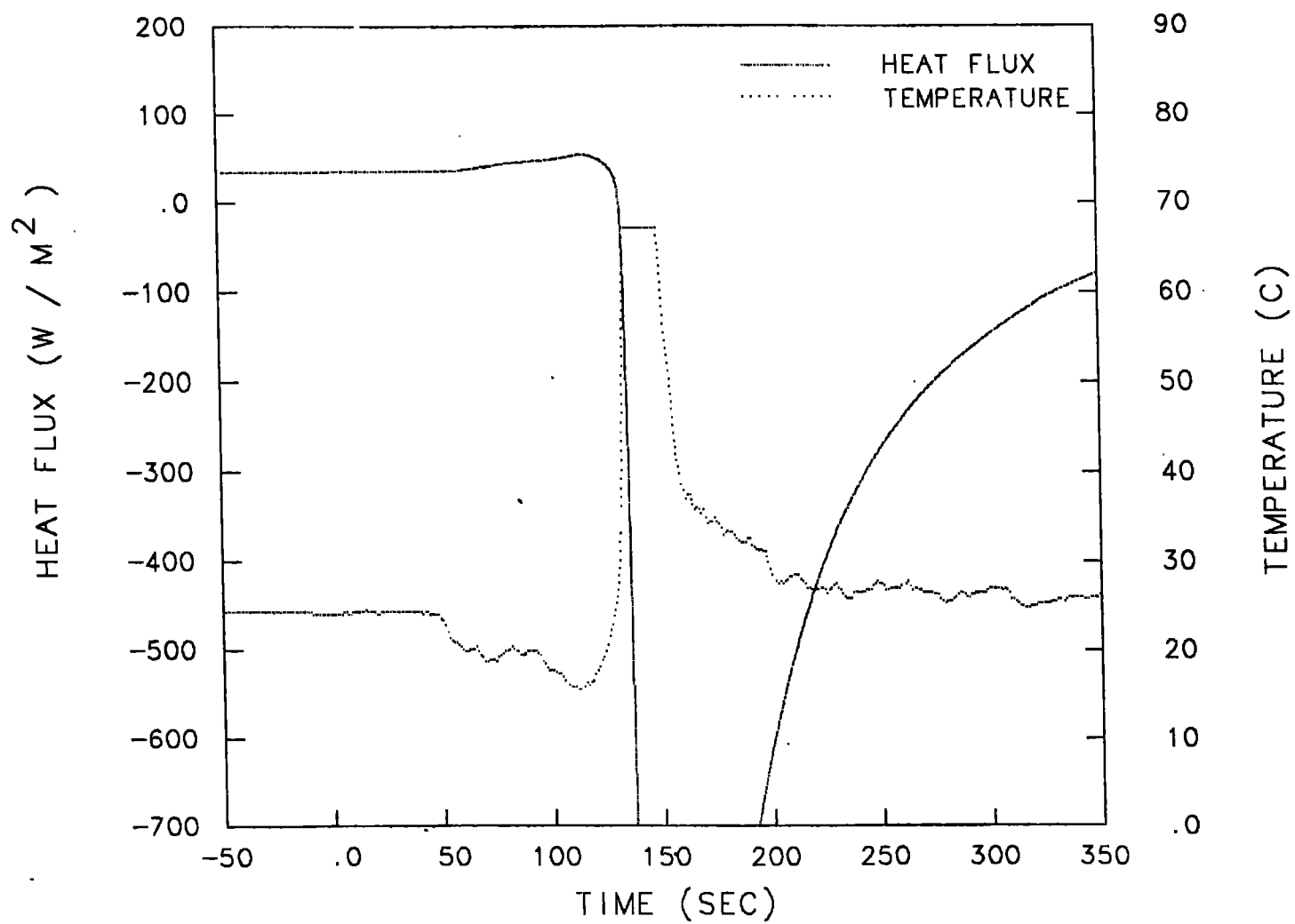
COYOTE 6 G4   200M 1L

Fig. 25a. Plots of heat flux at the ground surface at Station G04 during Coyote 6.
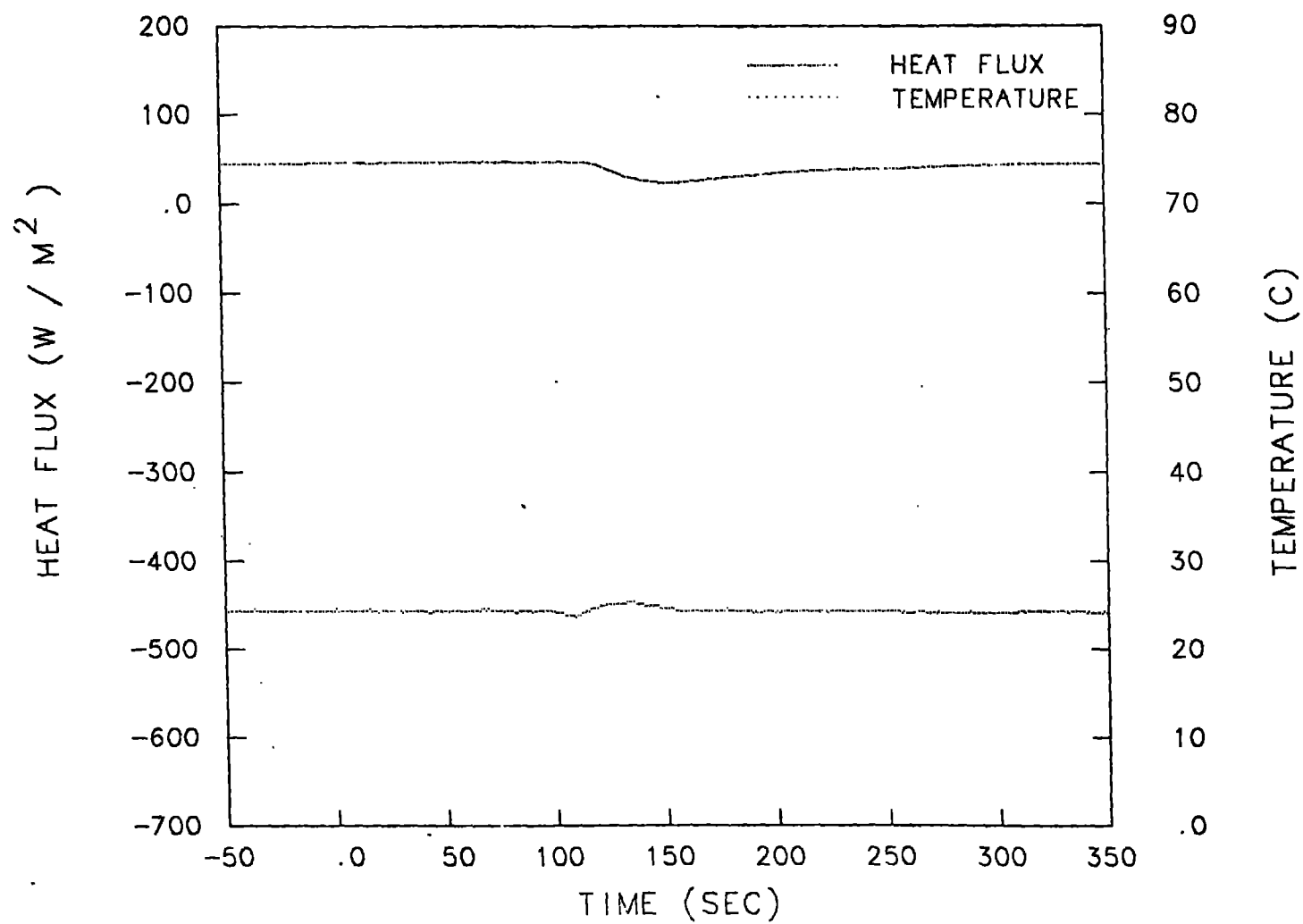
COYOTE 6 G5   200M 1R

Fig. 25b. Plots of heat flux at the ground surface at Station G05 during Coyote 6.
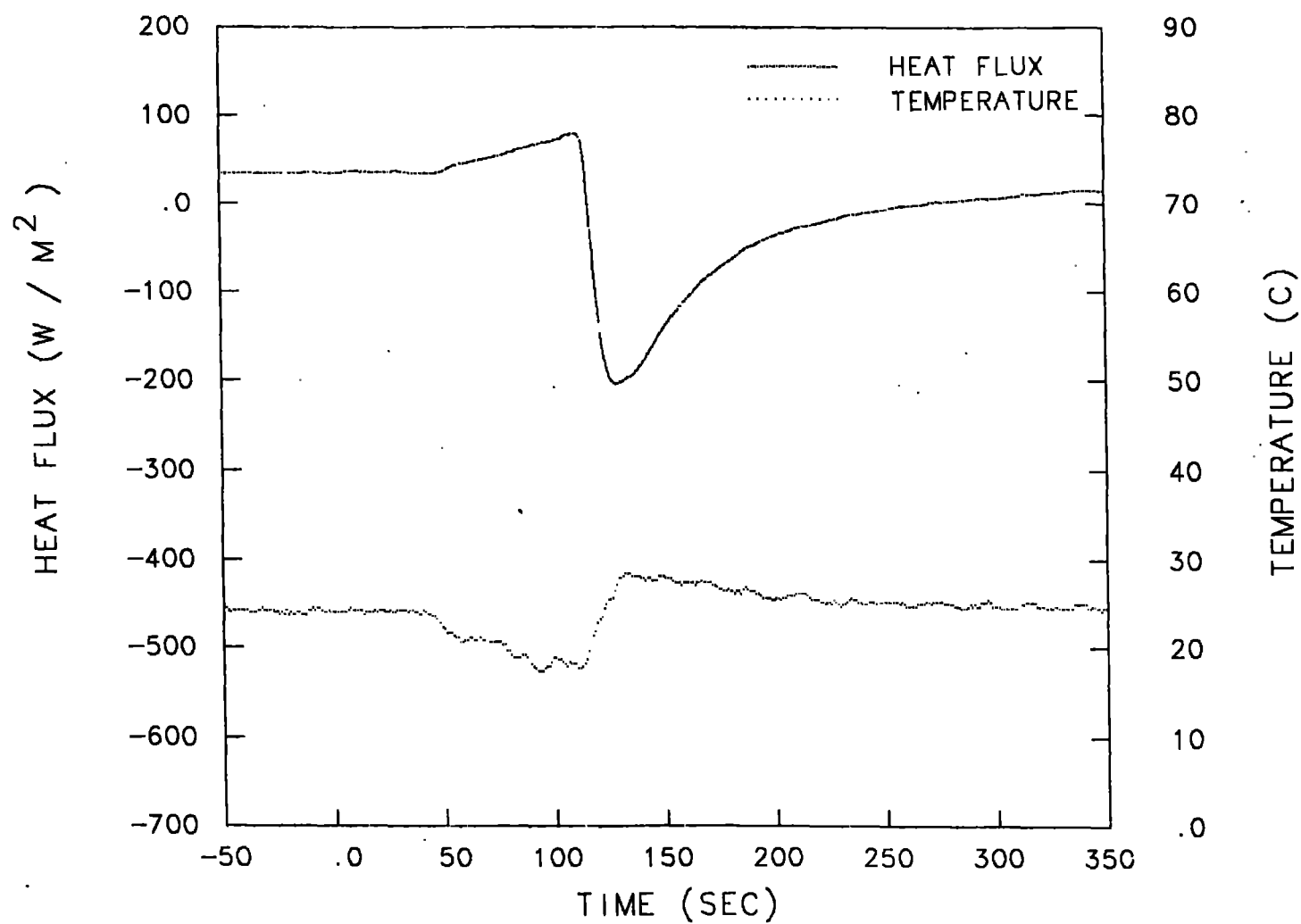
Fig. 25c. Plots of heat flux at the ground surface at Station G06 during
Coyote 6.
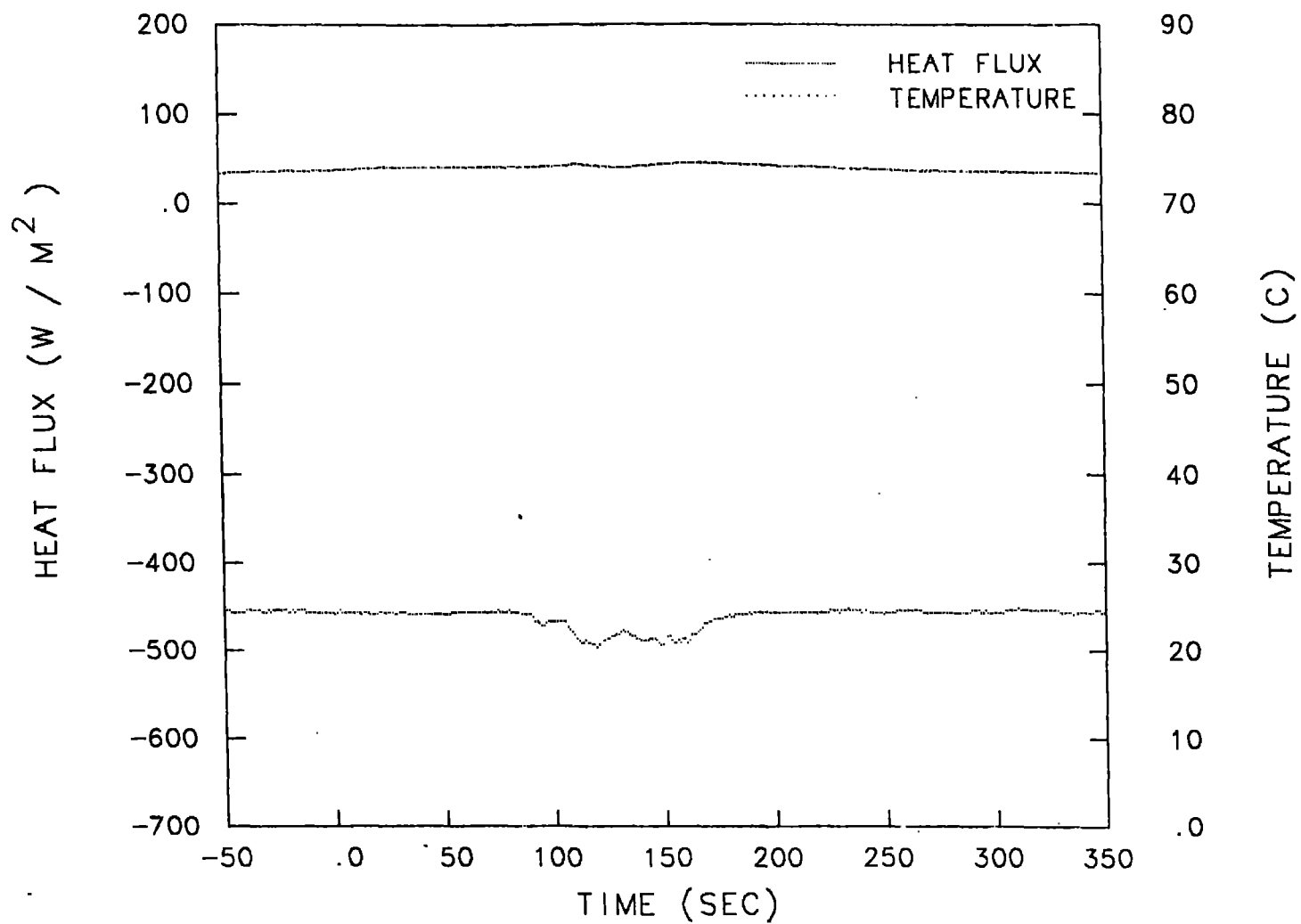
Fig. 25d. Plots of heat flux at the ground surface at Station G07 during
Coyote 6.
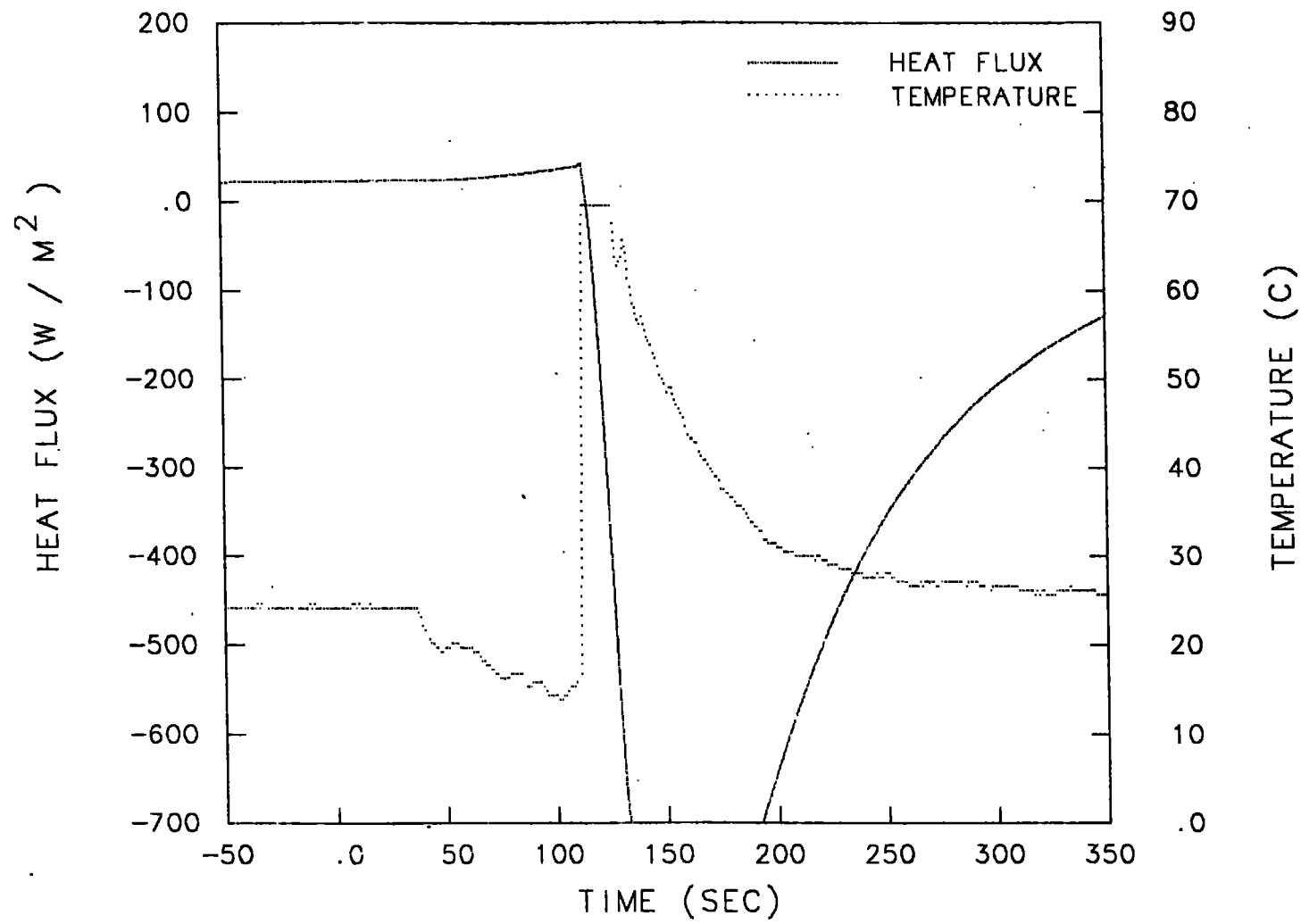
COYOTE 6 G8   110M CL

Fig. 25e. Plots of heat flux at the ground surface at Station G08 during Coyote 6.
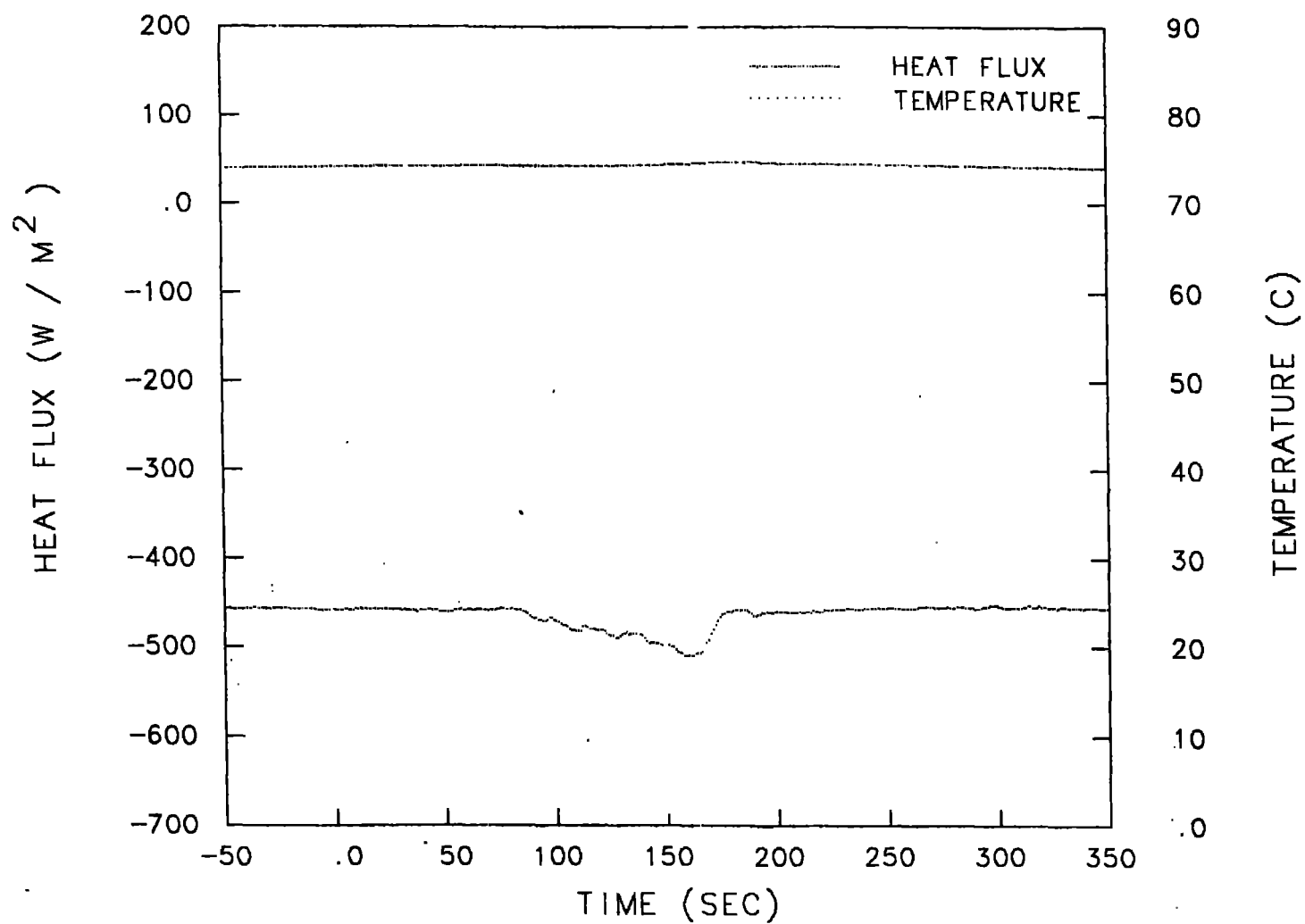
COYOTE 6 G10 400M 1L

Fig. 25f. Plots of heat flux at the ground surface at Station G10 during Coyote 6.

6.   GAS-CONCENTRATION DATA

One of the more important pieces of information provided by the Coyote
Test series is that of the temporal and spatial variations of the LNG vapors.
These data are provided by several different types of sensors as described in
Section 4.2. This section deals with the details of the processing of the gas
sensor data and its display in both time history and contour formats.

6.1 Gas Sensor Data Processing

Each of the four types of gas sensors (LLNL IR, JPL IR, IST, MSA) required
varying degrees of data processing. The simplest was the MSA, requiring only
the LLNL-generated postcalibration tables to convert from voltage to concentra-
tion. The IST hydrocarbon sensors required extensive processing to correct for
both humidity variations and for different methane and ethane sensitivities.
The necessary calibrations for these corrections were performed at LLNL. In
addition, baseline and full-scale calibrations were performed periodically in
the field, and used to process the data. The results were also modified to
account for a slower than desireable fall time. The resulting rise and fall
time constants are approximately 10 s.

The JPL IR sensor data were processed using laboratory calibration results
supplied by JPL and a slightly modified JPL algorithm. Although these were
fast-response sensors, capable of measuring both methane and ethane, sensor
fluctuations due to operation at lower than optimal voltage required smoothing
the results to an approximate time constant of 6 s (we would have preferred
smoothing to 10 s in order to agree with the time constant used for the LLNL
IR sensors for the Burro and Coyote series). Furthermore, the methane and
ethane results were combined and displayed as total hydrocarbons. This was
done in an effort to make the JPL results more in line with the MSA and IST
results for use in plotting the gas concentration contours.

The LLNL IR sensor data were processed using several methods, depending
upon the amount of gas and/or fog present. In some cases, fog persisted out
to the 140 m row; in some other cases, the amount of gas was so small that an
uncoupled solution assuming only methane was present was performed. These
sensors were calibrated at LLNL before and after the Coyote test series. To
conform to data from other sources, the results were smoothed to 10 s time

150r/23r

constant, and the methane and ethane data were combined to yield total hydrocarbons so that the contour plots could be made.

All the data sets required special processing for the period when the flame passed over a sensor. Corrections were done on an individual basis including attempts to remove flame-induced artifacts. In addition, smoothing of the results generally caused the rapid combustion of gas in the flame front to appear less rapid than was actually observed. For most cases, the gas concentrations went from flammable values (5-15%) almost to zero within the 1 s or slower sampling times of the sensor.

6.2 Cloud Concentration Time Histories

The gas concentration data for the Coyote tests is presented in two formats: time histories and contours. The time histories at the various downwind locations in each array row (140, 200, 300, and 500 m) for the three different heights (1, 3, and 8 m) are displayed in Appendix 2. A sample time-history plot of all sensors at the 8 m height for the 400 m row is shown in Fig. 26. In the case of G08 (the only station at 110 m), the time histories of all three levels are superimposed on one plot to save space. The pond data are plotted separately. The concentration time-history results begin at the time the spill valve opens (t = 0), and continue for a period sufficient to include all of the data for the spill being displayed. The legend for identifying each individual sensor is located in the upper right-hand corner of each plot. The test, downwind row location (row), and height are also indicated on each plot. As mentioned in Section 6.1, the various sensor results have been processed such that all of the time-history concentration data plots represent total hydrocarbon concentrations of approximately the same sample frequency. Stations not designated in the legend for a given plot, did not successfully acquire data. The legends thus serve as a means of determining the completeness of the data acquisition.

6.3 Gas-Concentration Contours

The LNG vapor-concentration data were used to generate two-dimensional contour plots at 10-s time intervals during the experiments. The contour plots are generated for two types of surfaces: horizontal surfaces at heights

150r/23r
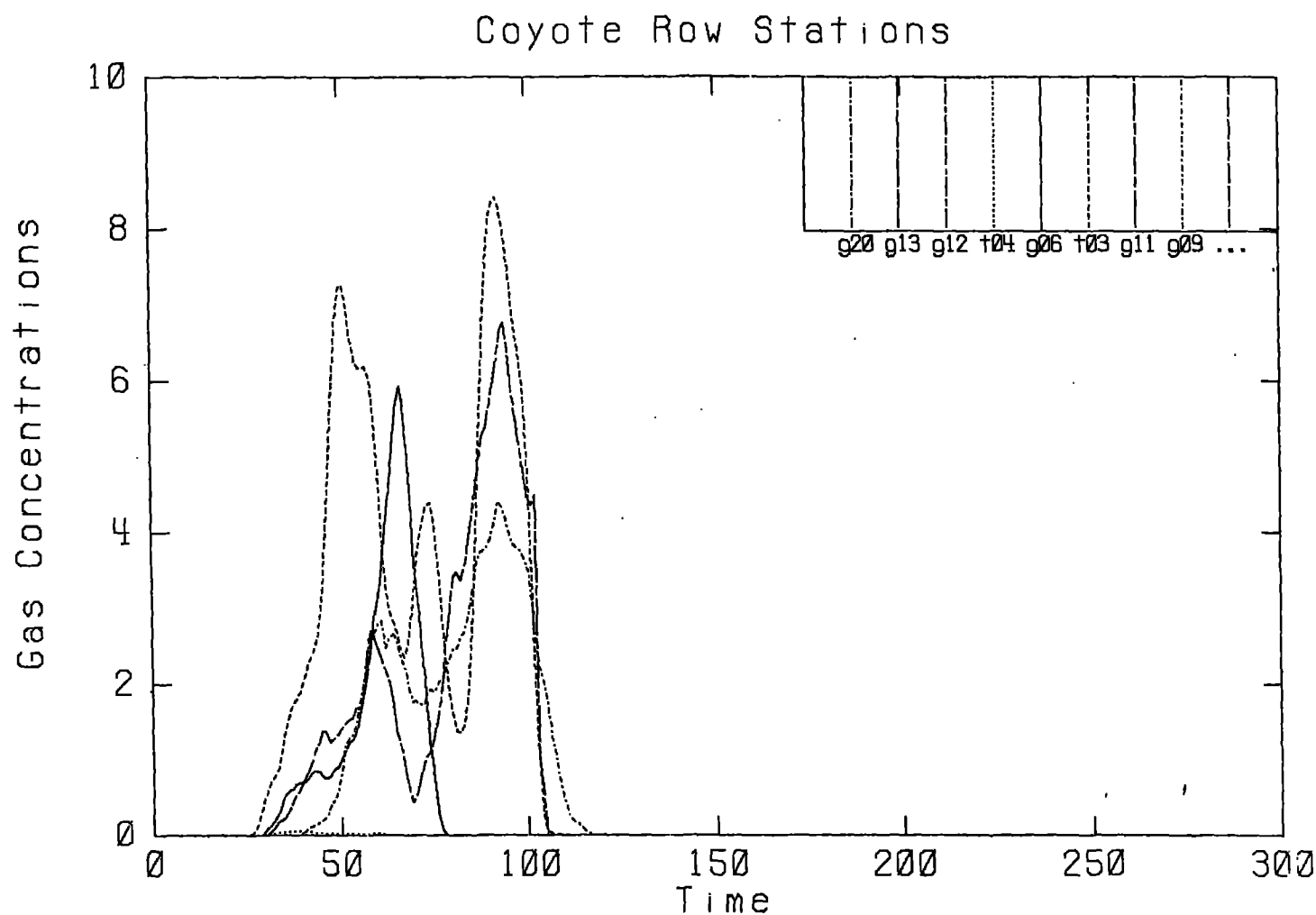
Coyote 3. Height 1. M. Row: 140 M.

Fig. 26. A sample time-history plot of gas concentration from Appendix 2.

of 1 and 3 m above the ground, and vertical crosswind surfaces at three of the rows of the sensor array. The data used to generate the contours are the same as those presented in Appendix 2 (a sample is given in Section 6.2). The techniques employed to produce contours are briefly described below, and in more detail in [8]. Selected gas concentration contours are calculated and plotted for the two types of surfaces.

6.3.1. Vertical contours

Plots of the vertical gas concentration contours at the 140, 200, and 400 m rows at 10 s intervals are shown in Appendix 3. A sample vertical contour plot is shown in Fig. 27. The time interval of the plot sequence for each row is indicated on each figure, as are the concentration levels of each contour. The contours are as they would appear when looking towards the spill pond. Notice that the horizontal and vertical plot scales are not the same, i.e., the gas cloud appears much higher, in respect to its width, than it really is. Prior to each vertical contour sequence is a vertical grid plot indicating the sensors which were operational during that particular test.

These contours were generated using <u>linear</u> interpolation, horizontally, between adjacent sensor concentration values at the specified levels and times. In addition to the three levels of actual measured results at a tower location, two other extrapolated levels were also used. The gas concentration at each station location was set equal to zero at a height of 12 m. When the 3 m concentration was less than the 1 m value, the ground-level concentration was determined by using a quadratic extrapolation that passes through the 1 and 3 m concentration values and has a zero concentration gradient at the ground. For those cases where the 3 m concentration was greater than the 1 m value, the ground-level concentration was linearly extrapolated from these two values. Contours were then produced using the graphics library GRAFLIB [9]. As a result of the small spacing between sensors in the vertical plane, the uncertainty in the location of the vertical contours is estimated to be less than 1 m.

6.3.2 Horizontal contours

Plots of the horizontal gas concentration contours at 1 and 3 m above the ground, and at 10 s intervals, are shown in Appendix 4. A sample horizontal contour plot is shown in Fig. 28. Also included in each time sequence is the
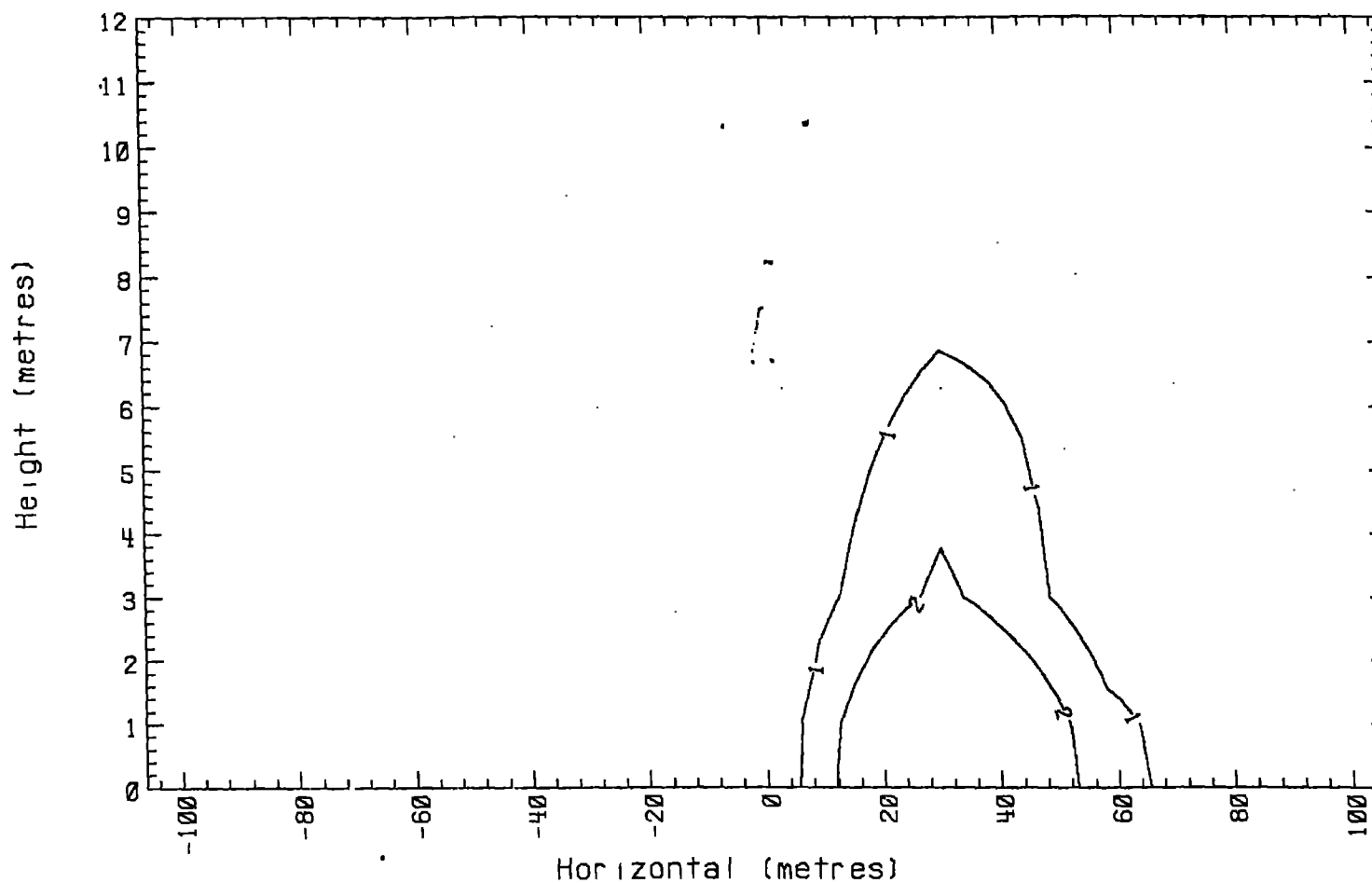
Fig. 27. A sample vertical gas concentration contour plot from Appendix 3.

Horizontal Concentration Contours
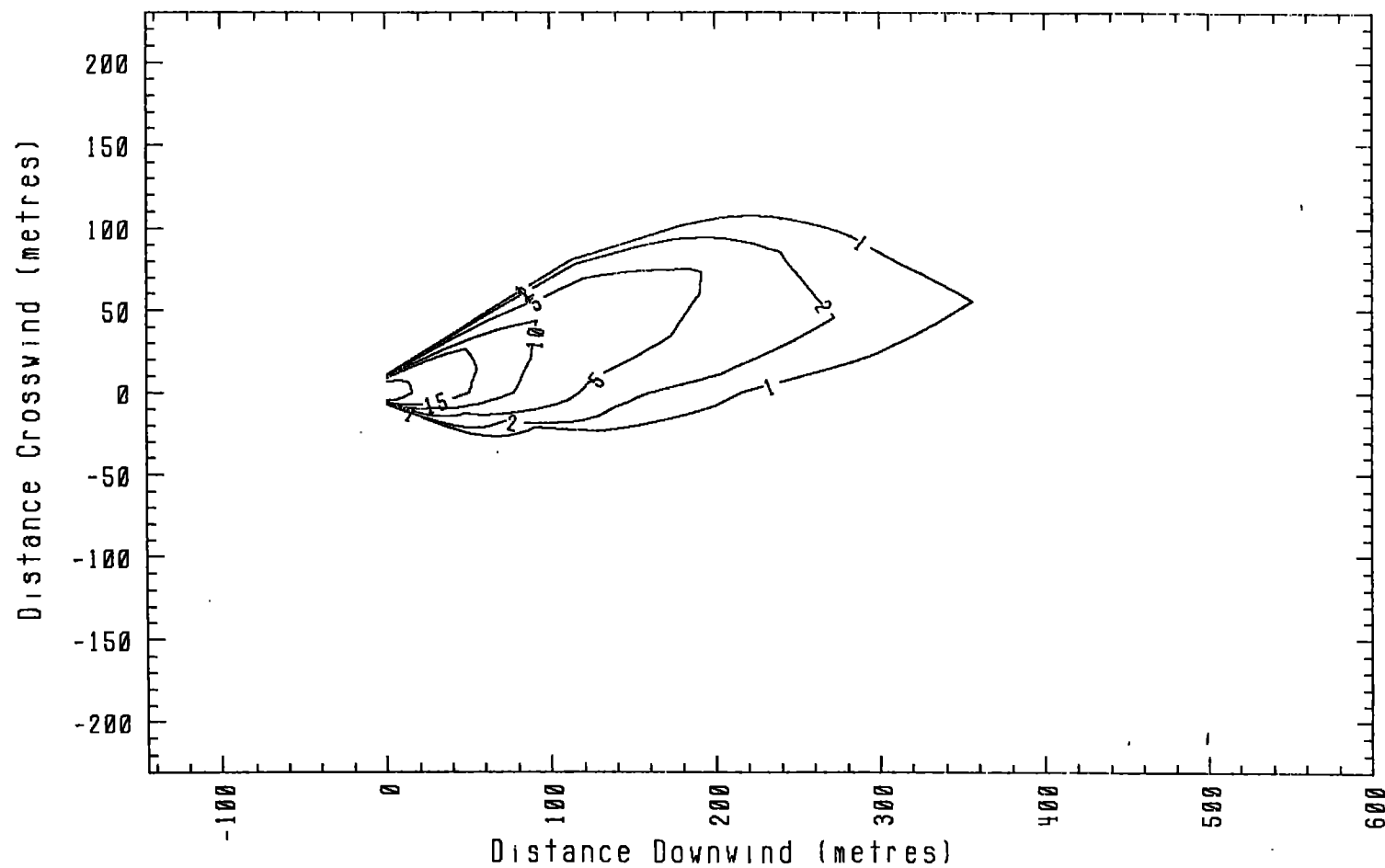
Coyote 6   LGF 81   Contours:

Time = 100 sec,   level   1m   1%,2%,5%,10%,15%,25%,35%

In conc, In x axis,   boundary =   460. m.

Fig. 28. A sample horizontal gas concentration contour plot from Appendix 4.

last concentration contour which is unperturbed by the presence of the flame; i.e., the preignition contour. These horizontal contours were created from the same concentration data used for the time histories (Section 6.2) and the vertical contours (Section 6.3.1). Towers within a row were relatively close together and, as mentioned earlier in the vertical contour discussion, linear interpolation of the gas concentrations and crosswind spatial tower positions were employed within an arc to produce intermediate points for the contour routines. However, because of the large downwind distances between measurement rows, and to better represent the physics of the downwind dispersion of the gas, both the natural log of the gas concentrations and other than strictly linear interpolation of the row-to-row spatial coordinates, was involved in the interpolation of the data used to form these horizontal contours. Finally, in order to prevent unrealistic distortion of the horizontal contours from irregular grid spacing, several fictitious or "dummy stations" were created. The assumptions and logic behind the choice of these dummy stations, and the effect on the contours is described below.

A layout of the gas sensor array is shown in Fig. 29. Two types of row-to-row (x-axis) interpolation schemes are used in generating the contours. Between the source and the 140 m row, a ln concentration, linear position (ln C/linear x) interpolation was used, whereas beyond the 140 m row, an ln concentration-ln position (ln C/ln x) interpolation was used. The x-axis spatial interpolation function and its first derivative for the combined regions, were forced to be continuous at x = 140 m. The ln C/linear x scheme was necessary close to the source because of the singularity of the natural logarithm at x = 0. The open circles of Fig. 29 indicate the locations of the dummy stations. The concentration levels of the dummy stations at the outer end of the 200 and 300 m arcs were determined by ln C/ln x interpolation between the closest real data stations in the upwind and downwind radial directions. The concentration levels of the dummy stations at the outer ends of the 110 m arc were determined by ln C/linear x interpolation between the measured concentrations of the source and the 140 m arc. These dummy stations were necessary to maintain a consistent grid for the contour routine which would cover the entire region of the array. The LNG spill was taken to be a 30-m long line source with a parabolic concentration distribution from one end (-y) to the other (+y). The maximum value of this line source (x = 0, y = 0) was the actual data obtained by the pond sampling system of station G01 (Section 4.4.3).

150r/23r
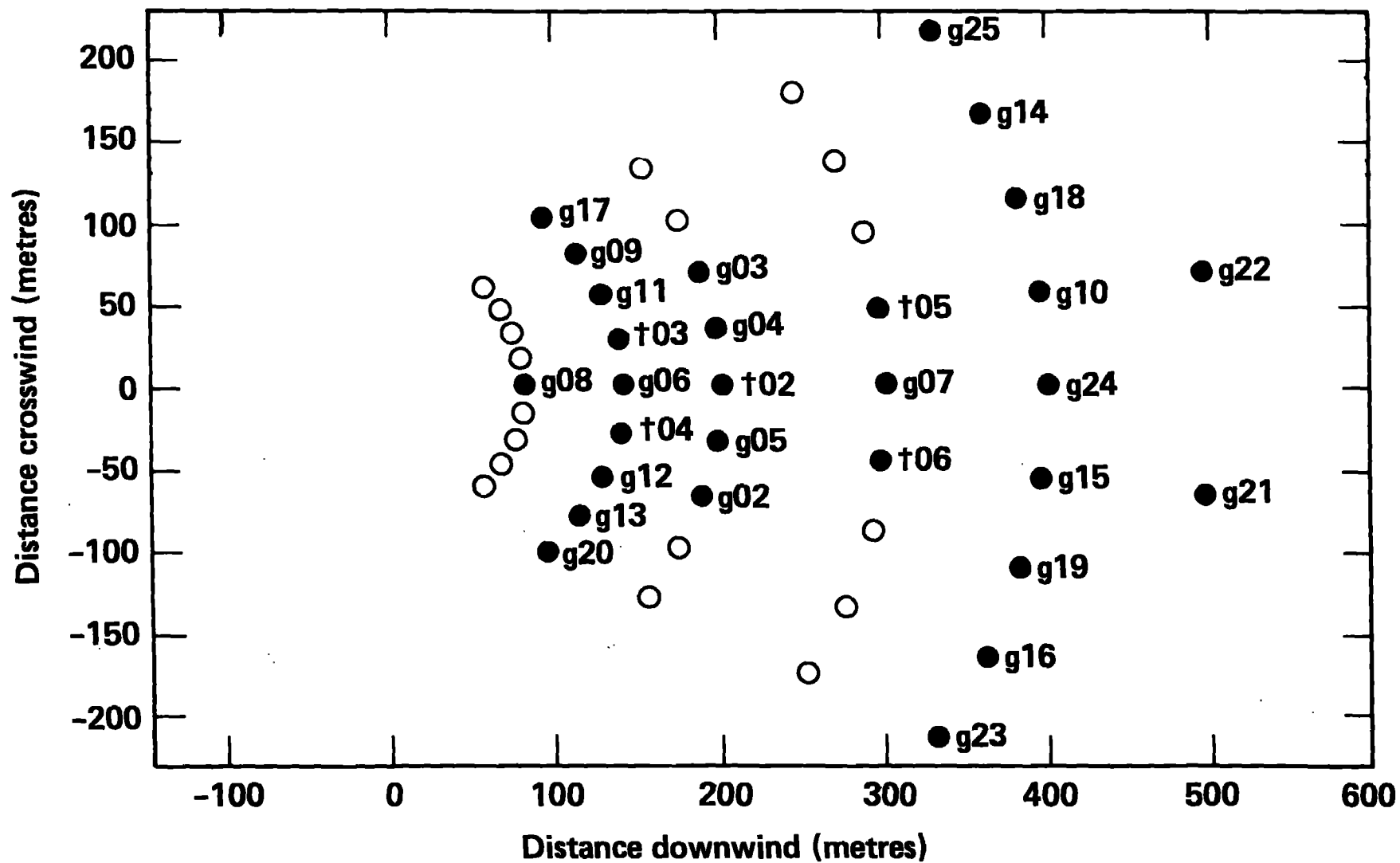
Fig. 29. The array (real and dummy stations) used in the construction of gas
concentration contour plots in the horizontal plane.

A particularly annoying problem associated with the long downwind inter-
polation distances is the acceleration or "jumping" of the concentration
contours as the cloud front passes an arc of sensors. While the use of the
ln C/ln x interpolation scheme is somewhat less sensitive to this contour
"jumping" than is a linear C/linear x interpretation scheme, it still proved
to be troublesome. The problem was finally solved by introducing an arc of
"zero" (i.e., very small) concentration levels, which moves downwind from the
pond at the local wind speed. With this approach, the maximum downwind inter-
polation point is never any further downwind than the initial spill vapors
could have traveled. A similar approach was taken to account for the ignition
and burning of the vapor cloud. In this case a dummy arc of stations was
placed at the location of the ignitors (see Table 3), whose initial concen-
tration values corresponded to the local interpolated values just prior to
ignition. Beginning at the time of ignition, and at its known location, the
concentrations of this dummy arc are systematically reduced to zero in both
directions ($\pm$ y) at a nominal flame speed of 5 m/s. This simulation of the
burn eventually severs the unburned upwind and downwind portions of the vapor
cloud and allows the closing of the two separate controlled regions formed by
the contours.

The contour routine employs two-dimensional, spatial linear interpolation
of ln C values within regions bounded by any four adjacent real or dummy
stations. The y-axis (normally crosswind) spatial variable is preserved as a
linear quantity. The ln C/linear x and ln C/ln x interpolation schemes are
accomplished by the appropriate transformation of the spatial location data
into either a ln concentration-linear distance, or ln concentration-ln distance
domain prior to submittal to the contour routine (the y-axis coordinate is
always linear). The routine then performs a linear interpolation in the trans-
formed spatial domain. However, before entering the plotting portion of the
routine, the reverse transformation is evoked on the interpolated results and
desired concentration contour levels are selected, plotted, and labeled. This
linear interpolation in the ln C/ln x domain to produce the selected contours
is, in effect, the same as using an ln C/ln x interpolation scheme to produce
contours in the linear domain. The interpolation of the concentration data in
the crosswind direction was linear-linear in all cases.

Proper construction of the desired contour levels depends upon usage of
appropriate interpolation schemes. Since the contour routine ends up doing
linear interpolation within its transformed domain to fix the contour

150r/23r
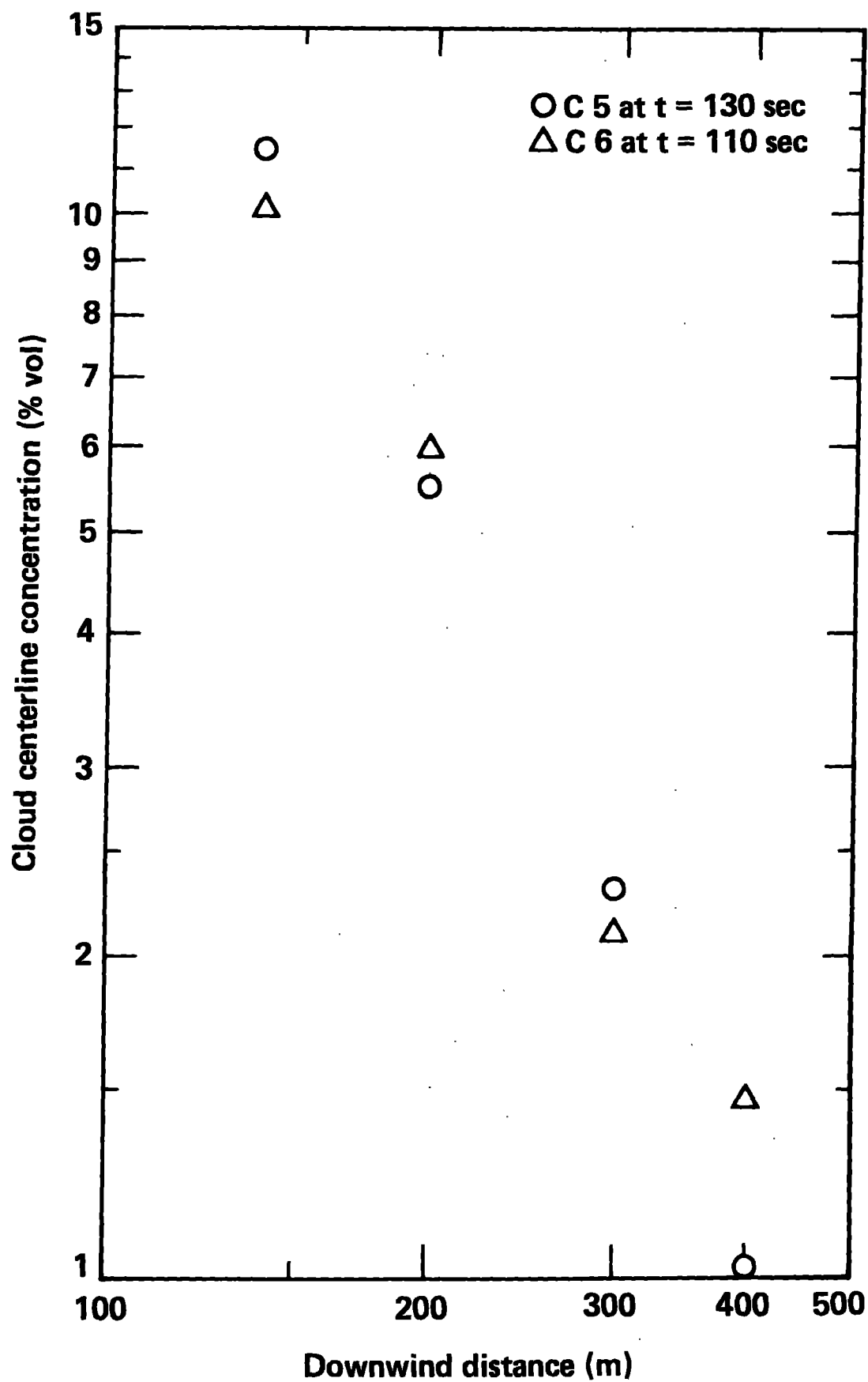
Fig. 30. Ln concentration vs ln downwind distance for Coyotes 5 and 6 just prior to ignition.

positions, the data transformations employed should reflect the results of the actual experiment. Specifically, the operations used to transform the input data must produce a <u>linear</u> relation between the concentration function and the distance function. To determine the appropriate transformations, the cloud centerline concentration vs downwind distance at various times during a spill has been examined. The ln C/ln x transformation appeared to be the most appropriate, especially later in the spill as the cloud approached a steady-state condition. A plot of ln concentration versus ln downwind distance just prior to cloud ignition for the Coyotes 5 and 6 spills is shown in Fig. 30. As can be seen, the ln C/ln x operation tends to linearize the data quite nicely and justifies its use in the contour generation scheme.

7. FLAME PROPAGATION DATA

Data related to ignition, flame propagation, and extent of the fire were obtained during Coyotes 2, 3, 5, 6, and 7 by some or all of the following, as shown in Table 1: high-speed color motion pictures, side and overhead IR imagery, and individual sensors in the array of gas and turbulence stations. The motion pictures are not included in this report; neither are the IR images with a few exceptions described below. The emphasis in this report is on the data from the individual sensors in the array.

7.1 Selected Overhead IR Images

The EG&G Remote Measurements Department processed the overhead IR imagery and generated color-coded images of the vapor cloud fires during Coyotes 6 and 7 [15]. These images show the spread of the flame front with time as observed through filtered and unfiltered channels of 3.3-3.5 μm and 8.5-12.5 μm bands, respectively. The unfiltered channel shows more landmark details which provide easier orientation of the recorded image, but suffer badly from blooming or overexposure. The filtered channel, as expected, gives more accurate information about the flame front as it propagates through the combustible cloud. A sample of these records are shown in black and white in Fig. 31, and a selection is shown in color in Appendix 5 to this report. These data were employed to produce flame speed vs time and position and have been presented elsewhere [16].

150r/23r
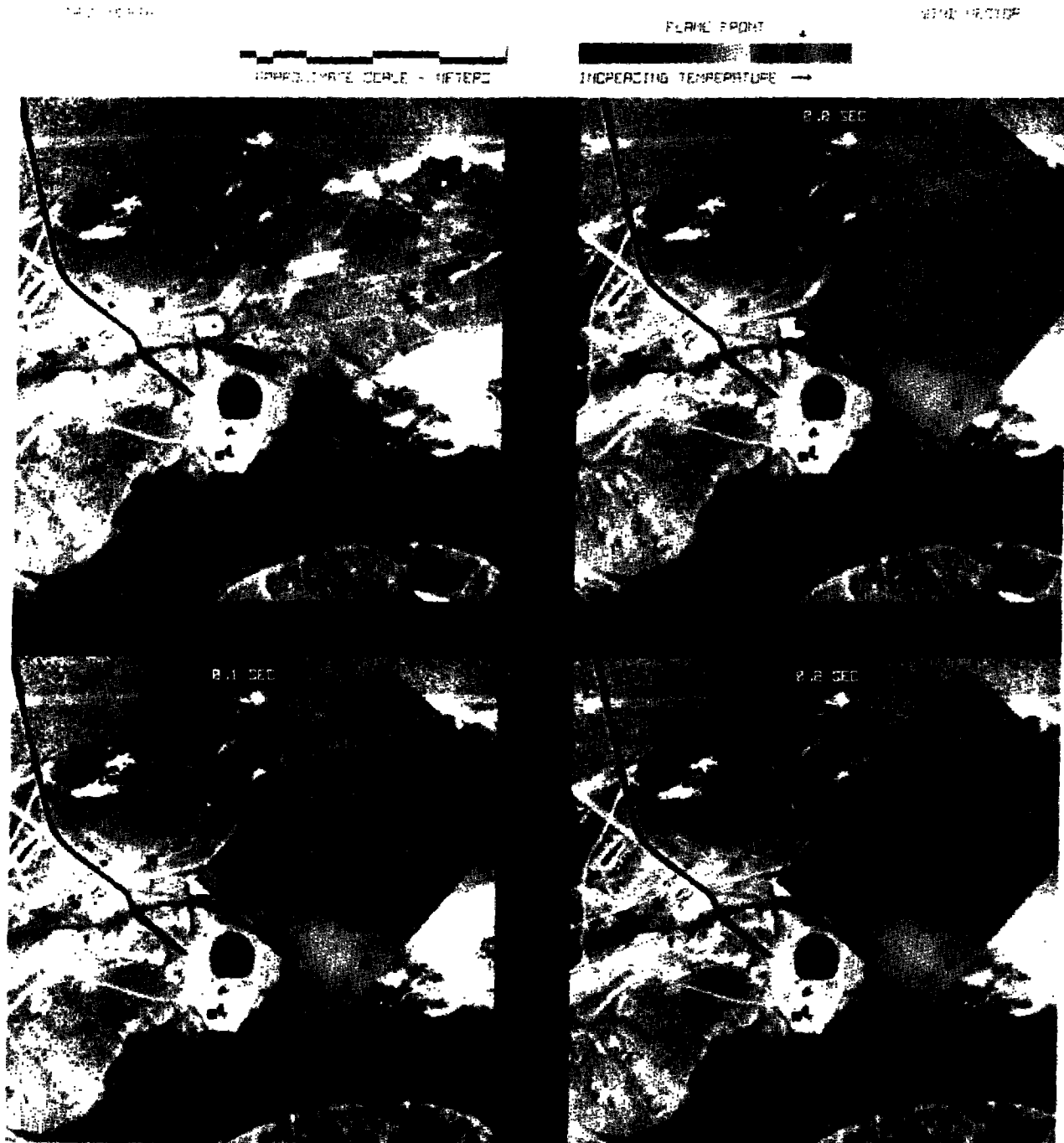
Fig. 31. A black and white reproduction of one of the colored IR images in Appendix 5.

7.2 Flame-Related Arrival Times and Extent

Flame-related arrival times and the horizontal extent of the fire were obtained from five different sensors in the array of gas and turbulence stations: heat-flux sensors (Section 4.1.4), thermocouples (Section 4.1.5), IR gas-concentration sensors (Sections 4.2.1 and 4.2.2), calorimeters (Section 4.3.1), and flame-velocity sensors (Section 4.3.2). The flame-related arrival times from these sensors are given in Tables 8-11 for Coyotes 3, 5, 6, and 7, respectively. These times represent the first significant appearance of flame or flame products. Often, the peak intensity of the burn occurred 1 to 2 s later. Station-time resolutions for the gas (G) and turbulence (T) stations are 1.0 and 0.3 s, respectively, although response time for some of the sensors is slower. Timing uncertainty on Coyotes 6 and 7 for the flame-velocity sensors is 60 ms. The estimated horizontal extent of the intense fire for Coyotes 3, 5, 6, and 7 is shown in Figs. 32-35, respectively. This estimate is based on whether or not the thermocouple sensors at a station saw a hot flame with $\Delta T > 50°C$. Such stations are marked by an asterisk in Tables 8-11.

In some cases, multiple occurrences of flame or flame products were seen at a station, generally at the higher sensors. Radiation from the active flame often was detected by the IR and thermocouple sensor for several seconds before the flame front reached the station. Such data were not allowed to affect the time of arrival determinations. Finally, the subsurface heat flux sensors generally lagged behind the other sensor types by up to several seconds. G04 flame arrival data for Coyote 6 were substantially later in time than for the other stations. Examination of the movies indicate that a second flame tongue had started from upwind and burned out to G04. Perhaps this was related to the fact that Coyote 6 had the lowest wind speed and most meandering wind direction of the burn tests.
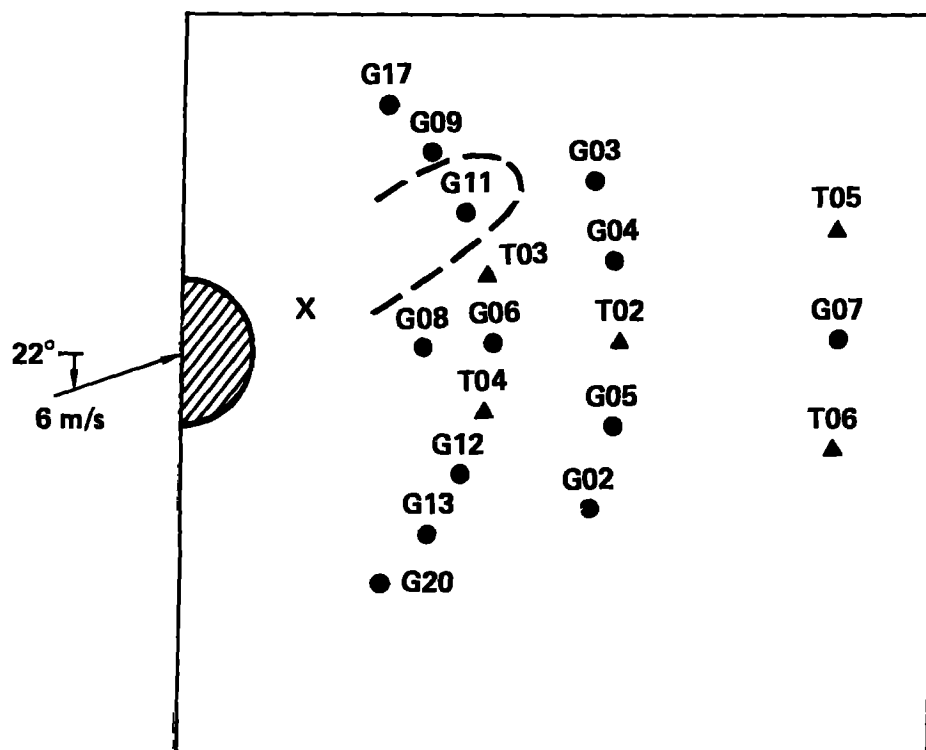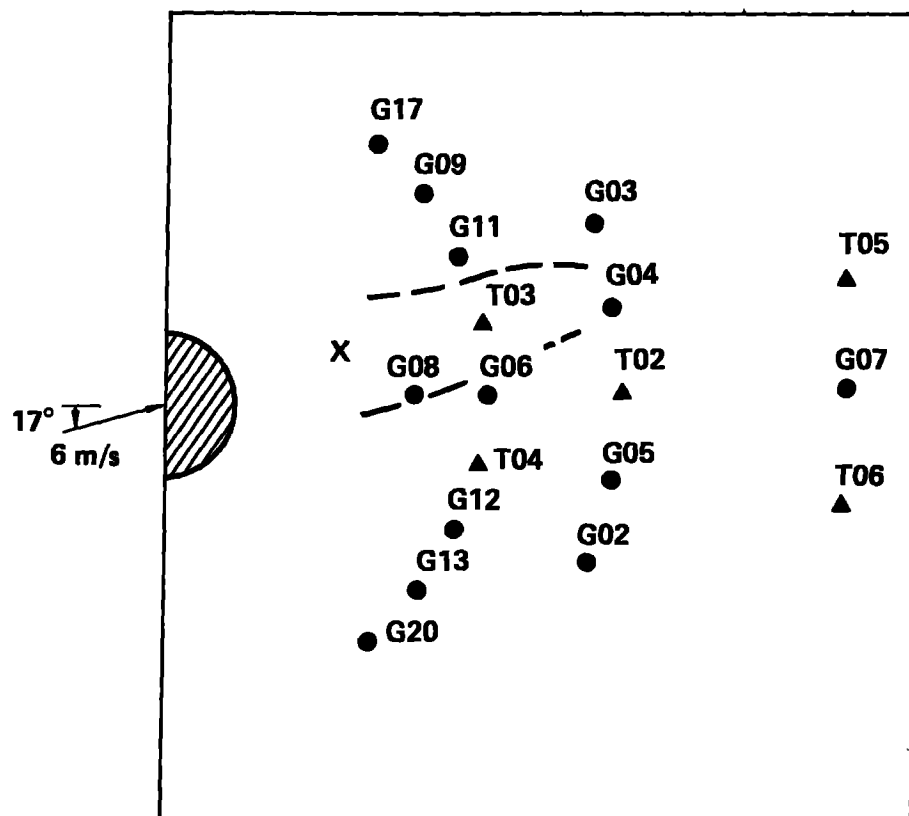
Fig. 32. The horizontal extent of the Coyote 3 fire based on the data from the thermocouples in Table 8. The semicircular hatched area is the spill pond. The x marks the ignition point. The wind velocity and direction relative to the array centerline are shown.

TABLE 8.
Flame or hot gas arrival times for Coyote 3.
The times are in seconds after the beginning of the spill.

Type of sensor	Station	Height above ground (m)						
		0	0.25	0.5	1	3	5	8
Thermo-couples	G06		102	102			102	
	G08					101	101	
	G09						102	
							124	124
	G11*				105	105	105	105
	G17							> 103
Heat Flux	G08	101						
Calori-meter	G08				101			

* ΔT > 50°C

TABLE 11.
Flame or hot gas arrival times for Coyote 7.
The times are in seconds after the beginning of the spill.

Type of sensor	Station	Height above ground (m)						
		0	0.25	0.5	1	3	5	8
Thermo-couples	G06		147	149	148	148	147	148
	G08	148			147	147	147	147
								155*
	T03*			150	150	150		150
Heat Flux	G06	150						
	G08	150						
Calori-meter	G06				150			
	G08				148			
Gas Sensor	T03				150	150		
Flm Vel Sensor	T03				150.5	150.5		

* ΔT > 50°C
150r/23r
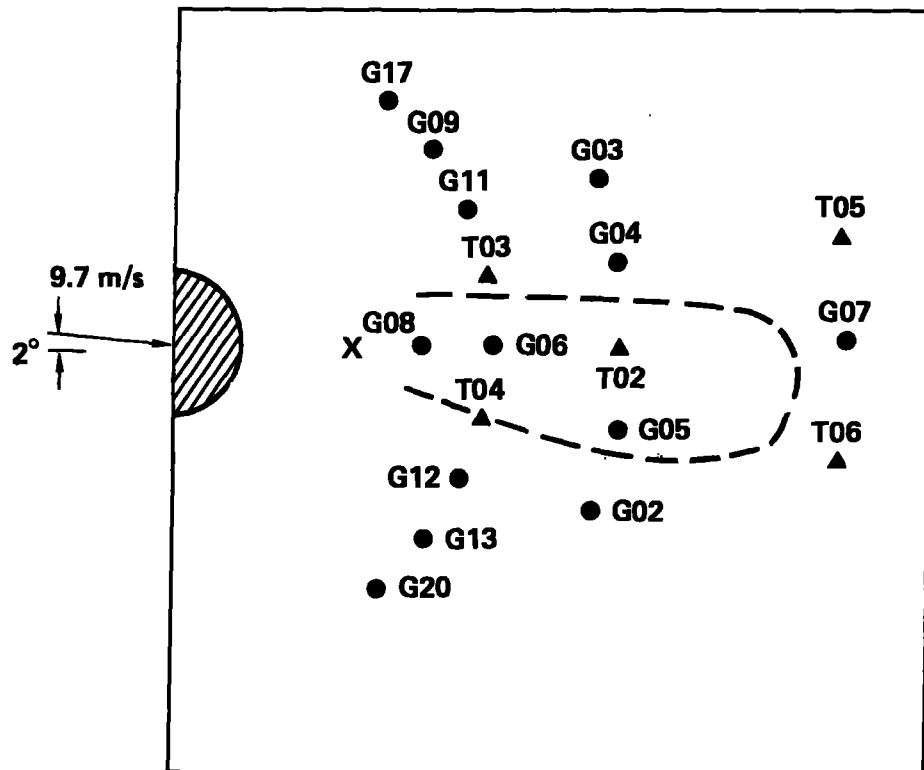
Fig. 33. The horizontal extent of the Coyote 5 fire based on the data from the thermocouples in Table 9. The semicircular hatched area is the spill pond. The x marks the ignition point. The wind velocity and direction relative to the array centerline are shown.

TABLE 9.
Flame or hot gas arrival times for Coyote 5.
The times are in seconds after the beginning of the spill.

Type of sensor	Station	Height above ground (m)						
		0	0.25	0.5	1	3	5	8
Thermo-	G02							134
couples	G04		134	134				135
	G05*	143	143	143	143	143		140
								143
	G06*	136	136	136	136	136	136	136
	G07						148	147
	G08*				134	134	134	134
	T02*		140.5		140.5	140.5		140.5
	T03			137				
	T04*			138	139	138.5		138.7
Heat Flux	G04	≤ 140						
	G05	142						
	G06	137						
	G07	148						
	G08	134						
Calori-	G06				137			
meter	G08				135			
	T03				137			
	T04				139			
Gas	G05				144	144		
Sensor	G06				136	137		
	G08				134	134		
	T02				141	141		
	T04				139.5	139.5		
Flm-Vel	G05				143			
Sensor	T02				140	140	140	
	T04				139			

* $\Delta T > 50°C$
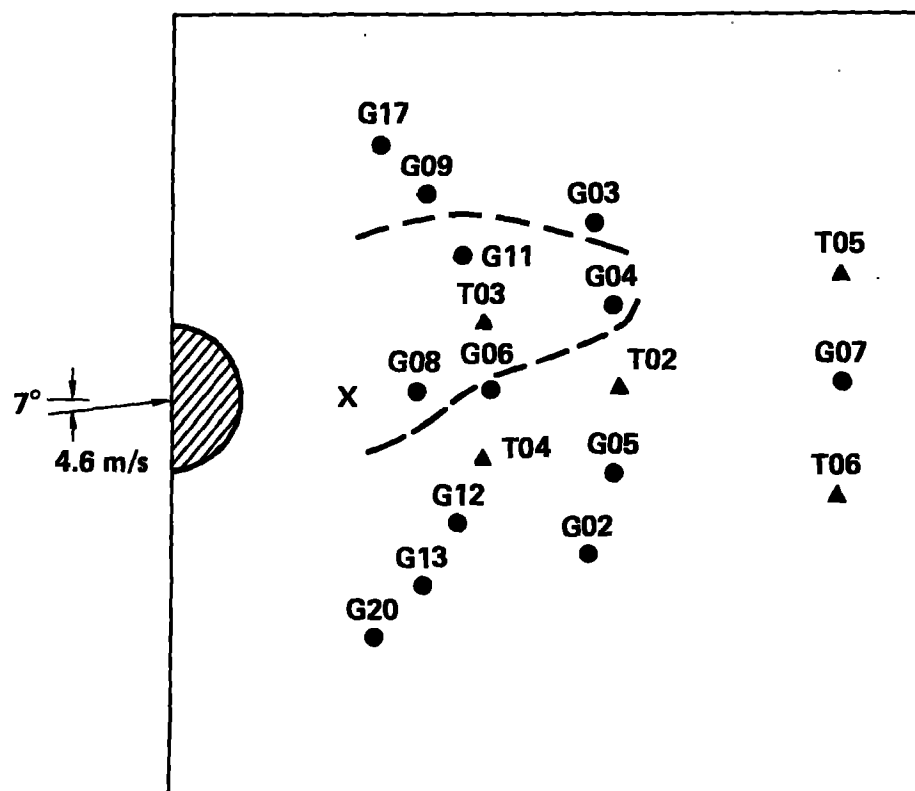
Fig. 34. The horizontal extent of the Coyote 6 fire based on the data from the thermocouples in Table 10. The semicircular hatched area is the spill pond. The x marks the ignition point. The wind velocity and direction relative to the array centerline are shown.

TABLE 10.
Flame or hot gas arrival times for Coyote 6.
The times are in seconds after the beginning of the spill.

Type of sensor	Station	Height above ground (m)						
		0	0.25	0.5	1	3	5	8
Thermo-couples	G02							110
	G04*		131		131	131		131
	G05	111			109	110		110
	G06		110	110	112	112	110	110
	G08*	110			111	111	110	110
	G09				117	117	113	116
	G11*				116	116	116	116
	G17				111	111		110
	T03*			105-17	117	116		116.5
Heat Flux	G04	133						
	G05	115						
	G06	112						
	G08	114						
Calori-meter	G06				112			
	G08				110			
	T03				117			
Gas Sensor	G03				122	122		
	G04				132.5	133		
	G08				112	112		
	G11				117	117		
	G18				170	170		
	T03				118.5	119		
Flm Vel Sensor	G04				132			
	G08				110	110		
	T03				118			

* ΔT > 50°C

Fig. 35. The horizontal extent of the Coyote 7 fire based on the data from the
thermocouples in Table 11. The semicircular hatched area is the
spill pond. The x marks the ignition point. The wind velocity and
direction relative to the array centerline are shown.

8. FIRE HEAT-FLUX DATA

Data relating to the heat flux from the burning vapor clouds were obtained from three types of instruments located both inside and outside the fires: ground heat-flux sensors, calorimeters, and radiometers.

Seven heat-flux sensors were buried just beneath the soil surface along and near the array centerline at distances 110 to 400 m from the spill point (Table 5 and Section 4.1.4). The data obtained from these ground heat-flux sensors are summarized in Table 7 and are presented in Figs. 23-25 for Coyotes 3, 5, and 6, respectively (see Section 5.3).

Four calorimeters were mounted at an elevation of 1 m above the ground along and near the array centerline at distances 110 and 140 m from the spill point (Table 5 and Section 4.3.1). The data obtained from these calorimeters are summarized in Table 12 and are presented in Figs. 36-38 for Coyotes 5-7, respectively.

Nine NWC radiometers were positioned to the side of the instrument array at x = +65 m: Two wide-angle sensors (R01-R02) and five narrow-angle sensors (R03-R07) reportedly at y = 57 m, and two wide-angle sensors (R08-R09) at y = 100 m (Fig. 13 and Section 4.3.5). Radiometer R09 was not operational during the later vapor-burn tests. The data obtained from these sensors are summarized in Table 12 and presented in Figs. 39-41 for Coyotes 3, 6, and 7, respectively. Since the radiometers were not cooled and some of them were engulfed in the Coyote 6 and 7 fires, the data for these two tests are essentially unuseable. This lack of cooling is apparent in the data of sensors R03-R06 in Fig. 40 for Coyote 6 and of sensors R01-R07 in Fig. 41 for Coyote 7. Note in these cases that the heat flux is initially positive and increasing after ignition, and then abruptly becomes negative for 5-10 s before recovering to the preignition value. The negative heat flux is a consequence of the sensor being heated to temperatures above that of the environment in its field-of-view. The extremely large, narrow spikes in these data are a result of the raw data. There is also a great deal of baseline drift associated with these data.

TABLE 12.
Summary of Fire Heat-Flux Plots.
(Ground heat-flux sensors: see Table 7.)

Calorimeters

Station		Experiments		
		Coyote 5	Coyote 6	Coyote 7
G06		X	X	X
G08		X	X	X
T03		X	X	X
T04		X		

Radiometers

Station	Type	Offset (y-m)	Experiments		
			Coyote 3	Coyote 6	Coyote 7
R01	wide	57	X	X	X
R02	wide	57	X	X	X
R03	narrow	57	X	X	X
R04	narrow	57	X	X	X
R05	narrow	57	X		X
R06	narrow	57	X	X	X
R07	narrow	57	X	X	X
R08	wide	100	X	X	X
R09	wide	100	X		

Note: R01 had a sapphire window; R02-R09 had IRTRAN windows.
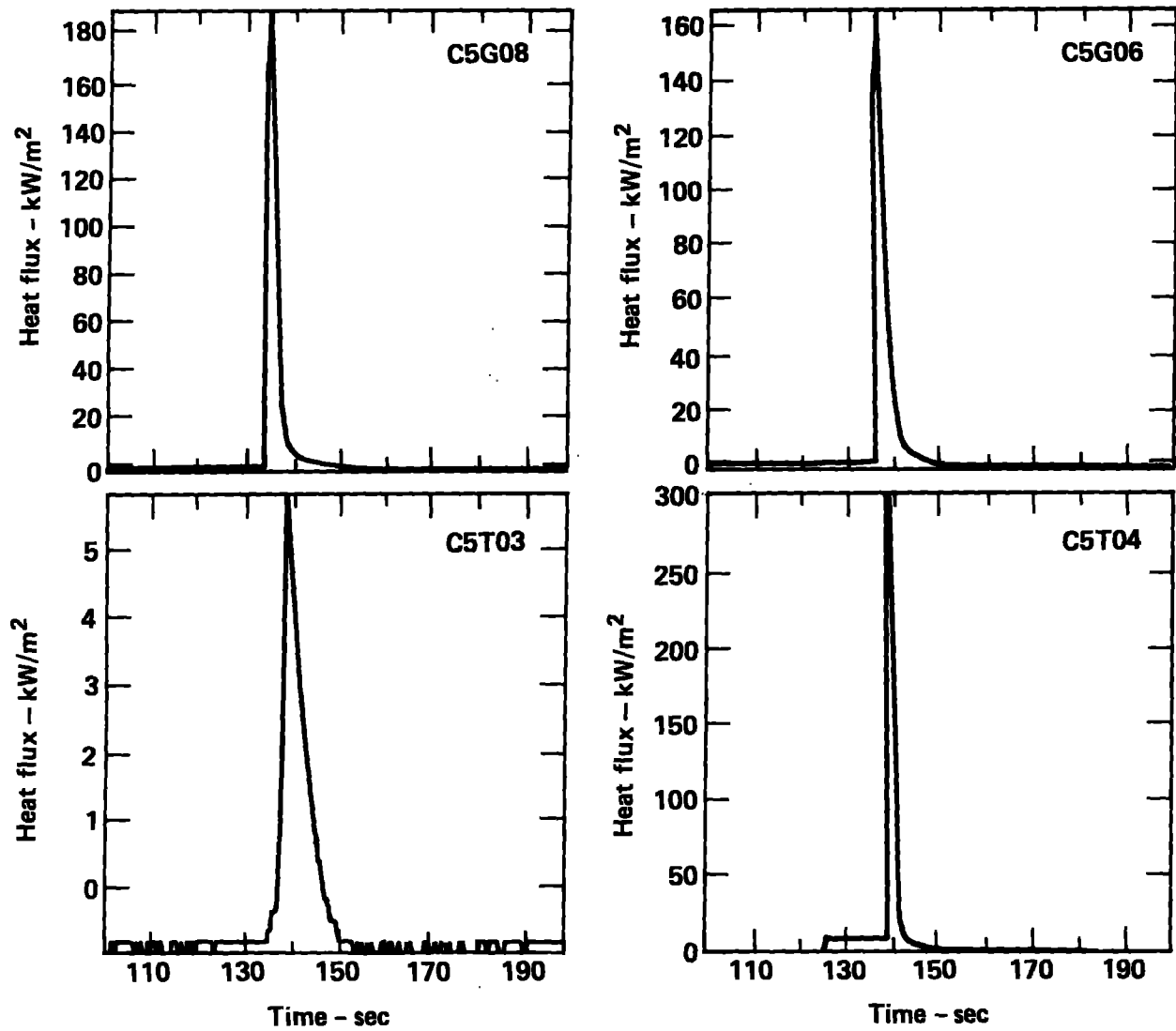
Fig. 36. Calorimeter heat-flux data for Coyote 5.
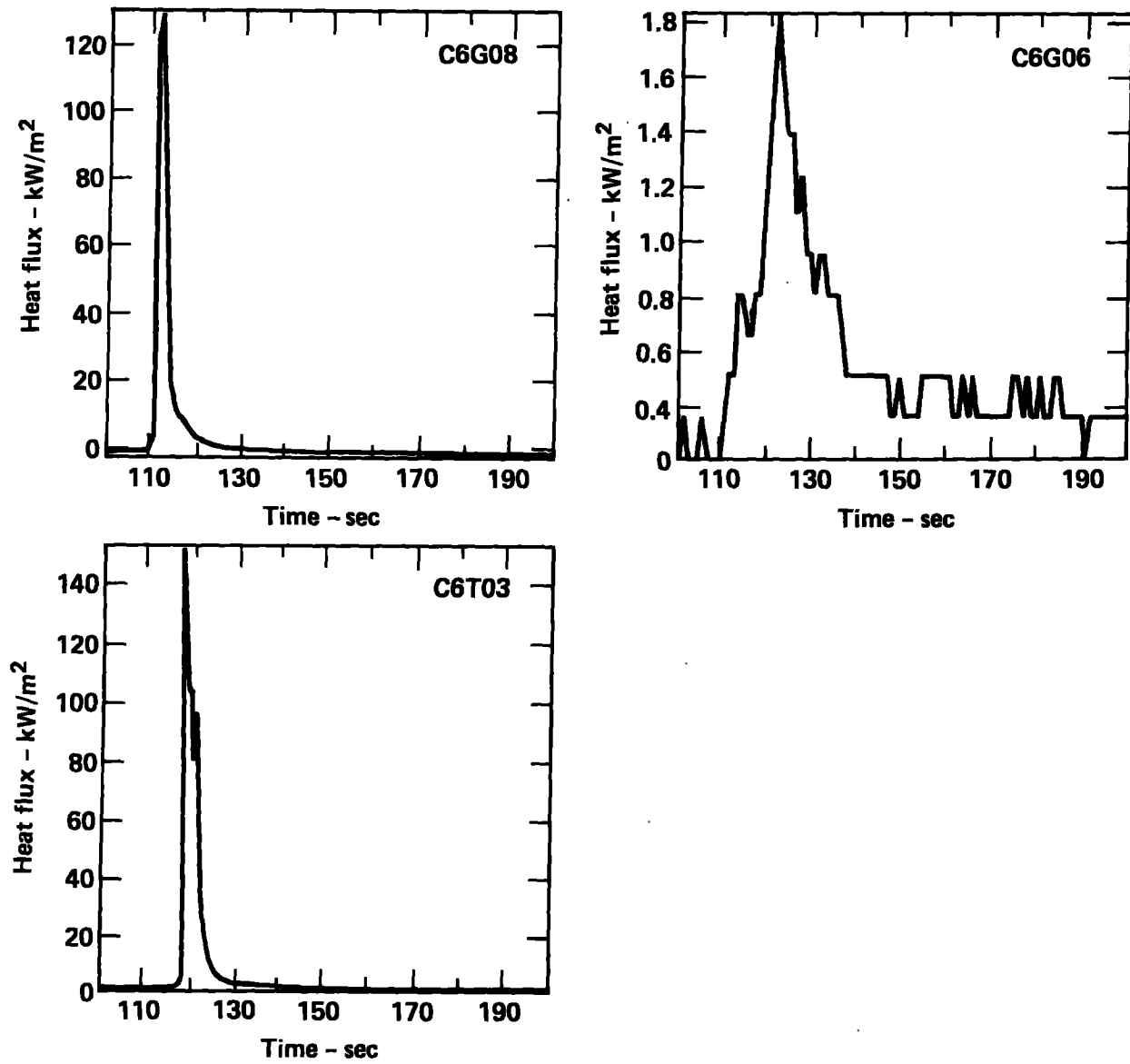
Fig. 37. Calorimeter heat-flux data for Coyote 6.
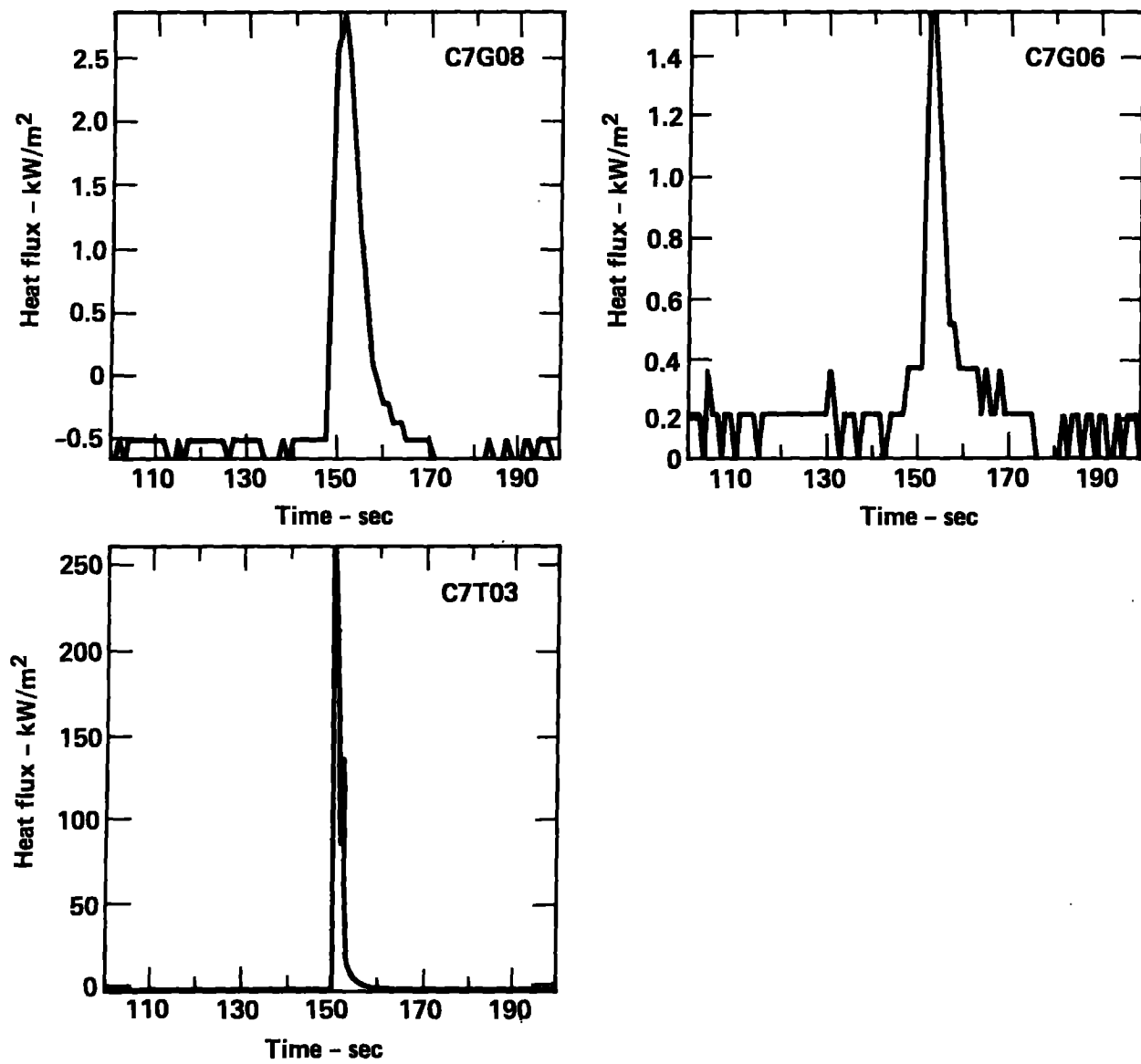
Fig. 38. Calorimeter heat-flux data for Coyote 7.
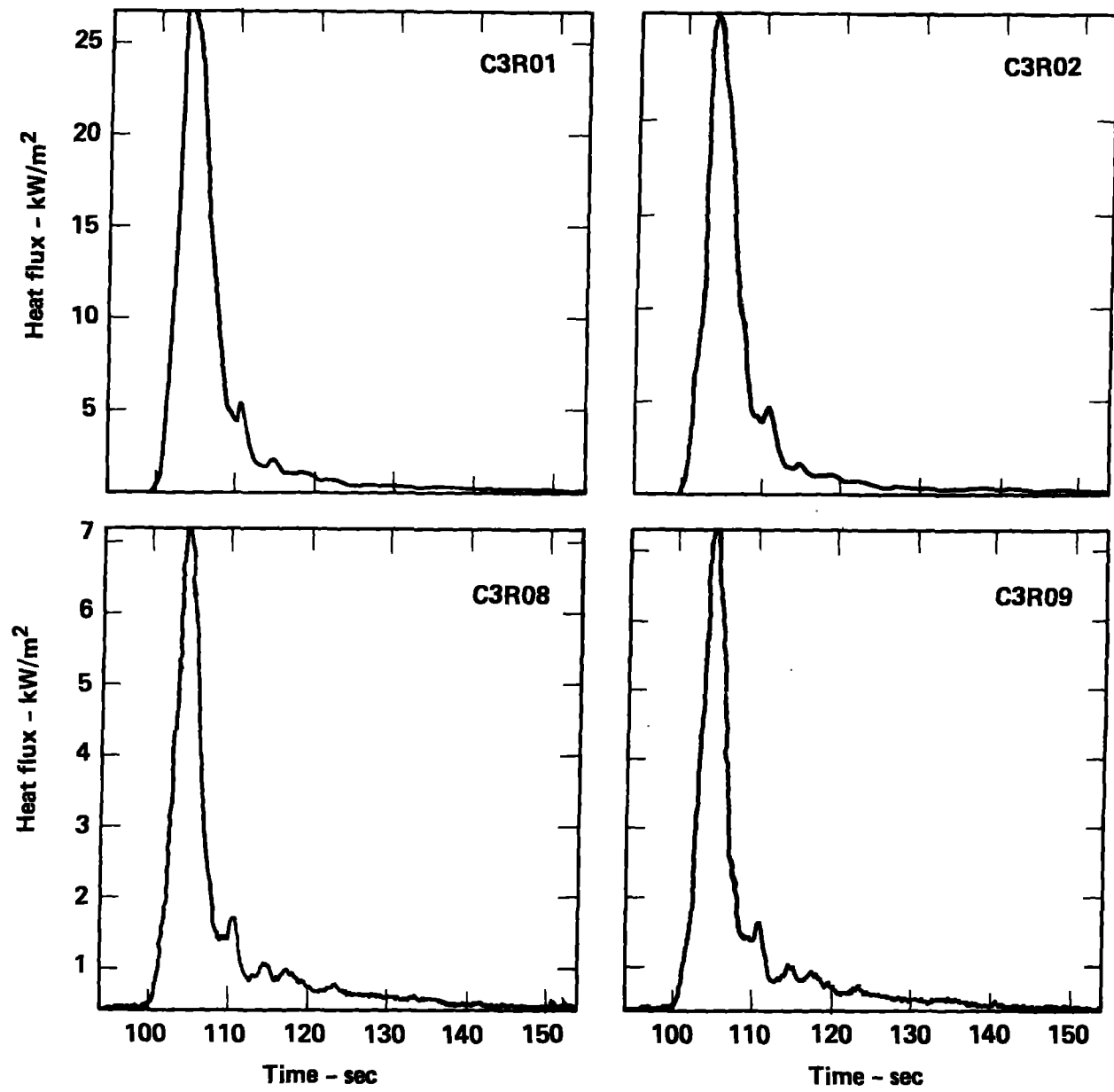
Fig. 39a. Wide-angle radiometer data for Coyote 3.
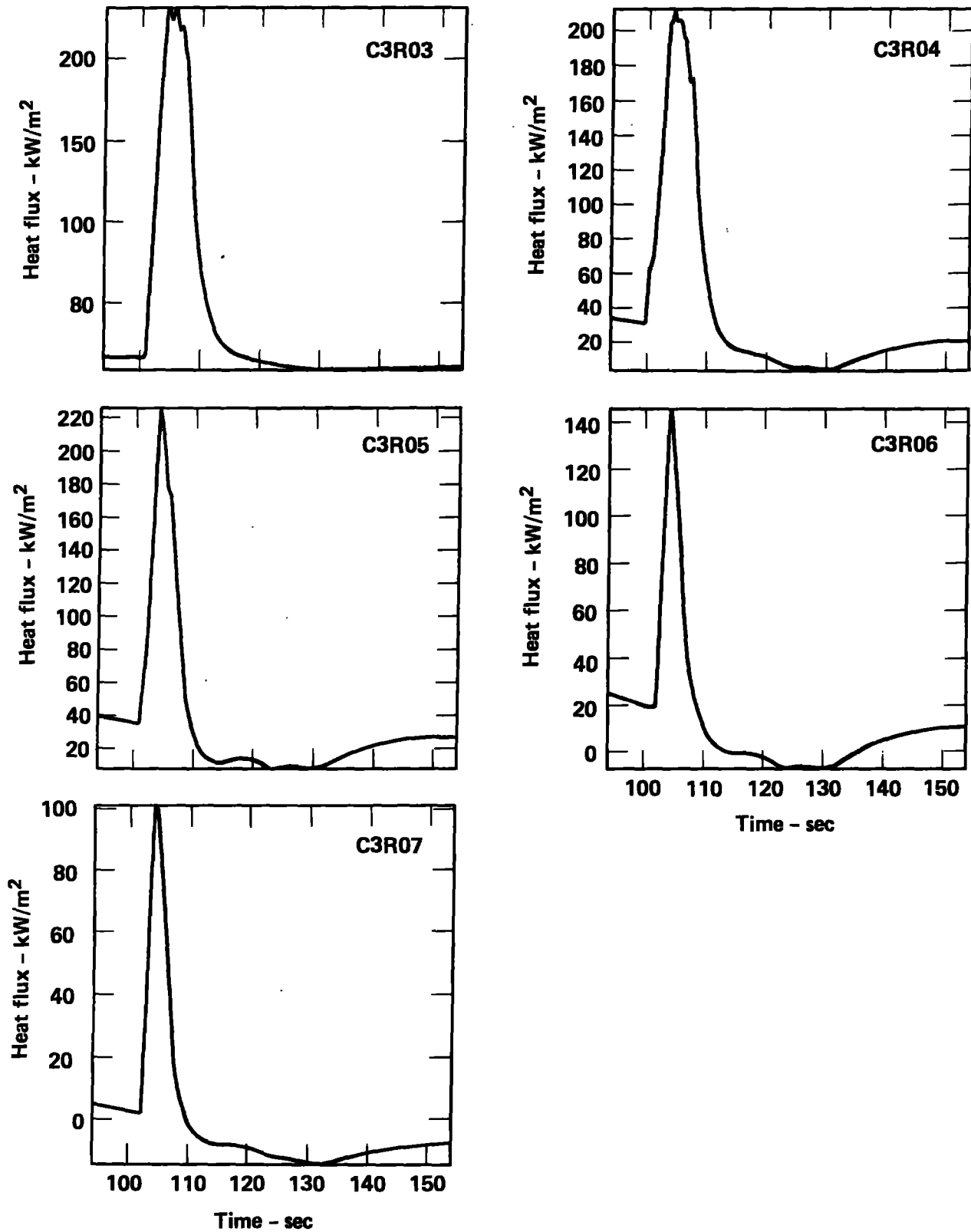
Fig. 39b. Narrow-angle radiometer data for Coyote 3.
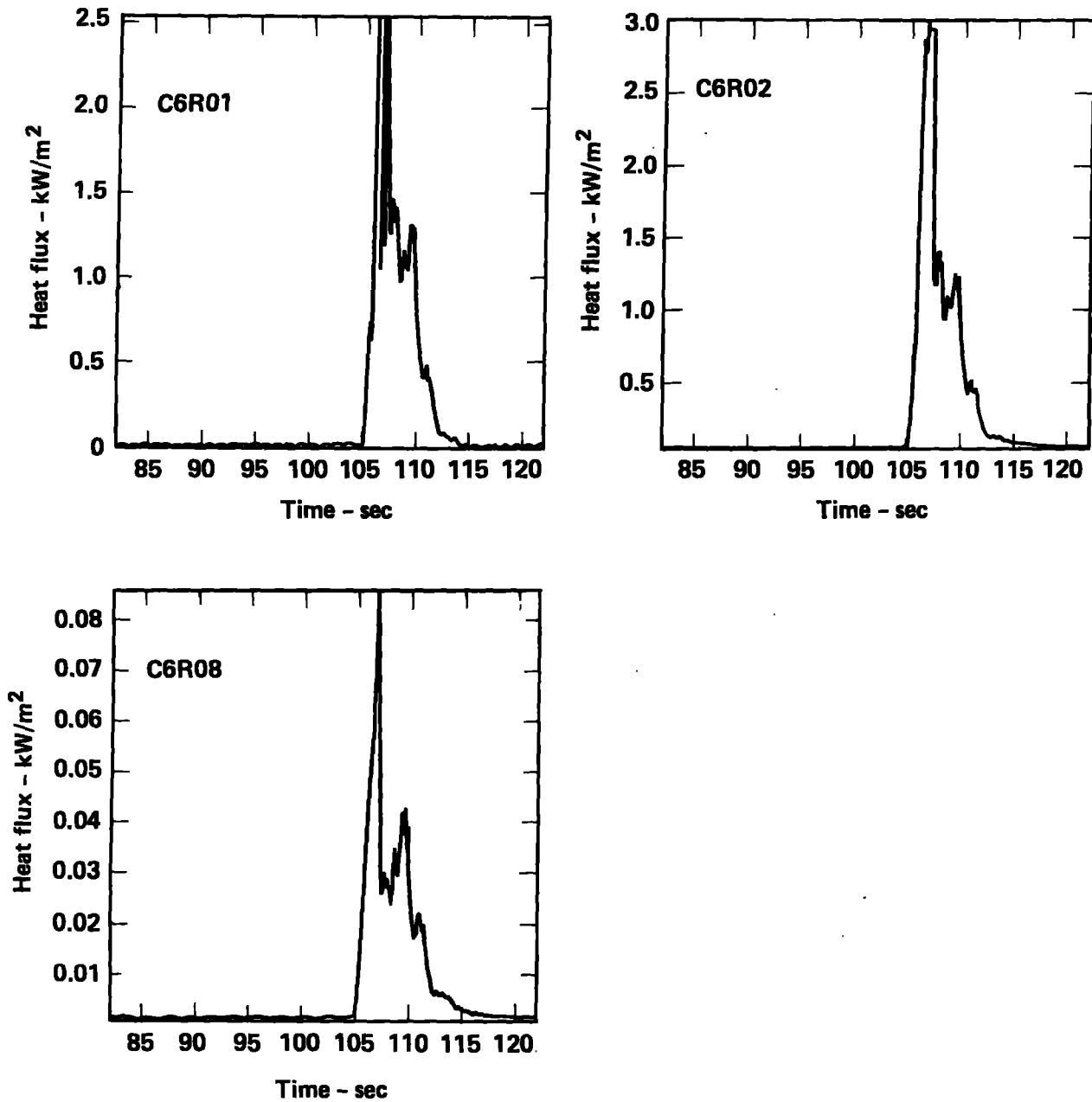
Fig. 40a. Wide-angle radiometer data for Coyote 6.
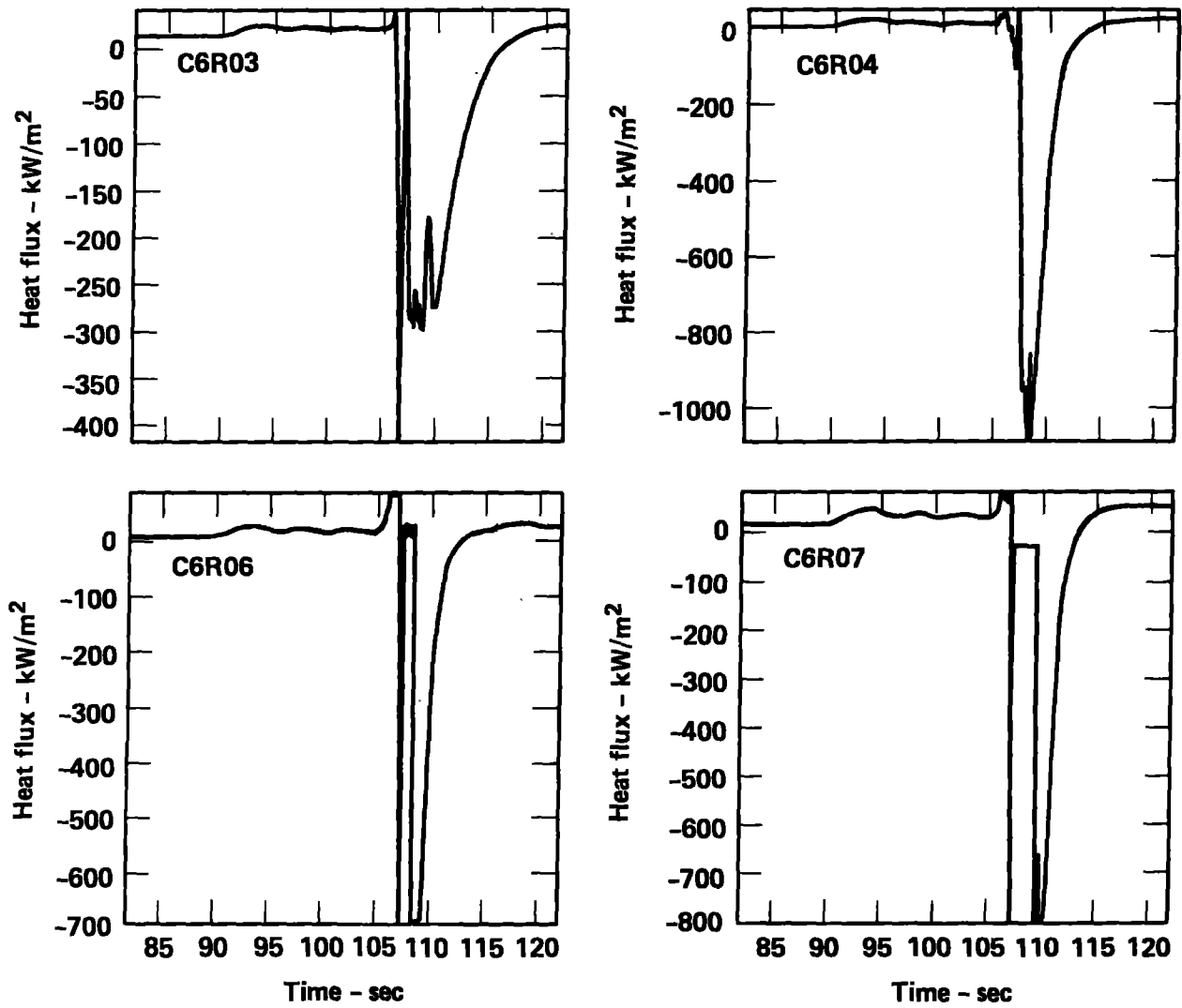
Fig. 40b. Narrow-angle radiometer data for Coyote 6.
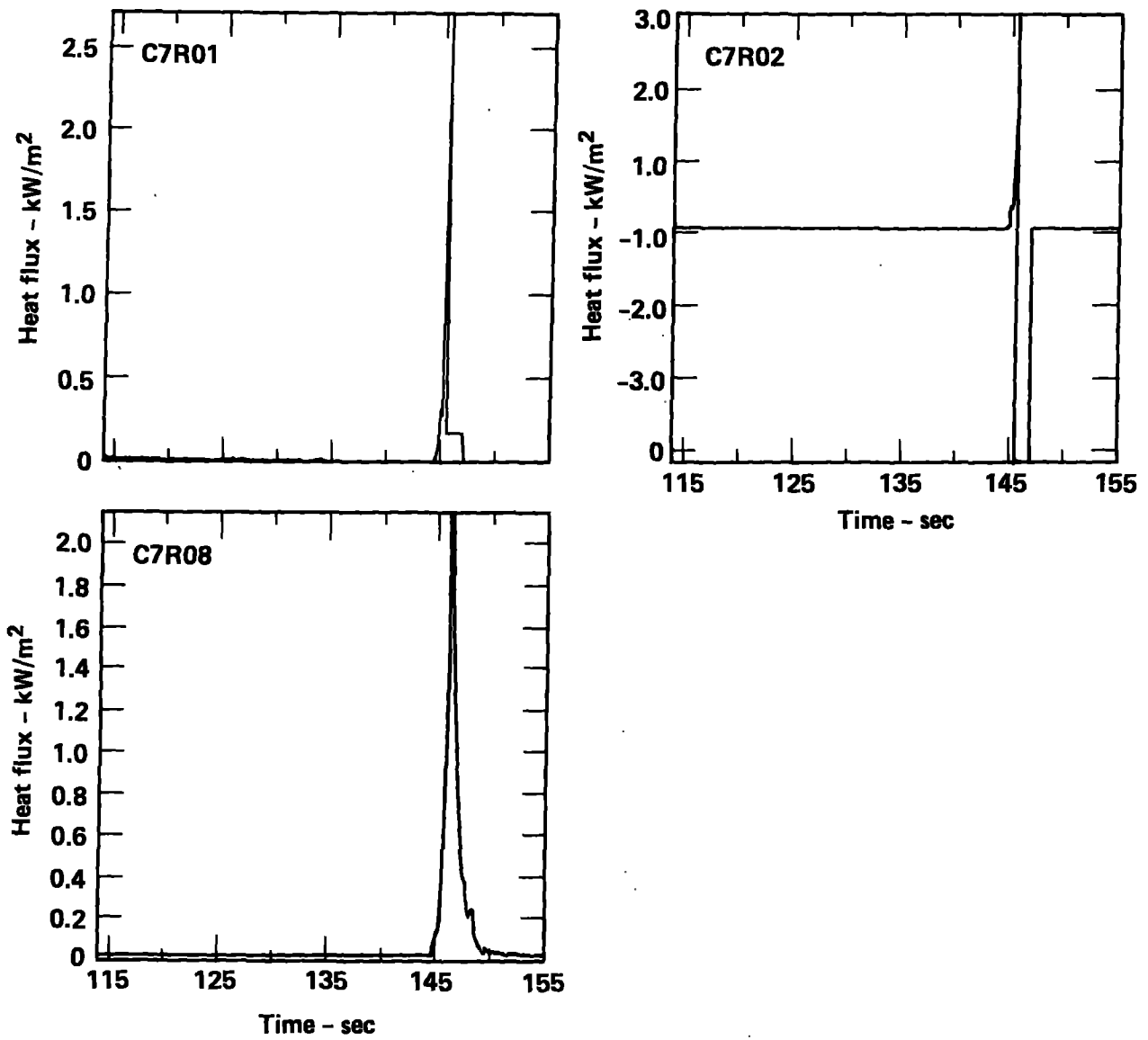
Fig. 41a. Wide-angle Radiometer data for Coyote 7.
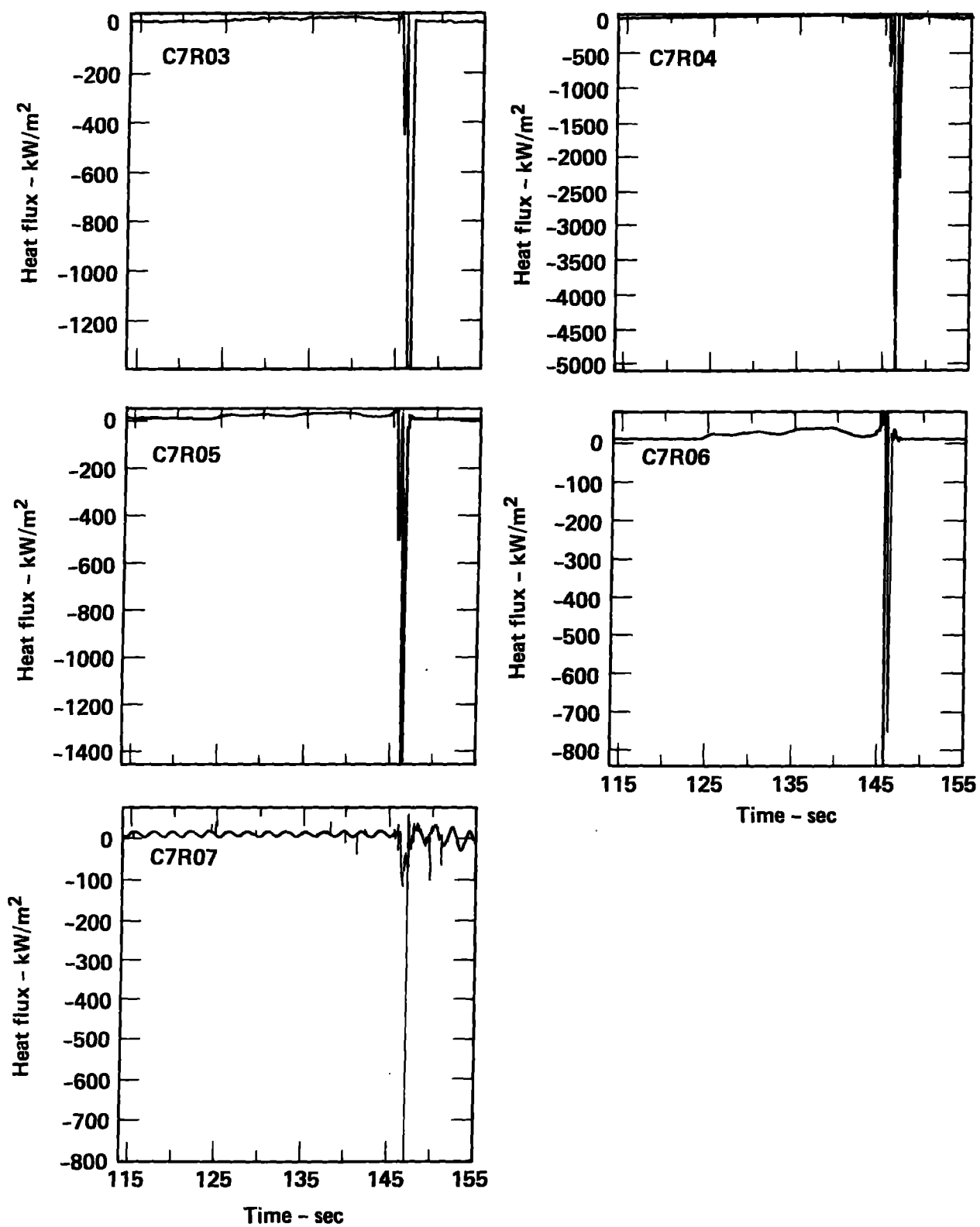
Fig. 41b. Narrow-angle Radiometer data for Coyote 7.

9. COYOTE SERIES RPT DATA

A summary of the important parameters for both the Burro and Coyote test series is given in Table 13. Of the 18 Coyote spills, six produced RPTs.

Two distinct types of RPTs occurred during the China Lake LNG spills--early RPTs and delayed RPTs. The early type of RPTs began immediately with the spill, and in some cases continued for the duration of the spill. These explosions were generally located near the spill point and appeared to be primarily underwater. Most of the RPTs that occurred during the Coyote test series were of this type.

The delayed type of RPTs occurred at the end of the spills, were generally located away from the spill point out on the LNG pool, and they appeared to occur at the pool surface. The delayed RPTs also showed a "chain reaction" tendency, in that once they began, a sequence of explosions followed, generally in the same vicinity. Delayed RPTs occurred on two tests--Coyotes 1 and 5.

Several of the spill experiments during the Coyote series were conducted solely for the purpose of studying RPTs (Coyotes 4, 8, 9, and 10). Each of these typically consisted of three short spills at low, medium, and high spill rates, separated in time by about 30 min. The other parameters (LNG composition, spill plate depth, water temperature, etc.) were essentially constant during the three consecutive spills. Spill tests with liquid methane (Coyote 8) and liquid nitrogen (Coyote 9) were performed to examine the effect of composition on the occurrence of RPTs. The Coyote 1 spill was to have been a three-spill sequence; however, the spill valve jammed in the open position during the first spill allowing the entire contents of the tank to slowly spill out over a period of about 6 min. Most of the LNG was spilled during the first 2 min, but a small quantity continued to dribble out for at least four more minutes as the tank slowly depressurized. At about 5 min, six to eight large RPTs occurred. These were located at the edges of the LNG pool and occurred in rapid succession as if the initial explosion triggered the others. Although no overpressure data were obtained during this spill, observers compared these RPTs to those of Coyote 4C, which were equivalent to about 1 kg of TNT.

The air-blast TNT equivalents of the observed RPTs, presented in Table 13, were calculated from peak overpressures measured at known distances from the spill point. These yields represent only that portion of the explosion which

TABLE 13. Coyote series summary of RPT data

Test	Estimated Tank Composition (% Vol) CH_4, C_2H_6, C_3H_8	Spill Rate (m^3/min.)	Spill Volume (m^3)	Spill Plate Depth (cm)	Impact Pressure Max/Average (psia)	Pond Temperature (°C)	RPT Explosions	Max Point Source Yield (kg TNT)
C1	81.7, 14.5, 3.8	6	14	30	0.8/0.2	30	Small early Large delayed	??
C2	70.0, 23.4, 6.6	16	8	2.5	5/5	27.6	Small early	0.23
C3	79.4, 16.4, 4.2	13.5	14.6	2.5	10/6	22.8	—	
C4a	78.8, 17.3, 3.9	6.8	3.8	25	2.4/0.4	22.4	Small early	0.001
C4b	78.8, 17.3, 3.9	12.1	6.0	25	5/3	20.6	—	
C4c	78.8, 17.3, 3.9	18.5	5.2	25	10/5	20.2	Large early	1.5
C5	74.9, 20.5, 4.6	17.1	28	6	13/8	17.2	Large delayed	3.0
C6	81.8, 14.6, 3.6	16.6	22.8	5	13/8	15	—	
C7	99.5, 0.5, 0	14.0	26	33	15/6	13.6	—	
C8a	99.7, 0.3, 0	7.5	3.7	33	2/0.6	12.8	—	
C8b	99.7, 0.3, 0	14.2	5.4	33	10/4	12.7	—	
C8c	99.7, 0.3, 0	19.4	9.7	33	14/11	12.3	—	
C9a	LN_2	7.2	3.6	36	2/0.2	14.1	—	
C9b	LN_2	9.9	3.3	36	8/3	14.8	—	
C9c	LN_2	13.3	8.2	36	15/10	15.8	—	
C10a	70.2, 17.2, 12.6	13.8	4.6	36	8/5	10.6	—	
C10b	70.2, 17.2, 12.6	19.3	4.5	36	14/10	10.6	—	
C10c	70.2, 17.2, 12.6	18.8	5.0	Removed	12/9	11.6	Small early	0.005

produced the air shock, as no underwater data on overpressure were obtained due to malfunction of NWC's sensors. The calculations assume that the explosion is a point source, similar to TNT in energy release times, and that the surface shock wave reflection produces an overestimate of the explosive energy by a factor of 1.8. The overpressure results for RPT explosions which occurred during the Coyote 4C and Coyote 5 tests are shown in Fig. 42.

The tank compositions in Table 13 were calculated using assays provided by San Diego Gas & Electric (SDG&E) and a tank boiloff rate of 1 m³ of methane per day. A linear interpolation of the SDG&E assay data was used to estimate the composition loaded on the tanker truck, with an additional 1 m³ of methane assumed to have evaporated in the transfer process. Assays were taken by NWC personnel prior to each spill; however, the sampling technique was not accurate enough to be useful. The LNG exit liquid composition data was also unusable due to questionable sample probe performance and to a malfunction of the gas analyzer system. The spill rate is an average value determined by dividing the total volume spilled by the spill duration.

The pond temperatures of Table 13 were recorded at two locations approximately 20 cm below the water surface, just prior to each spill (Fig. 2). Some typical water temperature variations during a spill are shown in Fig. 43. This was the maximum temperature drop observed during the entire Coyote series (∿ 7°C). In no case did the underwater pond temperature sensors record freezing temperatures (< 0°C), although ice was observed on the pond within the perimeter of the LNG pool.

Plots of the LNG impact pressures and exit temperatures for each spill are shown in Figs. 44-61. The impact pressures in Table 13 reflect the peak values observed during each spill, and a value averaged over the duration of each spill. The impact pressure for the Coyote 2 test was clipped at 5 psid ("d" means differential) due to amplifier saturation. Problems with the LNG exit temperature measurement were experienced during the Coyote 1, 5, and 10C spills. The exit temperature values for the Coyote 1 spill (Fig. 44) are not accurate because of a system calibration error, but this figure is presented for its qualitative value. The thermocouple was damaged during the cooldown period of the Coyote 5 spill, and only the initial portion of the Coyote 10C exit temperature data is believed to be accurate. The cold temperatures observed after the spill valve was closed were probably a result of evaporative cooling of the exiting gas due to the residual LNG in the pipe.
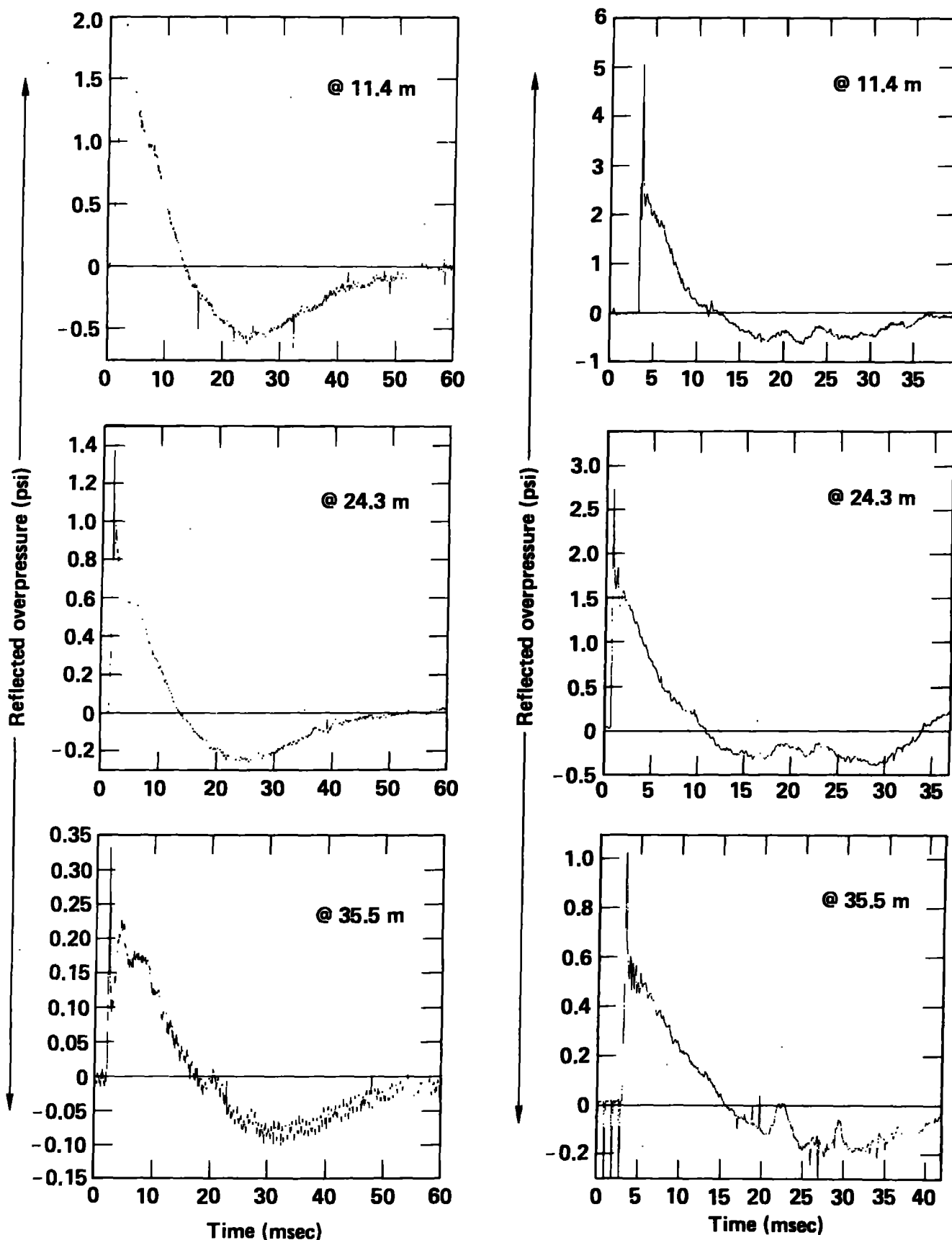
Fig. 42. RPT overpressure data plots. (left) Overpressures at three locations during a Coyote 4C RPT explosion. (right) Overpressures at three locations during a Coyote 5 RPT explosion.
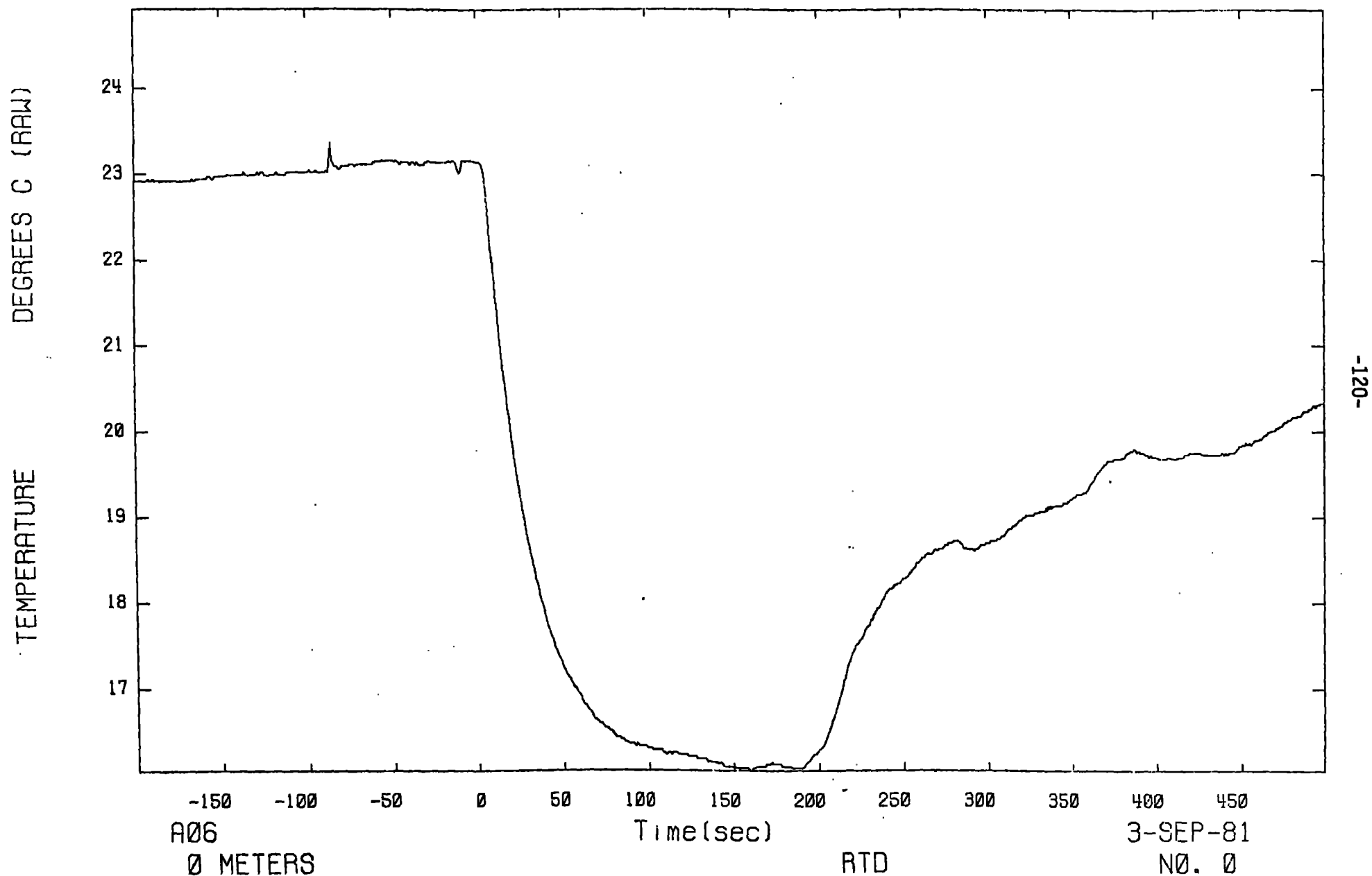
Fig. 43.   Typical water temperature variation during an LNG spill (Coyote 3).
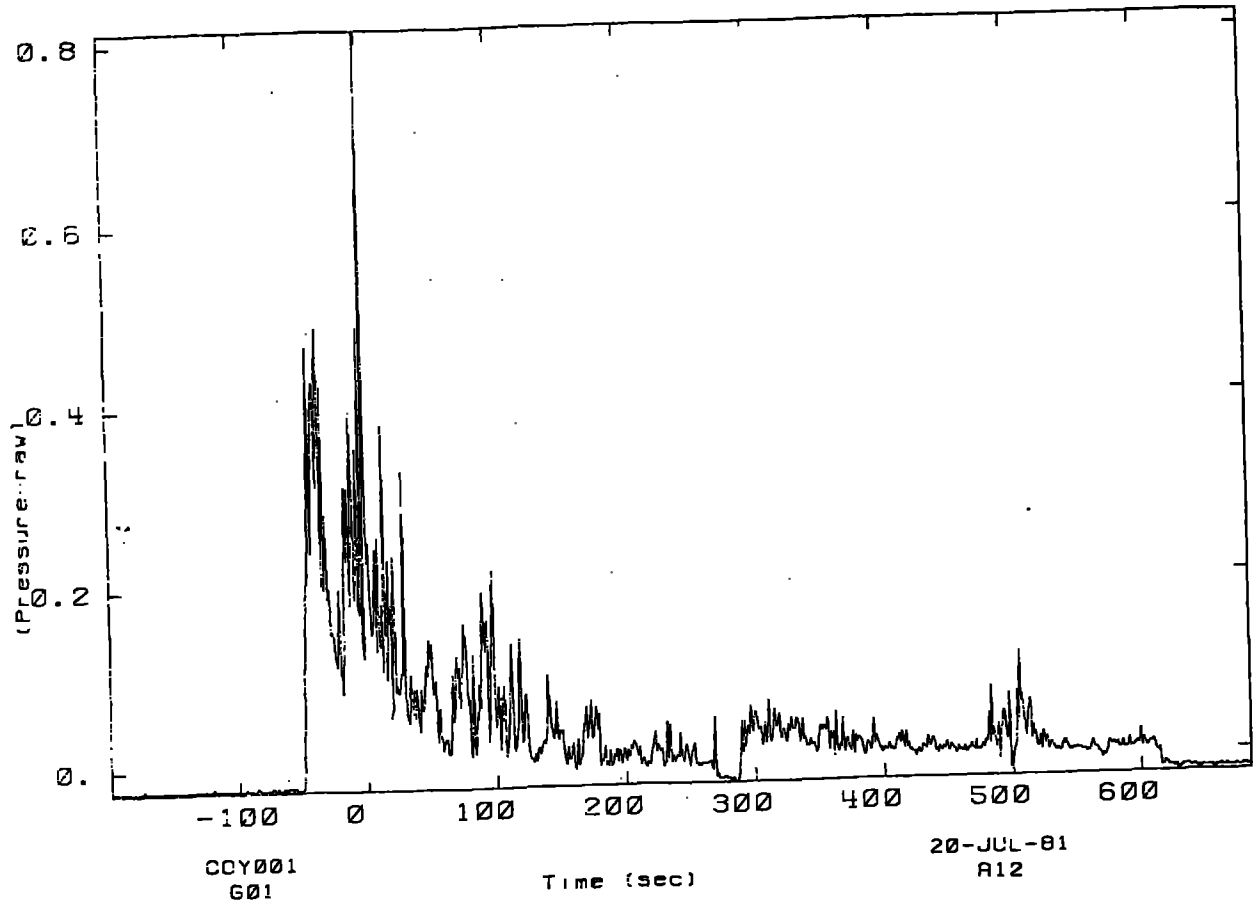
Fig. 44. LNG impact pressure and exit temperature during Coyote 1.

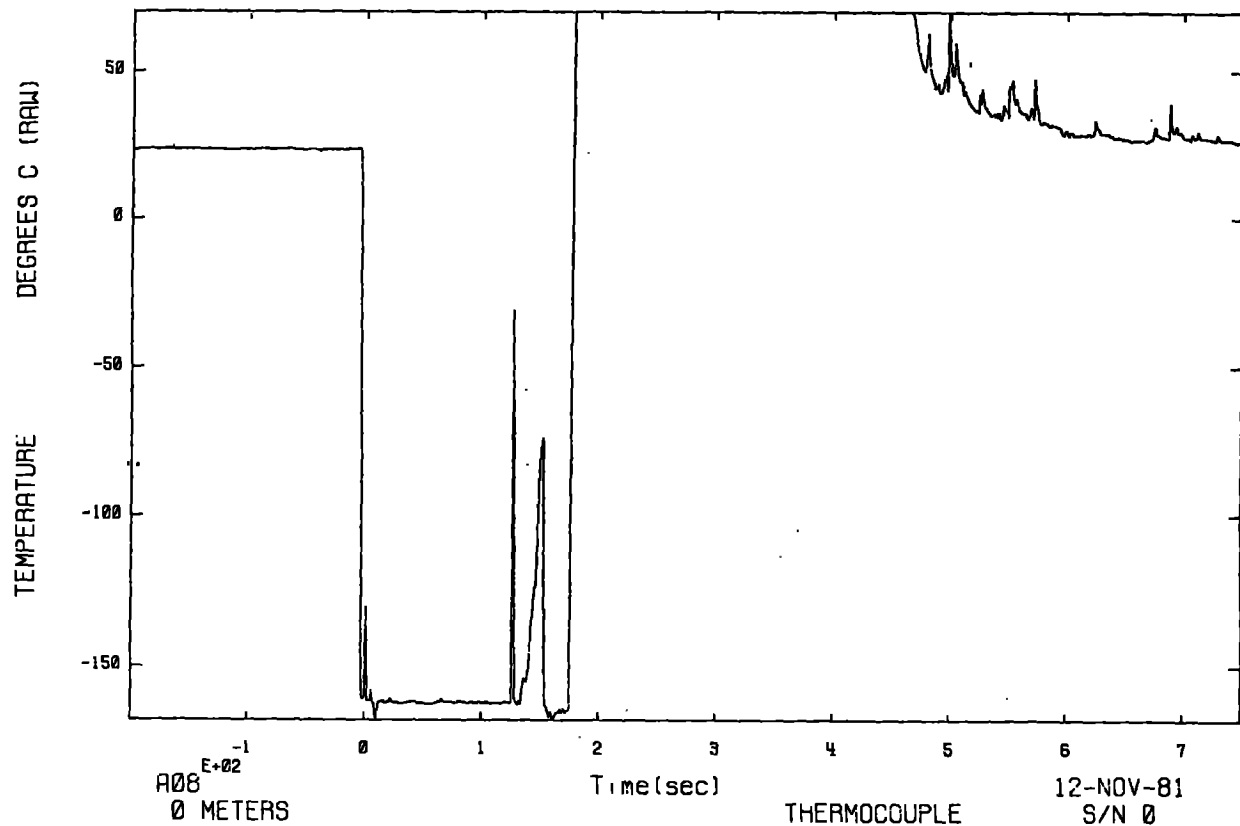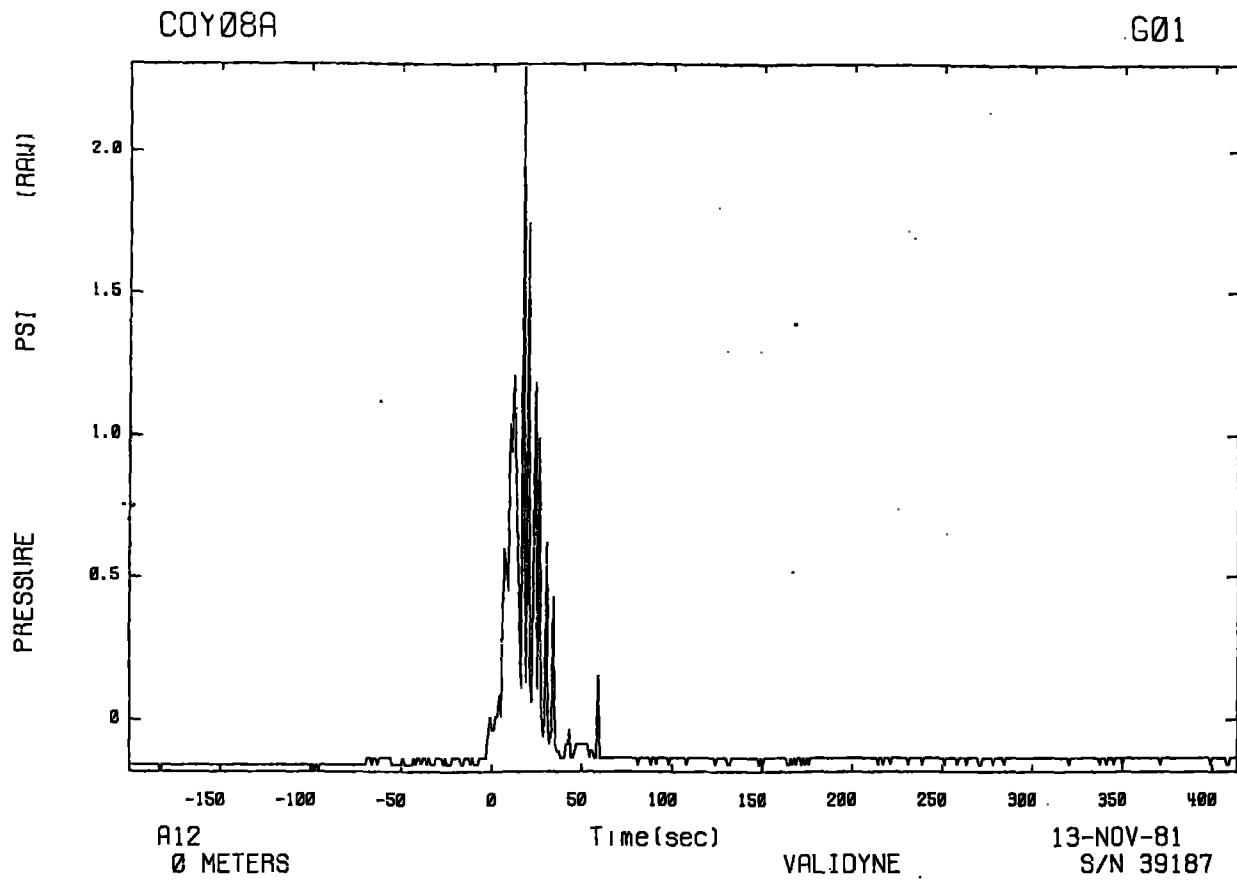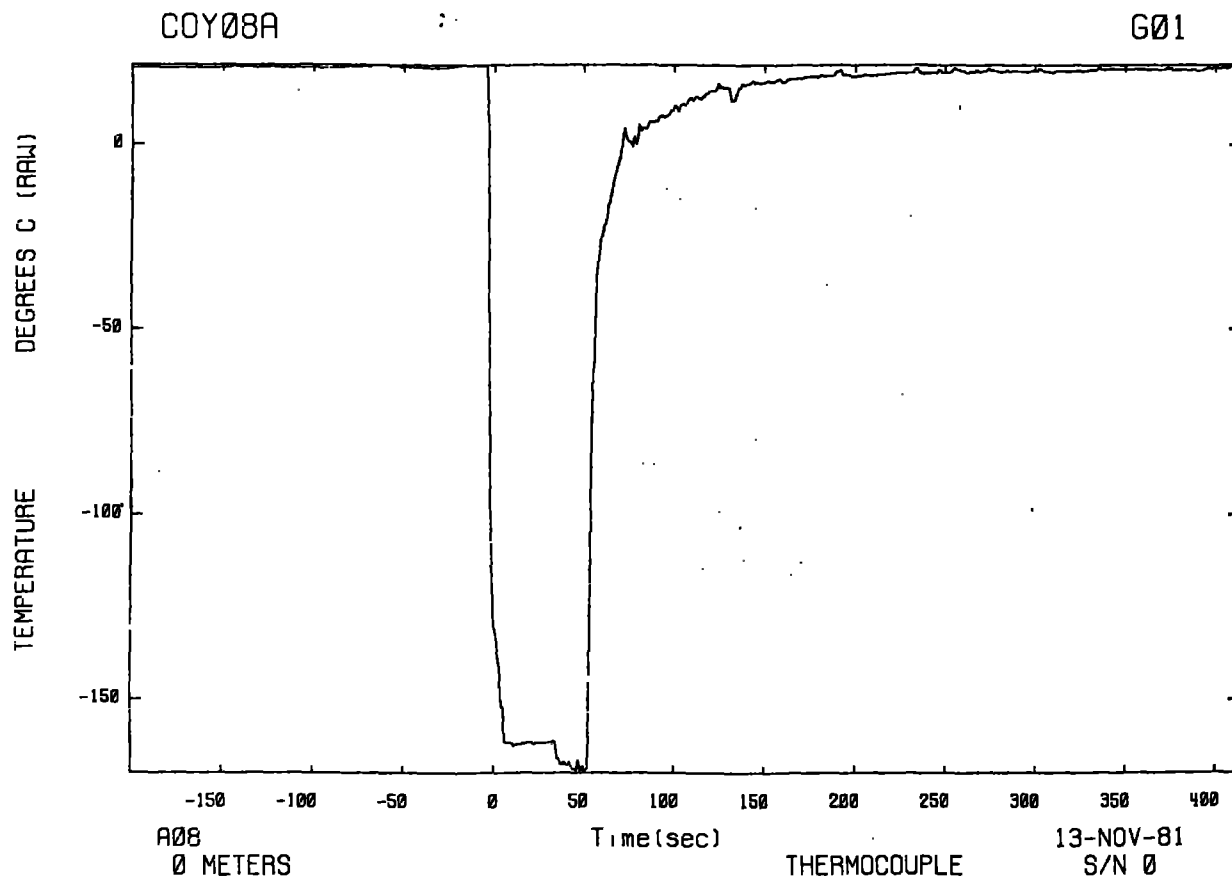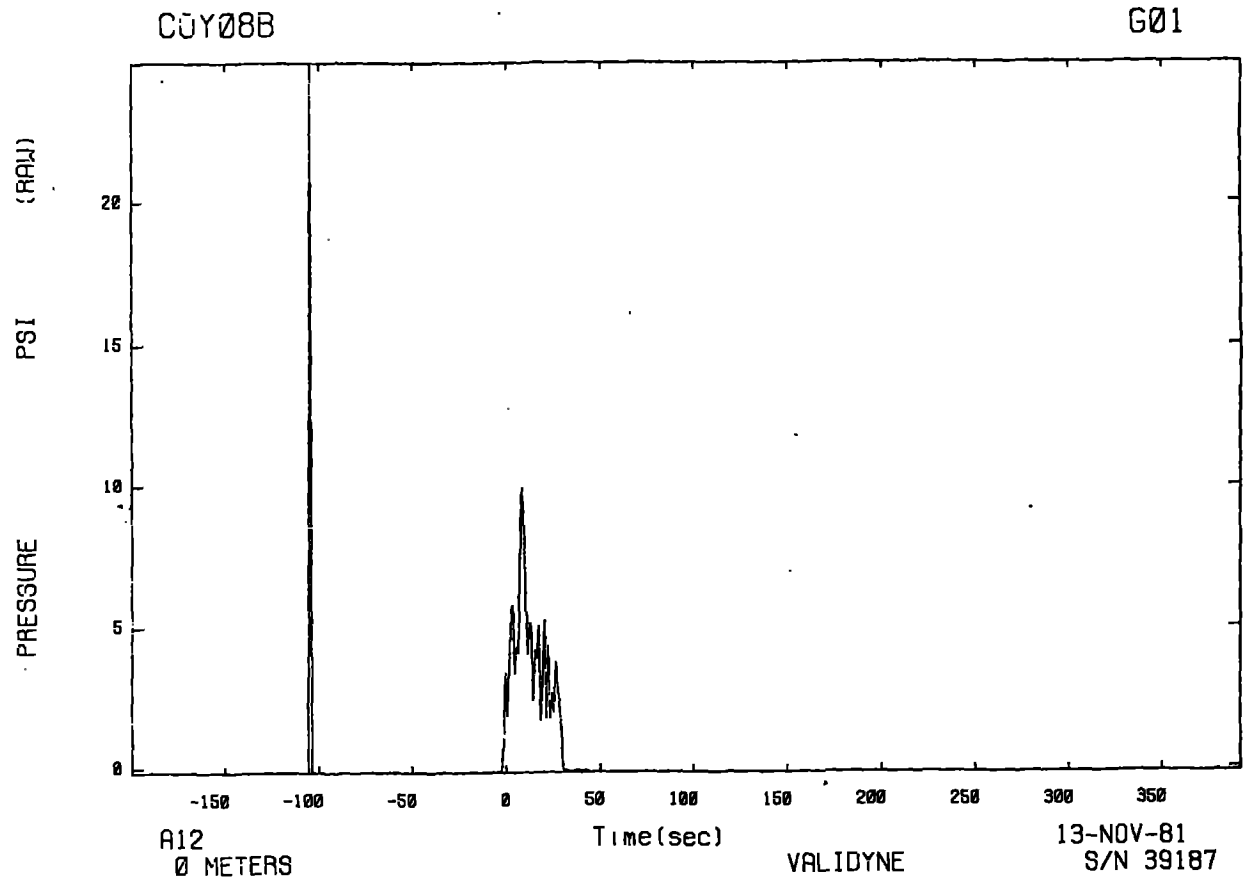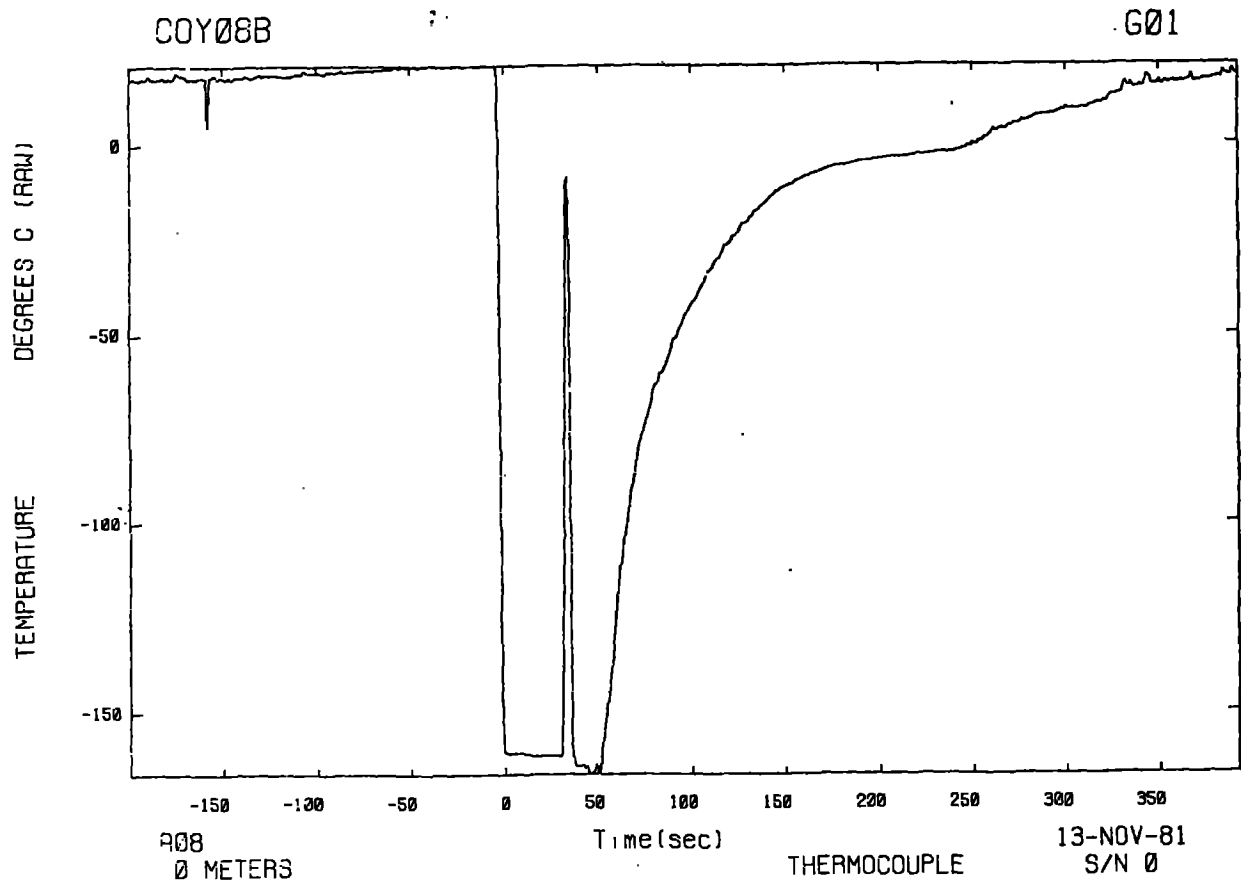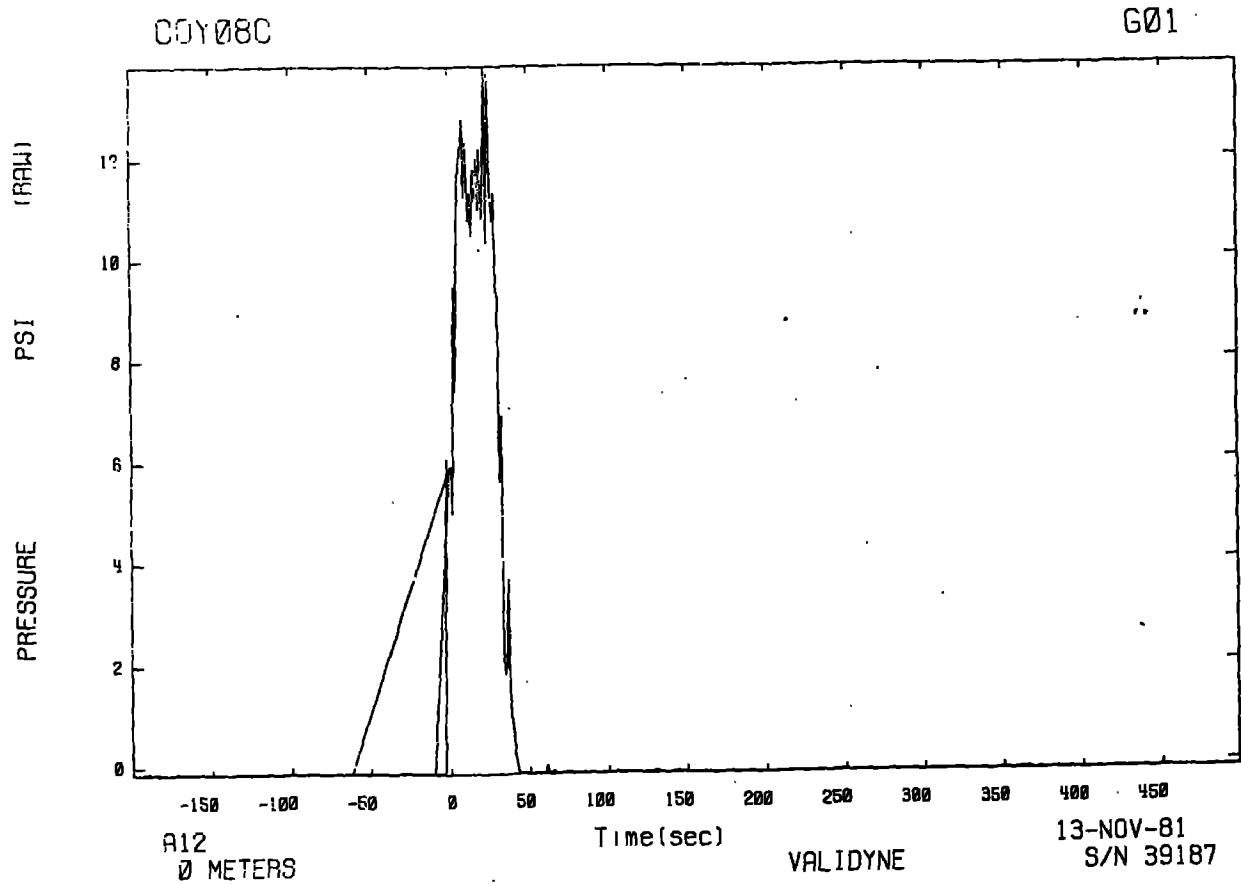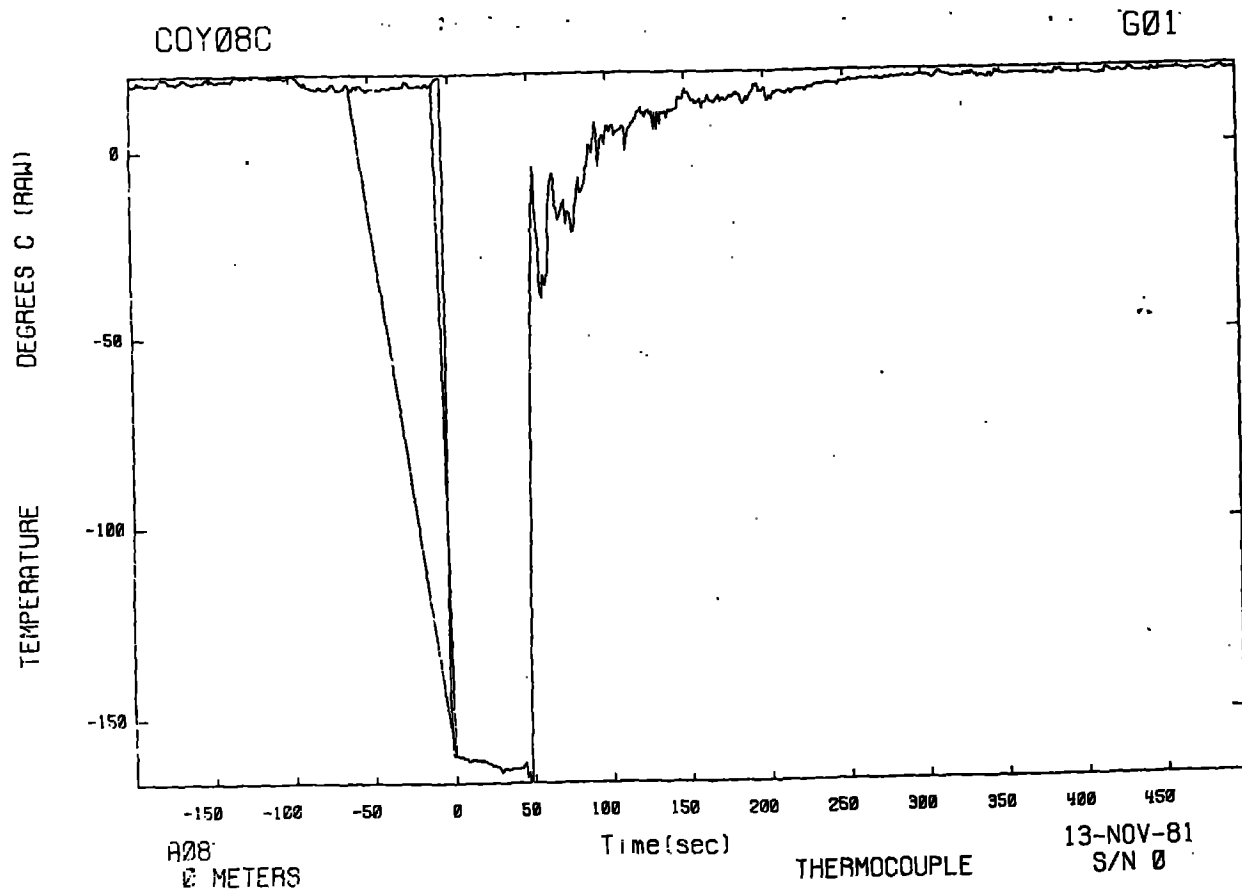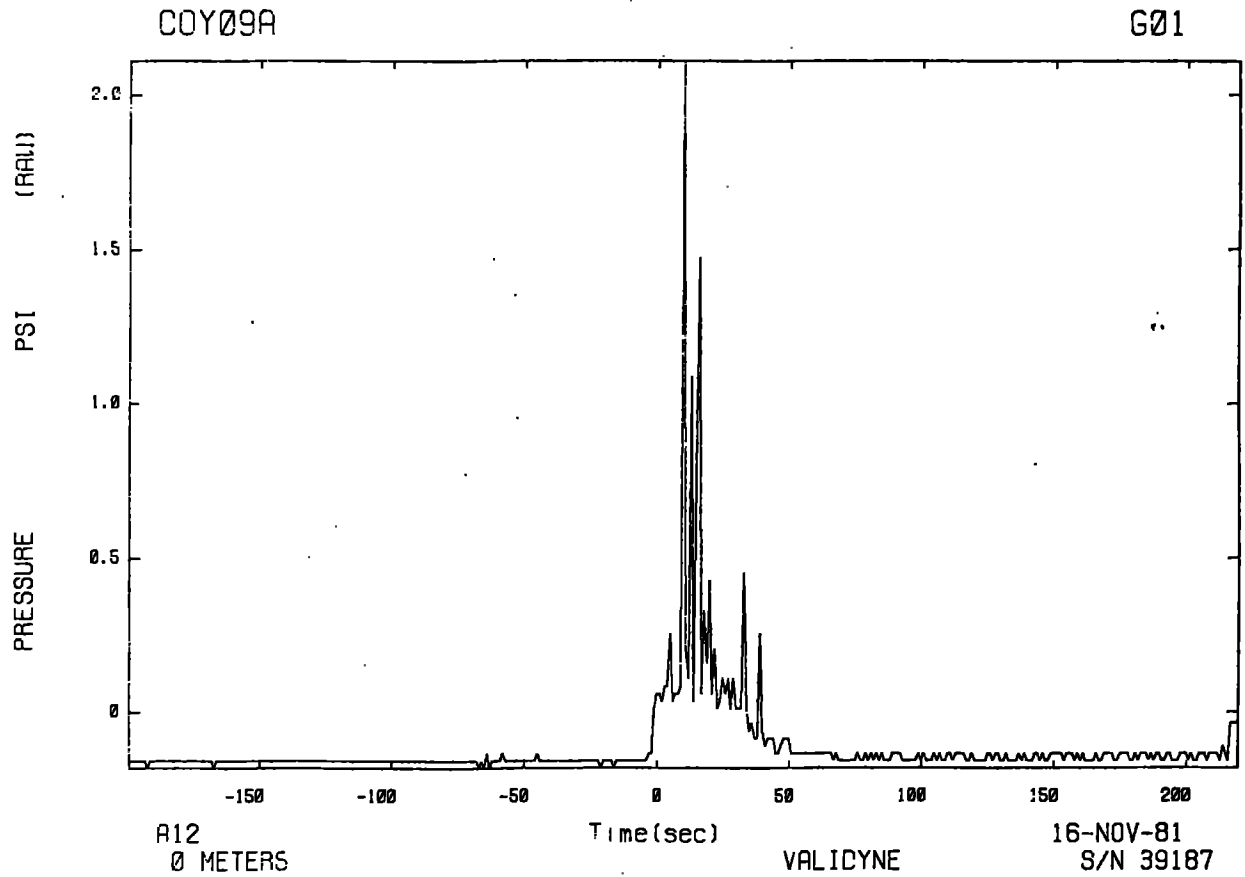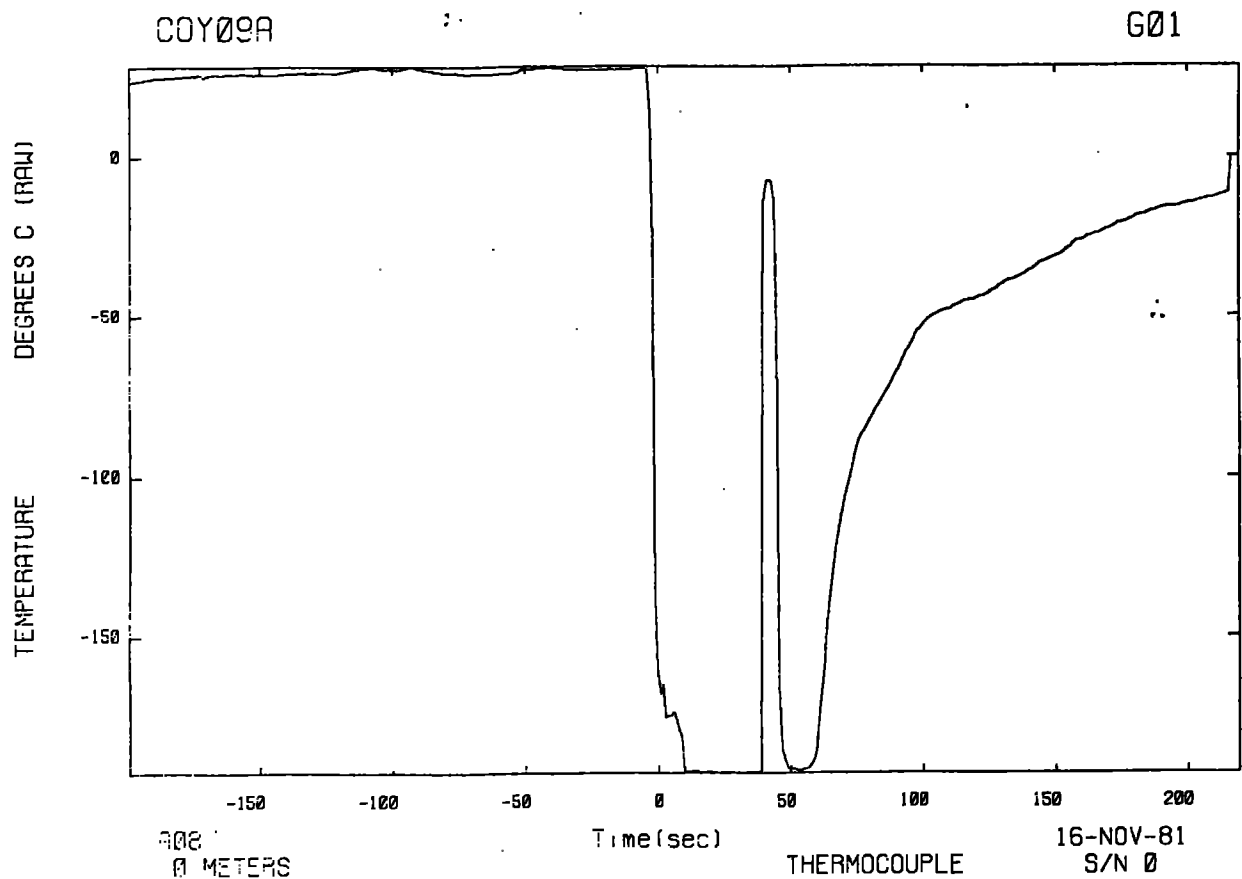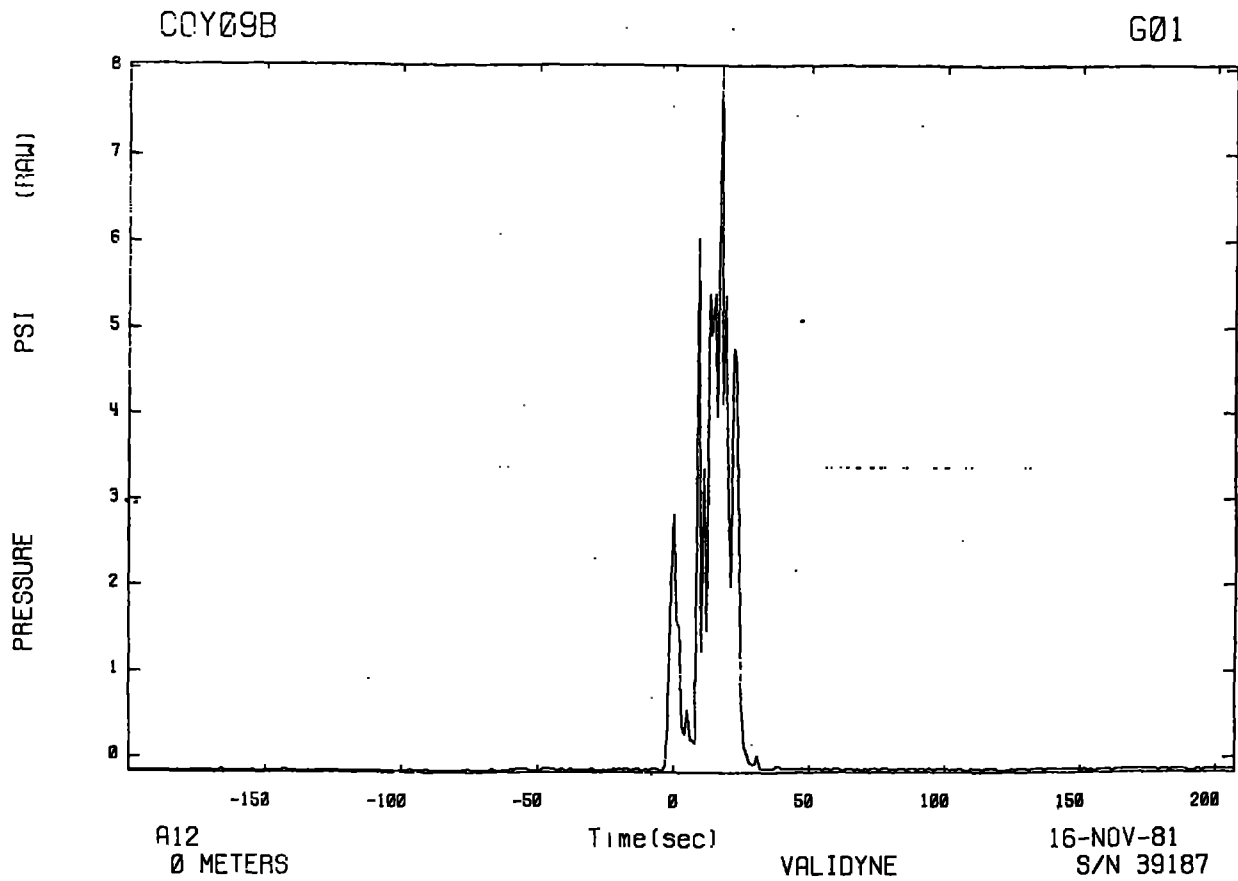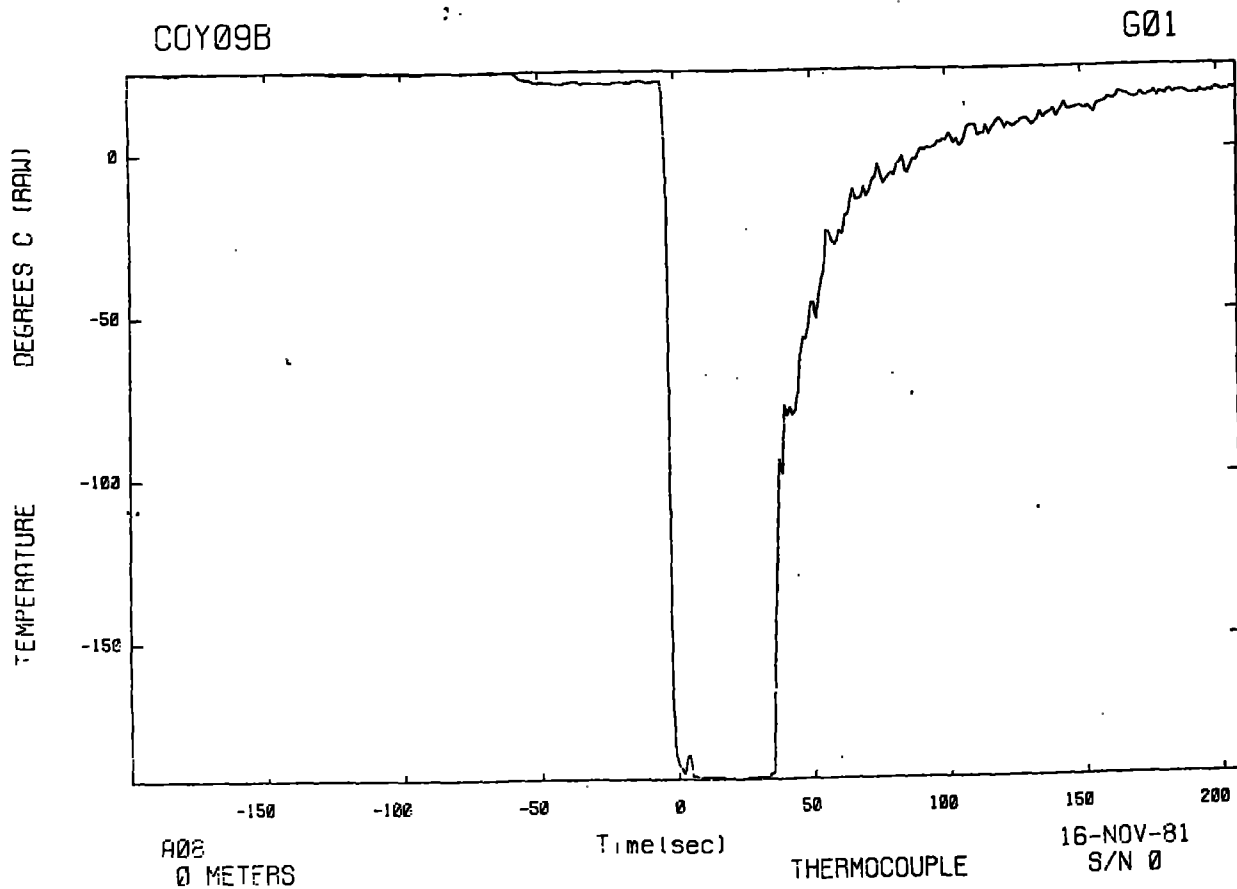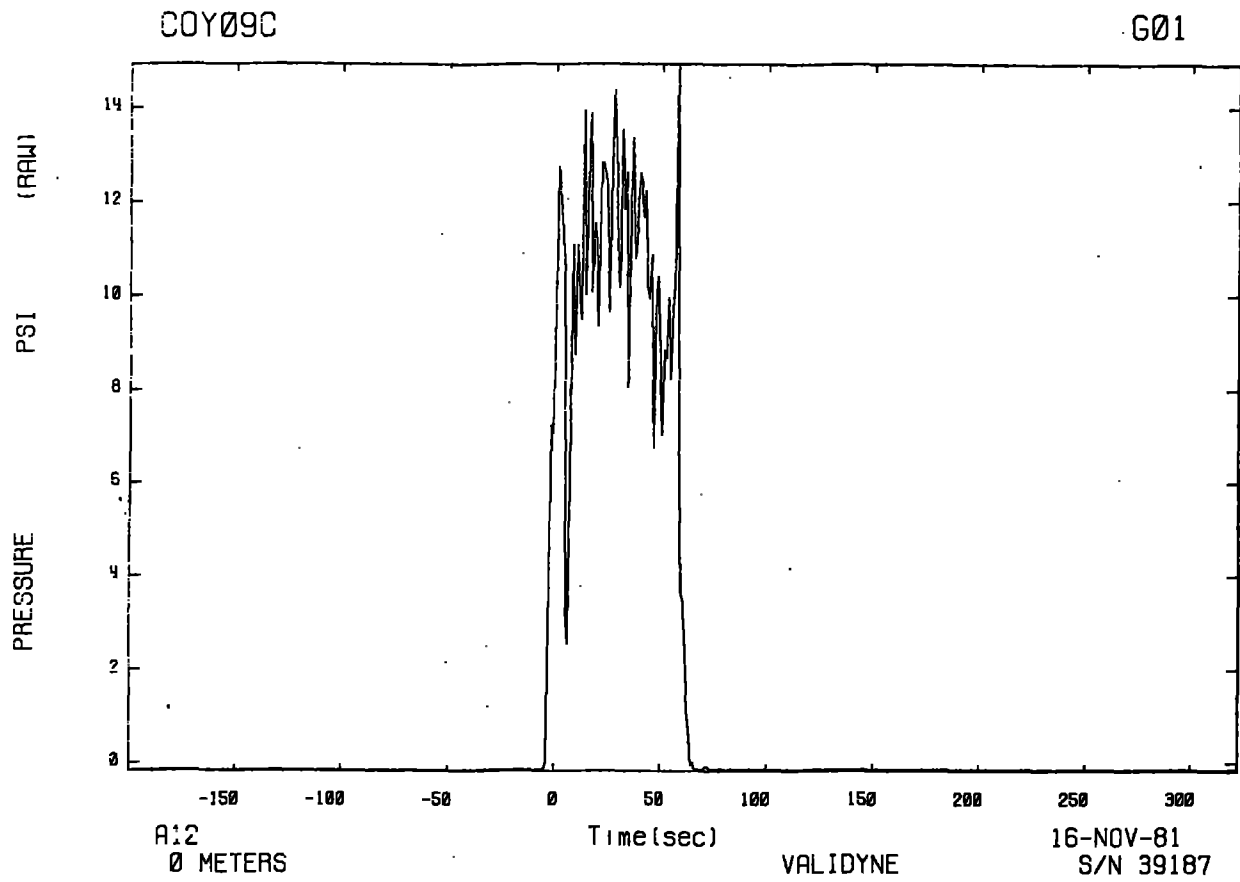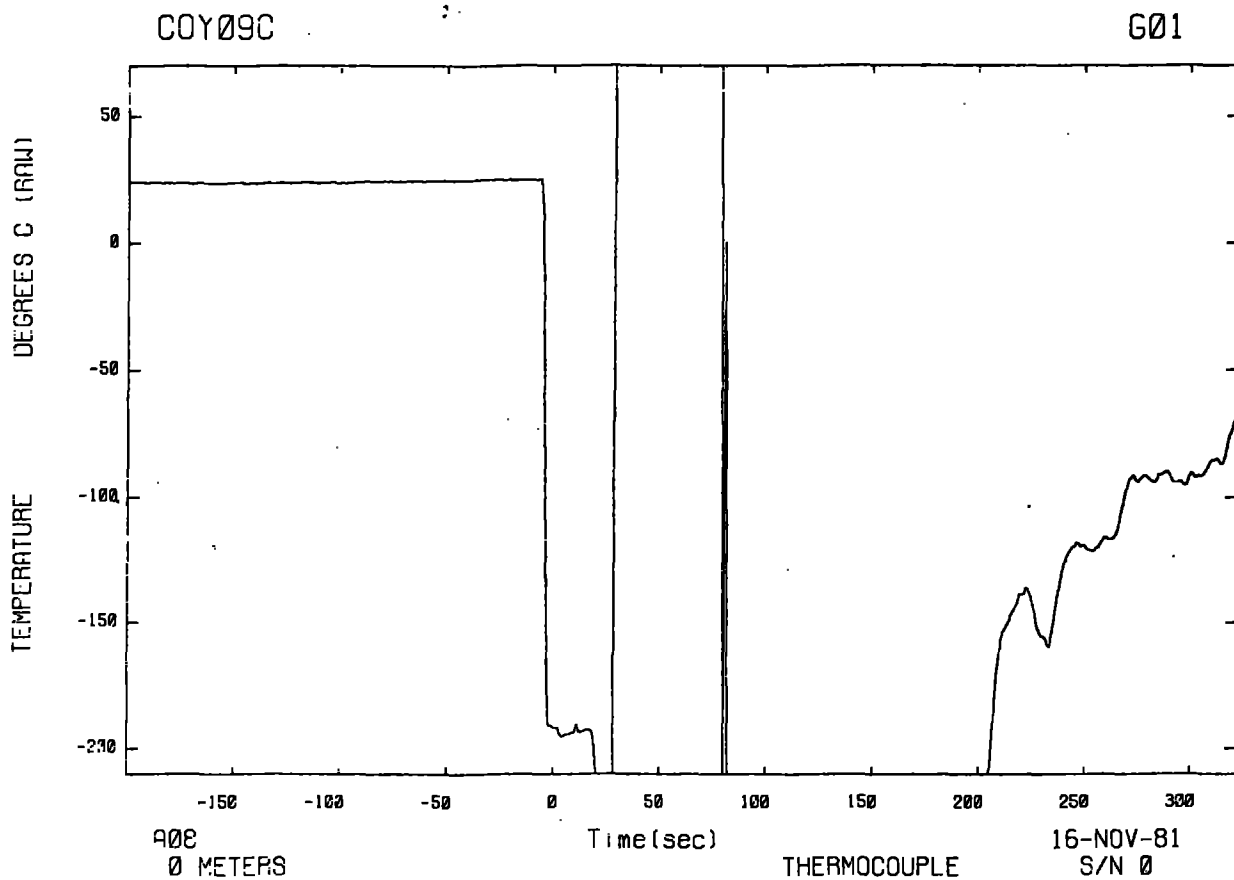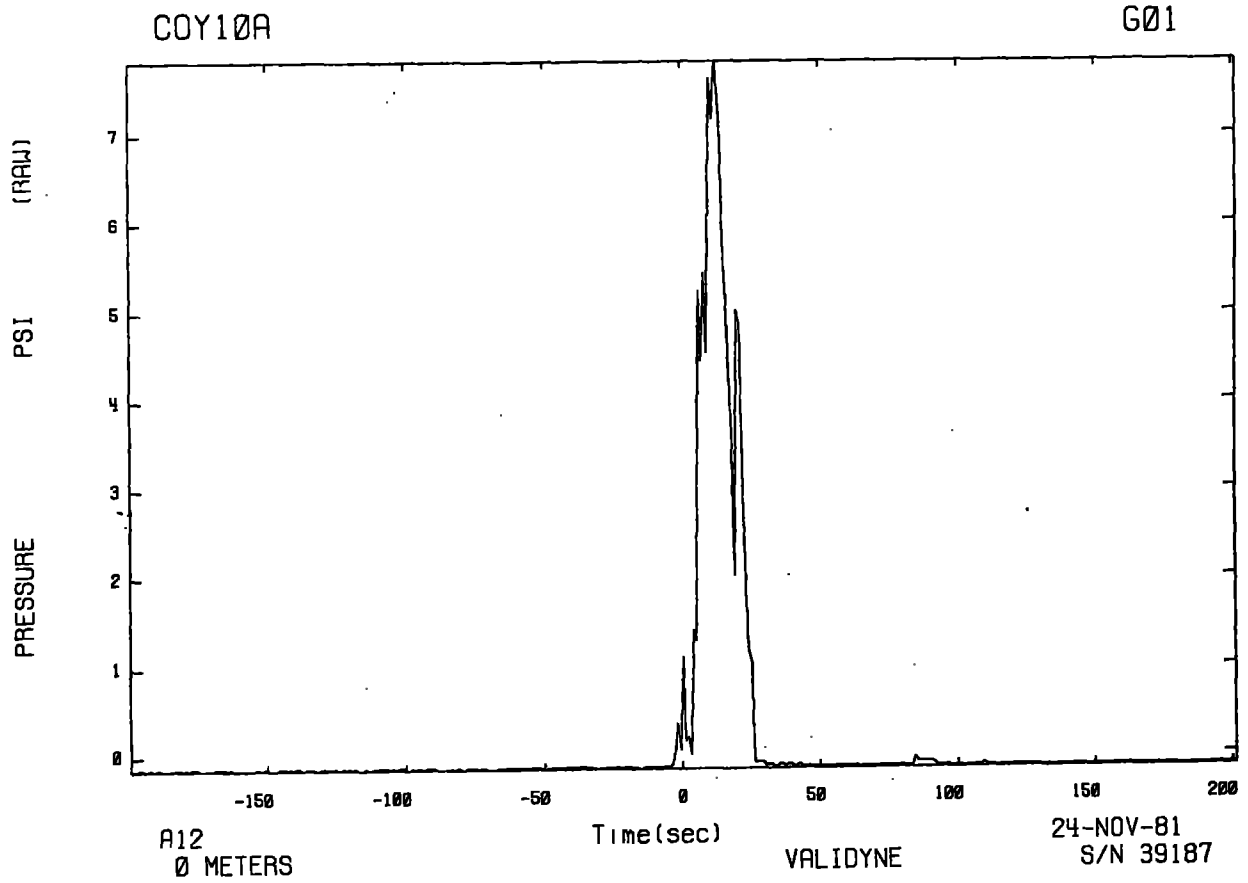COY002   G01

A12
0 METERS   VALIDYNE   20-AUG-81
                                                                    NO. DONE

Fig. 45. LNG impact pressure and exit temperature during Coyote 2.

COY002   ：   G01

A08
0 METERS   THERMOCOUPLE   20-AUG-81
                                                                    NO. 0
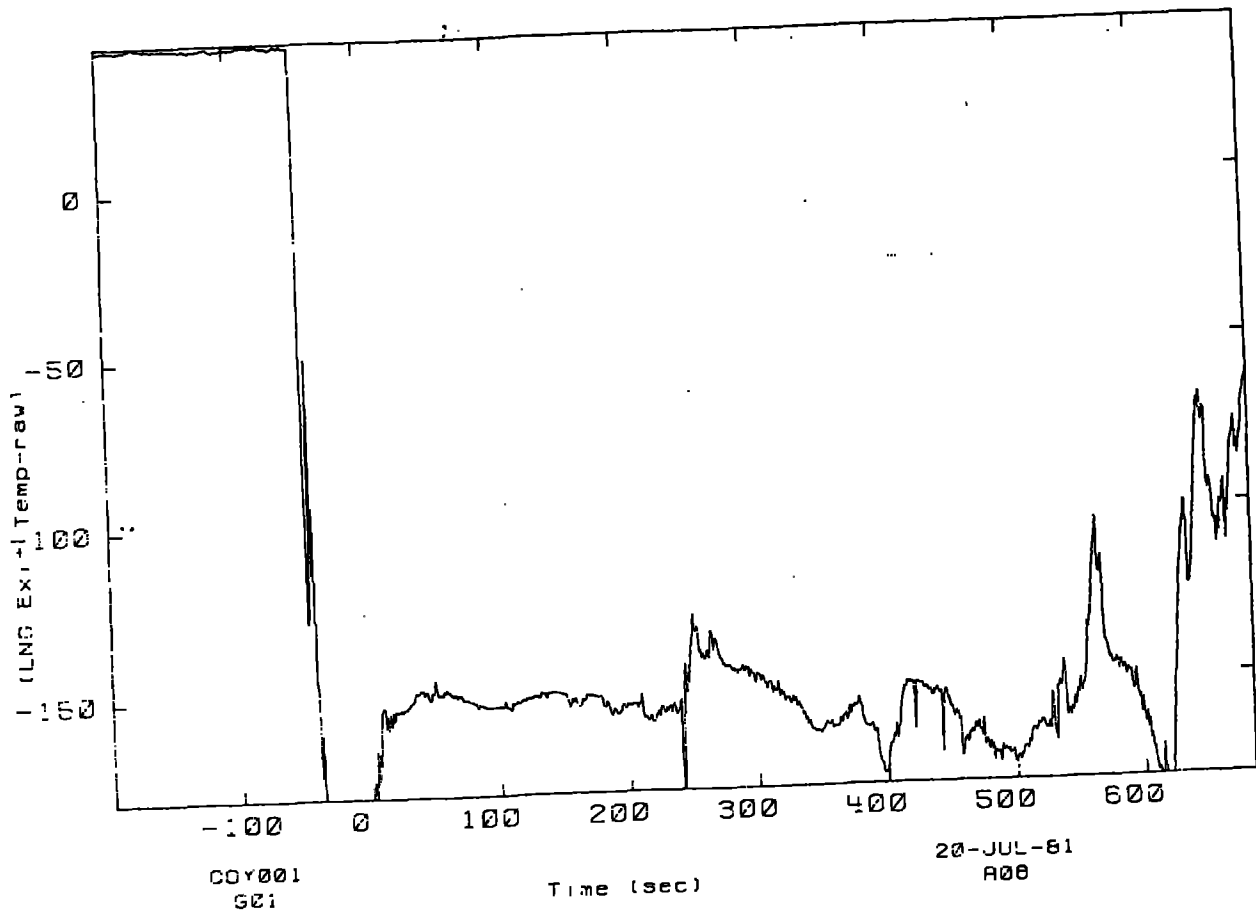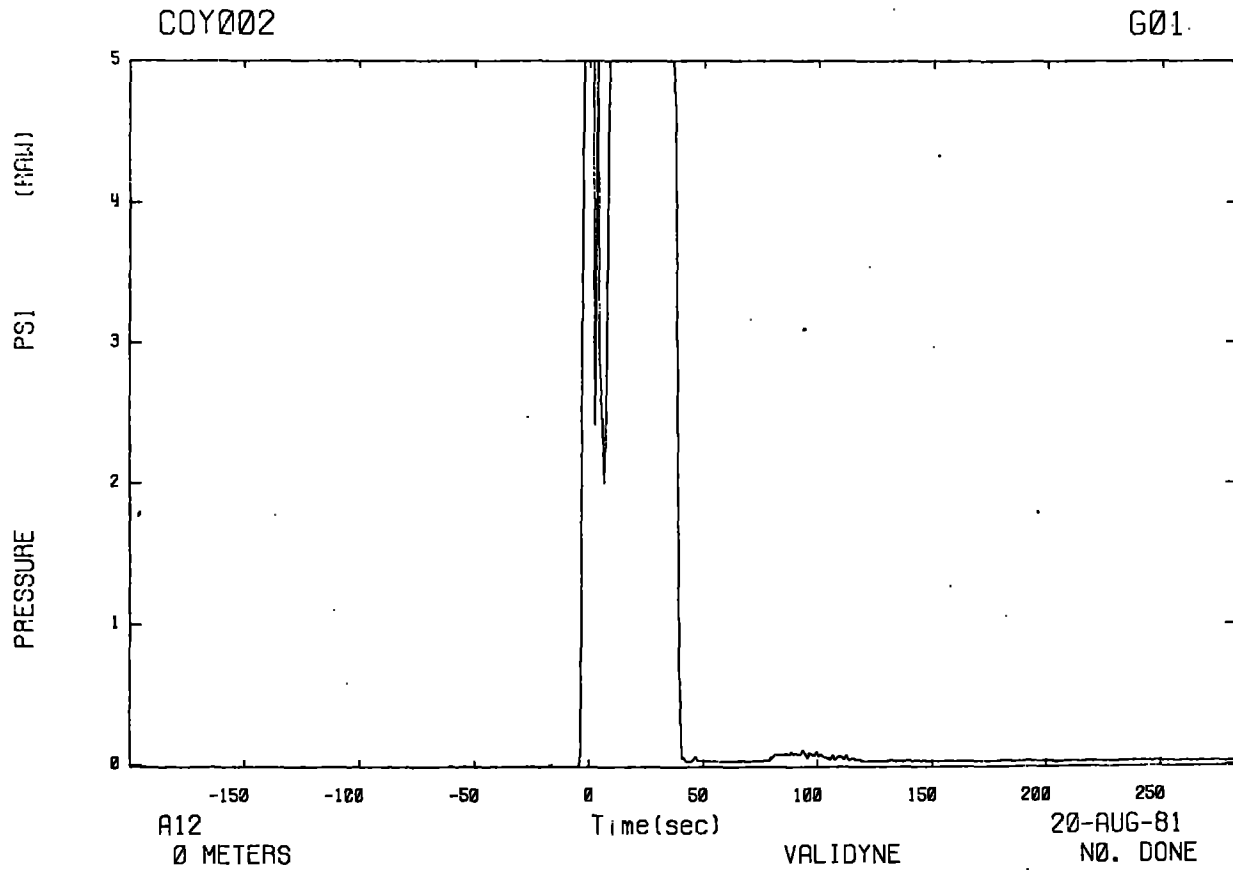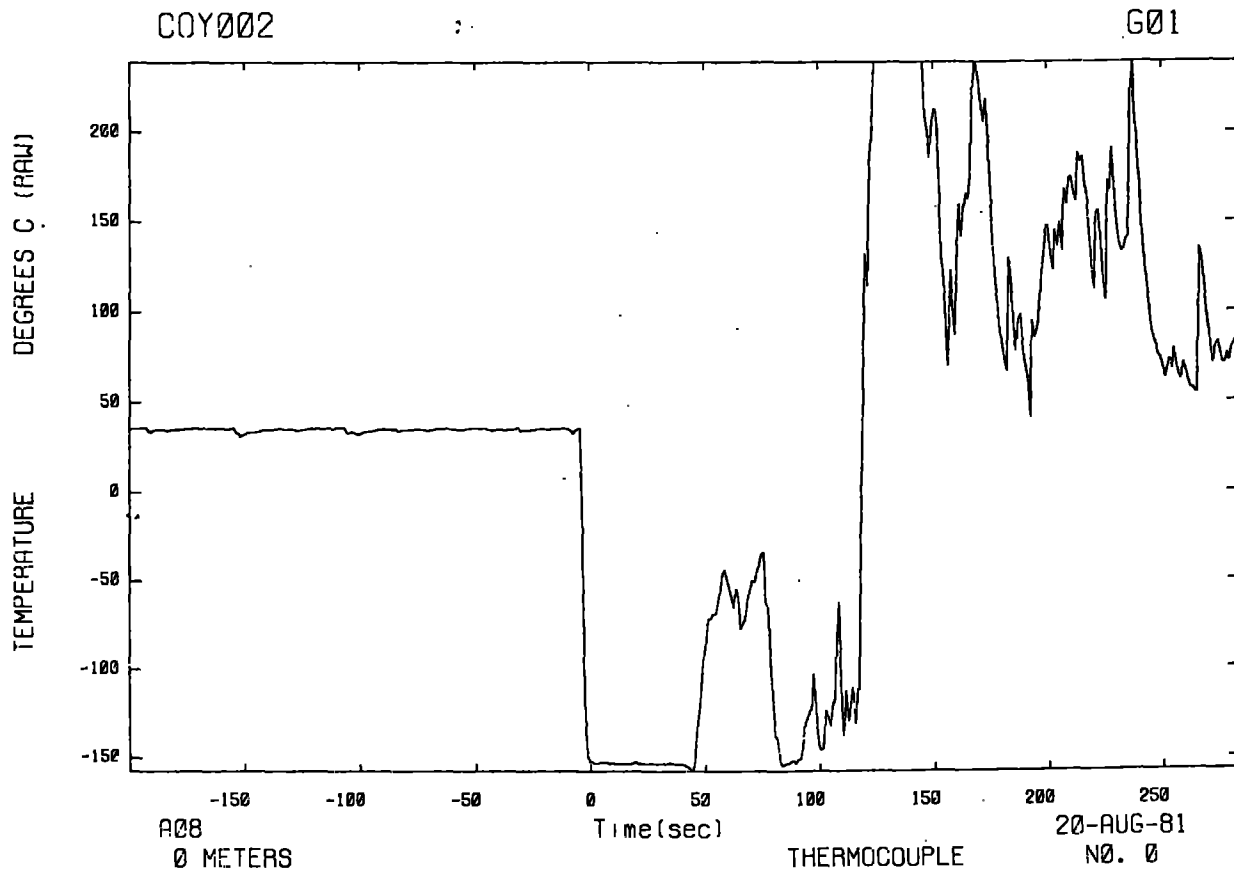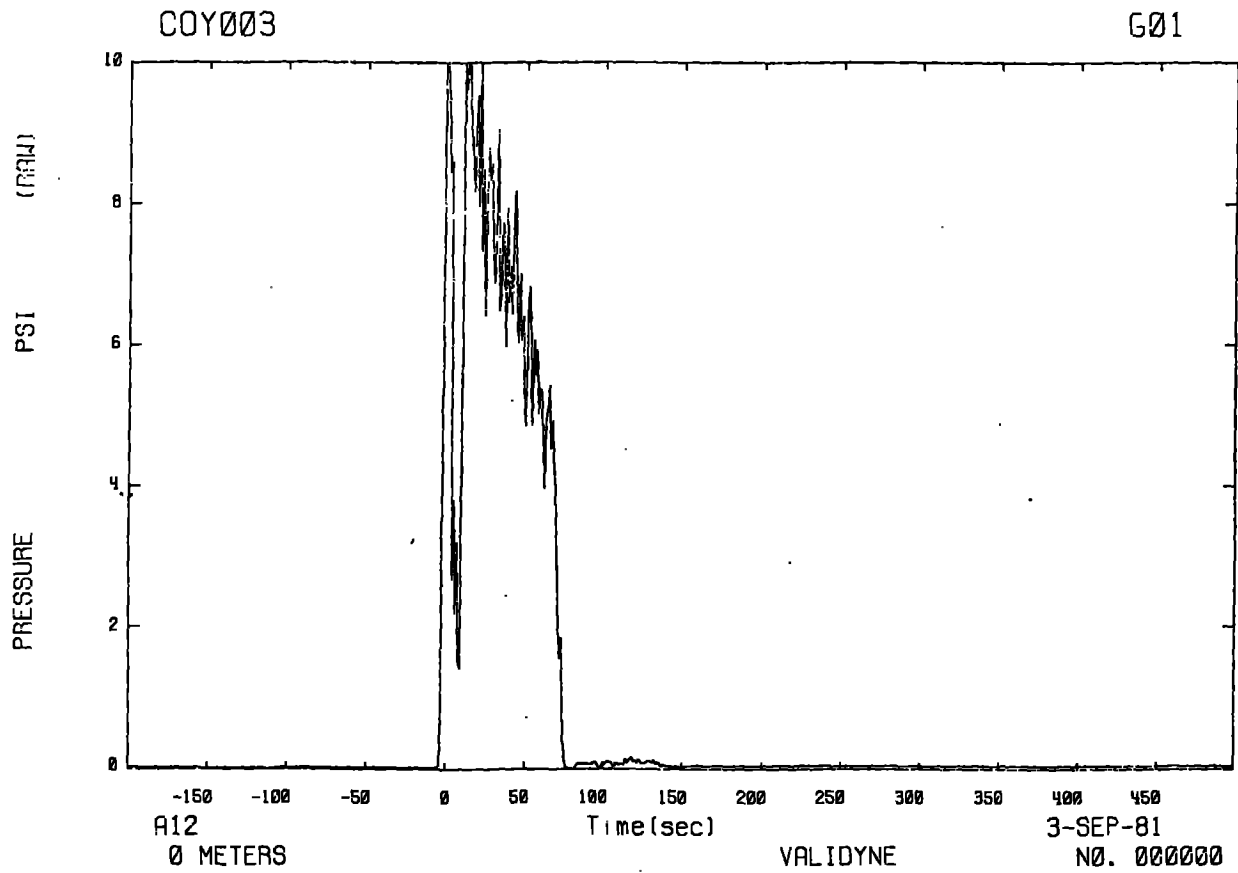
Fig. 46. LNG impact pressure and exit temperature during Coyote 3.

COY04A   G01

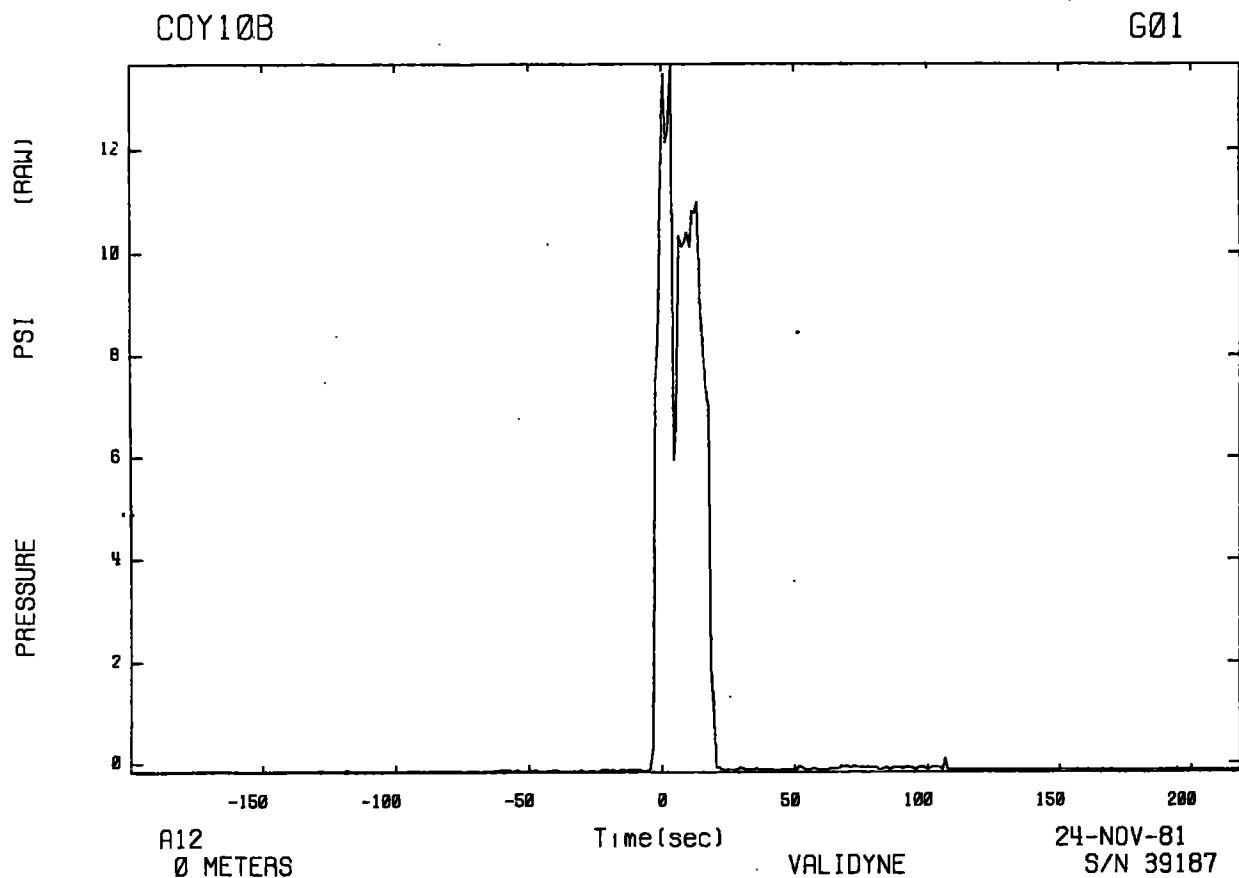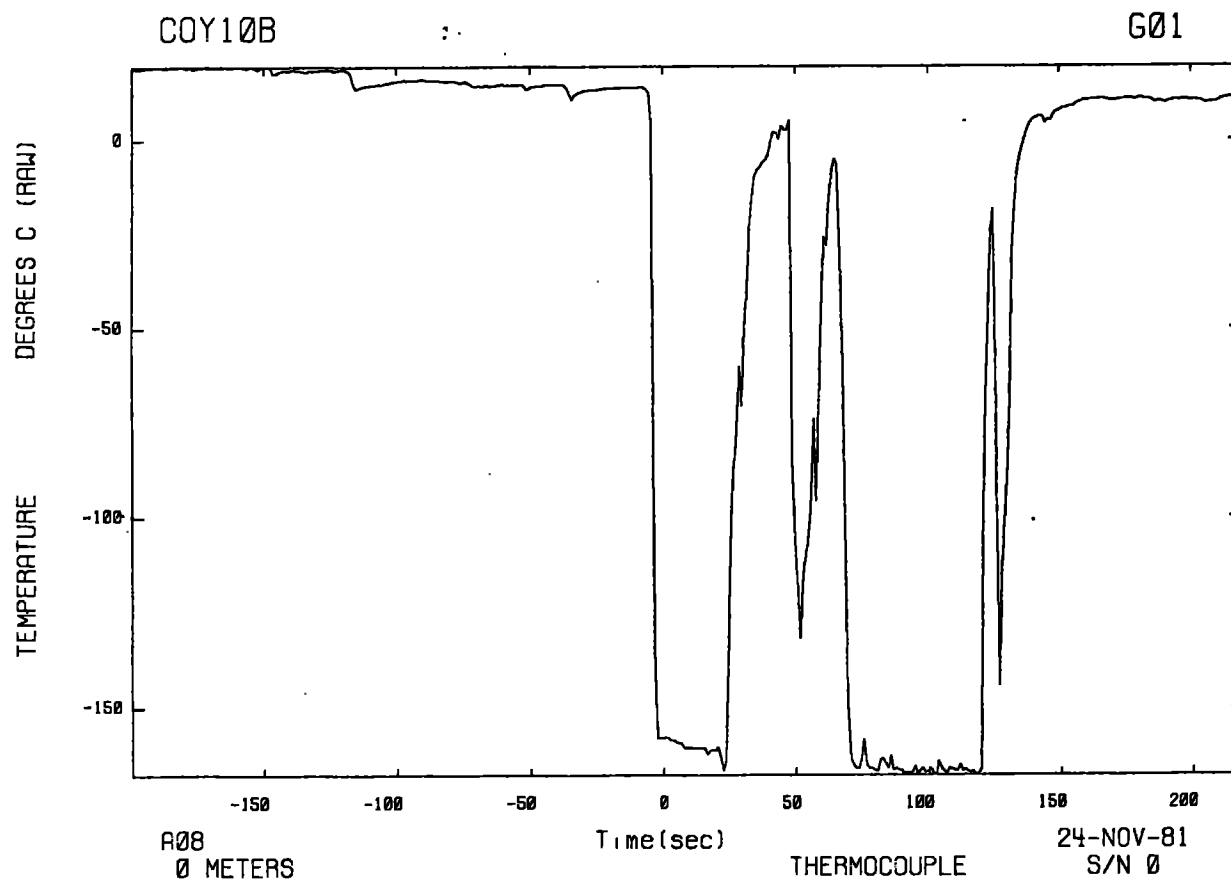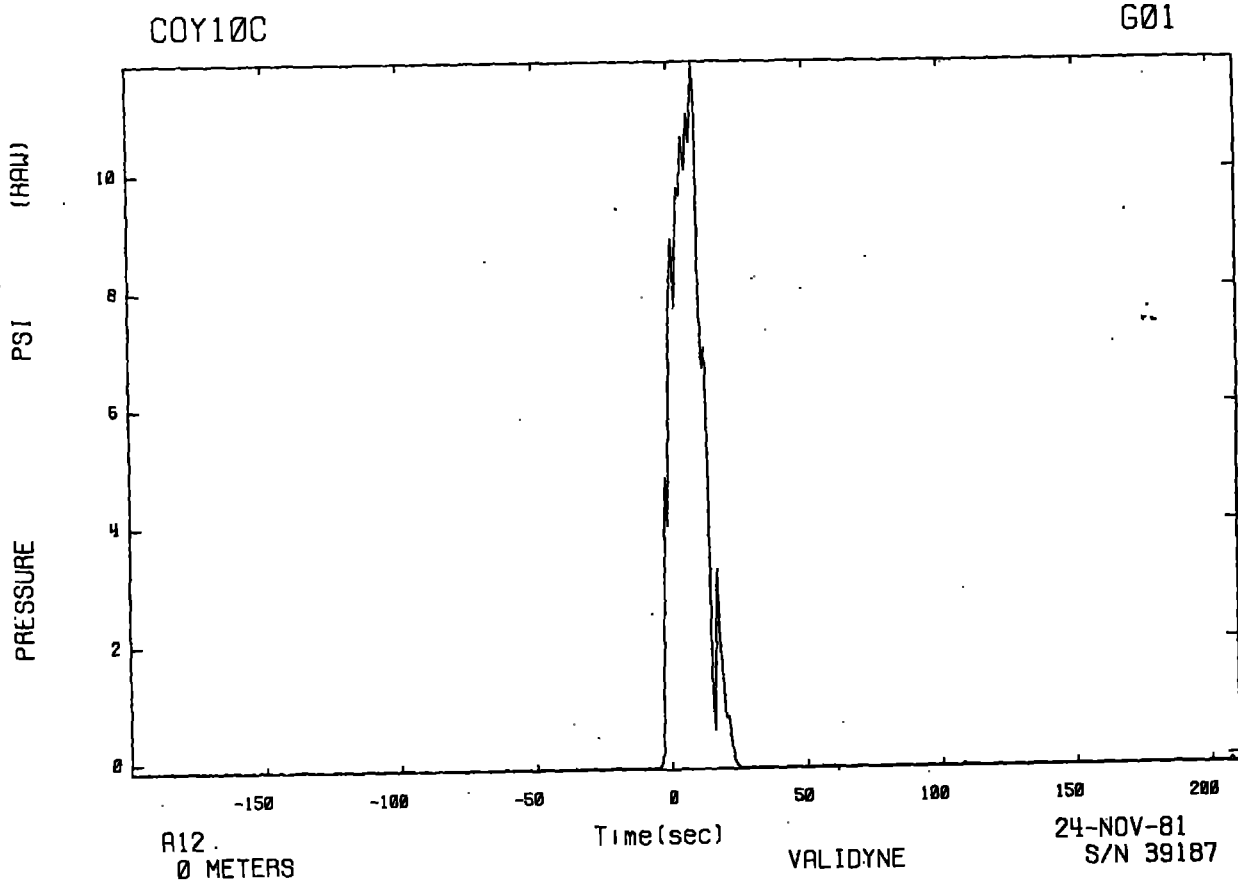**Fig. 47. LNG impact pressure and exit temperature during Coyote 4A.**

COY04A   G01

COY04B   G01

A12   Time(sec)   25-SEP-81
0 METERS   VALIDYNE   N0. 39187

Fig. 48. LNG impact pressure and exit temperature during Coyote 4B.

COY04B   G01

A08   Time(sec)   25-SEP-81
0 METERS   THERMOCOUPLE   N0. 0
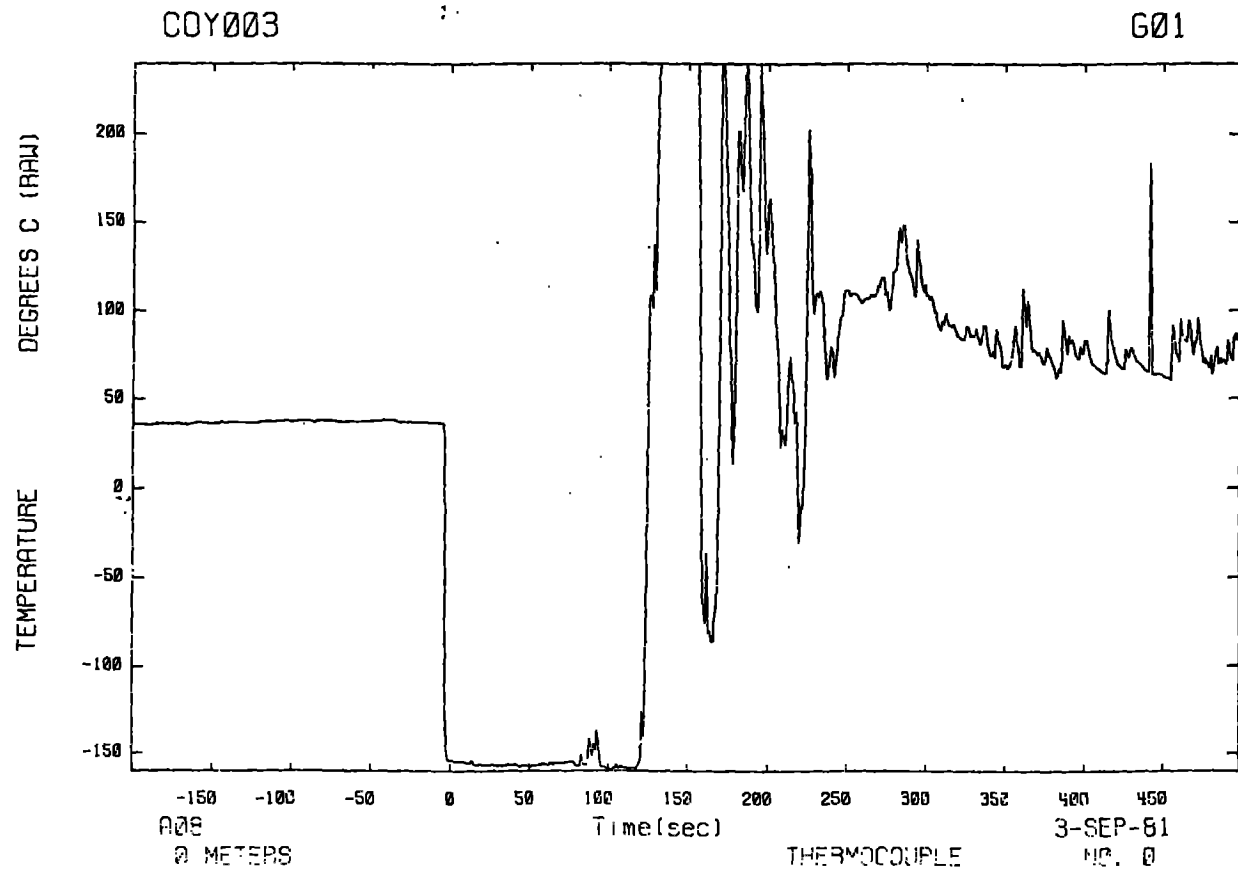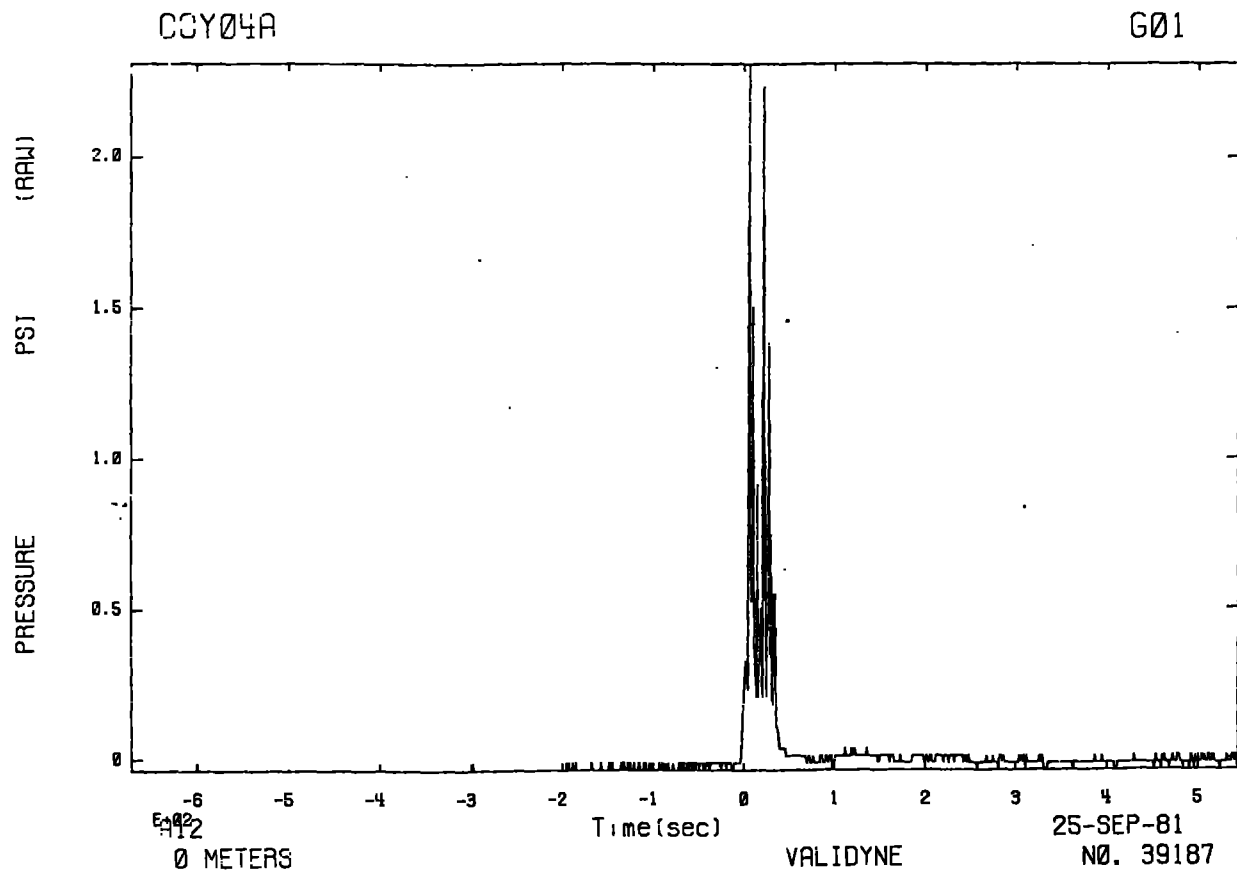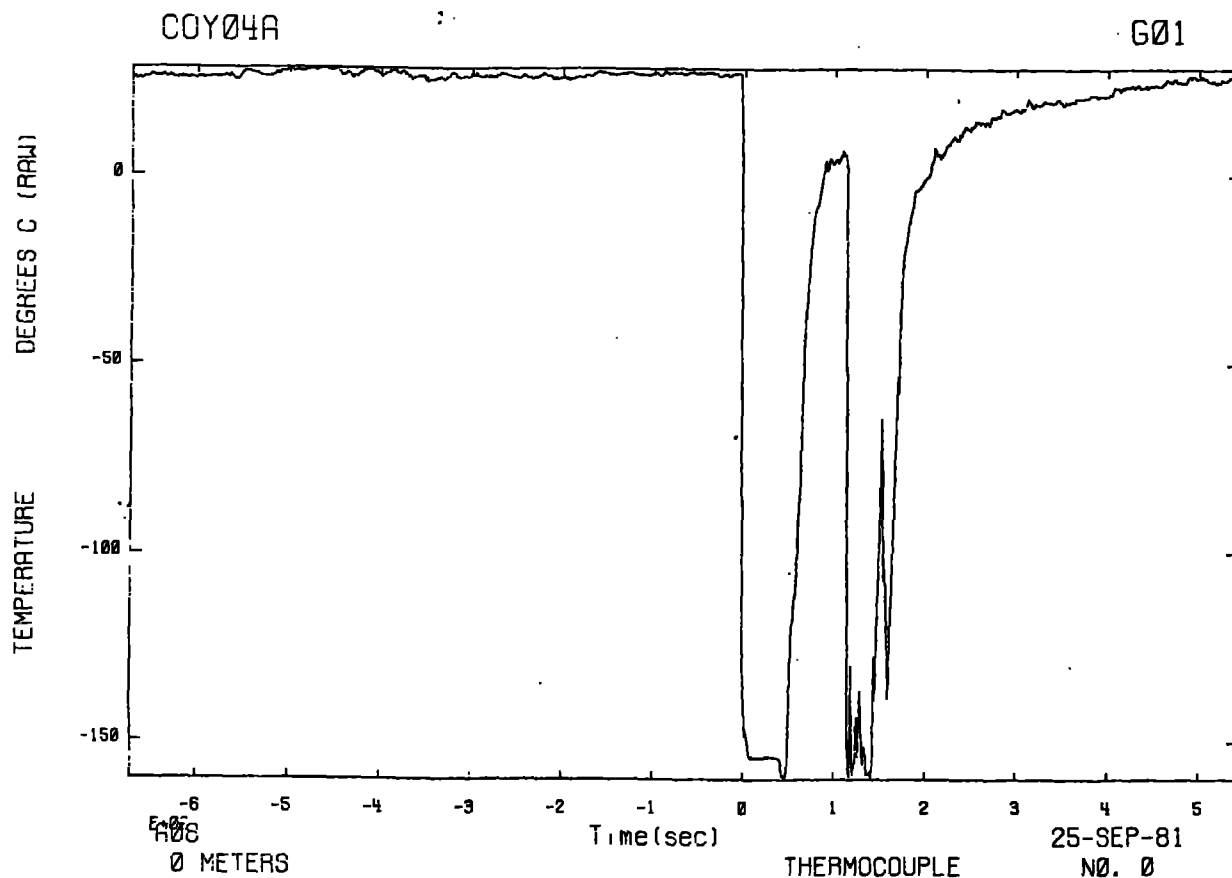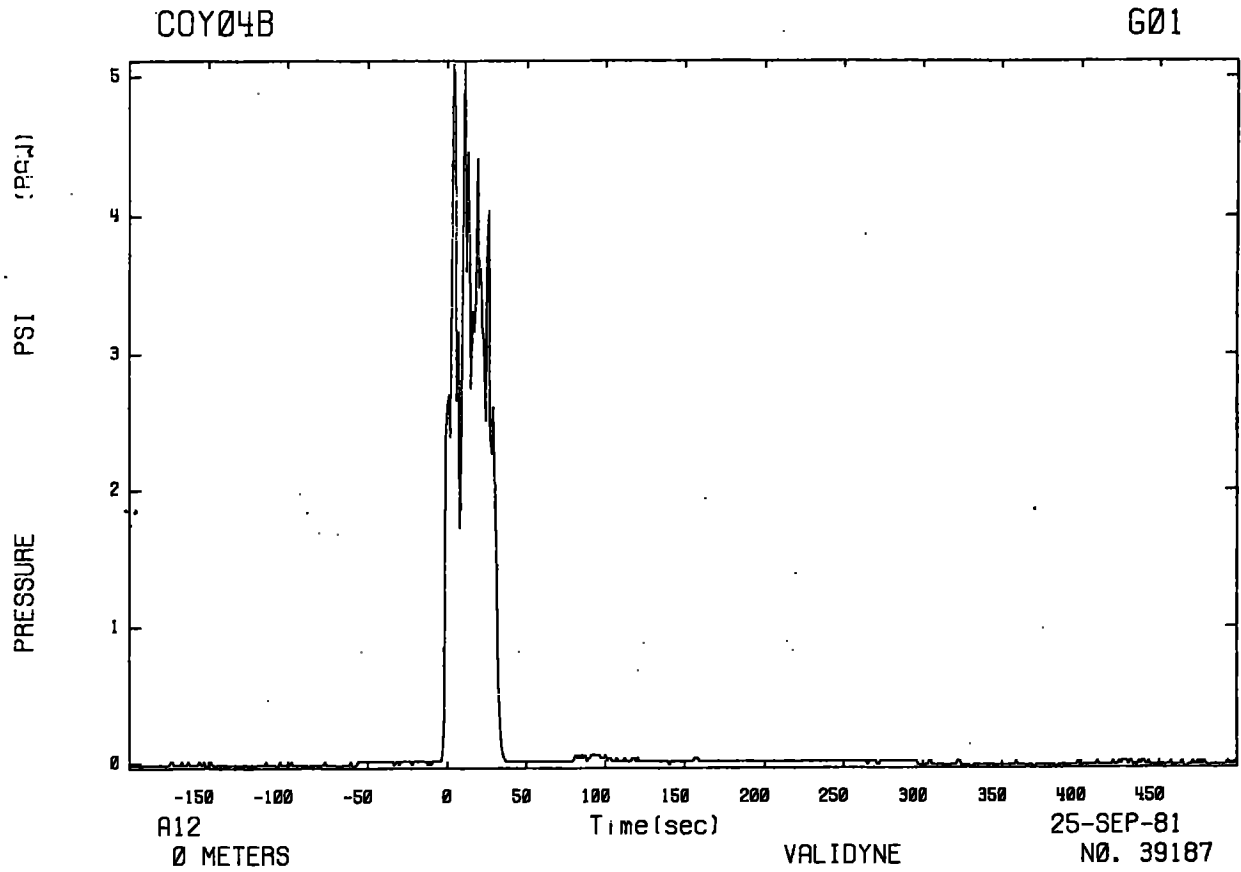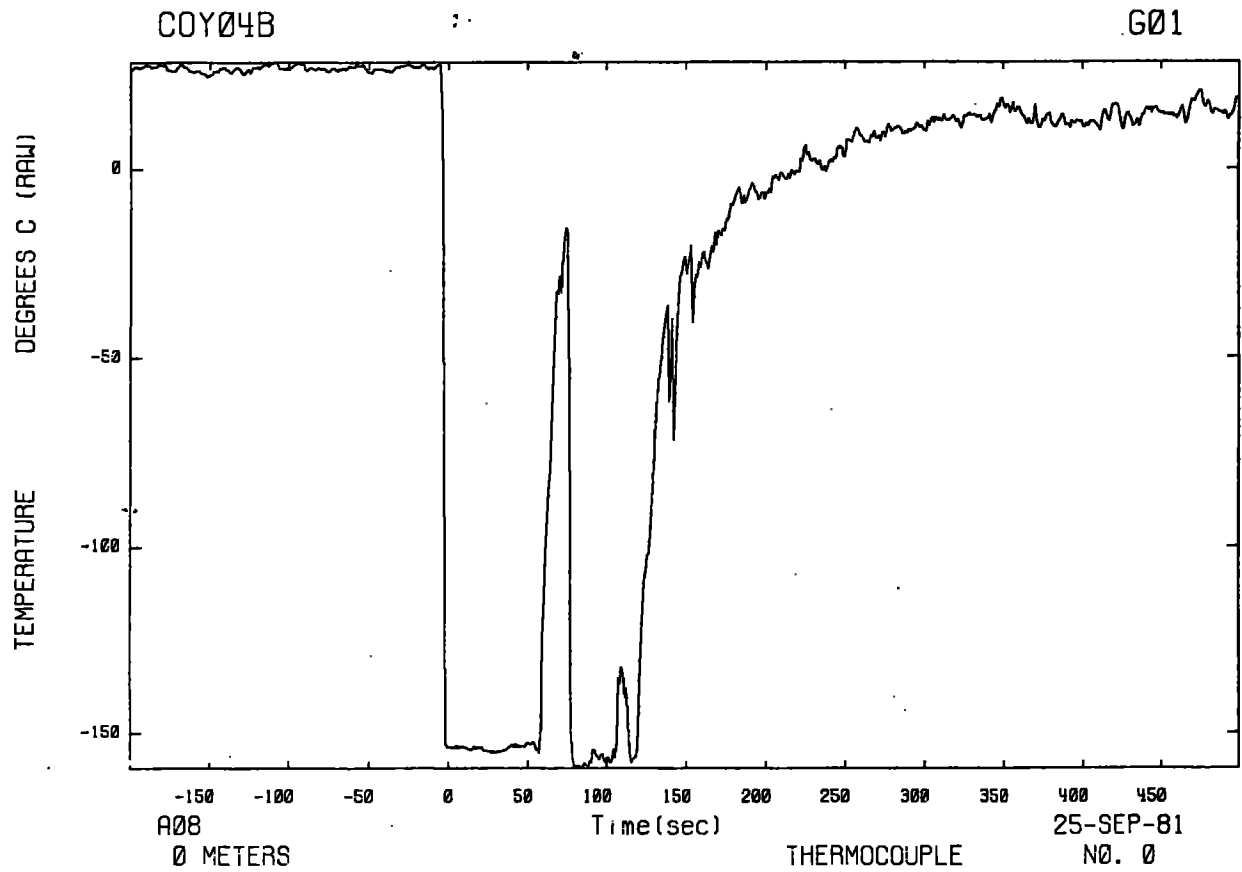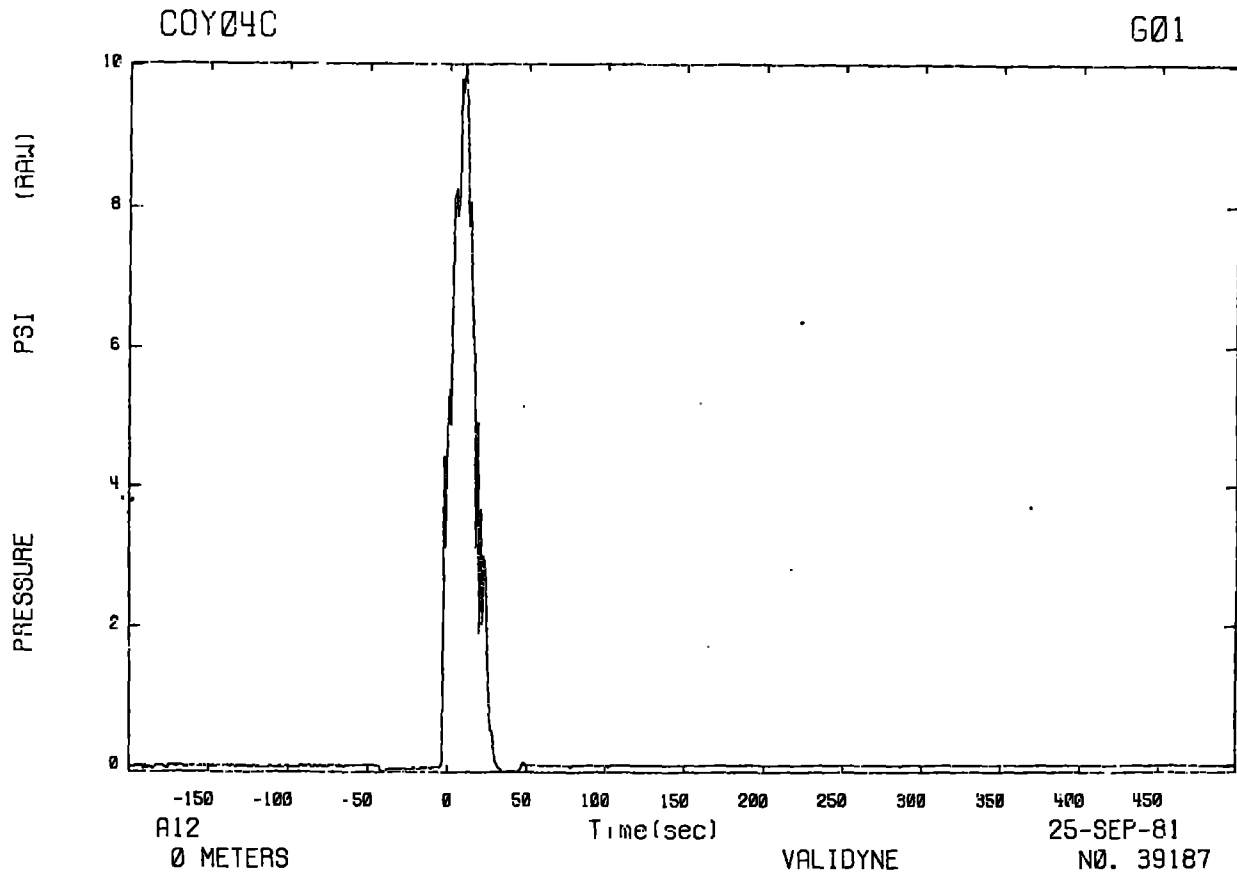
Fig. 49. LNG impact pressure and exit temperature during Coyote 4C.
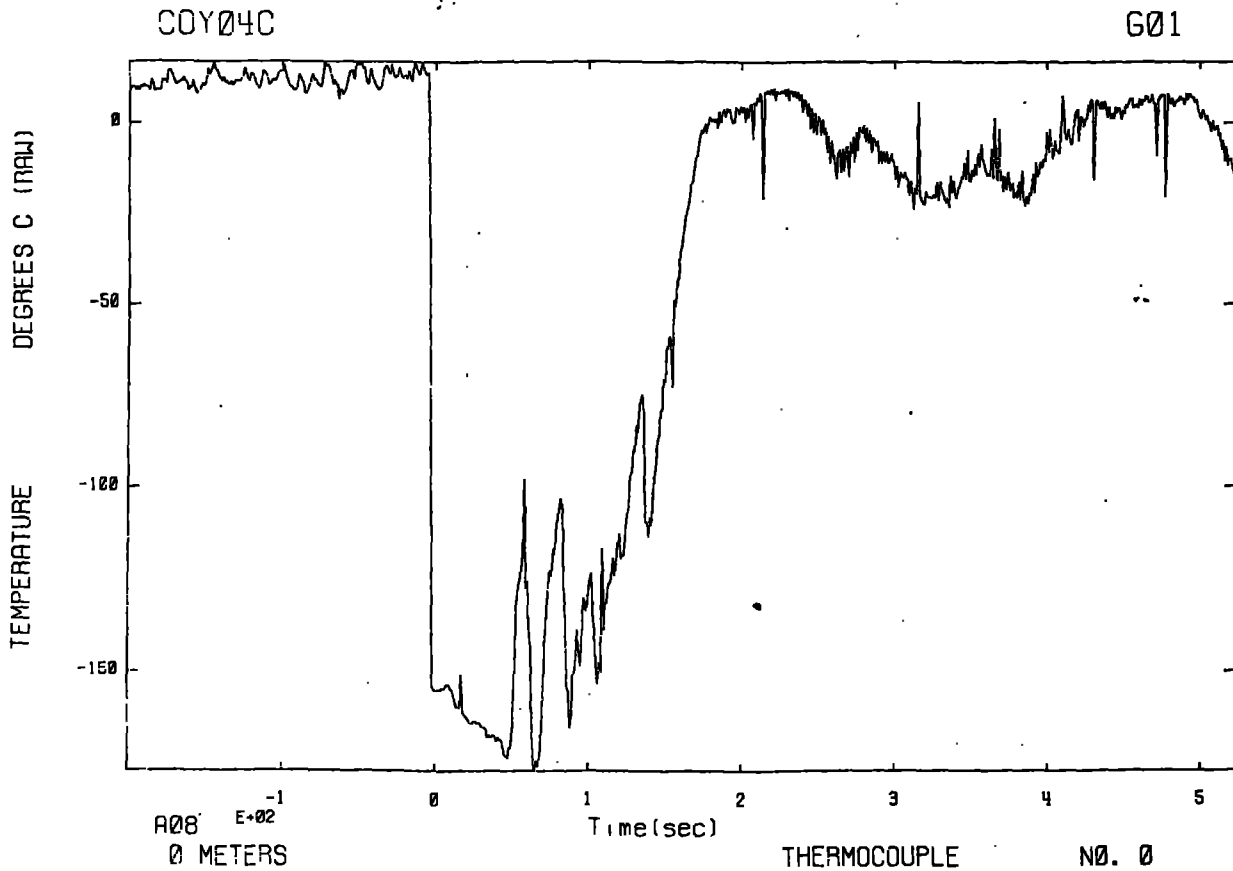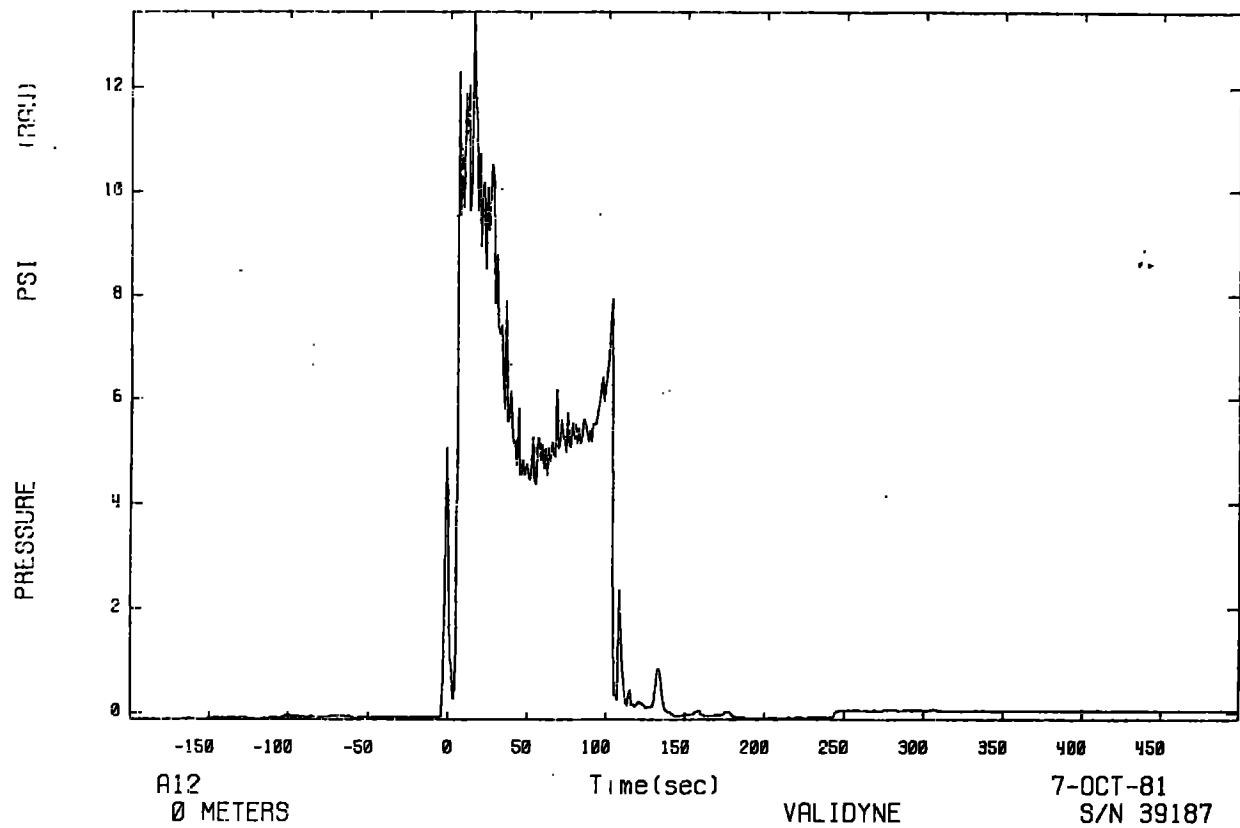
Fig. 50. LNG impact pressure and exit temperature during Coyote 5.
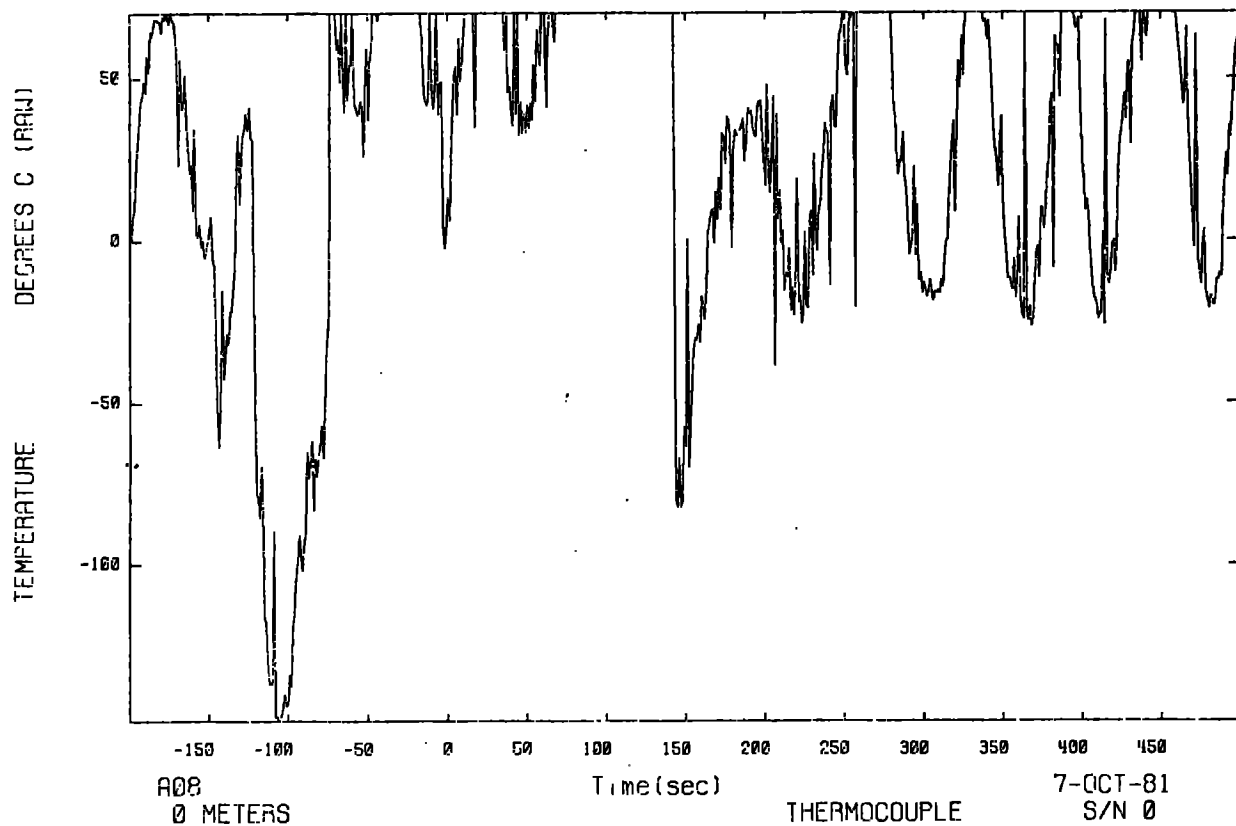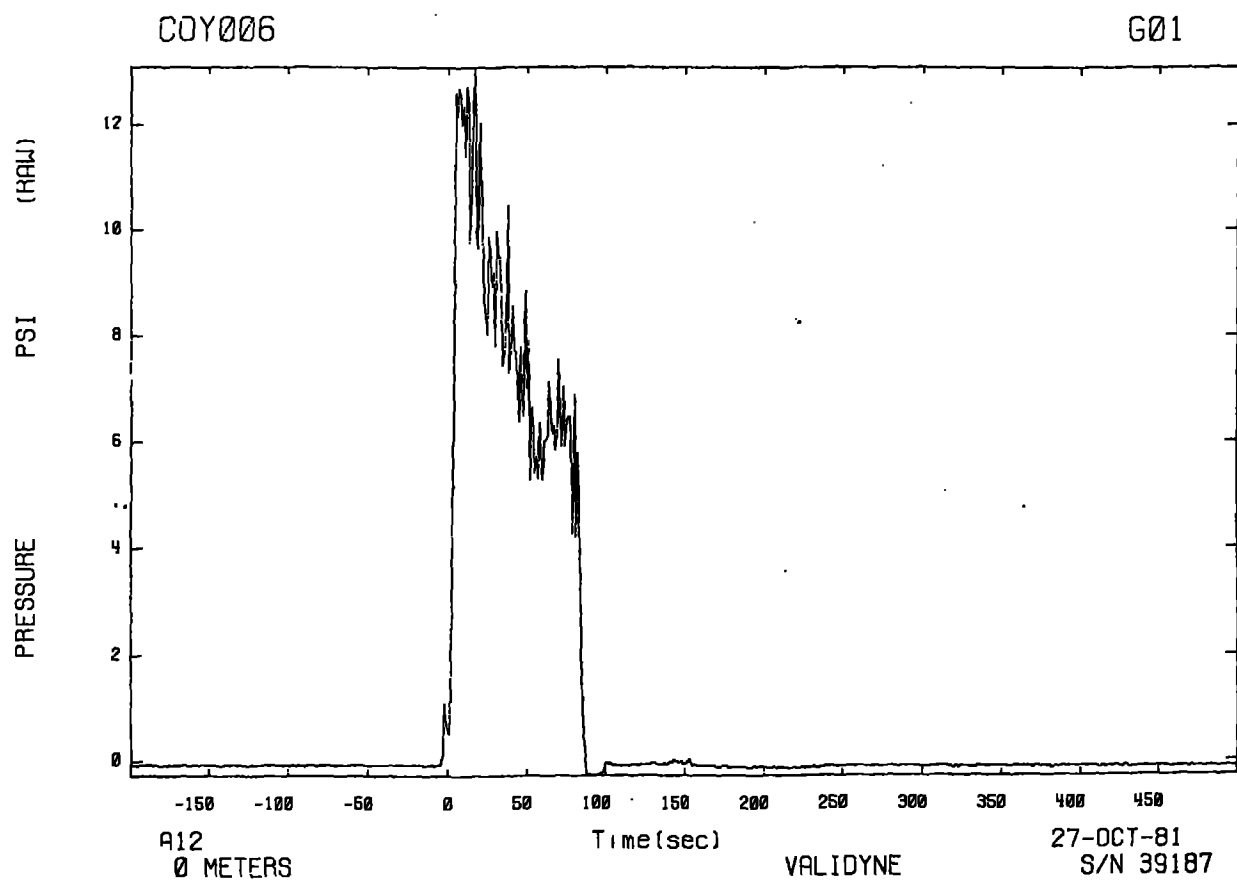
Fig. 51. LNG impact pressure and exit temperature during Coyote 6.
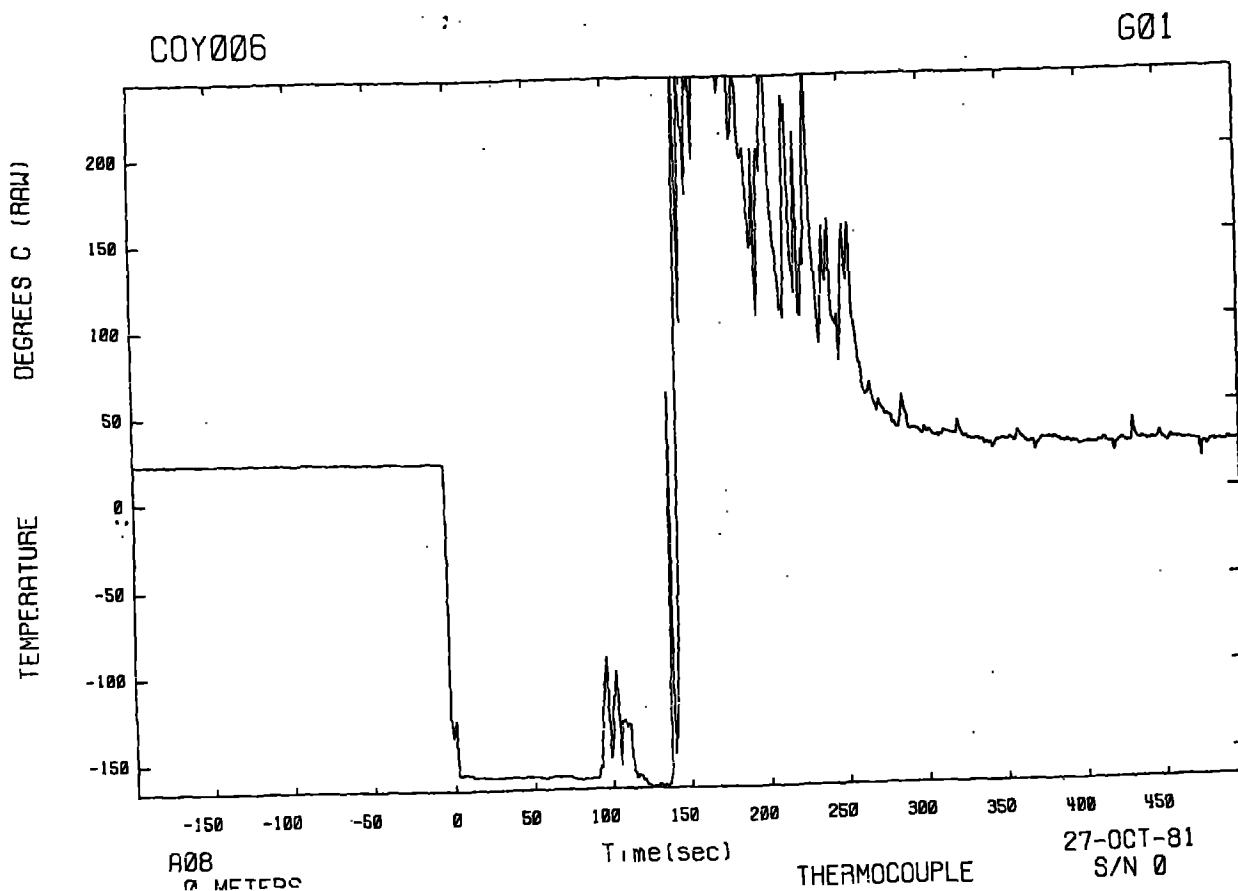
COY007   G01
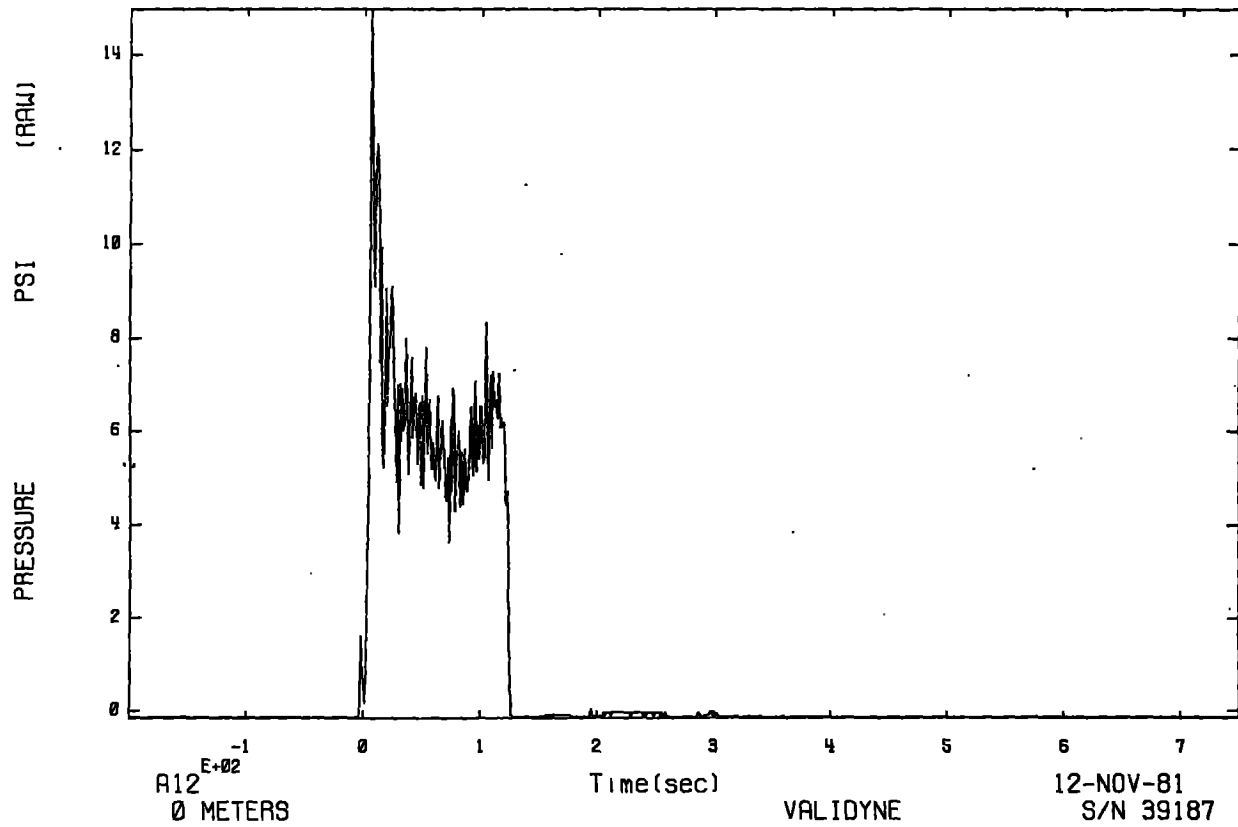
Fig. 52. LNG impact pressure and exit temperature during Coyote 7.

COY007   G01

COY08A   G01

A12
0 METERS   Time(sec)   VALIDYNE   13-NOV-81
                                                               S/N 39187

Fig. 53.   LNG impact pressure and exit temperature during Coyote 8A.

COY08A   G01

A08
0 METERS   Time(sec)   THERMOCOUPLE   13-NOV-81
                                                               S/N 0

Fig. 54. LNG impact pressure and exit temperature during Coyote 8B.

Fig. 55. LNG impact pressure and exit temperature during Coyote 8C.

COY09A   G01

A12
0 METERS   Time(sec)   VALICYNE   16-NOV-81
                                                                     S/N 39187

Fig. 56. LNG impact pressure and exit temperature during Coyote 9A.

COY09A   G01

0 METERS   Time(sec)   THERMOCOUPLE   16-NOV-81
                                                                     S/N 0

COY09B   G01

A12   Time(sec)   16-NOV-81
0 METERS   VALIDYNE   S/N 39187

Fig. 57.   LNG impact pressure and exit temperature during Coyote 9B.

COY09B   G01

A08   Time(sec)   16-NOV-81
0 METERS   THERMOCOUPLE   S/N 0

COY09C   G01

Fig. 58. LNG impact pressure and exit temperature during Coyote 9C.

COY09C   G01

COY10A   G01

Fig. 59. LNG impact pressure and exit temperature during Coyote 10A.

COY10A   G01

COY10B   G01
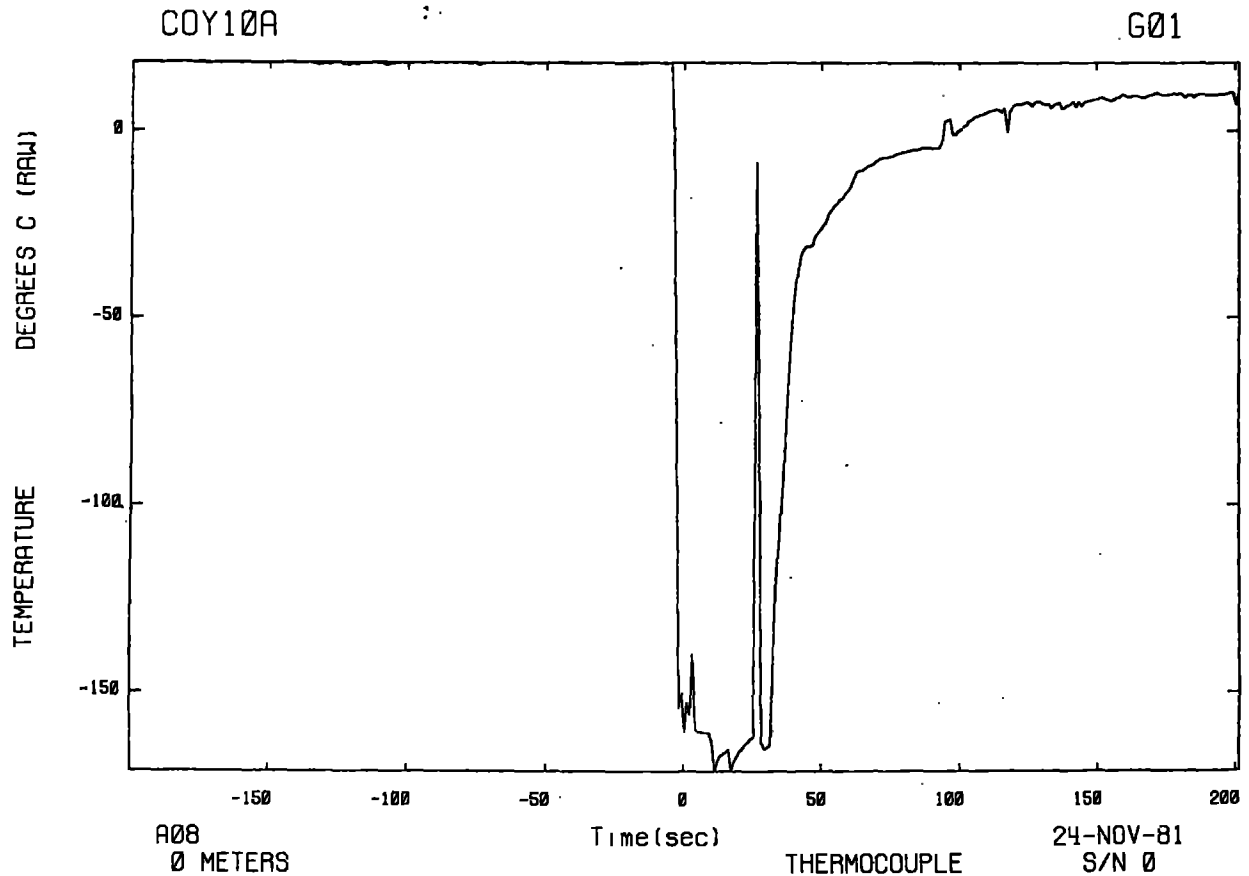
Fig. 60. LNG impact pressure and exit temperature during Coyote 10B.

Fig. 61. LNG impact pressure and exit temperature during Coyote 10C.
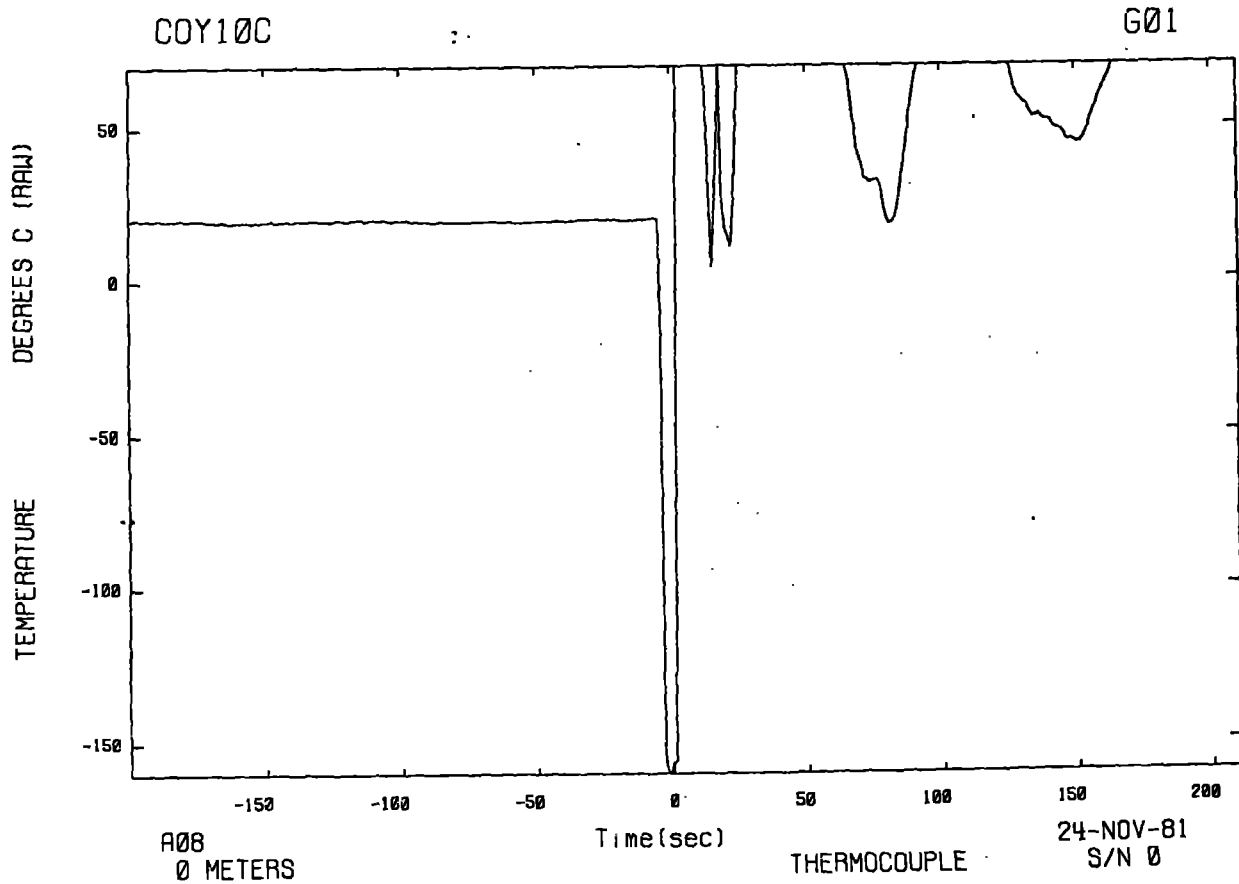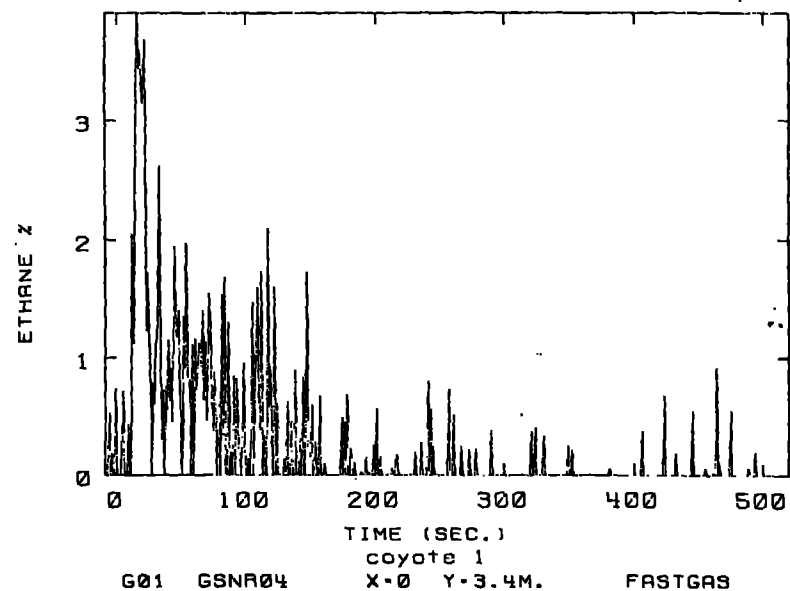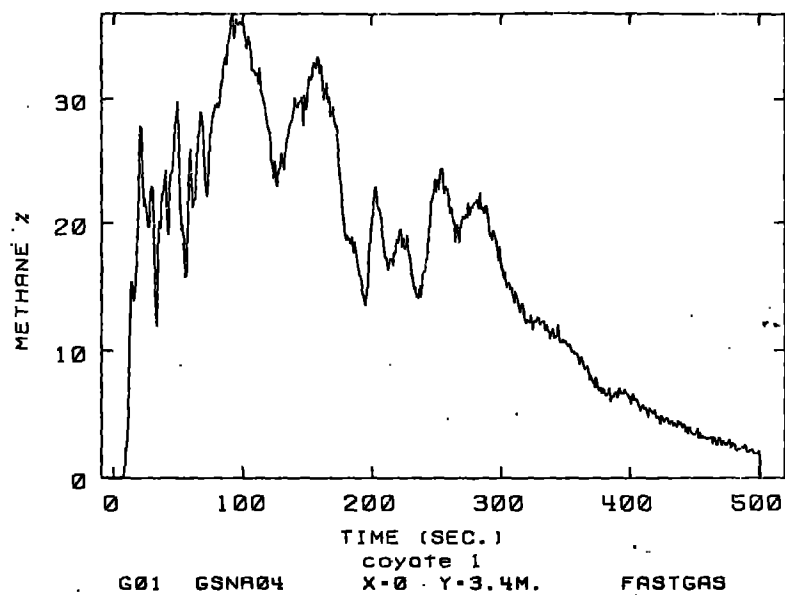
Fig. 62. Pond LNG vapor concentration during Coyote 1.
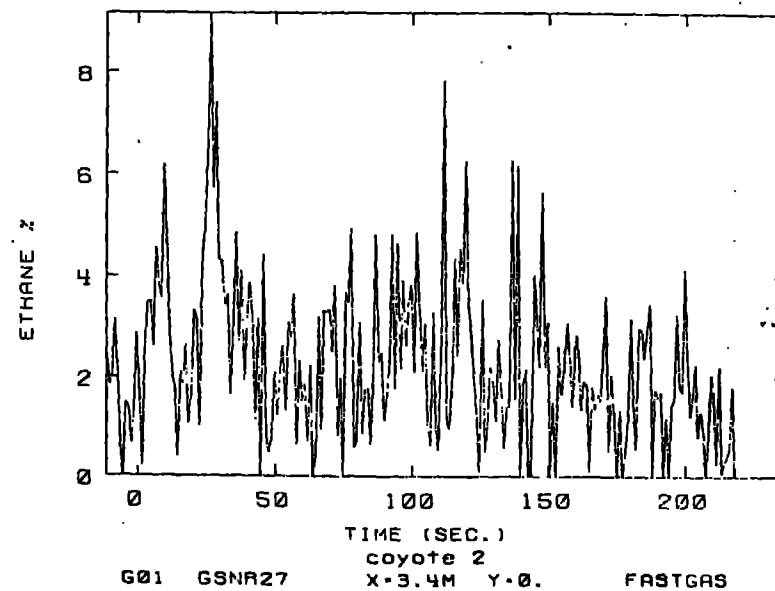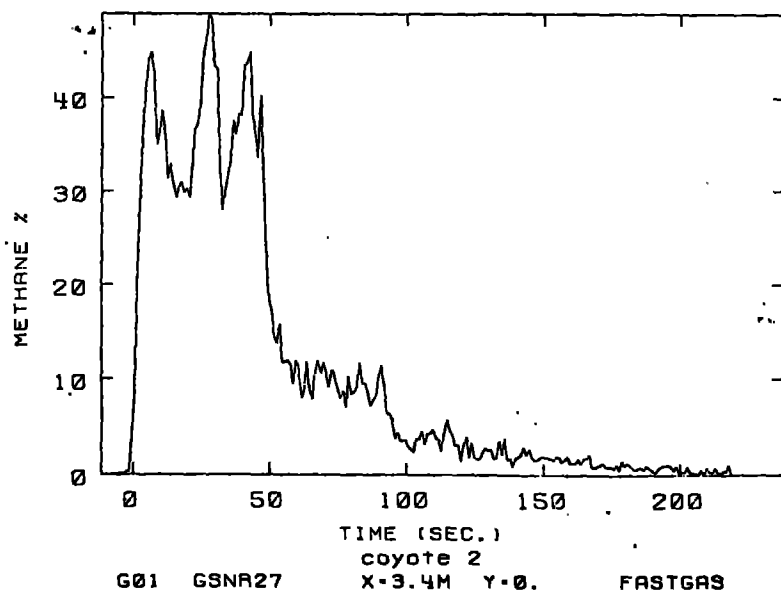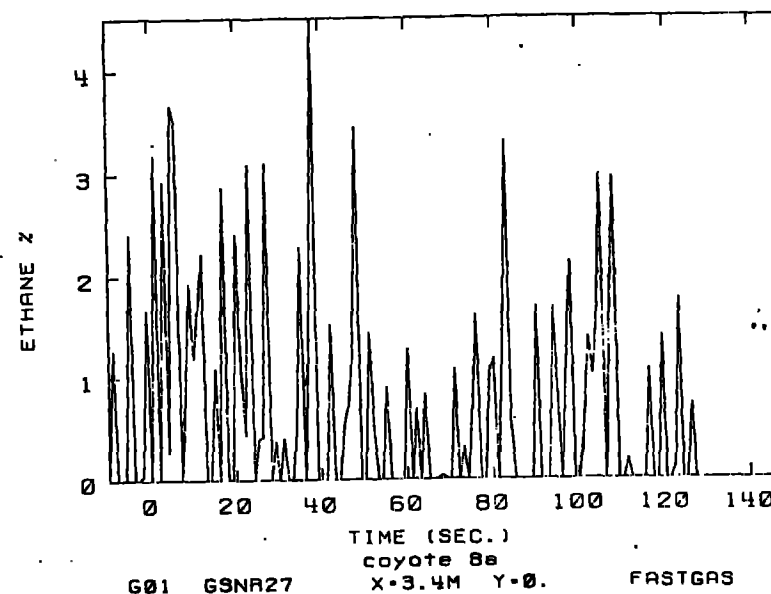

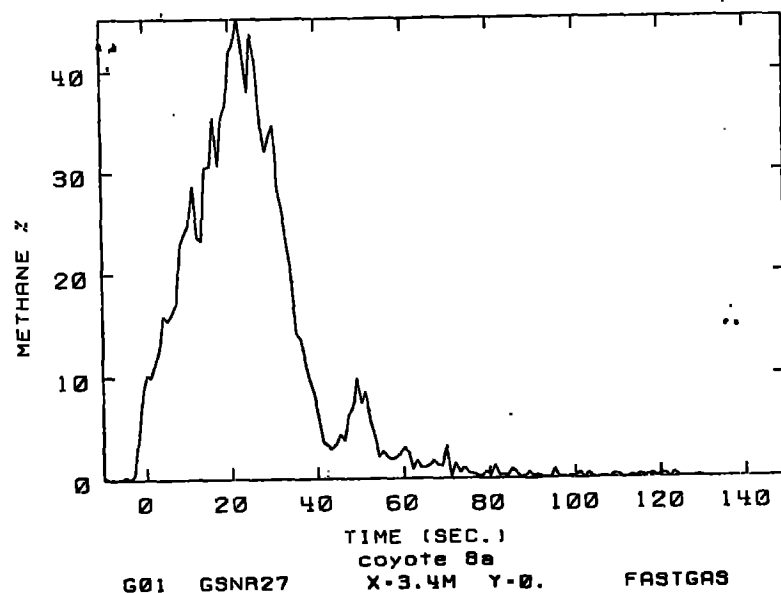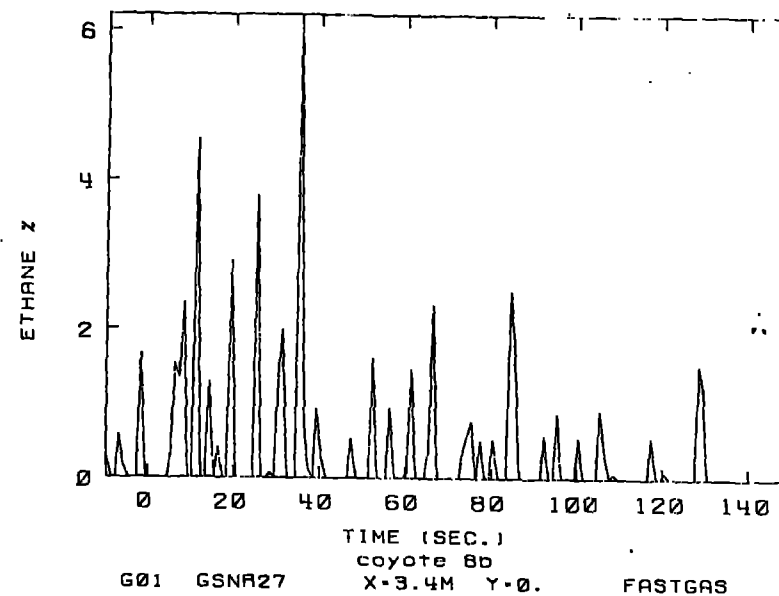Fig. 63. Pond LNG vapor concentration during Coyote 2.
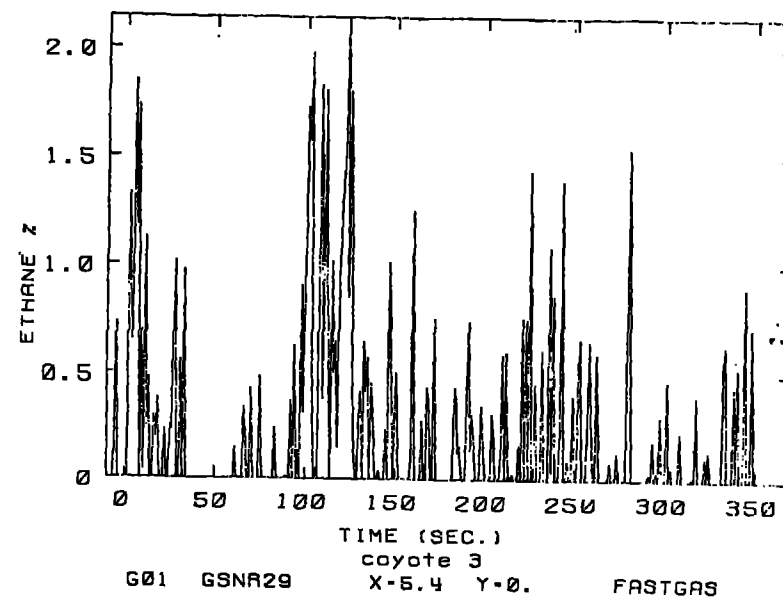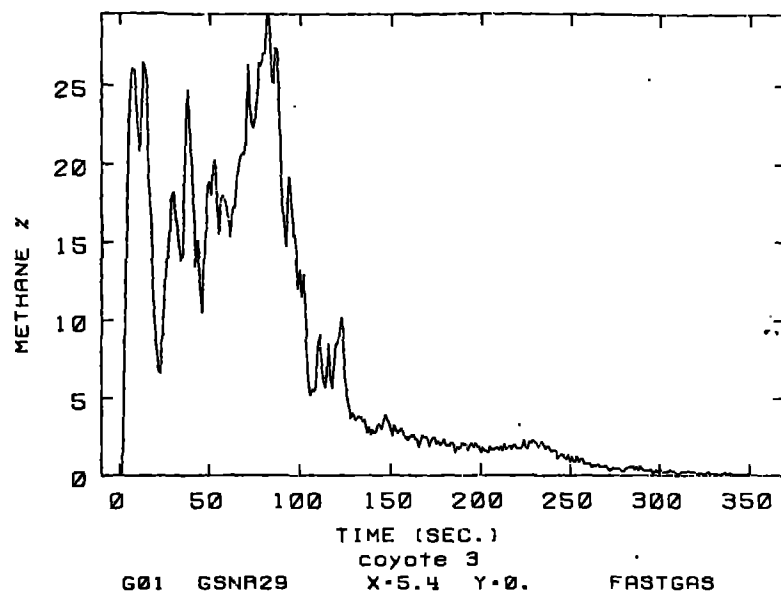
Fig. 64. Pond LNG vapor concentration during Coyote 3.
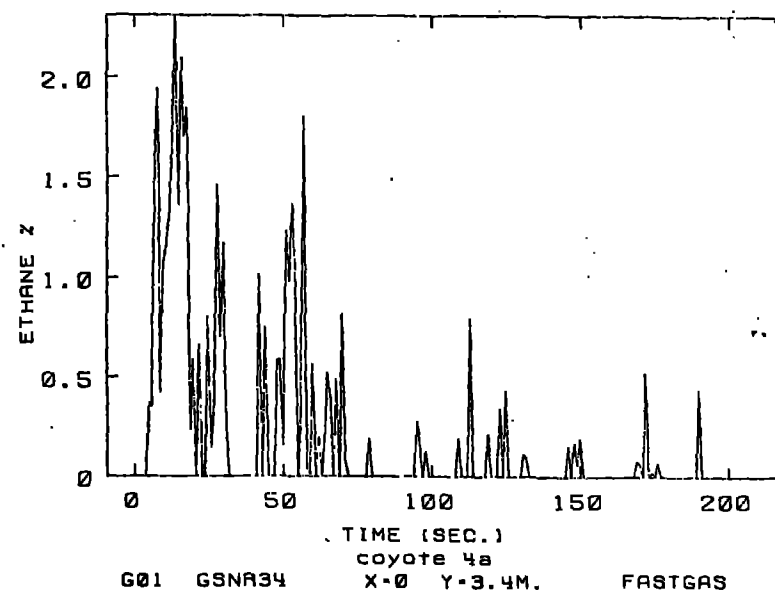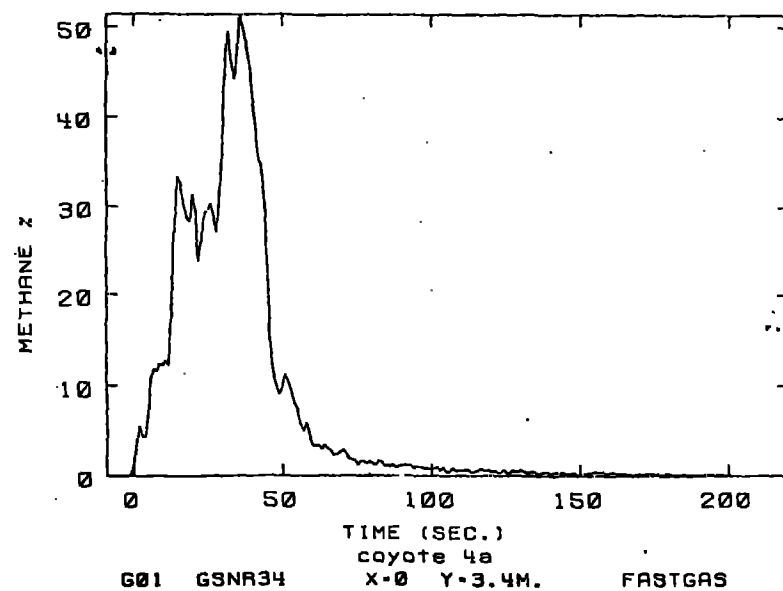
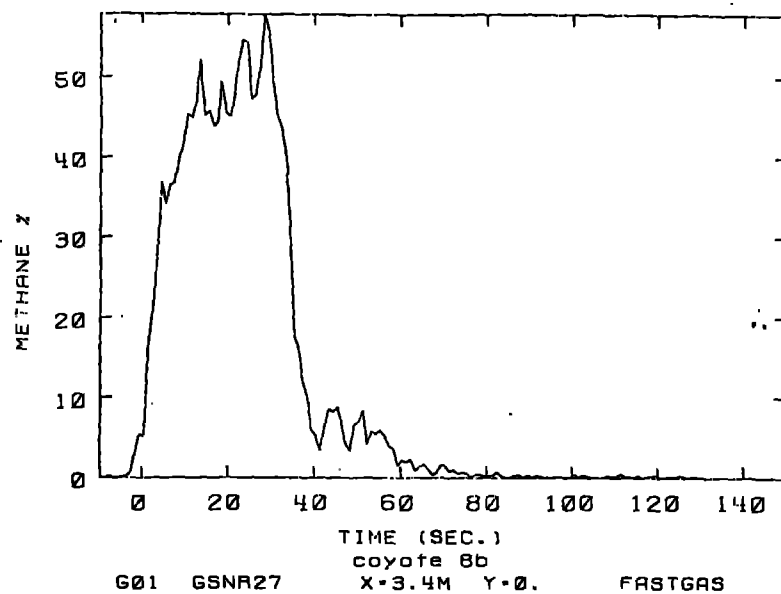Fig. 65. Pond LNG vapor concentration during Coyote 4A.
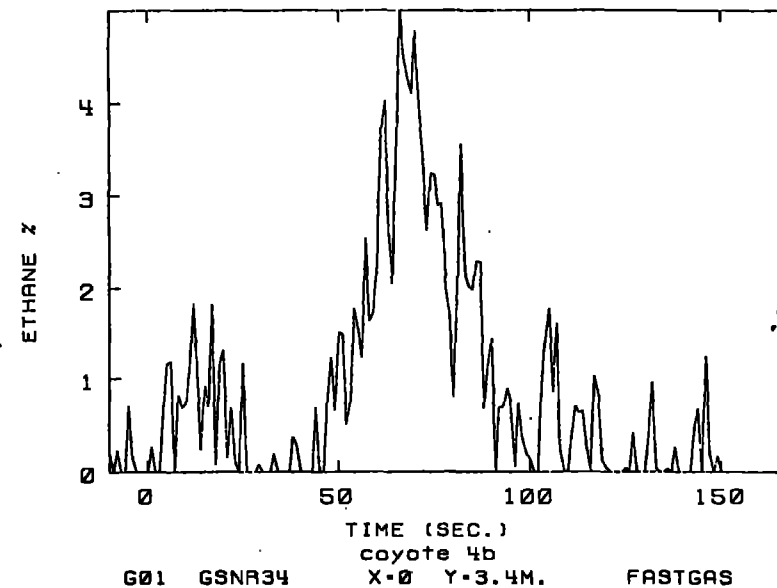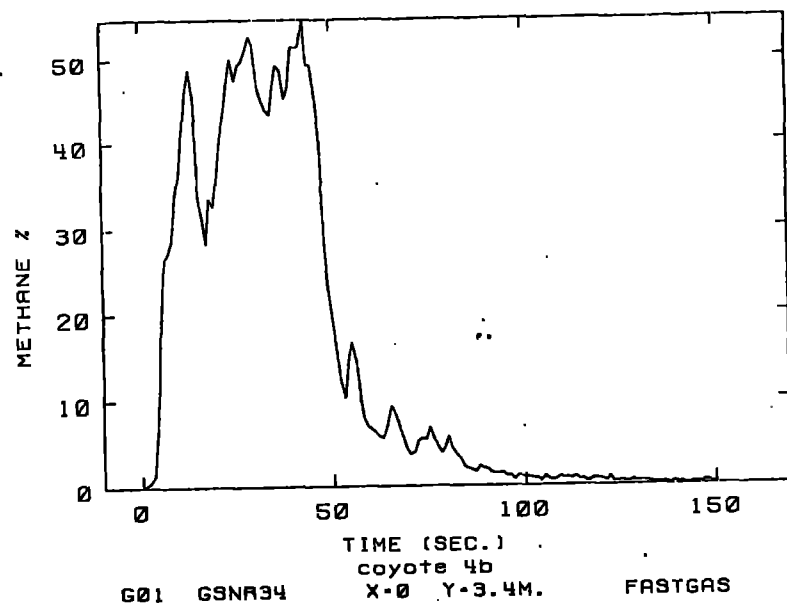
Fig. 66. Pond LNG vapor concentration during Coyote 4B.
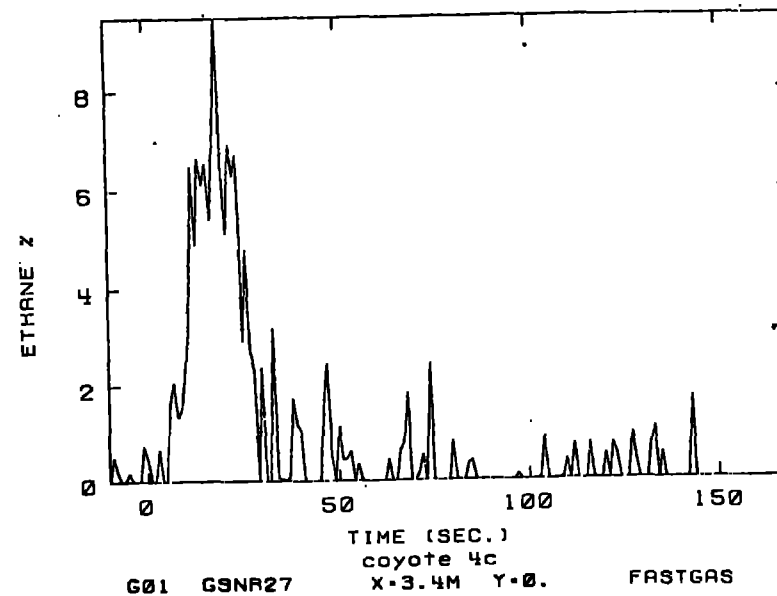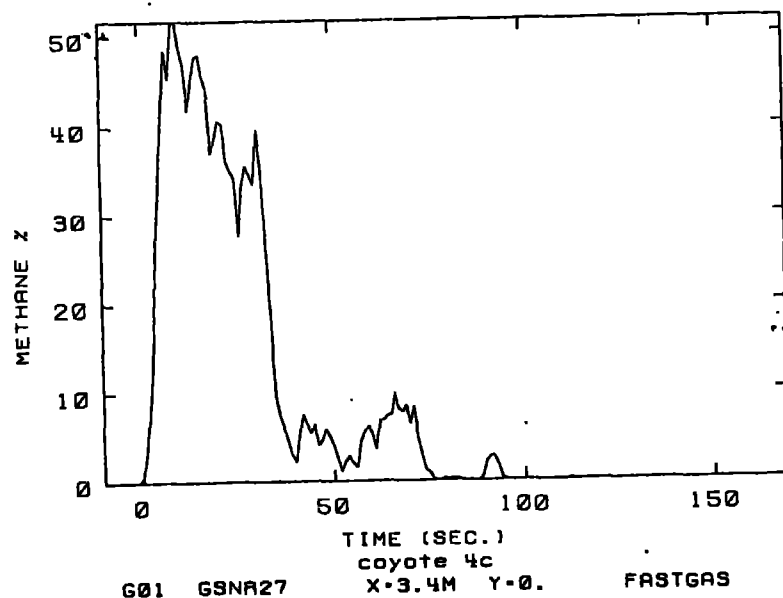
Fig. 67. Pond LNG vapor concentration during Coyote 4C.
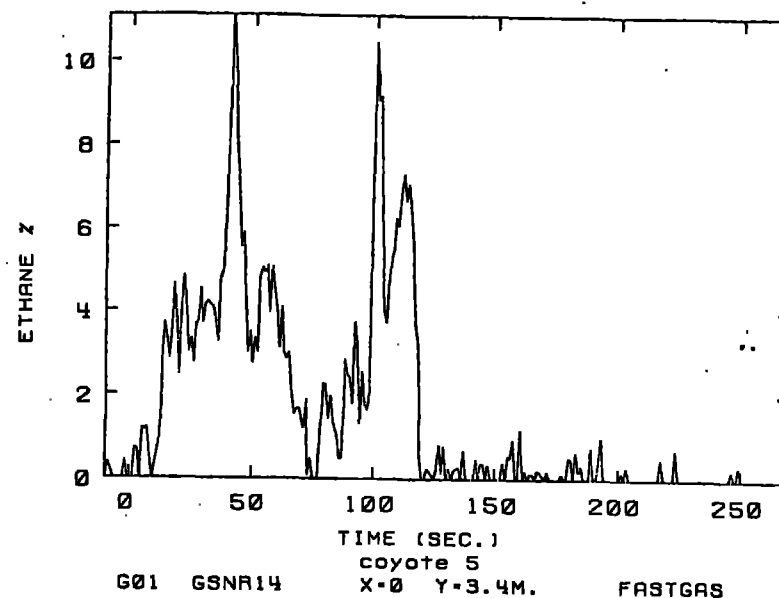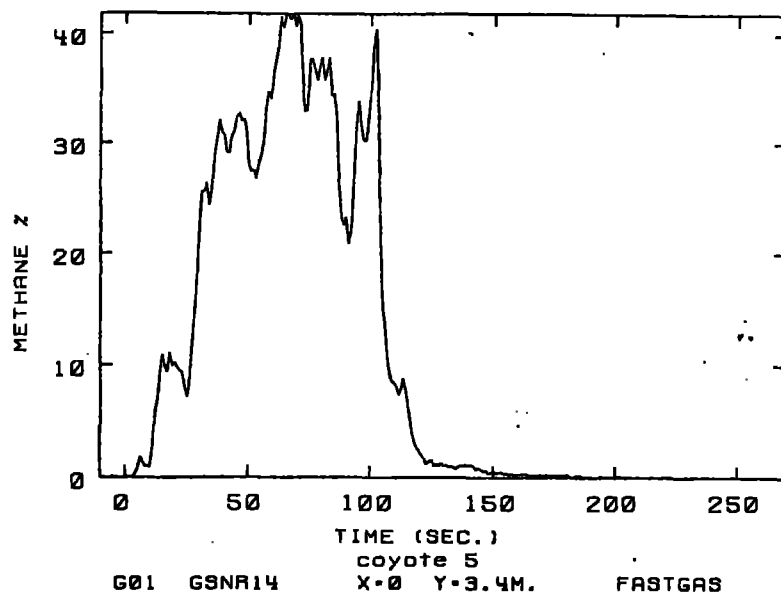
Fig. 68. Pond LNG vapor concentration during Coyote 5.
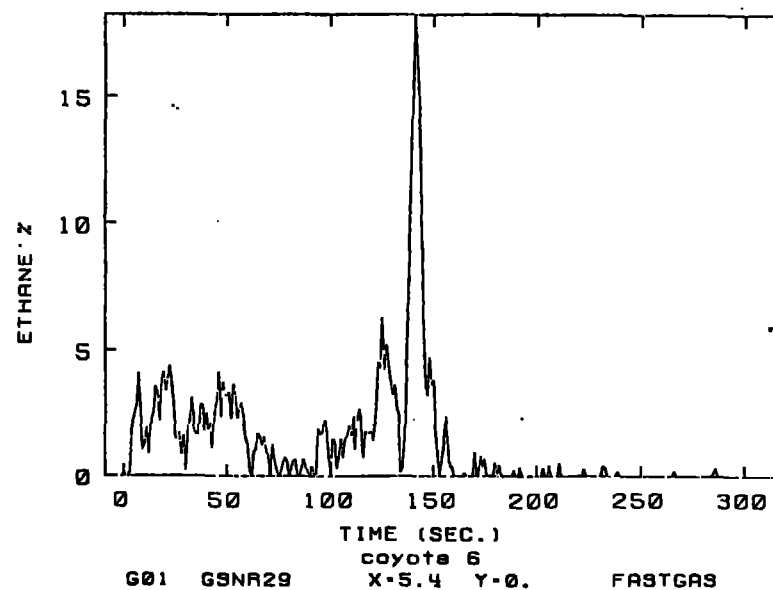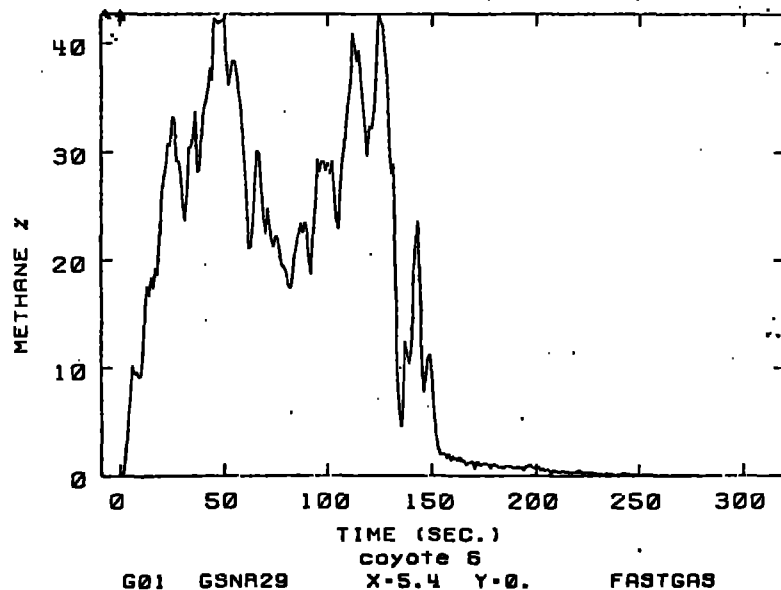
Fig. 69. Pond LNG vapor concentration during Coyote 6.
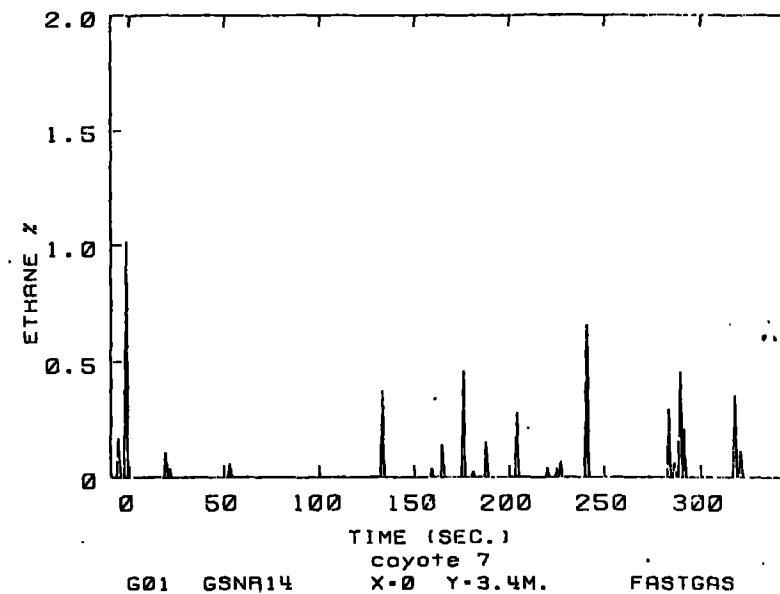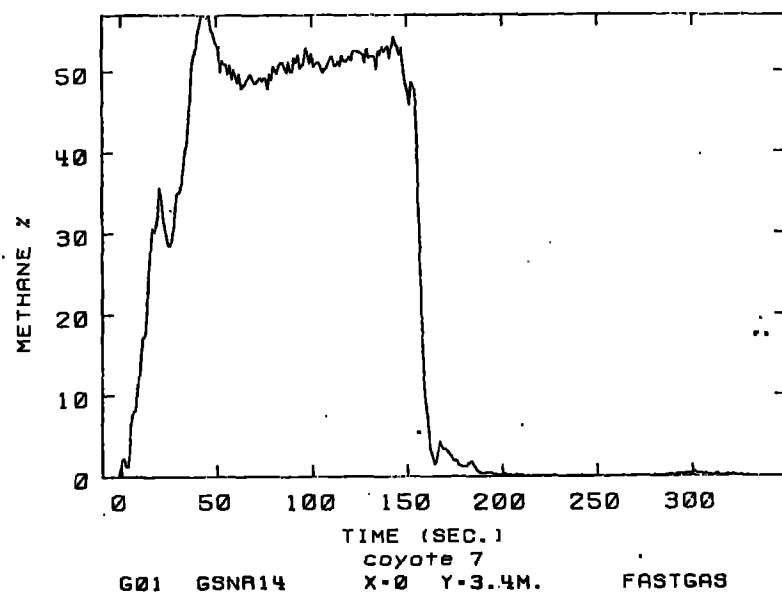
Fig. 70. Pond LNG vapor concentration during Coyote 7.

Fig. 71. Pond LNG vapor concentration during Coyote 8A.

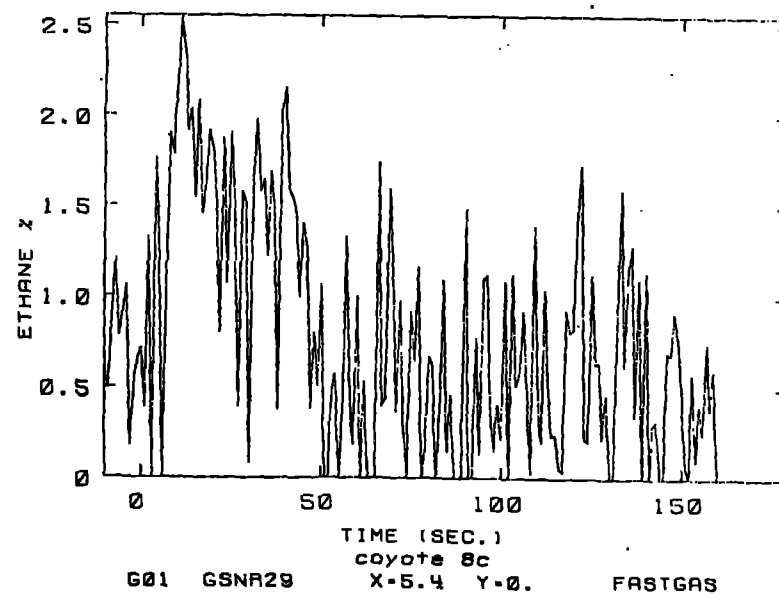Fig. 72. Pond LNG vapor concentration during Coyote 8B.
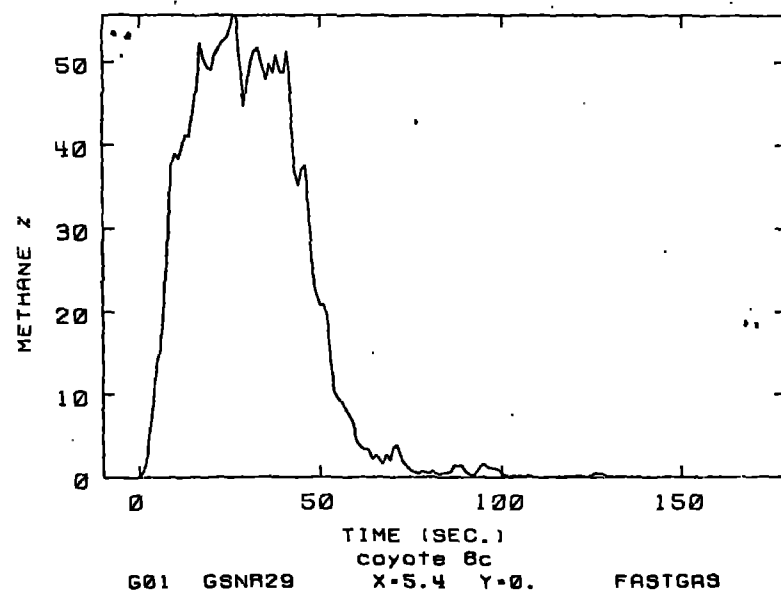

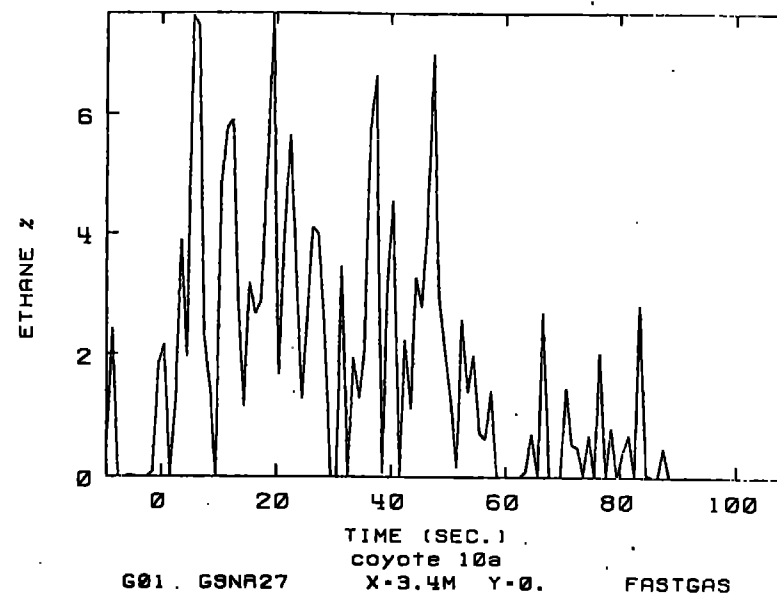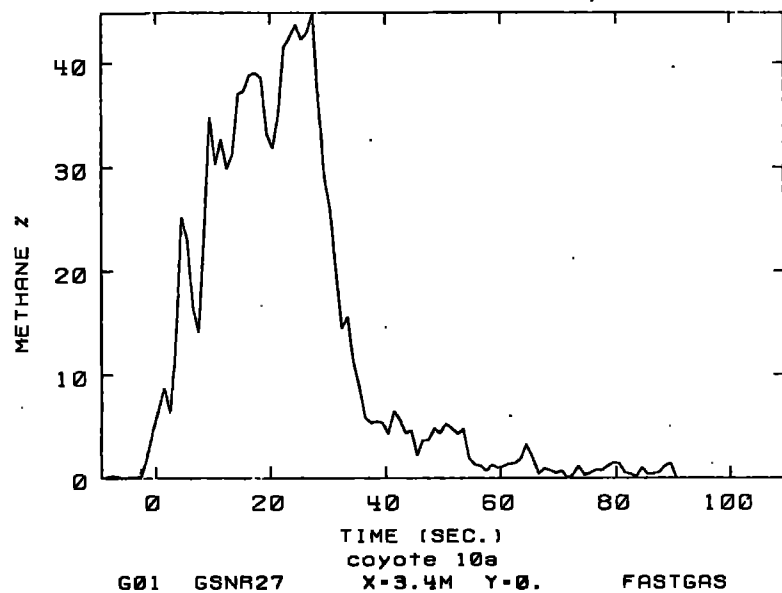Fig. 73. Pond LNG vapor concentration during Coyote 8C.

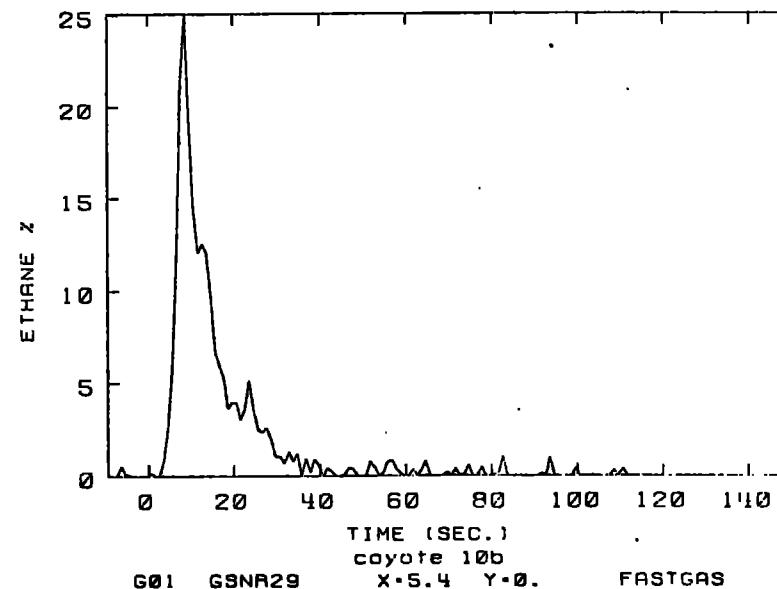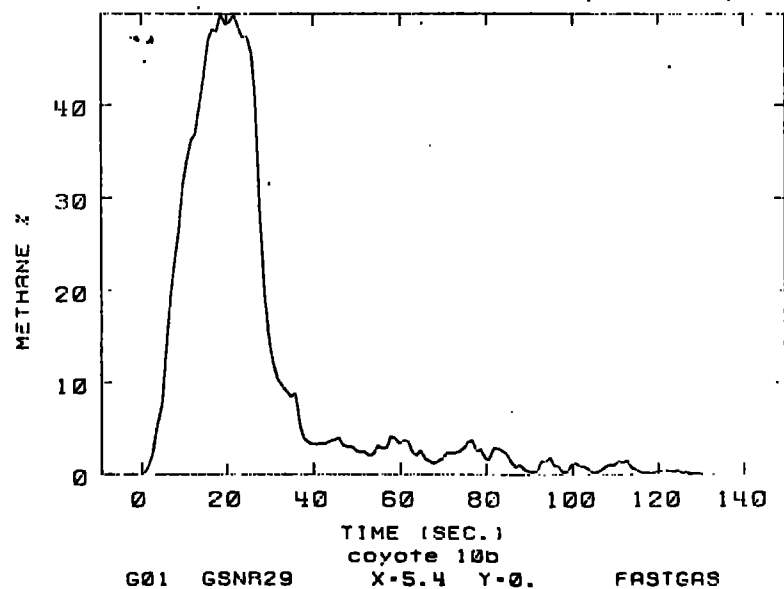Fig. 74. Pond LNG vapor concentration during Coyote 10A.

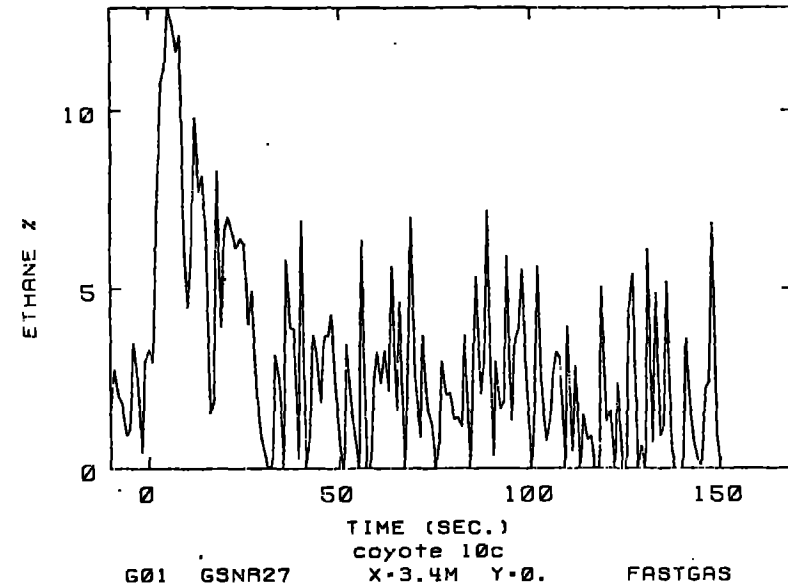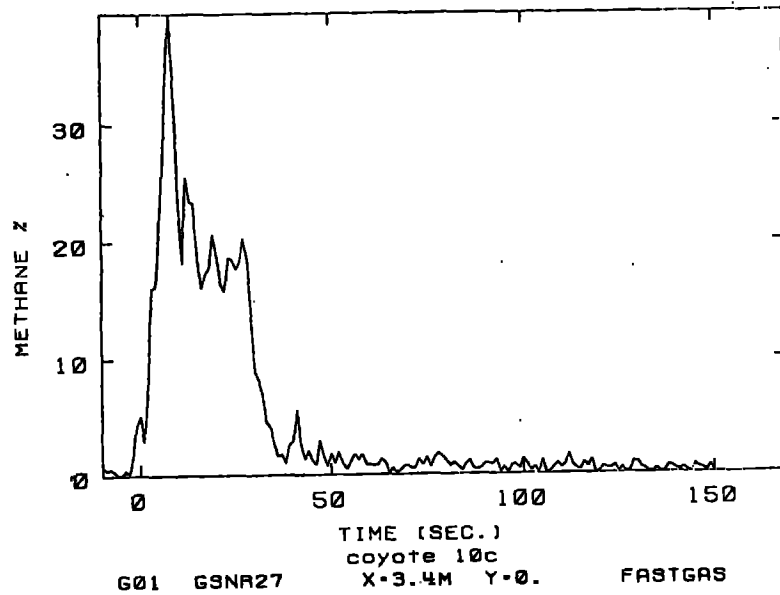Fig. 75. Pond LNG vapor concentration during Coyote 10B.

Fig. 76. Pond LNG vapor concentration during Coyote 10C.

The results of the LNG vapor concentrations directly above the pond are shown in Figs. 62-76. Although pond vapor samples were obtained at three locations as indicated in Fig. 5, for the sake of brevity, only one sample location per test is presented in this report. The choice of the location depended on the wind direction in effect for most of the spill. No data were obtained for the Coyote 9 spill as the gas detectors were not sensitive to nitrogen.

The results of the RPT tests have been analyzed and reported [17,18,19].

10. SUMMARY

The data in this report are in six categories: test parameters (Section 2), micrometeorology (Section 5 and Appendix 1), gas concentration (Section 6 and Appendices 2-4), vapor burn (Section 7 and Appendix 5), fire heat flux (Section 8), and RPT explosions (Section 9). Data presented for all these categories were obtained by the basic test facility instrumentation and by three arrays of instruments designed for the Coyote experiments. These three arrays are (1) wind-field stations deployed upwind and downwind of the spill pond, (2) gas and turbulence stations deployed mostly downwind of the spill pond, and (3) RPT diagnostics centered at the spill pond. Additional data relating to vapor burns were obtained by motion-picture cameras and IR imagers; only selected IR images are presented in this report. Additional fire heat-flux data were obtained by radiometers and are included in this report.

The RPT data are presented, mostly in summary form, for all 18 spills during the ten Coyote experiments. Large (> 1 kg TNT equivalent) RPT explosions were measured during Coyotes 4C and 5; a large (qualitative) explosion occurred during Coyote 1 but no quantitative measurements were made. Small explosions occurred during Coyotes 1, 2, 4A, and 10C.

The micrometeorological and gas concentration data are pertinent to the vapor dispersion during the vapor-burn experiments, and are presented for Coyotes 3, 5, and 6 when the gas and turbulence station array was fully operational. The atmospheric stability parameters are listed in Table 3, wind-field data are presented in Appendix 1, and gas concentration data in Appendices 2-4. Of these data, some are basic data (e.g., wind vectors and gas concentration time-histories at stations) and some are derived or constructed from data (e.g., atmospheric stability parameters, wind trajectories, and gas

150r/23r

concentration contours). The gas concentration time histories and contours constitute the major results and bulk of this work. Data for humidity enhancement (Section 5.2) and surface heat flux (Section 5.3) during passage of the gas cloud and (for heat flux only) the vapor burn data are also given.

Flame arrival times at different sensors and resultant estimates of the horizontal extent of the fires are presented in Section 7 for Coyotes 3, 5, 6, and 7. In addition, a selected set of colored IR images for Coyotes 6 and 7 are presented in Appendix 5.

Internal fire heat-flux data from ground surface sensors and protected calorimeters at 1 m are presented for Coyotes 3 and 5-6 in Section 8. Heat-flux data from external radiometers are also presented in Section 8 for Coyotes 3, 6, and 7. These radiometers were not protected as were the calorimeters and they were intended for use from outside the fires; some of them were close to the fire (as in Coyote 3) and some were inside the fire (Coyotes 6 and 7).

11. REFERENCES

1. R.P. Koopman, J. Baker, R.T. Cederwall, H.C. Goldwire, Jr., W.J. Hogan, L.M. Kamppinen, R.D. Kiefer, J.W. McClure, T.G. McRae, D.L. Morgan, L.K. Morris, M.W. Spann, Jr., and C.D. Lind, Burro Series Data Report LLNL/NWC 1980 LNG Spill Tests, Lawrence Livermore National Laboratory, Livermore, Calif., UCID-19075 (December 1982).

2. C.A. Paulson, "The Mathematical Representation of Wind Speed and Temperature Profiles in the Unstable Atmospheric Surface Layer," Journal of Applied Meteorology, 9 857-861 (December 1970).

3. A.J. Dyer, "A Review of Flux-Profile Relationships," Boundary-Layer Meteorology, 7, 363-372 (1974).

4. H.H. Lettau, "Wind and Temperature Profile Prediction for Diabatic Surface Layers Including Strong Inversion Cases," Boundary-Layer Meteorology, 17, 443-464 (1979).

5. C.D. Lind and J.C. Whitson, Liquefied Gaseous Fuels Safety and Environmental Control Assessment Program: Second Status Report, DOE/EV-0085, Report R (October 1980).

6. J. Baker, The LGF Data Acquisition System, Lawrence Livermore National Laboratory, Livermore, Calif., UCID-19431, (July 1982).

7. S.E. Jones and D.R. Ries, A Relational Data Base Management System for Scientific Data, Lawrence Livermore National Laboratory, Livermore, Calif., UCRL-80769 (1978).

8. L.K. Morris, XPLT: Gas Concentration Contour Plotting Scheme, Lawrence Livermore National Laboratory, Livermore, Calif, to be published.

9. K. O'Hair, P. Keller, J. Rowe, and G. Cronshagen, GRAFLIB User Manual, LCSD-425, Lawrence Livermore National Laboratory, 1982.

10. R.P. Koopman, Liquefied Gaseous Fuels Safety and Environmental Control Assessment Program: A Status Report, DOE/EV-0036, Report K (May 1979).

11. R.P. Koopman, B.R. Bowman, and D.L. Ermak, Liquefied Gaseous Fuels Safety and Environmental Control Assessment Program: Second Status Report, DOE/EV-0085, Report P (October 1980), and Lawrence Livermore National Laboratory, Livermore, Calif., UCRL-52876 (1980).

12. G.E. Bingham, R.D. Kiefer, C.H. Gillespie, T.G. McRae, H.C. Goldwire, Jr, and R.P. Koopman, A Portable, Fast-Response Multiwavelength Infrared Sensor for Liquefied Natural Gas Vapors, Lawrence Livermore National Laboratory, Livermore, Calif., UCRL-84850, Rev. 1 (1982). Rev. Sci. Instrum.

13. R.A. Diderrich. K.M. Barrett, and R.M. Cionco, Evaluation of Several Wire Mesh Screens for the Protection and Ventilation of Meteorological Sensors, Atmospheric Sciences Laboratory, U.S. Army Electronics Command, White Sands Missile Range, New Mexico, ECOM-5542 (1974).

150r/23r

14. J.M. Conley, J.J. Simmonds, R.A. Britten, and M. Sinna, Liquefied Gaseous Fuels Safety and Environmental Control Assessment Program: Second Status Report, DOE/EV-0085, Report L (October 1980).

15. J.E. Bristow, E.L. Doak, and S.B. Brewster, Jr., Thermal Infrared Study of Liquefied Gaseous Fuel Burn Tests Coyote 6 and 7 - 1981, EG&G, MRSD-8304 (1983).

16. D.L. Ermak, H.C. Goldwire, W.J. Hogan, R.P. Koopman, and T.G. McRae, Results of 40-m^3 LNG Spills Onto Water, Lawrence Livermore National Laboratory, Livermore, CA, UCRL-87640, May 1982; presented at the 2nd Symposium on Heavy Gases and Risk Assessment, Battelle-Institute e.V., Frankfurt, Germany, May 25-26, 1982.

17. T.G. McRae, Preliminary Analysis of RPT Explosions Observed in the LLNL/NWC LNG Spill Tests, Lawrence Livermore National Laboratory, Livermore, Calif., UCRL-87564 (May 1982). Presented at the GRI LNG Safety Research Workshop at the Massachusetts Institute of Technology, Boston, March 22-24, 1982.

18. T.G. McRae, Large-Scale RPT Explosions, Lawrence Livermore National Laboratory, Livermore, Calif., UCRL-88688 (1983). Presented at the 3rd Multi-Phase Flow and Heat Transfer Symposium, Miami Beach, Florida, April 18-20, 1983.

19. T.G. McRae and H.C. Goldwire, Analysis of Large-Scale LNG/Water RPT Explosions, Lawrence Livermore National Laboratory, Livermore, Calif., UCRL-88421 (1983). Submitted to the J. Haz. Mat.